

**Observations of Magnetic Reconnection and Plasma
Dynamics in Mercury's Magnetosphere**

by

Gina A. DiBraccio

A dissertation submitted in partial fulfillment
of the requirements for the degree of
Doctor of Philosophy
(Atmospheric, Oceanic and Space Sciences)
in The University of Michigan
2014

Doctoral Committee:

Professor James A. Slavin, Co-Chair
Professor Thomas H. Zurbuchen, Co-Chair
Professor Daniel N. Baker, University Colorado, Boulder
Lecturer Suzanne M. Imber, University of Leicester
Professor Mark Kushner

© Gina A. DiBraccio 2014
All Rights Reserved

For Mom and Dad:
Who gave me a telescope and told me to reach for the stars.
Thanks for being my biggest supporters.
This is for you.

ACKNOWLEDGEMENTS

There are truly no words to fully express the overwhelming gratitude I feel towards everyone that has encouraged me throughout my career thus far. This journey began long before the five years of my Ph.D. program and it would not have been possible without their support.

I would like to start by thanking my advisors, Jim Slavin and Thomas Zurbuchen. I still wonder how I was lucky enough to acquire not one, but two great role models who continue to inspire me on a daily basis. I will never be able thank them enough for giving me this opportunity and continuing to believe in me. Jim has provided me with countless hours of mentorship and discussion – both in science and life. His enthusiastic demeanor and contagious passion for the field have encouraged me even when I was doubtful of my own capabilities. Jim has had a huge impact on my graduate experience and for that I am very grateful. Thomas has offered essential advice that I will carry with me throughout my career. He has supported me through struggles and accomplishments while encouraging me to think outside the box.

I would like to thank the additional members of my dissertation committee: Dan Baker, Suzie Imber, and Mark Kushner. Their guidance and feedback throughout this process is appreciated. I am especially grateful that they found time to read this thesis of 200+ pages and provide me with detailed comments.

The Solar and Heliospheric Research Group (SHRG) has been a constant support system through this entire period, both as colleagues and friends. I would particularly like to thank Jim Raines who has been a friend, fellow student, and mentor. Jim has always offered words of wisdom when I needed advice and is someone that I am able to discuss science questions with, no matter how silly they may seem. Dan Gershman has also been a great friend and colleague. Between our morning gossip sessions and advice to choose ‘the green one,’ Dan never fails to amaze me with his vast knowledge and quick ability to understand and assess a problem. Jim and Dan both had incredible

patience with me as I was learning about FIPS and the plasma analysis techniques. I owe hundreds of hours to Jon Thomas, which would have otherwise been spent on nested loops in IDL. Sue Lepri has supplied career and personal advice throughout this journey. I would like to thank the remaining members of SHRG who have broadened my understanding of solar wind composition and heliospheric physics. I must also extend my gratitude to the faculty and staff of AOSS for taking the time to pass on their knowledge and offer support over the years.

Of course, my time in graduate school would not have been half as entertaining without the laughs and discussions I shared with my fellow graduate students: Shannon, Jacob, Ahmed, Micah, Aleida, Mark, Pat, Kai, Nicole, Rachael, Colin, Alex, Julie, Catherine, Sid, Kevin, and many other AOSS friends. The football tailgates, complete with cheesy potatoes, provided me with a proper Michigan football experience. The Red Zepplin camaraderie was something that I looked forward to both in the department and during the intramural games. My Michigan friends outside of AOSS have also been essential in making Ann Arbor feel like home.

I would not have made it to this point in my life without my internship and co-op at the NASA Glenn Research Center and my co-op at the NASA Goddard Space Flight Center. I am forever grateful to all who have opened these doors for me. Additionally, the work in this thesis was made possible through the support of the MESSENGER team. I am thankful to be given the opportunity to join such a successful science team and learn the inner workings of a mission – an opportunity that most graduate students are not fortunate enough to have.

My family and friends outside of Michigan have been a crucial support system over the years. When work required me to be away for longer than I had planned, they never questioned me but instead sent their love and encouragement. My aunts, uncles, and cousins have motivated me along the way and always provided a breath of fresh air when I returned home. My grandparents have been my biggest champions throughout my entire education, sporting NASA gear and eagerly asking question when I returned home. I would like to thank the Riemer family for being my home away from home during the times when I was unable to return to PA. The Critters always knew the right moment to offer a cry-face or Shannon pose to make me laugh and I can never thank them

enough. My PITT friends are truly an extension of my family and I look forward to our annual “best friends, paper towels” beach trips for the rest of our lives. Outside of these groups I have many other wonderful friends that have always supported me and I must extend my thanks to them as well.

I would not have survived the Ph.D. program without the support of my other half, Chris, who has been by my side during this entire experience. He listened whenever I needed to clear my mind, offered advice when I could no longer think straight, and reminded me to take a deep breath when I became too stressed. Chris was exceptionally helpful during the qualifying exams and thesis writing months when he gladly made extra trips to Ann Arbor, supplying me with chocolate desserts on the particularly difficult days. I am so incredibly appreciative for everything that he has done for me and I realize that he has been an essential part of my success.

My sister, Carly, has always been my partner in crime. Her relaxed outlook reminds me when I need to slow down and enjoy life. Carly has always supported me in my endeavors and we have had many exciting adventures through life. I have always been able to rely on her as a shoulder to cry on and someone to share a laugh with. Because she is younger than me, I try to serve as her role model; however, the truth is that she has set many examples for me as well. I am lucky to have her as my sister and best friend.

Finally, I am eternally grateful to my parents, to whom this thesis is dedicated. From a young age they encouraged me to have high aspirations and insisted that I was capable of anything I put my mind to. I would wake up in the mornings to find NASA articles clipped from the newspaper for me to read and on the weekends we would visit the local planetarium so that I could learn even more. My parents have supported both Carly and myself in all of our interests and offered us opportunities in life that they never had, which includes obtaining a higher education. During times of struggle they would listen and offer advice. During time of success, they celebrated right by my side. Most importantly, they served as a constant motivation and I cannot thank them enough.

This work was supported, in part, by the NASA GSFC Cooperative Education Program. The MESSENGER project is supported by the NASA Discovery Program

under contracts NASW-00002 to the Carnegie Institution of Washington and NAS5-97271 to the Johns Hopkins University Applied Physics Laboratory. The WSA ENLIL simulations and graphic displays were provided by the Community Coordinated Modeling Center at NASA Goddard Space Flight Center.

TABLE OF CONTENTS

DEDICATION	ii
ACKNOWLEDGEMENTS.....	iii
LIST OF FIGURES	x
LIST OF TABLES	xxiv
ABSTRACT	xxv

CHAPTER

I. INTRODUCTION	1
1.1 Planet.....	1
1.2 Exosphere.....	3
1.3 Intrinsic Magnetic Field.....	4
1.4 Interplanetary Environment	10
1.5 Mercury's Magnetosphere	13
1.6 Guiding Science Questions	22
II. METHODOLOGY	25
2.1 MESSENGER Mission.....	25
2.2 Magnetometer	31
2.3 Fast Imaging Plasma Spectrometer.....	33
III. MESSENGER OBSERVATIONS OF MAGNETOPAUSE STRUCTURE AND DYNAMICS AT MERCURY	37
Abstract.....	37
3.1 Introduction.....	38
3.2 Methodology	41
3.3 MESSENGER Observations.....	46
3.3.1. High- and Low-Shear Magnetopause Reconnection	46
3.3.2. Statistical Analysis.....	50
3.4 Discussion	56

IV. MESSENGER OBSERVATIONS OF FLUX ROPES IN MERCURY’S MAGNETOAIL..	64
Abstract.....	64
4.1 Introduction.....	65
4.2 Analysis Technique.....	69
4.3 MESSENGER Observations.....	71
4.3.1 Flux Rope Example.....	73
4.3.2 Statistics.....	75
4.4 Flux Rope Modeling.....	82
4.5 Discussion.....	86
4.6 Conclusions and Summary.....	90
V. FIRST OBSERVATIONS OF MERCURY’S PLASMA MANTLE AS SEEN BY MESSENGER.....	92
Abstract.....	92
5.1 Introduction.....	93
5.2 Instrumentation and Data.....	99
5.3 Plasma Mantle Observations.....	100
5.3.1 10 November 2012: 0600 UTC Orbit.....	102
5.3.2 10 November 2012: 1400 UTC Orbit.....	107
5.4 Cross-magnetosphere Electric Potential.....	110
5.5 Discussion and Conclusions.....	113
VI. MESSENGER OBSERVATIONS MERCURY’S DAYSIDE MAGNETOSPHERE UNDER EXTREME SOLAR WIND CONDITIONS.....	116
Abstract.....	116
6.1 Introduction.....	117
6.2 Extreme Solar Wind Event Overviews.....	123
6.3 Magnetopause Analysis.....	132
6.3.1 23 November 2011.....	134
6.3.2 8 May 2012.....	136
6.3.3 11 May 2012.....	138
6.4 Northern Cusp Observations.....	140
6.4.1 23 November 2011.....	141
6.4.2 8 May 2012.....	144
6.4.3 11 May 2012.....	147
6.5 Cusp Plasma Filaments and Flux Transfer Events.....	148
6.6 Magnetopause Altitude vs. Solar Wind Pressure.....	151
6.7 Discussion.....	154
6.8 Conclusions.....	161
VII. CONCLUSIONS.....	163
7.1 Summary of Guiding Science Questions.....	163
7.2 Future Work.....	166

APPENDIX I	FORCE-FREE FLUX ROPE FITTING TECHNIQUE.....	168
A1.1	Background.....	168
A1.2	Data Setup.....	170
A1.3	Force-Free Flux Rope Model.....	173
A1.4	Data-Model Fitting.....	174
A1.5	Discussion.....	176
REFERENCES	177

LIST OF FIGURES

<u>Figure</u>		
1.1	The internal structure of Mercury. Figure adapted from <i>Hauck et al.</i> [2012].	2
1.2	Mariner 10 spacecraft trajectories in Mercury-centered solar ecliptic (ME) coordinates. In this coordinate system the X_{ME} is directed towards the Sun, Y_{ME} is in the ecliptic plane and positive in the opposite direction of planetary orbital motion, and Z_{ME} completes the right-handed system. Figure adapted from <i>Ness et al.</i> , [1975].	5
1.3	(a) Mariner 10 observations during M10-I [<i>Ness et al.</i> , 1974] and (b) M10-III [<i>Ness et al.</i> , 1975]. The boundaries of Mercury’s magnetic environment (vertical dashed lines) are discussed in Section 1.5. Figures from <i>Ness et al.</i> [1974, 1975].	6
1.4	Magnetic field data from the (a) first and (b) second MESSENGER flybys presented in Mercury solar orbital (MSO) coordinates. In this coordinate system, X_{MSO} is directed from the center of the planet toward the Sun, Z_{MSO} is normal to Mercury’s orbital plane and positive toward the north celestial pole, and Y_{MSO} completes the right-handed system and positive in the direction opposite to orbital motion. From top to bottom the panels show: the field magnitude; the polar angle, θ , where $\theta = 0^\circ$ is northward; the azimuth angle, ϕ , where $\phi = 0^\circ$ and 90° are sunward and duskward, respectively; and the 1–10-Hz band-pass fluctuation amplitude. Magnetic field vectors were sampled every 0.05 s, and the 1–10-Hz band-pass amplitude was evaluated on-board every 1 s from the 0.05-s data. Magnetic boundaries are labeled as follows: SK for bow shock; MP for magnetopause; CS for the tail current sheet; TL for transition out of the tail lobe; CA for closest approach; and BL for entry into a boundary layer. Figures from <i>Anderson et al.</i> , [2010].	8
1.5	Analysis by <i>Anderson et al.</i> [2011a] to deduce the northward offset of Mercury’s intrinsic magnetic field where $Z_{\rho 0}$ indicates the local offset of the magnetic equator from the geographic equator of the planet. (a) Identification of magnetic equator from the zero crossing of the cylindrical radial component of the magnetic field. For a dipole	

approximately aligned with the planet’s spin axis, the north-south position of the $B_\rho = 0$ point coincides with the magnetic equator. For a case with a large axial offset, the point of zero inclination will overestimate the displacement relative to that given by the location of $B_\rho = 0$. (b) Magnetic equator offset versus planetary longitude. Color coding denotes IMF B_{X-MSO} averaged over a 2-hour period that combines 1 hour before the inbound bow-shock crossing and 1 hour after the outbound bow-shock crossing. Error bars are 3-SE uncertainties. Figures from *Anderson et al.* [2011a].....9

1.6 WSA-ENLIL model results of solar wind (a) radial velocity and (b) density in the equatorial plane at the time of the first MESSENGER flyby. Model results and figure from *Baker et al.* [2009].....12

1.7 WSA-ENLIL model results for the period of March 2011 through December 2011. Computed values of IMF field magnitude ($|B|$), solar wind density (n), solar wind temperature (T), solar wind speed ($|V|$), Alfvénic Mach number (M_A), and solar wind dynamic pressure (P_{dyn}) are shown from the first to the sixth panels, respectively. The red bar in the sixth panel shows the duration of the 88-day Mercury orbit around the Sun. Figure adapted from *Baker et al.* [2013].13

1.8 Illustration of Mercury’s magnetosphere with a reference to the scale of Earth’s diameter. The solar wind streaming from the Sun is flowing from left to right. Mercury’s intrinsic magnetic field is indicated by yellow lines that are attached to the planet with arrows marking their orientation. The direction of the magnetopause current sheet (J_{MP}) and cross-tail current sheet (J_{CT}) are also denoted with yellow arrows but are not connected to the planet. The main regions of the magnetosphere are labeled. Figure from *Slavin* [2004].....14

1.9 Spatial distribution of key plasma components in relation to magnetospheric structure. (Top) Overview of magnetospheric geometry from a magnetohydrodynamic simulation used to order the timeline of the MESSENGER flyby and the locations and encounter times of key components of the Mercury space environment. (A and B) Energy distribution of protons (at a resolution of 8 s, during which FIPS performs a complete E/q stepping sequence from 0.1 to 13 keV/e) and normalized He^{++} flux. Both species originate in the solar wind. The temporal variability of these components is associated with changes in plasma characteristics, as well as with temporal variability of the obstruction geometry, especially for solar wind protons. (C, D, and E) Normalized fluxes of ions in specified m/q ranges. All fluxes (B to E) are normalized to the peak flux in He^{++} . The fluxes of heavy ions with $10 < m/q < 42$ maximize near the planet but are also found throughout the magnetosphere. During the flyby, the spacecraft

	sunshade, one of the solar panels, and other spacecraft structures limit the field of view of FIPS to $\sim\pi$ steradians. Vertical dashed lines denote the crossing of the bow shock (green), the magnetopause (blue), and the point of closest approach (red), based on magnetic field data. Figure from <i>Zurbuchen et al.</i> [2008].	16
1.10	Reconnection region with two magnetic fields (blue and red) from different domains with opposite orientations. A current sheet forms between the sheared fields. The fields flow towards the current sheet and will meet at the X-line where they will reconnect. The newly formed fields (red/blue combination) will then exit the region at high speeds due to the release of magnetic tension.	18
1.11	A schematic of Mercury’s magnetosphere as the Dungey cycle progresses. The IMF (blue) reconnects with the intrinsic planetary field (green) at the dayside magnetopause. An open field line is generated (orange), which will get pulled past the planet by the solar wind to join the magnetotail. The open field lines of opposite orientation will meet in the cross-tail current sheet (\odot) and reconnect with each other. The result is a closed planetary field that will move back toward the planet and a detached field that rejoins the IMF.	19
1.12	Comparison of the experimentally measured reconnection layer profile for two cases: (a) Collisional regime and (b) Nearly collisionless regime. In-plane magnetic field is shown as arrows and out of plane field component by the color codes ranged from -50 G to 50 G. Dashed pink lines shows that the magnetic configuration changes from an elongated current sheet (Sweet-Parker type in (a)) to a double-wedge shape (Petschek-like) as collisionality is reduced. The predicted quadrupole structure of the out-of-plane magnetic component, a signature of Hall effects, is observed in (b). Figure adapted from <i>Yamada et al.</i> [2006].	22
2.1	MESSENGER payload instruments and their location on the spacecraft. From <i>Leary et al.</i> [2007].	26
2.2	MESSENGER launch on a Delta II 7925H-9.5 rocket from the Cape Canaveral Air Force Station Space Launch Complex 17B, Florida, on 3 August 2004. Image from <i>Solomon et al.</i> [2007].	27
2.3	North ecliptic pole view of MESSENGER’s heliocentric trajectory. The spacecraft will utilize one Earth gravity assist, two Venus gravity assists, three Mercury gravity assists, and five major course-correction maneuvers, or DSMs, during its 6.6-year ballistic trajectory to Mercury. Figure from <i>McAdams et al.</i> [2005].	28

2.4	Three views of MESSENGER’s initial orbit around Mercury. Figure from <i>McAdams et al.</i> [2012].	29
2.5	Selected MESSENGER orbits during the first three Mercury years of the MESSENGER orbital mission showing periapsis at four different local times. Mercury true anomaly angle (TAA) and radial distance to the Sun (R) are also given. Figure from <i>Raines et al.</i> [2013].	29
2.6	Two orbit-correction maneuvers (OCMs) provided the transition to the 8-hour extended mission. Figure from <i>McAdams et al.</i> [2012].	30
2.7	View of the MESSENGER spacecraft showing the instrument coordinates and the Magnetometer boom deployed in the + Y direction, which is the anti-sunward direction during orbital operations. The MAG sensor stowed location is indicated (yellow cylinder) as are the propulsion system helium tank, the star cameras, and the phased-array antenna nearest the stowed Magnetometer sensor. The spacecraft sunshade is on the $-Y$ side of the vehicle as shown in light green. Schematic from <i>Anderson et al.</i> [2007].	32
2.8	Flight MESSENGER MAG sensor (a) and electronics (b) with view of analog slice. The sensor is shown mounted to a test boom adapter flange. Sensor dimensions not including the flange are 8.1 cm \times 4.8 cm \times 4.6 cm. The electronics dimensions are 10.4 cm and 8.6 cm in cross section as shown and 13.0 cm deep. (c) Flight MESSENGER MAG sensor and sensor sunshade integrated to the boom and spacecraft prior to final thermal blanketing during deployment testing prior to installation of thermal blankets. Images from <i>Anderson et al.</i> , [2007].	32
2.9	The FIPS sensor. Image from <i>Andrews et al.</i> [2007].	33
2.10	Cross-section of the FIPS sensor showing major functional components. Ions are analyzed by their energy per charge (E/q), two-dimensional position, and total time of flight. Figure from <i>Andrews et al.</i> [2007].	34
2.11	Accumulated raw FIPS event data from 25 March 2011 through 22 November 2011 together with lines showing the lower (dotted) and upper (dashed) bounds on modeled TOF as a function of E/q for each species. The modeled TOF center as a function of E/q (solid) is also shown in green for He^{2+} and He^+ . Counts are normalized to the maximum value. Background removal has not yet been completed for the data shown in this figure. The darker region below 0.1 keV/e is due to less time spent observing in this energy range. Figure from <i>Raines et al.</i> [2013].	35

- 3.1 Direction of the FIPS FOV in spherical MSM coordinates for the magnetopause crossings in this study. The polar angle (θ_{FOV}) is the angle between the Z_{MSM} -axis and the FIPS boresight vector. The azimuthal angle (ϕ_{FOV}) ranges from -180 to 180° , where 0° is directed sunward along the X_{MSM} -axis and the sign of ϕ_{FOV} follows the sign of Y_{MSM} . Changes in FIPS orientation result from spacecraft maneuvers made to acquire observations with other MESSENGER instruments.43
- 3.2 MESSENGER orbital trajectories on 21 and 24 November 2011; the magnetopause model of *Moldovan et al.* [2011] is shown in MSM coordinates. The magnetopause has been corrected for solar wind aberration for an average solar wind velocity of 400 km s^{-1} and an average orbital velocity for Mercury of 50 km s^{-1} . Observed outbound magnetopause crossings are indicated by triangles.47
- 3.3 Plasma and magnetic field data in MVA coordinates transformed from the magnetopause crossing beginning at 10:29:04.49 UTC on 24 November 2011. Vertical black lines mark the accepted (solid) and rejected (dashed) magnetopause crossings (MP). The top two panels include a proton energy spectrogram with differential energy flux (color scale, in $\text{cm}^{-2} \text{ s}^{-1} \text{ kV}^{-1}$) and total proton counts, respectively. The next four panels are the minimum, intermediate, and maximum variance components of the magnetic field and the field magnitude, respectively. R_{MSM} is distance from the center of the planet. The minimum, intermediate, and maximum eigenvectors are $B_1 = B_N = (0.91, -0.39, 0.11)$, $B_2 = (0.40, 0.76, -0.52)$, and $B_3 = (0.12, 0.51, 0.85)$. The MVA utilized 44 magnetic field vector measurements, and the ratios of maximum to intermediate and intermediate to minimum eigenvalues are 16.51 and 64.24, respectively. 49
- 3.4 Plasma and magnetic field data in MVA coordinates transformed from the magnetopause crossing beginning at 10:29:22.39 UTC on 21 November 2011. Solid vertical lines mark the magnetopause crossing. The top two panels include a proton energy spectrogram with differential energy flux (color scale, in $\text{cm}^{-2} \text{ s}^{-1} \text{ kV}^{-1}$) and total proton counts. The minimum, intermediate, and maximum eigenvectors are $B_1 = B_N = (0.89, -0.46, 0.00)$, $B_2 = (0.45, 0.87, 0.22)$, and $B_3 = (-0.10, -0.20, 0.98)$. The MVA utilized 114 magnetic field vector measurements, and the ratios of maximum to intermediate and intermediate to minimum eigenvalues are 4.33 and 5.55, respectively.50
- 3.5 Survey of observed magnetopause crossings and the model magnetopause surface of *Moldovan et al.* [2011] in solar-wind-aberrated MSM coordinates. Triangles represent dayside magnetopause crossings. (a) Equatorial view of the crossings between

	local times of 0800 and 1600. (b) View from the Sun to Mercury illustrating that all crossings occur within $\pm 20^\circ$ latitude. The model magnetopause location is shown at the terminator plane.....	52
3.6	(a) Histogram of the ratios of intermediate to minimum eigenvalue for the observed dayside magnetopause crossings. Two ratios have values greater than 40 and are not shown on this graph. (b) Results of MVA error analysis (equation 3.4) derived following the method of <i>Sonnerup and Scheible</i> [1998] to describe the spread of errors in the calculated magnitude of B_N	53
3.7	Distribution of the normal component of the magnetic field at the magnetopause calculated from MVA. Three observations have magnitudes greater than 50 nT and are not shown on the graph.	54
3.8	Histogram of magnetopause thickness d on the dayside magnetopause determined from measurements of the duration Δt of each magnetopause crossing and for a normal component of the magnetopause velocity of 20 km s^{-1} . The calculated gyroradius r_g of a solar wind proton (16 km) is indicated. A single crossing with duration longer than 15 s is not included on the histogram.	55
3.9	Histogram of reconnection rates calculated from the ratio of the normal component of the magnetic field determined from MVA to the magnitude of the total field just inside the magnetopause.....	56
3.10	Magnetopause shear angle θ compared with the rate of reconnection for the magnetopause crossings meeting the criteria of this study. The average reconnection rate was calculated in 30° bins, as indicated by the red rectangles. Little correlation between the two quantities is evident, indicating that reconnection occurs at Mercury for a large range of shear angles.....	58
3.11	(a) Comparison of β to magnetic shear, together with the condition of <i>Swisdak et al.</i> [2010] for diamagnetic suppression of reconnection for $L = d_i$ (dashed line), to assess reconnection enhancements in the low- β environment. Black triangles are crossings with a reconnection rate < 0.25 , and red triangles show reconnection rates ≥ 0.25 . (b) Evaluation of the correlation between β and the rate of reconnection with a power-law fit (dashed line) to observations for the magnetopause crossings meeting the criteria of this study. One event with $\beta > 10$ is not shown on the plots.....	62
3.12	Histogram of magnetopause reconnection contribution to magnetosphere potential for a solar wind velocity of 200 km s^{-1} and an X-line length of $3 R_M$. Three magnetopause crossings for which the	

	estimated contribution to the potential exceeds 80 kV are not included on the plot.	63
4.1	Schematic of flux ropes that are formed as a result of reconnection occurring at multiple X-lines (marked by \times) within the plasma sheet. Mercury is located to the left and the arrows indicate the opposite direction of the magnetic field within the lobes.....	67
4.2	Examples of the variation in magnetic field signatures of flux ropes dependent on the trajectory at which they are encountered by the spacecraft. Flux ropes are identified on the basis of: (1) A pronounced bipolar variation in the north-south (B_Z) component of the magnetic field; (2) A local maximum in the east-west (B_Y) direction denoting the strong, axial core field; and (3) An increase in the total magnetic field magnitude ($ B $).....	69
4.3	(a) MESSENGER “hot season” orbit on 14 May 2012. The portion of the orbit highlight in red indicates the location of the spacecraft as it encountered the current sheet. (b) A 20 min interval of MESSENGER MAG data during the current sheet crossing on 14 May 2012.	72
4.4	MESSENGER MAG observations, in MSM coordinates, of a tailward traveling flux rope encountered in Mercury’s cross-tail current sheet on 14 May 2012. A north-then-south bipolar signature is evident in B_Z and a peak in B_Y and $ B $ occur at the inflection point of this B_Z perturbation.	74
4.5	Results of minimum variance analysis (MVA) for the example flux rope encounter on 14 May 2012. (a) The magnetic field measurements transformed into MVA coordinates where B_1 , B_2 , and B_3 are the minimum, intermediate, and maximum variance directions, respectively. (b and c) Hodograms of the magnetic field data in MVA coordinates are used to illustrate the rotation of the field during the flux rope encounter.	75
4.6	Histograms showing the distribution of the ratios of (a) intermediate to minimum eigenvalue and (b) maximum to intermediate eigenvalue resulting from minimum variance analysis (MVA) for the observed flux ropes. A higher ratio means the MVA-coordinate directions are well-determined.	77
4.7	Location of the 49 selected flux ropes in aberrated MSM coordinates with a view from the (a) meridional and (b) equatorial plane. Orange circles represent NS flux ropes that are traveling away from the planet while black circles indicate SN flux ropes traveling planetward. The Sun is located to the left.....	78

4.8	Location of plasmoids in aberrated MSM coordinates with the eigenvectors resulting from MVA projected onto the plane in each plot. (a) Projection of \mathbf{B}_1 onto the $X'-Y'$ plane. (b) Projection of \mathbf{B}_2 onto the $X'-Y'$ plane. (c) Projection of \mathbf{B}_3 onto the $X'-Z'$ plane.	79
4.9	Duration of flux ropes calculated from peak-to-peak in bipolar B_Z signature.	80
4.10	Plasma parameters of the plasma sheet directly adjacent to the encountered flux ropes determined from one minute-averaged FIPS data: (a) Proton density; (b) Proton temperature; (c) Alfvén speed; and (d) Plasma β , ratio of plasma pressure to magnetic pressure, calculated using one minute-averaged MAG data to determine the magnetic pressure; and (d) Alfvénic speed.	81
4.11	Histogram of the minimized χ^2 values resulting from the flux rope fitting. The vertical dashed red line marks the upper limit threshold of 0.01 implemented in order to accept a flux rope fitting.	84
4.12	(a) The correlation between R_0 and χ^2 illustrates the least squares minimization for the 14 May 2012 flux rope example. The vertical dashed red line illustrated the point at which χ^2 is at its minimum value. This corresponds to a modeled radius of 488 km. (b) Example of the best-fit resulting from flux rope fitting for an event on 14 May 2012. Normalized magnetic field axial, B_A and tangential, B_T components are plotted to compare the data (red lines) and modeled (black lines) results. The minimized χ^2 value for this example is 0.003.	85
4.13	Histograms of the 16 accepted fits, with $\chi^2 \geq 0.01$ resulting from the flux rope fitting. (a) Flux rope radius, R_0 , determined using the χ^2 minimization technique. (b) Magnetic field magnitude of the flux rope core field, B_0 . (c) Impact parameter, Y_0/R_0 , describes the proximity of the spacecraft's trajectory to the center of the flux rope during the encounter.	85
4.14	A superposed epoch analysis for (a) 26 SN planetward traveling flux ropes and (b) 23 NS tailward traveling flux ropes. The epoch is taken to at the inflection point in the B_Z bipolar signature.	88
5.1	Figure 5.1: Schematic of Mercury's magnetosphere with the plasma mantle located in the high-latitude magnetotail (red shaded region). The planetary magnetic field and its orientation are represented indicated by black lines and arrows, along with the magnetopause boundary (dashed line) and the cross-tail current sheet (\odot). Solar wind particles enter along open field lines near the dayside with a	

velocity parallel to the magnetic field (V_{\parallel}). As the particles feel the effects of the cross-tail electric field they will $E \times B$ drift toward the central plasma sheet, surrounding the current sheet, at a velocity of $V_{E \times B}$. The particles disperse as low-energy particles drift deeper into the magnetosphere and higher energy particles flow further downstream.....97

5.2 Figure 5.2: MESSENGER orbit and plasma mantle observations are shown in aberrated MSM coordinates. (a) The view from the Sun where the model magnetopause is indicated at the terminator, $X'_{\text{MSM}} = 0 R_M$, (dotted line) and at $X'_{\text{MSM}} = -2.5 R_M$ (dashed line). (b) The meridional view where the model magnetopause location is indicated by the solid line. In both plots, the thick dashed lines display MESSENGER orbits on 10 November 2012. The extent of the orbit when the plasma mantle was observed is highlighted in red for the 06:00 UTC orbit and blue for the 14:00 UTC orbit.....101

5.3 MESSENGER FIPS and MAG measurements taken during the inbound magnetopause crossing during the 06:00 orbit on 10 November 2012. The vertical red dashed lines represent the beginning and end of the plasma mantle. The beginning of the plasma mantle (first vertical red dashed line) is also the magnetopause crossing. The magnetosheath, plasma mantle, and tail lobe regions are labeled at the top. Shown from top to bottom is the: proton energy spectrogram in units of flux (counts $s^{-1} \text{ cm}^{-2} \text{ sr}^{-1} \text{ kV}^{-1}$); proton pitch angle distribution (normalized units); total proton counts; magnetic field components B_X , B_Y , B_Z ; and total field magnitude. The white line in the top two panels represent the running weighted averages of the proton energy (top panel) and calculated pitch angle (second panel from the top).....103

5.4 Kinetic properties of protons within the plasma mantle for the 06:00 UTC orbit on 10 November 2012. (a) The angular flux distribution map, in units of integrated flux ($\text{cm}^{-2} \text{ s}^{-1} \text{ sr}^{-1}$), indicates flow direction for protons. The average direction of the magnetic field during the plasma mantle encounter is indicated by the pink \times symbol. On this map, the white bins are unobserved and black bins are no measurements. Integrated flux has been normalized to 1. (b) Phase space density as a function of energy per charge (E/q). The vertical dashed line marks the weight average energy of the observed protons. See text for details.....106

5.5 MESSENGER FIPS and MAG measurements taken during the inbound magnetopause crossing during the 14:00 orbit on 10 November 2012. The vertical red dashed lines represent the beginning and end of the plasma mantle. The beginning of the plasma mantle (first vertical red dashed line) is also the magnetopause crossing. The

	magnetosheath, plasma mantle, and tail lobe regions are labeled at the top. Shown from top to bottom is the: proton energy spectrogram in units of flux (counts s ⁻¹ cm ⁻² sr ⁻¹ kV ⁻¹); proton pitch angle distribution (normalized units); total proton counts; magnetic field components B_X , B_Y , B_Z ; and total field magnitude. The white line in the top two panels represent the running weighted averages of the proton energy (top panel) and calculated pitch angle (second panel from the top).....	108
5.6	Kinetic properties of protons within the plasma mantle for the 14:00 UTC orbit on 10 November 2012. (a) The angular flux distribution map, in units of integrated flux (cm ⁻² s ⁻¹ sr ⁻¹), indicates flow direction for protons. The average direction of the magnetic field during the plasma mantle encounter is indicated by the pink × symbol. On this map, the white bins are unobserved and black bins are no measurements. Integrated flux has been normalized to 1. (b) Phase space density as a function of energy per charge (E/q). The vertical dashed line marks the weight average energy of the observed protons. See text for details.....	109
6.1	(a) Mercury’s bow shock, some dayside magnetic field lines, and large iron core are displayed. The outermost dipolar field line (yellow) lies at a distance of ~ 1.4–1.5 R_M sunward of the planetary rotation axis while the nose of the bow shock (red) is at ~ 1.9–2.0 R_M [Winslow <i>et al.</i> , 2013]. The MESSENGER spacecraft orbit has periapsis ranging from 200 to 500 km at a latitude of ~ 60° and an inclination of ~82.5° is shown (white). (b-e) Magnetic field measurements (sampling rate: 20 s ⁻¹) taken during a typical MESSENGER periapsis pass.....	118
6.2	(a) Increases in solar wind pressure drive induction currents on the surface of Mercury’s large iron core (green loops). The senses of these currents is to oppose the compression of the intrinsic magnetic field (yellow) by generating additional magnetic flux (green field lines) which, when added to the intrinsic flux, acts to balance the increased solar wind pressure. (b) Magnetic reconnection between the interplanetary magnetic field and the intrinsic planetary magnetic field opposes the effectiveness of induction by removing magnetic flux from the dayside magnetosphere and transporting it into the tail.....	122
6.3	MESSENGER orbits projected into the aberrated MSM (a) Y - X' and (b) Z - X' planes relative to Mercury (dotted line) and its average magnetopause location (solid line) [Winslow <i>et al.</i> , 2013]. Note the displacement of the magnetopause relative to the planet due to the northward offset of the magnetic dipole by ~0.2 R_M . The extreme compression of the dayside magnetosphere on these passes is evident in the very low altitudes of the magnetopause crossings on 23 November 2011, 8 May 2012, and 12 May 2012 (diamonds, squares	

	and triangles, respectively). The 23 November 2011 (DOY 327) orbit is before the reduction in orbital period from 12 hr to 8 hr, while the other two are afterwards. Note: The 23 November 2011 trajectory arcs farther downstream to intersect the mid-plane of the tail at greater distances than the 8 hr orbits.....	125
6.4	ENLIL-WSA models of the (a) solar wind speed and (b) solar wind density multiplied by the square of distance from the Sun in AU for 23 November 23 at 24:00 UT. The center of a coronal mass ejection impacted Mercury and its magnetosphere (yellow circle). The locations of Earth, Venus, and Mercury are all indicated by small colored dots. The inner domain of the model (where WSA is utilized) is denoted by the white central circle. Magnetic field measurements (sampled at a rate of 20 s^{-1}) taken during a CME-driven compressed magnetosphere pass on 23 November 2011 are displayed in MSM coordinates. The locations of the northern cusp, the magnetopause (MP), and the bow shock (BS) are labeled.	127
6.5	ENLIL-WSA models of the (a) solar wind speed and (b) density multiplied by the square of distance from the Sun in AU on 8 May 2012 at 12:00 UT. As shown, the edge of a coronal mass ejection moves over Mercury as it moves radially away from the Sun. Magnetic field measurements (sampled at a rate of 20 s^{-1}) taken during a CME-driven compressed magnetosphere pass on 8 May 2012 are displayed in MSM coordinates. The locations of the northern cusp, the magnetopause (MP), and the bow shock (BS) are labeled.	130
6.6	ENLIL-WSA models of the (a) solar wind speed and (b) density multiplied by the square of distance from the Sun in AU on 11 May 2012 at 24:00 UT. As shown, the edge of a co-rotating interaction region driven by a high-speed stream passes over Mercury and compresses its magnetosphere. Magnetic field measurements (sampled at a rate of 20 s^{-1}) taken during a high-speed stream interval on 11 May 2012 are displayed in MSM coordinates. The locations of the northern cusp, the magnetopause (MP), and the bow shock (BS) are labeled.	132
6.7	Magnetic field measurements in boundary normal coordinates across the dayside magnetopause on 23 November 2011. The magnetopause normal used here was determined from the average magnetopause of <i>Winslow et al.</i> [2013]. The start and stop times for the main magnetopause current layer and the occurrence of flux transfer events are indicated with a red bar and vertical dashed lines.	135
6.8	Magnetic field measurements in boundary normal coordinates across the dayside magnetopause on 8 May 2012. The magnetopause normal	

	used here was determined from the average magnetopause of <i>Winslow et al.</i> [2013].	137
6.9	Magnetic field measurements in boundary normal coordinates across the dayside magnetopause on 11 May 2012. The magnetopause normal used here was determined from the average magnetopause of <i>Winslow et al.</i> [2013].	139
6.10	(a) Proton differential energy flux as a function of UTC for the 23 November 2011 periapsis pass. (b) Heavy ion counts binned by three composition types: He ⁺ , O ⁺ group ($m/q = 14-20$), and Na ⁺ group ($m/q = 21-0$). (c) B_z component of the magnetic field in MSM coordinates and (d) total magnetic field intensity plotted versus UTC. The locations of the cusp and magnetopause are labeled.	142
6.11	(a) All-sky map of integrated proton flux in the plasma depletion layer on 23 November 2011 with the north and south poles and the dawn and dusk directions indicated. (b) Proton phase space distribution. (c) Single temperature fit to the proton distribution function.	143
6.12	(a) Proton differential energy flux as a function of UTC for the 8 May 2012 periapsis pass. (b) Heavy ion counts binned by three composition types: He ⁺ , O ⁺ group, and Na ⁺ group. (c) B_z component of the magnetic field in MSM coordinates, (d) total magnetic field intensity plotted versus UTC, (e) proton density and temperature, and (f) magnetic and proton thermal pressure. The locations of the cusp and magnetopause are shown.	145
6.13	(a) All-sky map of integrated proton flux in the northern cusp on 8 May 2012 with the north and south poles and the dawn and dusk directions indicated. (b) Proton phase space distribution. (c) Single temperature fits to the proton distribution function.	146
6.14	(a) Proton differential energy flux as a function of UTC for the 11 May 2012 periapsis pass. (b) Heavy ion counts binned by three composition types: He ⁺ , O ⁺ group, and Na ⁺ group. (c) B_z component of the magnetic field in MSM coordinates and (d) total magnetic field intensity plotted versus UTC. The locations of the cusp and magnetopause are shown.	147
6.15	(a) All-sky map of integrated proton flux in the northern cusp on 23 November 2011 with the north and south poles and the dawn and dusk directions indicated. (b) Proton phase space distribution. (c) Single temperature fit to the proton distribution function.	149

6.16	(a) Proton differential energy flux over plotted versus UTC. The intensity of the magnetic field is shown in black. (b) Differential flux plotted versus energy along gray diagonal bands depicting energy step as function of UTC. The intensity of the magnetic field is shown in black. (c) B_Z is displayed in MSM coordinates. Vertical dashed lines indicate cusp filament events.	150
6.17	(a) Proton differential energy flux over plotted versus UTC. The intensity of the magnetic field is shown in black. (b) Differential flux plotted versus energy along gray diagonal bands depicting energy step as function of UTC. The intensity of the magnetic field is shown in black. (c) B_Z is displayed in MSM coordinates. Vertical dashed lines indicate flux transfer events.	151
6.18	The <i>Winslow et al.</i> [2013] magnetopause model surface is displayed in aberrated cylindrical coordinates for mean, $R_{SS} = 1.45 R_M$, and extreme $R_{SS} = 1.05 R_M$, solar wind pressure conditions. The 23 November 2011, 8 May 2012, and 11 May 2012 magnetopause crossings are indicated with diamonds, x's, and triangle symbols.	152
6.19	(a) The subsolar solar wind ram pressure, P_{SS} , is plotted against the extrapolated magnetopause stand-off distance for the magnetopause crossings observed during the three extreme solar wind events, $P_{SS} \sim 45$ to 65 nPa, are shown as diamonds, X's and triangle. The sixth-root relationship determined by <i>Winslow et al.</i> [2013] (short dashes) determined from a large dataset of MESSENGER magnetopause encounters at typical upstream pressures of ~ 5 to 15 nPa is shown as a dashed line. A theoretical model that includes the effects of induction in Mercury's interior developed by <i>Glassmeier et al.</i> [2007] is graphed as bold dashes.	154
6.20	Total magnetic field intensity is displayed versus UTC for each of the extreme solar wind passes when MESSENGER was between magnetic latitudes between 82° and 20° . The center of the central magnetic cusp depression in $ B $ and the lowest latitude where the narrow magnetic field depressions associated with plasma filaments are observed. The occurrence of flux transfer events and magnetopause crossings and the dimensionless reconnection rates, measured at the magnetopause, are also called out.	156
A1.1	Bessel functions of the first kind, J_0 and J_1 , plotted as a function of distance from the flux rope center. Here, $\alpha = 2.4048$ and r' is the fractional radial distance. The dashed vertical line marks the flux rope edge where $\alpha r' = 2.4048$	170

A1.2	A cross-sectional view of a flux rope with an example spacecraft trajectory (dashed line). The solid black horizontal line marks the cross-sectional axis of the flux rope. The spacecraft trajectory is always parallel to the solid black line. This is useful because Y_0 , the distance from the flux rope center at closest approach, will be perpendicular to the trajectory. The distance traveled by the spacecraft from closest approach to the edge of the flux rope is X_0 and R_0 is the flux rope radius. The three parameters Y_0 , X_0 , and R_0 create a right-handed triangle.....	172
A1.3	The ratio of the Bessel functions of the first kind, J_0 and J_1 , which is proportional to B_{A_OBS}/B_{T_OBS} , plotted as a function of distance from the center of the flux rope. The vertical dashed line represents the edge of the flux rope where $\alpha r' = 2.4048$. By determining where the value of B_{A_OBS}/B_{T_OBS} at closest approach intersects the curve, the associated $\alpha r'$ can be calculated.....	172
A1.4	A cross-sectional view of a flux rope with an example spacecraft trajectory (dashed line). The solid black horizontal line marks the cross-sectional axis of the flux rope. This closest distance along the spacecraft trajectory to the flux rope center is Y_0 . Making up the red triangle, R_0 is the flux rope radius and X_0 is the distance from closest approach to the flux rope edge. The blue triangle varies with each incremental step set to match the resolution of the data, marked by the small vertical blue lines. X_i is the distance from closest approach to a particular incremental step and R_i is the radial distance from the flux rope center to the location along the trajectory. Both the blue and red triangles are right-handed.	173

LIST OF TABLES

Table

1.1	Summary of constituents in Mercury's atmosphere and their abundances from Mariner 10 and ground-based observations. Table from <i>Domingue et al.</i> [2007].	3
1.2	(a) Typical interplanetary conditions scaled from 1 AU to the orbits of the other terrestrial planets: solar wind velocity (V_{sw}), proton number density (n_p), IMF field strength (B), and proton (T_p) and electron (T_e) temperatures. (b) Basic parameters computed from the scaled interplanetary conditions: solar wind pressure (P_{sw}), sonic mach number (M_S), Alfvénic Mach number (M_A), plasma beta (β), square of the Alfvénic Mach number (Q), ion inertial length (c/ω_{pi}), and IMF spiral angle. Tables from <i>Slavin and Holzer</i> [1981].	11
1.3	WSA-ENLIL modeling results of solar wind parameters for the three MESSENGER flybys. These parameters include solar wind velocity (V_{sw}), density (N), temperature (T), IMF magnitude (B_{IMF}), and IMF polarity. Table from <i>Baker et al.</i> [2011].	12
1.4	Comparison of magnetic reconnection in different plasmas. L is the reconnection sheet length, B is the magnetic field magnitude, δ_i is the ion skin depth, and δ_{SP} is the Sweet-Parker width. Table adapted from <i>Yamada et al.</i> [2009].	21
5.1	Plasma mantle properties from the 06:00 and 14:00 UTC orbits on 10 November 2012. The location listed in the table marks the position where MESSENGER first entered the plasma mantle as it crossed the magnetopause. E_{conv} and Φ_{Tail} calculations are determined using the first method described in Section 4.	112
5.2	Plasma mantle properties from the 06:00 and 14:00 UTC orbits on 10 November 2012. The location listed in the table marks the position where MESSENGER first entered the plasma mantle as it crossed the magnetopause.	113
6.1	Extreme solar wind events.	126
6.2	Magnetopause analysis.	129

ABSTRACT

Mercury's magnetosphere is formed as a result of the supersonic solar wind interacting with the planet's intrinsic magnetic field. The combination of the weak planetary dipole moment and intense solar wind forcing of the inner heliosphere creates a unique space environment, which can teach us about planetary magnetospheres. In this work, we analyze the first *in situ* orbital observations at Mercury, provided by the MErcury Surface, Space ENvironment, GEochemistry, and Ranging (MESSENGER) spacecraft. Magnetic reconnection and the transport of plasma and magnetic flux are investigated using MESSENGER Magnetometer and Fast Imaging Plasma Spectrometer measurements. Here, we report our results on the effect of magnetic reconnection and plasma dynamics on Mercury's space environment: (1) Mercury's magnetosphere is driven by frequent, intense magnetic reconnection observed in the form of magnetic field components normal to the magnetopause, B_N , and as helical bundles of flux, called magnetic flux ropes, in the cross-tail current sheet. The high reconnection rates are determined to be a direct consequence of the low plasma β , the ratio of plasma to magnetic pressure, in the inner heliosphere. (2) As upstream solar wind conditions vary, we find that reconnection occurs at Mercury's magnetopause for all orientations of the interplanetary magnetic field, independent of shear angle. During the most extreme solar wind forcing events, the influence of induction fields generated within Mercury's highly conducting core are negated by erosion due to persistent magnetopause reconnection. (3) We present the first observations of Mercury's plasma mantle, which forms as a result of magnetopause reconnection and allows solar wind plasma to enter into the high-latitude magnetotail through the dayside cusps. The energy dispersion observed in the plasma mantle protons is used to infer the cross-magnetosphere electric field, providing a direct measurement of solar wind momentum transferred into the system. We conclude that Mercury's magnetosphere is a dynamic environment with constant plasma and magnetic flux circulation as a result of frequent and intense magnetic reconnection. These results are

directly applicable to the understanding of geomagnetic storms at Earth, when coronal mass ejections produce solar wind parameters similar to those regularly experienced by Mercury.

CHAPTER I

INTRODUCTION

1.1 Planet

Mercury has a unique position in the solar system with its orbital distance from the Sun ranging between only 0.31 and 0.47 AU. This change in its proximity to the Sun varies by more than 50% over the course of a single Mercury year (1 Mercury year = 88 Earth days). For this reason, Mercury's orbital eccentricity is greater than any other planet's in the solar system. As a result of this highly eccentric orbit, the orbital velocity ranges between $\sim 40\text{--}60 \text{ km s}^{-1}$ to account for the drastic shift in distance. One direct consequence of the orbit is the ever-changing solar parameters in Mercury's local space environment that vary with radial distance from the Sun (discussed in Sections 1.3 and 1.4).

Compared to the 88-Earth-day length of a Mercury year, a single day on Mercury takes roughly 59 Earth days, creating a 3:2 spin-orbit resonance. The main effect of such an extended day is the large temperature gradient that forms between the day and night sides of the planet. Temperatures can reach as high as 700 K near local noon and as low as 100 K near local midnight.

Mercury has a radius of 2440 km (R_M), which is less than half the radius of Earth (6371 km), making it the smallest planet to orbit the Sun. Its interior has a high bulk density, implying that the composition is enriched in metallic iron. Therefore, models used to deduce the internal structure assume a core composition between pure iron and iron sulfide. The structure (depicted in Figure 1.1) is characterized as a possible solid metallic core surrounded by a liquid metallic core, which is estimated to extend out to a

radius of ~ 2020 km, or $\sim 0.8 R_M$. The liquid core is overlaid by a solid outer shell that is only ~ 420 km, or $\sim 0.2 R_M$, thick [Hauck *et al.*, 2013].

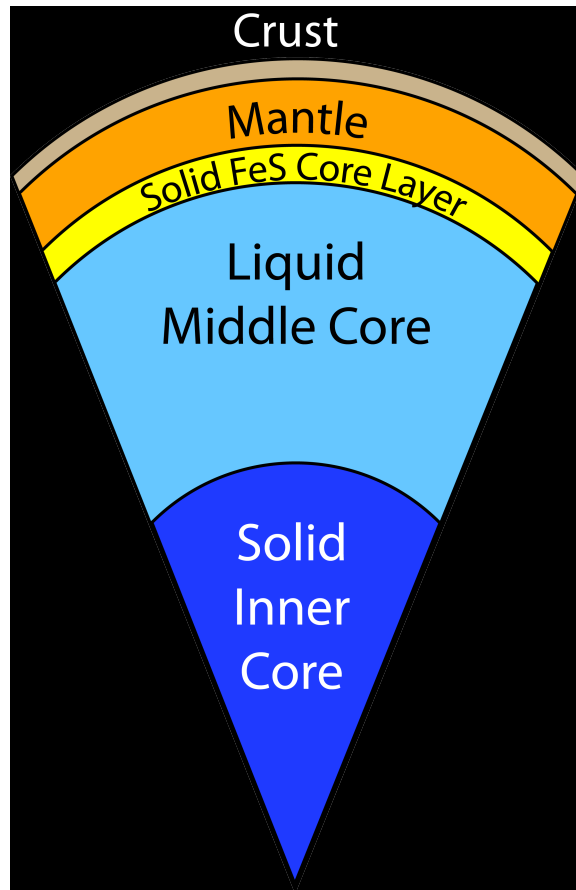


Figure 1.1: The internal structure of Mercury. Figure adapted from Hauck *et al.* [2012].

The majority of Mercury's surface is dark and heavily cratered with only $\sim 27\%$ of the surface consisting of smooth plains that are volcanic in origin [Denevi *et al.*, 2013]. The spectrum of Mercury's surface has a low average reflectance, indicating that the surface has a different composition than expected and experiences a high level of space weathering from impinging solar particles (see Izenberg *et al.* [2014] and references therein). Mercury's surface is magnesium-rich with low concentrations of aluminum and calcium [Nittler *et al.*, 2011; Weider *et al.*, 2012]. Also, despite the iron-rich core, Mercury's surface contains a low total amount of iron (Fe) [Nittler *et al.*, 2011; Evans *et al.*, 2012]. An abundance of sulfur (S) was measured to be an order of magnitude greater than what has been observed on the terrestrial planets. This low-Fe, high-S abundance combination suggests that Mercury's surface composition is unlike any other terrestrial

planet and provides clues on possible planetary formation mechanisms. The reader is referred to *Nittler et al.* [2011] for more information regarding Mercury’s surface composition and planet formation hypotheses.

1.2 Exosphere

At Mercury, the interface separating the planet from the local space environment is defined as a tenuous, surface-bounded exosphere: a regime of collisionless neutrals with its exobase located at Mercury’s surface. The exosphere was first discovered during the three Mercury flybys of the Mariner 10 spacecraft in 1974 and 1975 via ultraviolet (UV) airglow and occultation experiments [*Broadfoot et al.*, 1974]. More specifically, emissions of hydrogen (H), helium (He), and oxygen (O) were detected in UV airglow spectrometer observations [*Broadfoot et al.*, 1976; *Kumar*, 1976]. Following this discovery, ground-based observations from Earth provided additional measurements of Mercury’s exosphere including the detection of sodium (Na), potassium (K), and calcium (Ca) through their resonance scattering emission lines [*Potter and Morgan*, 1985, 1986; *Bida et al.*, 2000]. A summary of the observed constituents and their relative abundances in Mercury’s exosphere, from both Mariner 10 and ground-based observations, are listed in Table 1.1. We now know that magnesium is also present in Mercury’s exosphere [*McClintock et al.*, 2009].

Constituent	Discovery reference	Column abundance (atoms per cm ²)
Hydrogen (H)	Broadfoot et al. (1976)	$\sim 5 \times 10^{10}$
Helium (He)	Broadfoot et al. (1976)	$\sim 2 \times 10^{13}$
Oxygen (O)	Broadfoot et al. (1976)	$\sim 7 \times 10^{12}$
Sodium (Na)	Potter and Morgan (1985)	$\sim 2 \times 10^{11}$
Potassium (K)	Potter and Morgan (1986)	$\sim 1 \times 10^9$
Calcium (Ca)	Bida et al. (2000)	$\sim 1 \times 10^7$

Table 1.1: Summary of constituents in Mercury's atmosphere and their abundances from Mariner 10 and ground-based observations. Table from *Domingue et al.* [2007].

Mercury's exosphere is produced from a series of surface processes operating as sources and sinks for neutral atoms, therefore creating the coupled surface-exosphere system. These processes are also responsible for the production of a small quantity of ions in Mercury's space environment. A detailed description of these source and sink processes is beyond the scope of this dissertation; however, the reader is referred to *Domingue et al.* [2007] for supplementary information.

The exosphere experiences seasonal effects resulting from both the large variation in orbital velocities from Mercury's highly eccentric orbit and the planet's 3:2 spin orbit resonance. Under these conditions, exospheric atoms are subjected to fluctuating solar radiation acceleration as solar intensity changes by more than an order of magnitude between Mercury's orbital periapsis and apoapsis [*Potter et al.*, 2007]. Additionally, photon flux and solar wind density scales as $1/R^2$, where R is Mercury's distance from the Sun, such that they change by more than a factor of 2 between periapsis and apoapsis. These changes directly affect space-weathering processes and have an impact on exospheric abundances.

1.3 Intrinsic Magnetic Field

At altitudes above the tenuous exosphere, Mercury's intrinsic magnetic field shields the planet from the external space environment. Prior to the Mariner 10 flybys of Mercury in 1974 and 1975, it was believed that Mercury did not possess an intrinsic field. However, during the first Mariner 10 encounter (M10-I) on 29 March 1974, the magnetic field investigation provided evidence to suggest that an intrinsically generated magnetic field exists at Mercury [*Ness et al.*, 1974]. Although the second Mariner 10 flyby occurred well upstream of Mercury and was unable to measure the planetary field, the third Mariner 10 encounter (M10-III) on 16 March 1975 confirmed that Mercury does in fact possess a modest, intrinsic magnetic field [*Ness et al.*, 1975, 1976]. Figure 1.2 shows the trajectories of Mariner 10 during the first and third flybys of Mercury. M10-I passed downstream of the planet with a closest approach altitude of 723 km where it observed a peak magnetic field of 98 nT. During M10-III, the spacecraft passed over the

northern hemisphere of Mercury, reaching a closest approach altitude of 327 km in the polar region, and measured a peak magnetic field intensity of 400 nT.

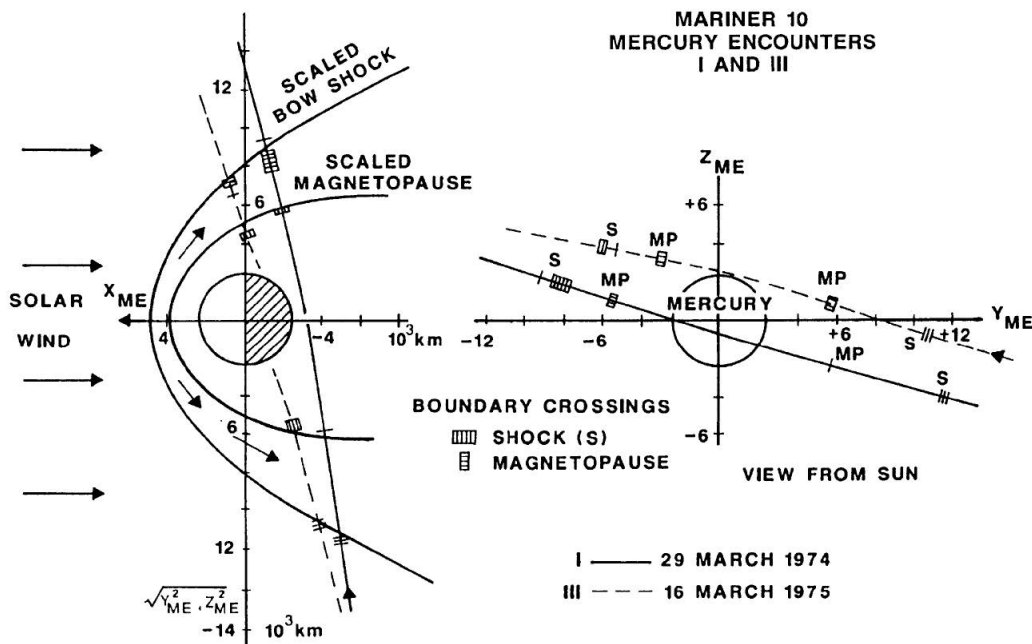


Figure 1.2: Mariner 10 spacecraft trajectories in Mercury-centered solar ecliptic (ME) coordinates. In this coordinate system the X_{ME} is directed towards the Sun, Y_{ME} is in the ecliptic plane and positive in the opposite direction of planetary orbital motion, and Z_{ME} completes the right-handed system. Figure adapted from *Ness et al.*, [1975].

The magnetic field observations during M10-I and M10-III leading to the discovery and confirmation of Mercury’s intrinsic magnetic field are shown in Figure 1.3. In Figure 1.3a, B_x is the dominant component and remains negative between the vertical dashed lines, marking the magnetopause crossing (see Section 1.5) and closest approach, with the magnitude increasing from ~ 50 nT up to ~ 95 nT. A steady field with few fluctuations in all three magnetic field components characterizes the interval between the magnetopause and closest approach. This quiet field is a strong indicator that the spacecraft was measuring a planetary field as opposed to the highly variable magnetic field of the Sun.

Mercury’s magnetic field was confirmed by the data from M10-III shown in Figure 1.3b. The planetary field is measured between the magnetopause crossings at $\sim 22:30$ and just after $22:44$ UTC. Mercury’s field is much more constant when compared to the high-frequency fields of the Sun measured before and after the magnetopause

crossings. The magnetic field magnitude increases until it peaks at Mariner 10's closest approach to the planet.

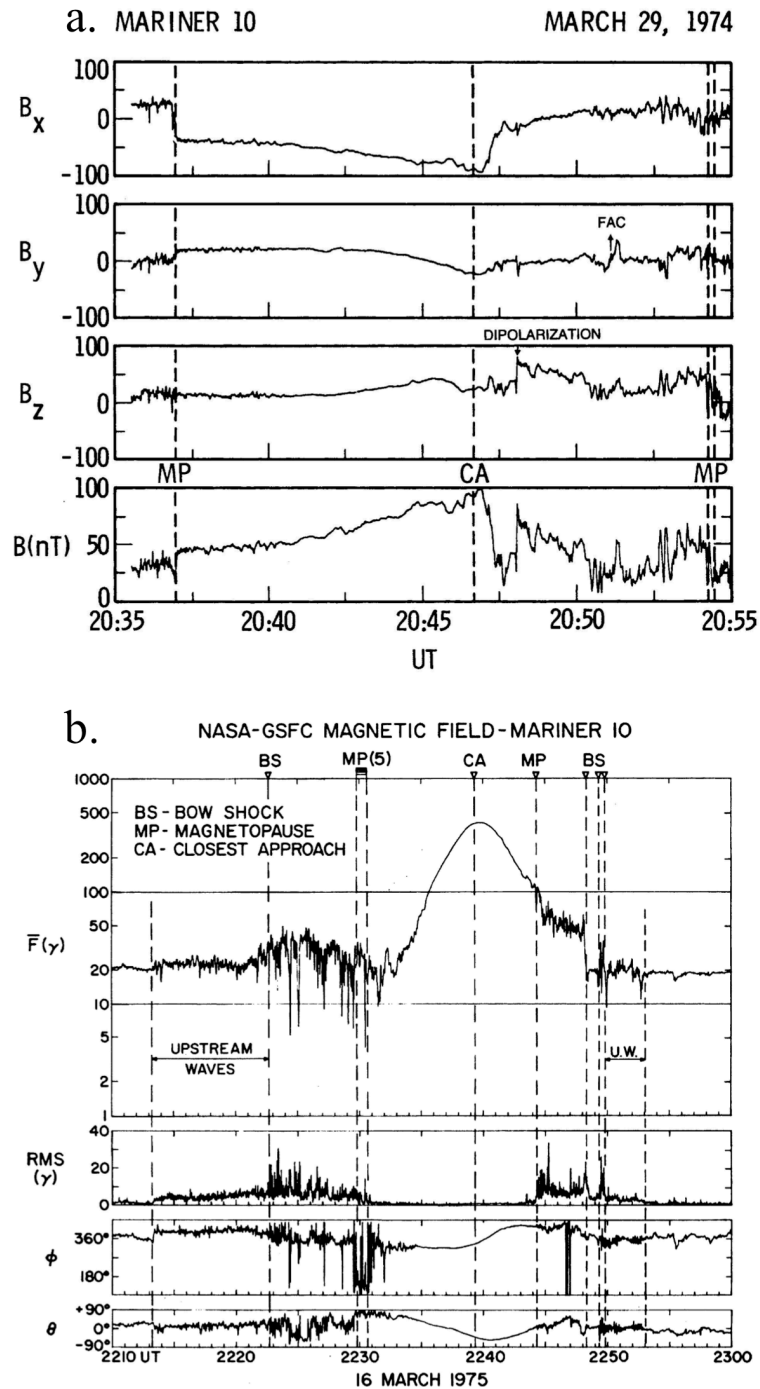


Figure 1.3: (a) Mariner 10 observations during M10-I [Ness *et al.*, 1974] and (b) M10-III [Ness *et al.*, 1975]. The boundaries of Mercury's magnetic environment (vertical dashed lines) are discussed in Section 1.5. Figures from Ness *et al.* [1974, 1975].

In order to estimate the magnetic moment of Mercury, *Ness et al.* [1974] conducted a least-squares fit to the M10-I data (shown in Figure 1.3a) assuming an offset dipole with a 10° tilt, relative to the planetary rotation axis, to obtain a moment of $227 \text{ nT}\cdot R_M^3$. Also considering M10-I observations, *Ness et al.* [1975] obtained a higher moment of $349 \text{ nT}\cdot R_M^3$ for a centered dipole with the assumption of an external contribution to the measured field. A spherical harmonic analysis applied to M10-III observations, assuming a centered dipole with a 12° tilt, resolved a magnetic moment of $342 \text{ nT}\cdot R_M^3$ [*Ness et al.*, 1976]. *Jackson and Beard* [1977] and *Whang* [1977] assessed the possibility of higher-order contributions (i.e., quadrupole and octupole) and both studies established best fits for a dipole moment of $170 \text{ nT}\cdot R_M^3$.

More recently, MErcury, Surface, Space ENvironment, GEochemistry, and Ranging (MESSENGER) Magnetometer observations (described in further detail in Chapter II) have facilitated the determination and verification of the planetary field's global structure. Using measurements from the first MESSENGER flyby (M1), where a maximum field magnitude of 159 nT was measured at closest approach (Figure 1.4a), *Anderson et al.* [2008] applied a spherical harmonic analysis to a combination of M1, M10-I, and M10-III observations in order to assess Mercury's magnetic field. This evaluation yielded centered dipole solutions for a southward planetary moment between $230\text{--}290 \text{ nT}\cdot R_M^3$ tilted within $5\text{--}12^\circ$ from the rotation axis. Data from the second MESSENGER flyby (M2) exhibited a peak of 158 nT in magnetic field intensity (Figure 1.4b) and was used to further resolve Mercury's dipole tilt to be less than 5° [*Anderson et al.*, 2010]. For the third and final MESSENGER flyby of Mercury (M3), the spacecraft entered a "safe hold" during its magnetosphere traversal and instrument observations ceased prior to reaching closest approach.

The M1 and M2 magnetic field observations in Figure 1.4 present similar signatures compared to the M10-III results in Figure 1.3b. The bow shock crossings are marked by a significant increase (decrease) in the total field magnitude as MESSENGER enters (exits) the system. The influence of the planetary field is observed between the vertical dashed lines of the magnetopause crossings. These fields have minimal fluctuations when compared to the magnetic fields measured before and after the magnetopause crossings. The peak magnetic fields were measured near closest approach

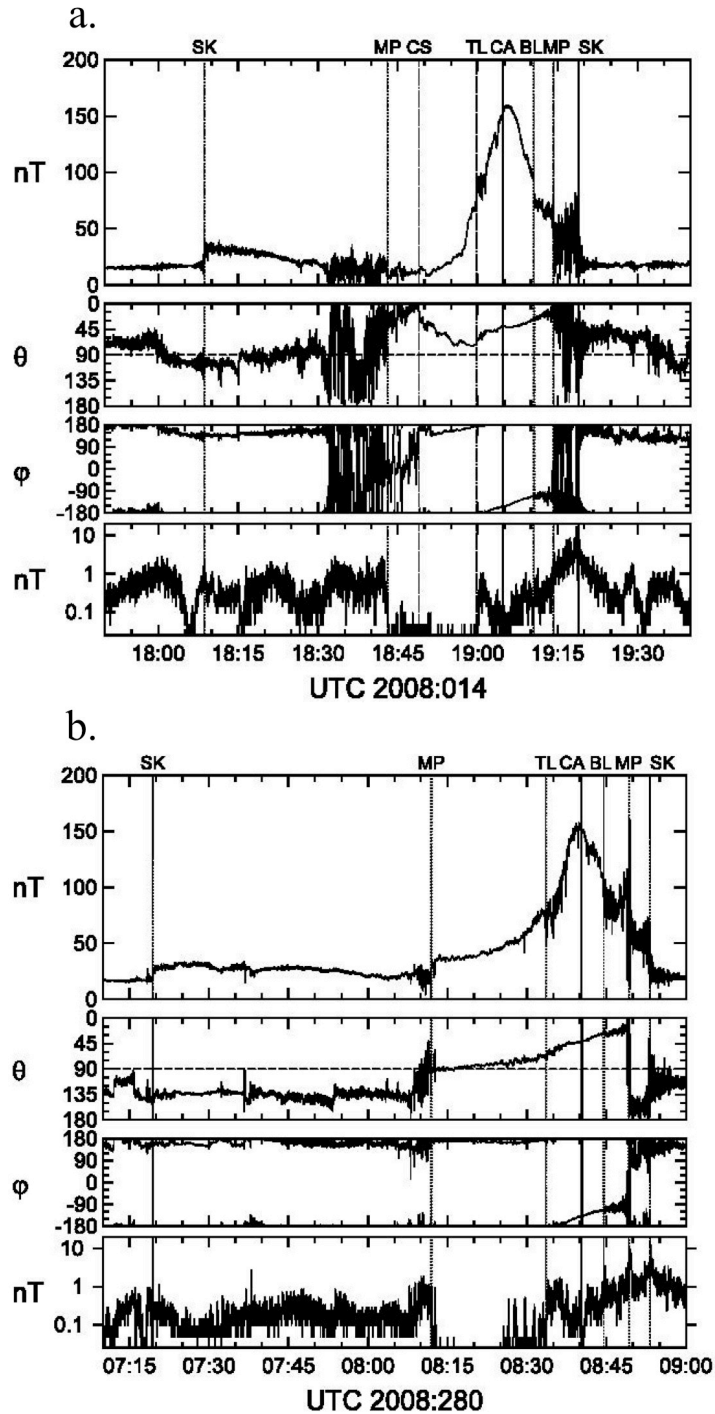


Figure 1.4: Magnetic field data from the (a) first and (b) second MESSENGER flybys presented in Mercury solar orbital (MSO) coordinates. In this coordinate system, X_{MSO} is directed from the center of the planet toward the Sun, Z_{MSO} is normal to Mercury’s orbital plane and positive toward the north celestial pole, and Y_{MSO} completes the right-handed system and positive in the direction opposite to orbital motion. From top to bottom the panels show: the field magnitude; the polar angle, θ , where $\theta = 0^\circ$ is northward; the azimuth angle, ϕ , where $\phi = 0^\circ$ and 90° are sunward and duskward, respectively; and the 1–10-Hz band-pass fluctuation amplitude. Magnetic field vectors were sampled every 0.05 s, and the 1–10-Hz band-pass amplitude was evaluated on-board every 1 s from the 0.05-s data. Magnetic boundaries are labeled as follows: SK for bow shock; MP for magnetopause; CS for the tail current sheet; TL for transition out of the tail lobe; CA for closest approach; and BL for entry into a boundary layer. Figures from *Anderson et al.*, [2010].

at ~ 10 min prior to exiting the magnetosphere.

The characteristics of Mercury’s intrinsic magnetic field were better constrained by the more complete coverage collected during MESSENGER’s orbital phase. *Anderson et al.* [2011a] determined a northward offset of the magnetic dipole by identifying the zero crossing of the magnetic field radial component ($B_\rho = 0$) and then calculating the displacement ($Z_{\rho 0}$) for 141 MESSENGER passes (Figure 1.5). This statistical survey concluded that Mercury’s magnetic field has a northward offset of 484 ± 11 km, or $\sim 0.2 R_M$. This substantial displacement in the dipole location strongly suggests a north-south asymmetry in the surface field and also has implications for magnetospheric effects (discussed in Section 1.5). Additionally, *Anderson et al.* [2011a] concluded that the magnetic axis of the southward-directed, offset dipole is tilted $< 3^\circ$ from the planetary rotation axis and best-fit results indicate a planetary moment of $195 \pm 10 \text{ nT}\cdot R_M^3$.

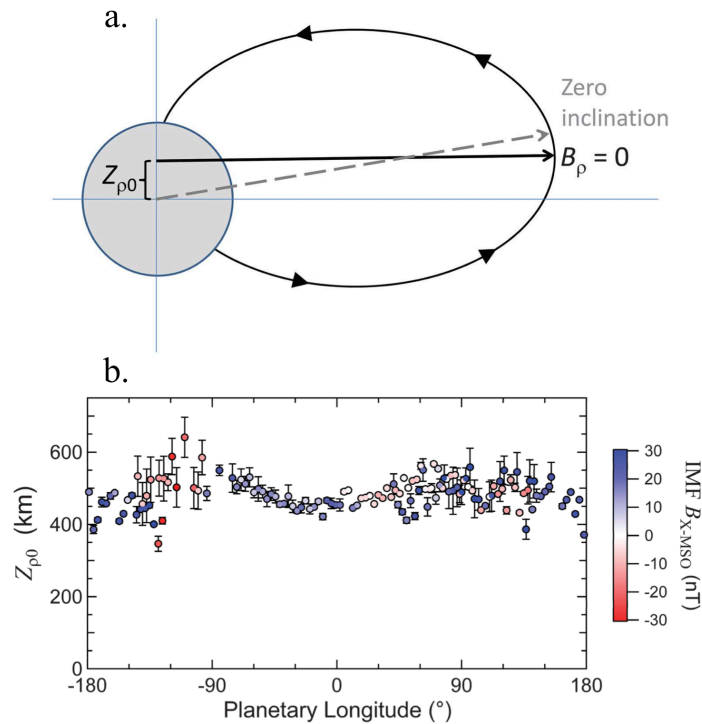


Figure 1.5: Analysis by *Anderson et al.* [2011a] to deduce the northward offset of Mercury’s intrinsic magnetic field where $Z_{\rho 0}$ indicates the local offset of the magnetic equator from the geographic equator of the planet. (a) Identification of magnetic equator from the zero crossing of the cylindrical radial component of the magnetic field. For a dipole approximately aligned with the planet’s spin axis, the north-south position of the $B_\rho = 0$ point coincides with the magnetic equator. For a case with a large axial offset, the point of zero inclination will overestimate the displacement relative to that given by the location of $B_\rho = 0$. (b) Magnetic equator offset versus planetary longitude. Color coding denotes IMF B_{x-MSO} averaged over a 2-hour period that combines 1 hour before the inbound bow-shock crossing and 1 hour after the outbound bow-shock crossing. Error bars are 3-SE uncertainties. Figures from *Anderson et al.* [2011a].

1.4 Interplanetary Environment

The parameters of Mercury’s local space environment are dictated by its proximity to the Sun. The Sun’s influence on the planet is set by the strength of its interplanetary magnetic field (IMF) as well as the velocity, temperature, and density of its solar wind plasma at Mercury’s orbit. The IMF magnitude and solar wind density and temperature each decrease with increasing distance from the Sun but the solar wind velocity is roughly constant throughout the heliosphere. Additionally, Mercury’s eccentric orbit creates a variation in the solar wind parameters as the planet’s heliocentric distance varies between 0.31 and 0.47 AU. As a result, Mercury experiences a more intense and variable interplanetary environment than any other planet. Table 1.2 provides a list of typical IMF and solar wind conditions at each terrestrial planet, including estimates for both the periapsis and apoapsis of Mercury’s orbit. When calculating these parameters, *Slavin and Holzer* [1981] scaled long-term average conditions at 1 AU to each planet’s respective orbit, using the scaling factors listed in Table 1.2a. When comparing Mercury’s orbital extremes, the greatest changes occur in solar wind proton density (n_p) and IMF magnitude (B), which fluctuate by more than 50%.

From the resulting interplanetary conditions, basic upstream plasma parameters of the local space environments were calculated (Figure 1.2b). Mercury experiences solar wind densities that are ~ 5 – 10 times greater than Earth with IMF magnitudes that are ~ 3 – 8 times greater than Earth. These factors create an environment with low plasma β (the ratio of plasma pressure to magnetic pressure) and low Alfvénic Mach number M_A (the ratio of the bulk plasma velocity to the local Alfvén speed). *Slavin and Holzer* [1979] predicted that the low- β , low- M_A space environment at Mercury has extreme consequences on solar wind-planetary interactions (discussed in Section 1.4). Yet another significant difference is the nearly-radial IMF spiral angle at Mercury’s orbit, compared to the average angle of 45° at Earth, indicating that not only the strength but also the IMF orientation is much different at Mercury.

a.	Planet	R , AU	V_{sw} , Km/S	n_p , cm^{-3}	B , nT	T_p , 10^4°K	T_e , 10^4°K
	Mercury	0.31	430	73	46	17	22
		0.47	430	32	21	13	19
	Venus	0.72	430	14	10	10	17
	Earth	1.00	430	7	6	8	15
	Mars	1.52	430	3.0	3.3	6.1	13
	(Scaling)	***	R°	R^{-2}	$R^{-1}(2R^{-2}+2)^{1/2}$	$R^{-2/3}$	$R^{-1/3}$

b.	Planet	R , AU	P_{sw} , 10^{-8} dynes/cm ²	M_s	M_A	β	Q	c/ω_{pi} , km	Spiral Angle, deg
	Mercury	0.31	26	5.5	3.9	0.5	15	27	17
		0.47	11	6.1	5.7	0.9	32	40	25
	Venus	0.72	5.0	6.6	7.9	1.4	62	61	36
	Earth	1.00	2.5	7.2	9.4	1.7	88	86	45
	Mars	1.52	1.1	7.9	11.1	2.0	120	130	57

Table 1.2: (a) Typical interplanetary conditions scaled from 1 AU to the orbits of the other terrestrial planets: solar wind velocity (V_{sw}), proton number density (n_p), IMF field strength (B), and proton (T_p) and electron (T_e) temperatures. (b) Basic parameters computed from the scaled interplanetary conditions: solar wind pressure (P_{sw}), sonic mach number (M_s), Alfvénic Mach number (M_A), plasma beta (β), square of the Alfvénic Mach number (Q), ion inertial length (c/ω_{pi}), and IMF spiral angle. Tables from *Slavin and Holzer* [1981].

MESSENGER flybys and orbital observations have provided *in situ* measurements of Mercury’s space environment as the planet orbits around the Sun. The IMF orientation was notably different at the time of each MESSENGER flyby: northward (M1), southward (M2), and persistent north-south variations (M3). In order to understand the local solar wind parameters for these passes, *Baker et al.* [2009, 2011] performed a model-data comparison by coupling the Wang-Sheeley-Arge (WSA) model, a combined empirical and physics-based model, with a global numerical magnetohydrodynamic model called ENLIL (WSA-ENLIL) and then proceeded to relate model results with the flyby data. An example of WSA-ENLIL radial solar wind velocity (V_r) and density (N) model results during M1 is shown in Figure 1.6. Additionally, Table 1.3 provides the modeled parameters for all three MESSENGER flybys, which are in close agreement with the scaled values determined by *Slavin and Holzer* [1981].

In order to better quantify typical solar wind and IMF characteristics at Mercury, *Baker et al.* [2013] produced WSA-ENLIL model results for the first 10 months of MESSENGER’s orbital mission (see Chapter II) between March 2011 and December 2011 (Figure 1.7). To ensure that the model outputs are in good agreement with MESSENGER measurements, the results were compared to magnetic field observations. Clear periodic signatures in the IMF magnitude ($|B|$), solar wind density (n), and solar wind dynamic pressure (P_{dyn}) demonstrate the change in solar wind parameters at Mercury’s local space environment over the course of the planet’s highly eccentric orbit.

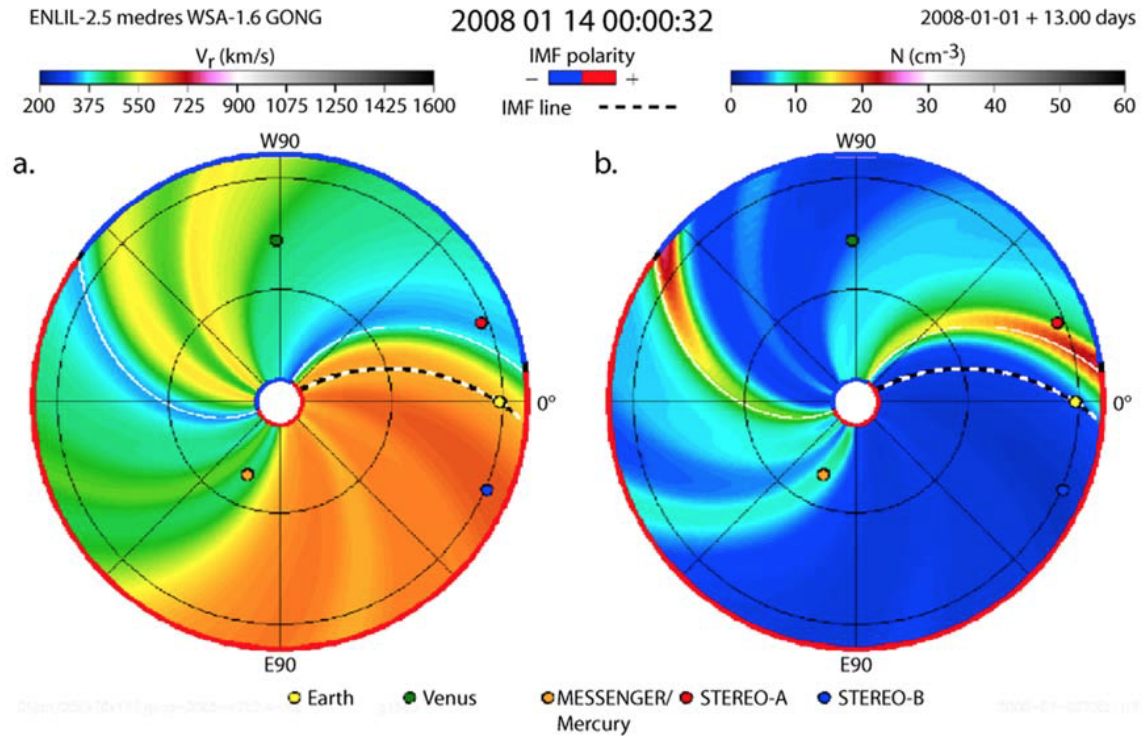


Figure 1.6: WSA-ENLIL model results of solar wind (a) radial velocity and (b) density in the equatorial plane at the time of the first MESSENGER flyby. Model results and figure from *Baker et al. [2009]*.

The horizontal red line highlights the duration of the 88-day Mercury year. Additionally, the shorter variations observed in all components in Figure 1.7 are a result of solar wind stream structures. Once again, these values are in agreement with the *Slavin and Holzer [1981]* scaling. It should also be mentioned that during times of individual extreme solar events, the solar wind parameters have been observed to drastically increase from these base parameters. In fact, the IMF magnitude has been measured at values upward of 80 nT, which has harsh consequences on the planet’s intrinsic magnetic field (see Chapter VI).

Encounter	V_{sw} (km/s)	N (cm^{-3})	T (K)	B_{IMF} (nT)	IMF polarity
M1	420	60	1.2×10^5	18	Away
M2	380	60	2.0×10^5	15	Toward
M3	390	50	1.0×10^5	20	Away

Table 1.3: WSA-ENLIL modeling results of solar wind parameters for the three MESSENGER flybys. These parameters include solar wind velocity (V_{sw}), density (N), temperature (T), IMF magnitude (B_{IMF}), and IMF polarity. Table from *Baker et al. [2011]*.

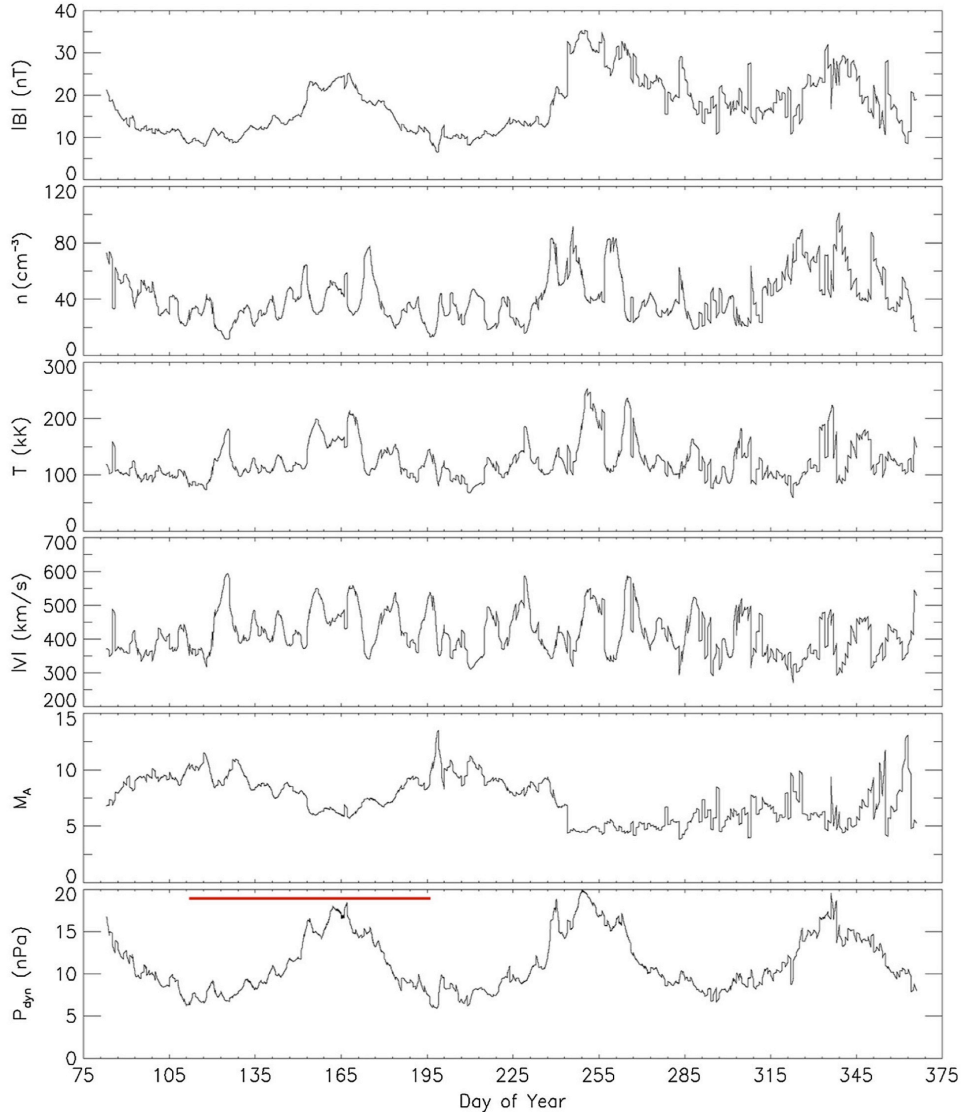


Figure 1.7: WSA-ENLIL model results for the period of March 2011 through December 2011. Computed values of IMF field magnitude ($|B|$), solar wind density (n), solar wind temperature (T), solar wind speed ($|V|$), Alfvénic Mach number (M_A), and solar wind dynamic pressure (P_{dyn}) are shown from the first to the sixth panels, respectively. The red bar in the sixth panel shows the duration of the 88-day Mercury orbit around the Sun. Figure adapted from *Baker et al.* [2013].

1.5 Mercury’s Magnetosphere

As the supersonic, super-Alfvénic solar wind interacts with Mercury’s intrinsic magnetic field, a small, but dynamic, planetary magnetosphere is formed. Although Mercury’s magnetosphere has a structure similar to those of other magnetized planets – with boundaries and regions including the upstream bow shock, magnetopause, cross-tail

current sheet, and northern and southern tail lobes – the combination of Mercury’s weak magnetic moment and amplified solar wind parameters create an unparalleled magnetic environment. When directly compared to other planetary magnetospheres, the spatial and temporal scales at Mercury are significantly reduced. For example, *Ogilvie et al.* [1977] proposed a linear scaling factor of ~ 8 as the ratio of Earth to Mercury magnetosphere lengths. An illustration of Mercury’s magnetosphere is depicted in Figure 1.8.

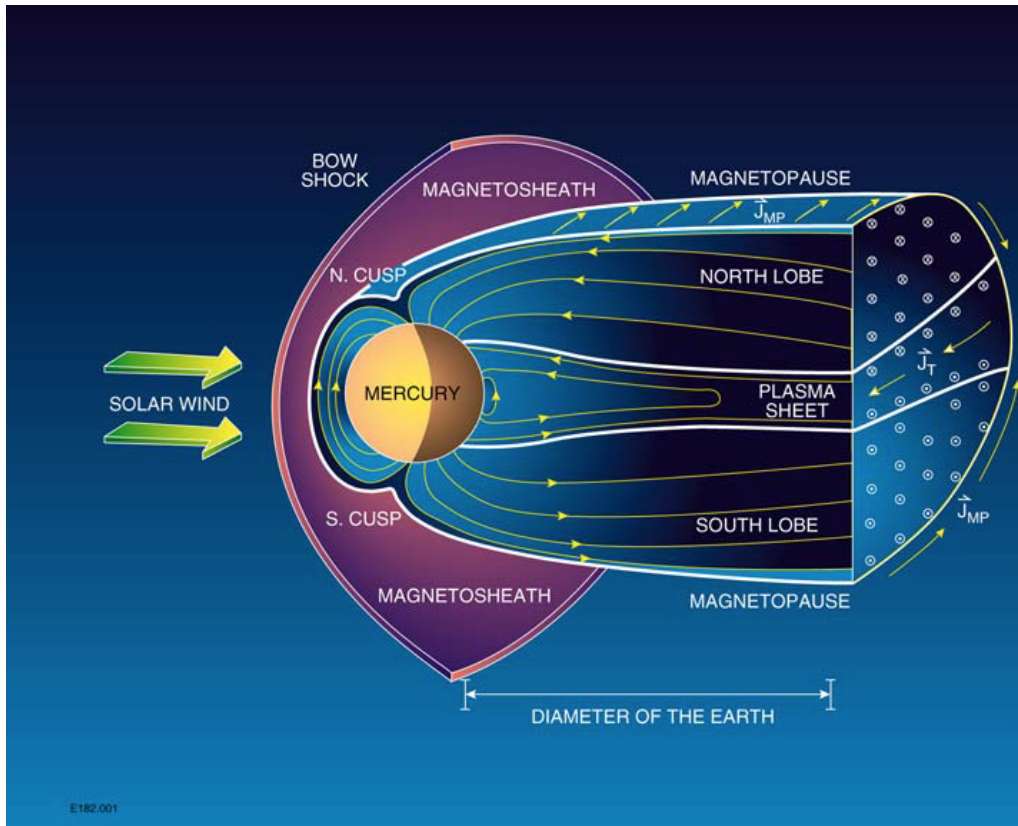


Figure 1.8: Illustration of Mercury’s magnetosphere with a reference to the scale of Earth’s diameter. The solar wind streaming from the Sun is flowing from left to right. Mercury’s intrinsic magnetic field is indicated by yellow lines that are attached to the planet with arrows marking their orientation. The direction of the magnetopause current sheet (J_{MP}) and cross-tail current sheet (J_T) are also denoted with yellow arrows but are not connected to the planet. The main regions of the magnetosphere are labeled. Figure from *Slavin* [2004].

On the dayside, the bow shock marks the transition from super- to sub-magnetosonic solar wind flows. Across this discontinuity, solar wind velocity decreases while the density simultaneously increases. Furthermore, the IMF experiences a rotation and the field magnitude is sharply enhanced. Typical bow shock subsolar standoff distance ranges between $1.89\text{--}2.29 R_M$ with an average distance of $1.96 R_M$ [*Winslow et*

al., 2013]. The magnetopause boundary is defined at the location where the total pressure, comprised of the plasma and magnetic pressures, in the magnetosheath and magnetosphere are balanced. The subsolar magnetopause standoff distance typically ranges between $1.35\text{--}1.55 R_M$ with an average distance of $1.45 R_M$ [Winslow *et al.*, 2013]; therefore, despite its weak magnetic moment, Mercury’s field is able to shield the surface from solar wind bombardment for most upstream conditions. Application of the Mercury-to-Earth scaling factor of 8 [Ogilvie *et al.*, 1977] to the average Mercury bow shock and magnetopause distances correspond to Earth locations of $\sim 15.5 R_E$ (where R_E is Earth’s radius) and $\sim 11.5 R_E$, respectively. These values are consistent with typical terrestrial bow shock and magnetopause observations [Fairfield, 1971]. The small size of Mercury’s magnetosphere indicates that, in terms of planetary radii, Mercury occupies a larger volume fraction of its magnetosphere than Earth.

On the nightside, a magnetotail is created as the solar wind flows past the magnetic obstacle and elongates the field lines. The northern and southern lobes of the tail are all but devoid of plasma, characterized as a low- β environment, and the fields are oppositely oriented, pointing toward the planet in the north lobe and away from the planet in the southern lobe. This antiparallel configuration creates a cross-tail current sheet between the two lobes. The current sheet is surrounded by a plasma sheet, which is a region populated with plasma that has moved to the central magnetotail region due to an $\mathbf{E} \times \mathbf{B}$ drift, where \mathbf{E} is the convection electric field and \mathbf{B} is the magnetic field in each lobe. With its dense plasma population and weaker magnetic field magnitude, this plasma sheet is a high- β magnetosphere region [see Raines *et al.*, 2011].

The plasma distribution throughout Mercury’s magnetosphere plays an integral role in the dynamics. The planetary ions can have gyroradii that are comparable in size to the magnetosphere. This enables finite gyroradius effects in which the ions may either be lost to the planetary surface or escape across the magnetopause. These effects are expected to cause anisotropic distributions throughout the magnetosphere [Delcourt *et al.*, 2002, 2003]. In Mercury’s magnetosphere, the flux of planetary ions peak in the northern magnetic cusp region and at equatorial latitudes on the nightside [Zurbuchen *et al.*, 2011]. At the subsolar point on the dayside, planetary ions show minimum observed densities within 30° of the equator [Raines *et al.*, 2013]. Additionally, altitude and local time

dependencies are observed for different ion species [Raines *et al.*, 2013]. Temporal variations in these observed quantities signify the magnetospheric response to fluctuating solar wind conditions. Figure 1.9 shows the plasma distribution in relation to magnetospheric structure at the time of the first MESSENGER flyby.

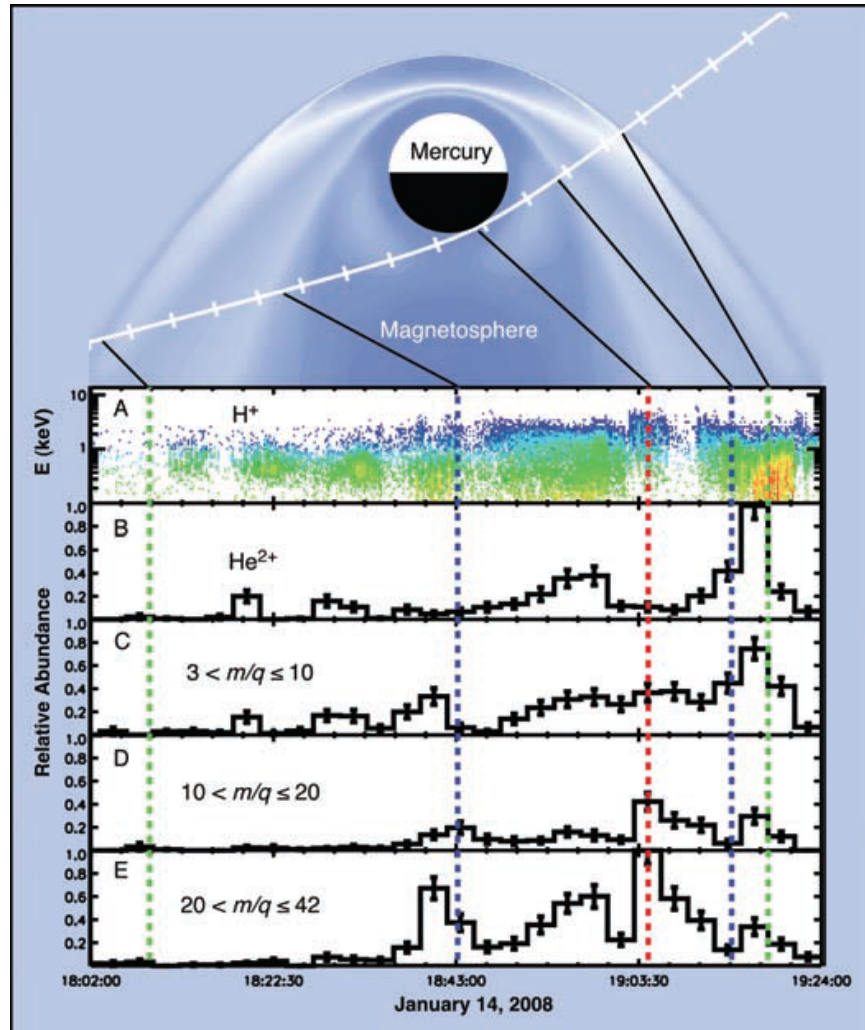


Figure 1.9: Spatial distribution of key plasma components in relation to magnetospheric structure. (Top) Overview of magnetospheric geometry from a magnetohydrodynamic simulation used to order the timeline of the MESSENGER flyby and the locations and encounter times of key components of the Mercury space environment. (A and B) Energy distribution of protons (at a resolution of 8 s, during which FIPS performs a complete E/q stepping sequence from 0.1 to 13 keV/e) and normalized He^{2+} flux. Both species originate in the solar wind. The temporal variability of these components is associated with changes in plasma characteristics, as well as with temporal variability of the obstruction geometry, especially for solar wind protons. (C, D, and E) Normalized fluxes of ions in specified m/q ranges. All fluxes (B to E) are normalized to the peak flux in He^{2+} . The fluxes of heavy ions with $10 < m/q < 42$ maximize near the planet but are also found throughout the magnetosphere. During the flyby, the spacecraft sunshade, one of the solar panels, and other spacecraft structures limit the field of view of FIPS to $\sim\pi$ steradians. Vertical dashed lines denote the crossing of the bow shock (green), the magnetopause (blue), and the point of closest approach (red), based on magnetic field data. Figure from Zurbuchen *et al.* [2008].

It is important to realize, however, that these regions of Mercury's magnetosphere are anything but stable. As discussed in Section 1.4, the dynamic solar wind creates an ever-changing environment to which the magnetosphere must respond. This response triggers additional interactions throughout the different regions of the magnetosphere. One of the most commonly observed dynamic process in Mercury's magnetosphere is magnetic reconnection. Magnetic reconnection, a ubiquitous process in space plasmas, is responsible for the exchange of mass, momentum, and energy between two plasmas of different origins. It occurs in thin current sheets, created by sheared magnetic fields, at sites called X-lines. Figure 1.10 represents an illustration of a reconnection region. As the sheared fields on either side of the current sheet flow inward (vertical yellow arrows), they will eventually meet at the X-line. At this location, the fields of different sources (red and blue) are spliced together, or reconnected, and two new field lines are formed. The new fields (combined red/blue), driven by the release of magnetic tension, are then ejected away from the reconnection region at high speeds (horizontal yellow arrows). In addition to the changing field line topology, magnetic reconnection also enables the exchange of plasma between magnetic fields of two different origins. The outflow of the newly formed fields can be observed in the form of plasma jets. Magnetic reconnection has three main consequences: (1) reconfiguring magnetic field lines; (2) converting magnetic energy into kinetic energy, therefore heating the particles; and (3) producing jets of outflowing plasma. This process plays a particularly important role in planetary magnetospheres, because there are many regions where sheared magnetic fields are present.

Two of the most common sites for reconnection to occur in planetary magnetospheres are at the magnetopause and in the cross-tail current sheet. At the magnetopause boundary, the ever-changing IMF in the magnetosheath is directly adjacent to the planetary magnetic field and the two often become sheared, presenting conditions that are favorable for reconnection. In the magnetotail, reconnection is common in the cross-tail current sheet, which provides a high-sheared environment between the oppositely directed fields in the north and south tail lobes. At Mercury, frequent occurrence of reconnection at the magnetopause and tail current sheet dictates

the circulation of plasma and magnetic flux throughout the magnetosphere in a sequence called the Dungey cycle [Dungey, 1961], depicted in Figure 1.11.

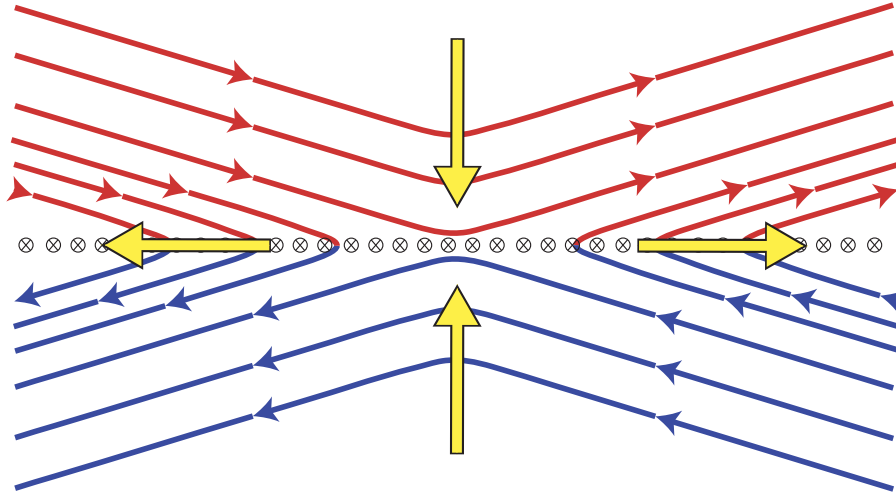


Figure 1.10: Reconnection region with two magnetic fields (blue and red) from different domains with opposite orientations. A current sheet forms between the sheared fields. The fields flow towards the current sheet and will meet at the X-line where they will reconnect. The newly formed fields (red/blue combination) will then exit the region at high speeds due to the release of magnetic tension.

The Dungey cycle is initiated by reconnection at the magnetopause, depicted in Figure 1.11, between the IMF (blue) and the closed planetary magnetic field (green) to form a newly open field line (orange) with one end attached to the planet and the other in the solar wind. This open field is transported around the planet by the solar wind flow where it becomes elongated and forms the magnetotail. The open fields in the north and south lobes will reconnect once again in the cross-tail current sheet (denoted by \odot) to produce two new fields: a closed planetary field that will convect back towards the planet and a detached field that will rejoin the solar wind as it exits down the tail. The location of the near-Mercury neutral line in the cross-tail current sheet is expected to form close to Mercury, i.e., $2-3 R_M$ [Baker *et al.*, 1986].

Because this process is driven by solar wind interaction, and Mercury experiences more vigorous solar wind forcing than any other planet, Mercury's Dungey cycle was expected to be much shorter in comparison [Siscoe *et al.*, 1975; Baker *et al.*, 1986]. In agreement with this prediction, observations have revealed typical Dungey cycle times of ~ 2 min at Mercury [Slavin *et al.*, 2009, 2010], which are much shorter than the ~ 1 h

convection times at Earth. Another factor believed to contribute towards this drastic difference in global convection patterns is Mercury's lack of a collisional ionosphere [Slavin *et al.*, 2007].

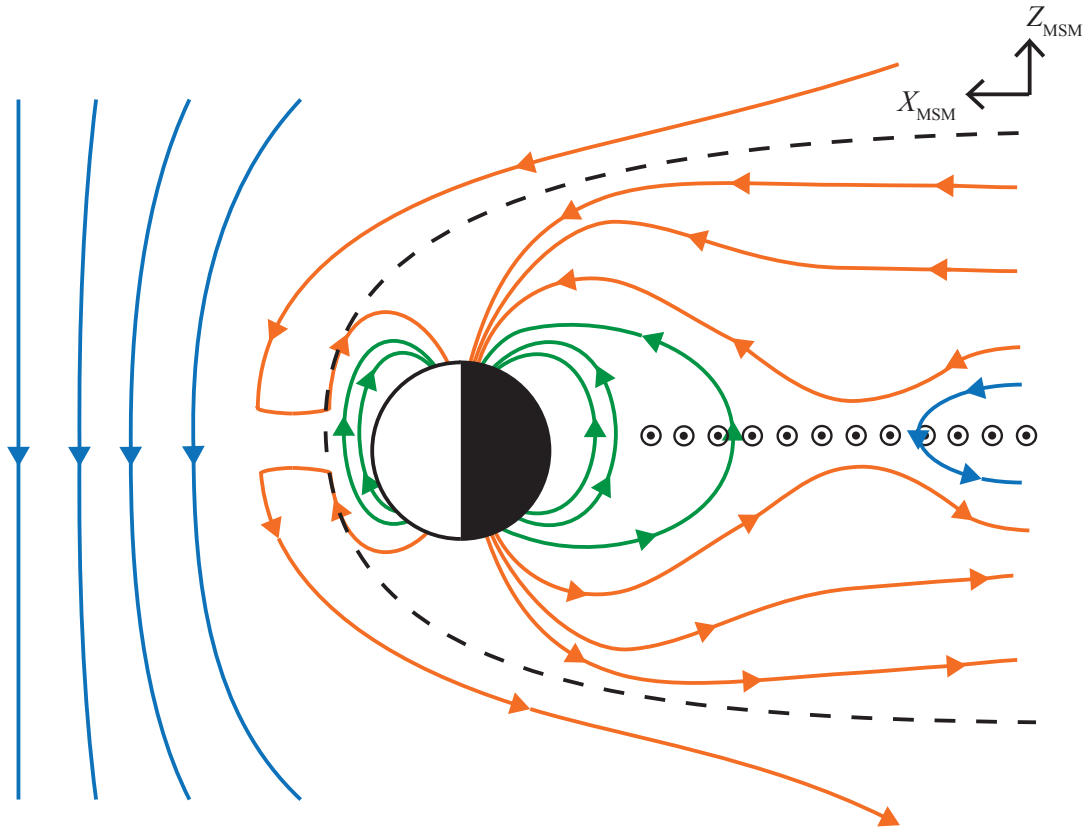


Figure 1.11: A schematic of Mercury's magnetosphere as the Dungey cycle progresses. The IMF (blue) reconnects with the intrinsic planetary field (green) at the dayside magnetopause. An open field line is generated (orange), which will get pulled past the planet by the solar wind to join the magnetotail. The open field lines of opposite orientation will meet in the cross-tail current sheet (\odot) and reconnect with each other. The result is a closed planetary field that will move back toward the planet and a detached field that rejoins the IMF.

In addition to the effects on planetary magnetospheres mentioned above, reconnection occurs in magnetic fields throughout the universe. Events such as solar flares and coronal mass ejections at the Sun, discontinuities in the solar wind, and the formation of stars beyond the heliosphere are observed to experience reconnection [e.g., Priest and Forbes, 2000; Gosling *et al.*, 2005]. Reconnection plays a vital role in dynamics throughout these regions by reconfiguring magnetic field lines and altering local plasma characteristics. However, despite the broad impact of reconnection throughout space plasmas, the process is still not well understood and many outstanding

questions remain: (1) Why does reconnection occur at such a fast rate in collisionless plasmas? (2) What determines the structure of the reconnection region? (3) What triggers the explosive onset of reconnection?

Progress on our understanding of magnetic reconnection has been made possible with not only space and astrophysical observations but also by laboratory plasma experiments. Although space and astrophysical experimentation provides evidence of reconnection through direct observations, these measurements are limited by the location of the spacecraft and its orbit. Laboratory experiments are able to reproduce reconnection in collisionless plasmas while measuring the reconnection region at various points simultaneously [Yamada, 2001]. Experimental observations of reconnection are made through the self-organization of fusion plasmas, most of which are carried out in toroidal systems (see review in Yamada *et al.*, 2010). Additionally, dedicated laboratory investigations, such as the Magnetic Reconnection Experiment (MRX) [Yamada *et al.*, 1997], have been designed to study the fundamentals of magnetic reconnection in a collisionless regime. MRX geometry is initially 2-dimensional and axisymmetric but also has the capabilities of being non-axisymmetric in order to study 3-dimensional features. For these investigations the ion gyroradius is much smaller than the size of the plasma, 1–5 cm versus 30–50 cm, respectively, with a mean-free-path ranging from 0.1 to 20 cm, indicating that the plasma is described by magnetohydrodynamics (MHD). Typical MRX plasma parameters used to create a magnetized MHD plasma facilitating reconnection (see review on reconnection in MHD plasmas by Kulsrud, 1998) are $n_e \sim 0.1\text{--}1 \times 10^{14} \text{ cm}^{-3}$, $T_e = 5\text{--}15 \text{ eV}$, $B = 0.2\text{--}1 \text{ kG}$, $S > 500$, where n_e is the electron density, T_e is the electron temperature, B is the magnetic field magnitude, and S is the Lundquist number. Table 1.4 compares the spatial scales of reconnection in MRX and magnetospheric plasmas using the ratio of the ion skin depth, δ_i , to the Sweet-Parker width, δ_{SP} .

Recent advancements in our understanding reconnection have come from laboratory experiments. MRX data has illustrated that the reconnection current sheet thickness scales with δ_i [Ono *et al.*, 1997; Kornack *et al.*, 1998] and the width of the electron diffusion region, the region where demagnetized electrons are accelerated in the

System	L (cm)	B (G)	$\delta_i = c/\omega_{pi}$ (cm)	δ_{SP} (cm)	δ_i/δ_{SP}
MRX	10	100-500	1-5	0.1-5	0.3-10
Magnetosphere	10^9	10^{-3}	10^7	10^4	1000

Table 1.4: Comparison of magnetic reconnection in different plasmas. L is the reconnection sheet length, B is the magnetic field magnitude, δ_i is the ion skin depth, and δ_{SP} is the Sweet-Parker width. Table adapted from *Yamada et al.* [2009].

reconnection plane, scales with the electron skin depth as 5.5–7.5 δ_e while outflow velocities are ~ 1.2 – 1.6 times the electron Alfvén speed [*Ren et al.*, 2008]. Further results have demonstrated that as the mean free path increases and plasma collisionality is reduced the reconnection rate increases and the 2-dimensional profile of the reconnection layer changes from a rectangular shape to a wedge shape as shown in Figure 1.12 [*Yamada et al.*, 2006]. Additionally, the scaling from MRX suggests that the reconnection rate will begin to increase when δ_i/δ_{SP} exceeds ~ 2 . The existence of a substantial guide field in MRX has indicated that the resistivity will decrease by a factor of ~ 2 [*Kuritsyn et al.*, 2006], which agrees with earlier findings that the reconnection speed decreases as the guide field increases [*Yamada et al.*, 1990]. However, MRX has been most useful in confirming the importance of Hall effects by providing observations of an out-of-plane quadrupolar magnetic field, which is believed to facilitate fast reconnection (Figure 1.12b). These results have demonstrated that electrons are initially $E \times B$ accelerated in the reconnection region and then experience an additional acceleration due to the Hall effects [*Ren et al.*, 2005; *Yamada et al.*, 2006].

Laboratory experiments provide a method to verify possible processes dictating reconnection as well as testing analysis techniques. They also have certain advantages over spacecraft observations, e.g., the ability to take measurements at numerous points simultaneously, and serve as an important tool to enhance our understanding of the reconnection region. However, *in situ* measurements of reconnection in space plasmas provide direct measurements of this phenomenon as it naturally evolves. Evidence of solar wind-planetary reconnection in a Dungey cycle-driven magnetosphere has been limited to Earth observations because there are other dictating dynamics at Jupiter and Saturn. Mercury’s local space environment provides a new plasma regime to observe reconnection between the IMF and planetary magnetic field. Studying reconnection in

this low- β environment will test predictions of enhanced reconnection rates and provide direct measurements of reconnection in a space environment different than that of Earth. It is through the combined efforts of space observations and laboratory plasma experiments that the outstanding questions on the process of magnetic reconnection will finally be resolved.

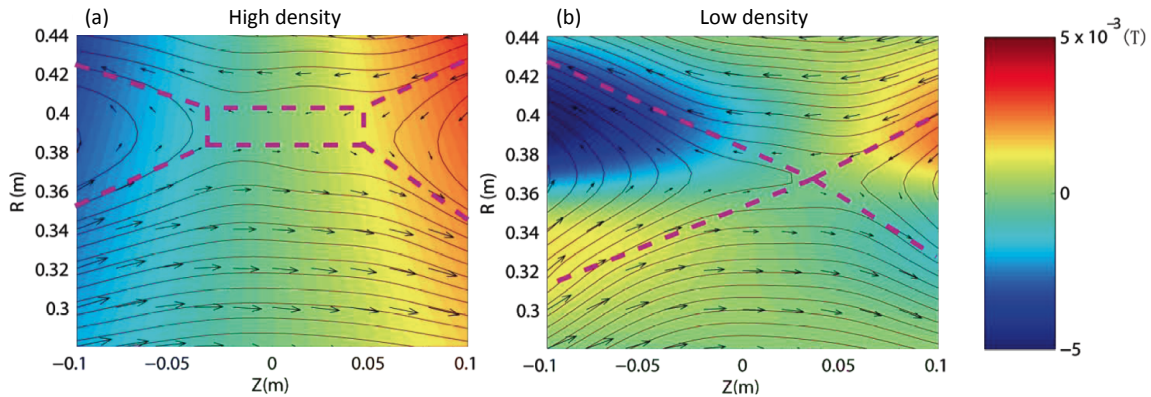


Figure 1.12: Comparison of the experimentally measured reconnection layer profile for two cases: (a) Collisional regime and (b) Nearly collisionless regime. In-plane magnetic field is shown as arrows and out of plane field component by the color codes ranged from -50 G to 50 G. Dashed pink lines shows that the magnetic configuration changes from an elongated current sheet (Sweet-Parker type in (a)) to a double-wedge shape (Petschek-like) as collisionality is reduced. The predicted quadrupole structure of the out-of-plane magnetic component, a signature of Hall effects, is observed in (b). Figure adapted from *Yamada et al.* [2006].

1.6 Guiding Science Questions

The combination of Mercury’s intense local space environment with its weak intrinsic magnetic field offers an extreme case from which we can better understand the Earth’s magnetosphere. The decreased spatial and temporal scales in Mercury’s magnetosphere, outlined in the sections above, raise questions as to which factors are responsible for driving magnetospheric dynamics. When investigating global effects we must consider the consequences due to the solar wind parameters in the inner heliosphere, processes such as magnetic reconnection, and the planet’s internal structure. Determining these differences and their impact on Mercury’s magnetosphere is the

foundation upon which this work is based. In order to achieve this level of understanding, there are three principal science questions that we address in the subsequent chapters:

Q1. What impact does magnetic reconnection have on Mercury's magnetosphere?

It was predicted by *Slavin and Holzer* [1979] that the low Alfvénic Mach number, and therefore low- β , plasma in the inner heliosphere should be responsible for producing high reconnection rates in Mercury's magnetosphere. The Dungey cycle was determined to be ~ 2 min at Mercury, or ~ 30 times shorter than at Earth, supporting the hypothesis of reconnection-driven magnetosphere [*Slavin et al.*, 2009, 2010]. Although research suggests that reconnection plays a crucial role in the dynamics of Mercury's magnetosphere, its effects have never been quantified. Determining characteristics of magnetic reconnection throughout Mercury's magnetosphere is crucial for understanding the planet's space environment.

Q2. What dynamics are associated with solar wind plasma entry and flux circulation throughout Mercury's magnetosphere?

Not only is the solar wind an external driver of Mercury's magnetosphere, under certain conditions solar wind ions are able to gain access to the inner magnetosphere. The internal presence of these particles affects the pressure balance throughout the magnetosphere as well as length and time scales associated with different dynamics. Once the solar wind has entered the system, its transportation mechanisms throughout the magnetosphere will provide clues to the inner workings of Mercury's environment. Determining the mechanisms responsible for solar wind entry and transport in Mercury's magnetosphere is essential for understanding general magnetospheric structure and characteristics. By understanding the processes that promote solar wind access into the magnetosphere, we can build from this knowledge to determine the plasma's influence in different regions of the magnetosphere.

Q3. *How does Mercury's magnetosphere respond to changing upstream solar wind conditions?*

It is already understood that Mercury's local space environment, discussed in Section 1.4, has increased solar wind densities compared to other planets in the solar system as well as constantly fluctuating IMF magnitudes. However, the impact of these variations has never been addressed. If magnetic reconnection is the ultimate driver of this magnetospheric system, it is necessary to understand whether this process is dependent on the changing upstream conditions. If the solar wind does impact the occurrence of reconnection at Mercury, determining which specific parameters affect reconnection are crucial to the understanding of dynamics at Mercury.

The question of magnetospheric dependencies on changing solar wind parameters is not only applicable to Mercury's environment. As the closest planet to the Sun, Mercury's location in the heliosphere provides an extreme environment when compared to other planetary magnetospheres. By understanding how Mercury's magnetosphere functions under the most extreme solar conditions it is possible to apply this knowledge to better understand the workings of Earth's environment.

These overarching science questions can only be answered using *in situ* magnetic field and plasma observations of Mercury's space environment. Here, we analyze data from the MESSENGER spacecraft in order to better understand the driving forces in Mercury's magnetosphere. Chapter II address the MESSENGER mission along with the instruments and data utilized in this work. Chapters III through VI explain the analyses and conclusions for each science question listed above. Chapter VII summarizes the results and conclusions from each study with an explanation of their contribution to understanding the dynamics of Mercury's magnetosphere.

CHAPTER II

METHODOLOGY

2.1 MESSENGER Mission

In order to address the guiding science questions outlined in Section 1.6, we have utilized *in situ* measurements from the MErcury Surface, Space ENvironment, GEOchemistry, and Ranging (MESSENGER) spacecraft during its orbital mission phase at Mercury. Prior to MESSENGER's arrival, Mariner 10 had been the only spacecraft to visit Mercury and its local space environment, offering minimal observations from three planetary flybys in 1974 and 1975. As a consequence of the limited *in situ* data, Mercury remained an enigma of uncharted territory. Three decades after Mariner 10 encountered the planet, MESSENGER became the first spacecraft to orbit Mercury and provide continuous measurements of the innermost planet's space environment. As part of the Discovery Program of the U.S. National Aeronautics and Space Administration (NASA), the MESSENGER mission was designed to answer six fundamental science questions with respect to Mercury [Solomon *et al.*, 2007]: (1) What planetary formational processes led to the high ratio of metal to silicate in Mercury? (2) What is the geological history of Mercury? (3) What are the nature and origin of Mercury's magnetic field? (4) What are the structure and state of Mercury's core? (5) What are the radar-reflective materials at Mercury's poles? (6) What are the important volatile species and their sources and sinks on and near Mercury?

MESSENGER must provide a corresponding set of measurements in order to meet these mission science objectives. Therefore, the spacecraft is equipped with a payload consisting of seven instruments plus radio science. The instruments and their location on the spacecraft are displayed in Figure 2.1. Of these instruments, two are

crucial for measuring and understanding Mercury’s local space environment: (1) the Magnetometer (MAG) [Anderson *et al.*, 2007] and (2) the Energetic Particle and Plasma Spectrometer (EPPS) [Andrews *et al.*, 2007], which consists of the Energetic Particle Spectrometer (EPS) and the Fast Imaging Plasma Spectrometer (FIPS). Further information regarding MAG and FIPS is provided in Sections 2.2 and 2.3.

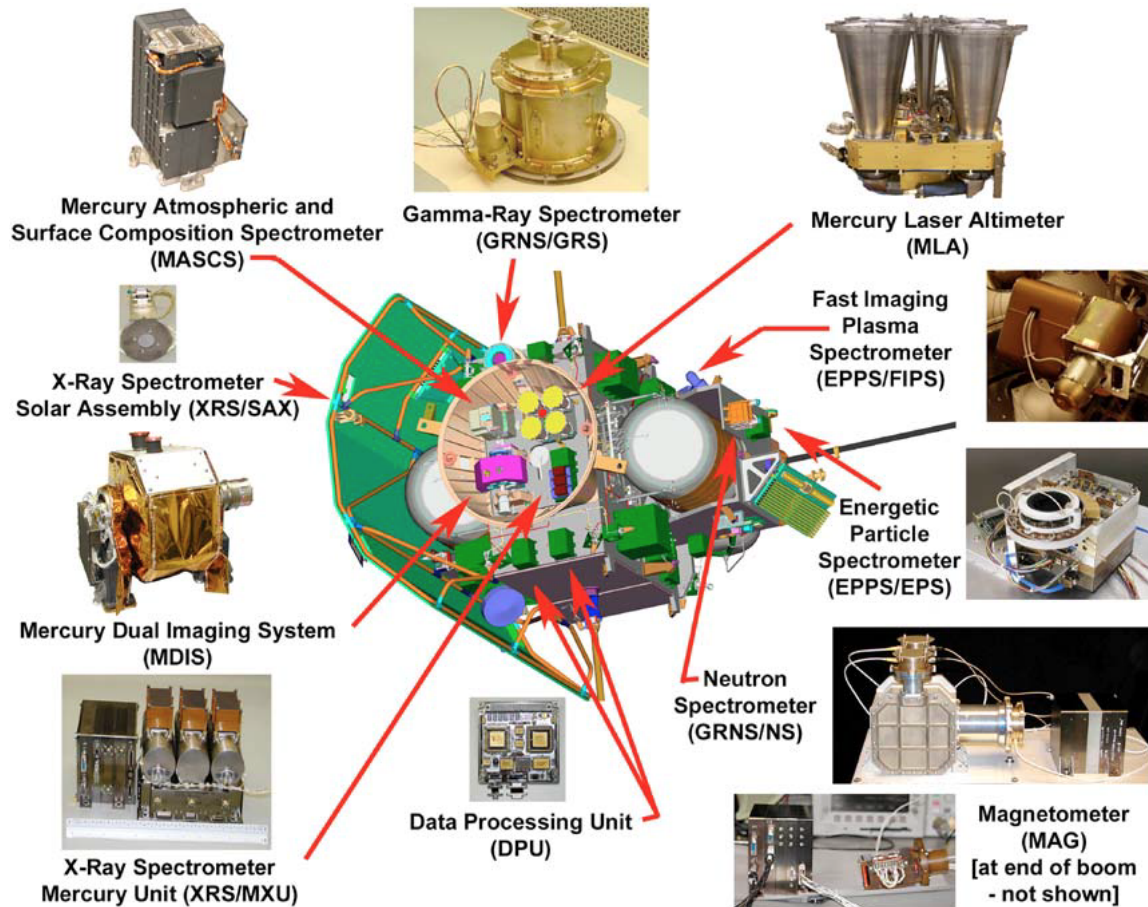


Figure 2.1: MESSENGER payload instruments and their location on the spacecraft. From Leary *et al.* [2007].

In addition to the instrument payload, the spacecraft has a ceramic-cloth sunshade that eliminates a majority of energy input from the Sun due to its heat-resistant and highly reflective properties. To ensure that the sunshade remains pointed towards the Sun, while allowing a rotation about the spacecraft–Sun line for instrument viewing, MESSENGER is three-axis stabilized. This spacecraft attitude permits that MESSENGER’s main source of power is provided from two solar arrays.

MESSENGER was successfully launched by a Delta II 7925H-9.5 rocket from the Cape Canaveral Air Force Station Space Launch Complex 17B, Florida, on 3 August

2004 (Figure 2.2). The 6.6-year cruise phase of the mission included numerous trajectory corrections and six planetary flybys: one of Earth, two of Venus, and three of Mercury. During the Mercury flybys, which occurred on 14 January 2008, 6 October 2008, and 29 September 2009, MESSENGER passed within 200 km of the planet's surface. The chronology of the planetary flybys and MESSENGER's trajectory from the time of launch until orbital insertion are outlined at the bottom of Figure 2.3. The mission's cruise phase ended on 18 March 2011 when MESSENGER was inserted into orbit around Mercury, becoming the first spacecraft to orbit the planet.



Figure 2.2: MESSENGER launch on a Delta II 7925H-9.5 rocket from the Cape Canaveral Air Force Station Space Launch Complex 17B, Florida, on 3 August 2004. Image from *Solomon et al.* [2007].

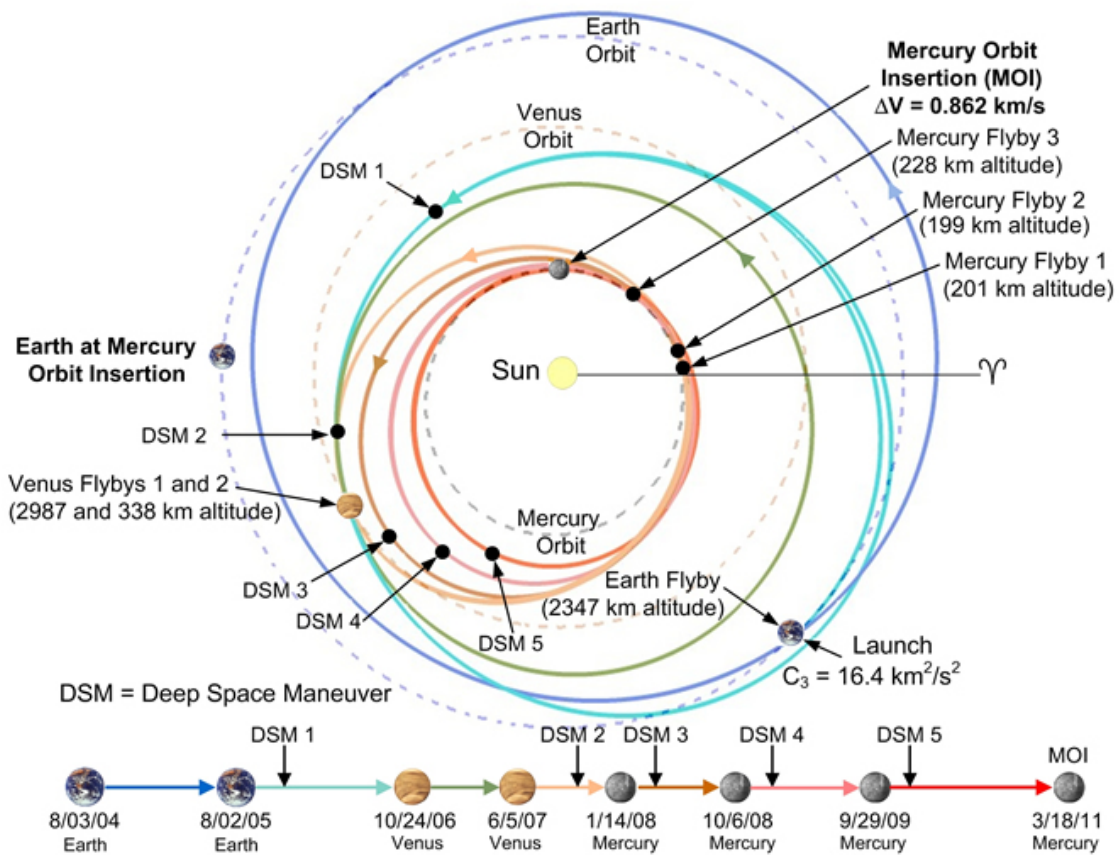


Figure 2.3: North ecliptic pole view of MESSENGER's heliocentric trajectory. The spacecraft will utilize one Earth gravity assist, two Venus gravity assists, three Mercury gravity assists, and five major course-correction maneuvers, or DSMs, during its 6.6-year ballistic trajectory to Mercury. Figure from *McAdams et al.* [2005].

Following orbital insertion, MESSENGER was put into a 12-hour highly eccentric and nearly polar orbit, with an 82.5° inclination with respect to Mercury's equator. Orbital periapsis, which occurred over 60° N latitude, and apoapsis were located at altitudes of ~ 200 km and $\sim 15,000$ km, respectively. A schematic of MESSENGER's orbit around Mercury is provided in Figure 2.4. The spacecraft's orbital plane is approximately fixed in inertial space, which causes a counterclockwise precession of the orbit by 0.2 h/day in local time as Mercury moves around the Sun. Figure 2.5 shows four sample orbits over the course of a Mercury year in order to demonstrate the rotation of the periapsis location. The true anomaly angle (TAA) and radial distance are provided in the figure to describe the planet's position as it orbits the Sun.

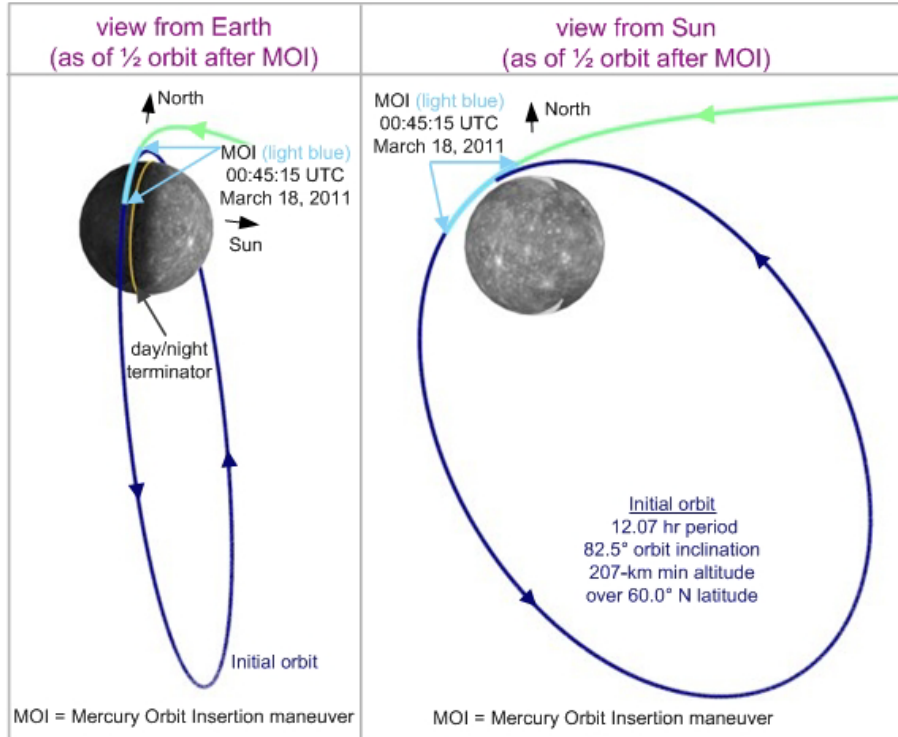


Figure 2.4: MESSENGER's initial orbit around Mercury. Figure adapted from *McAdams et al.* [2012].

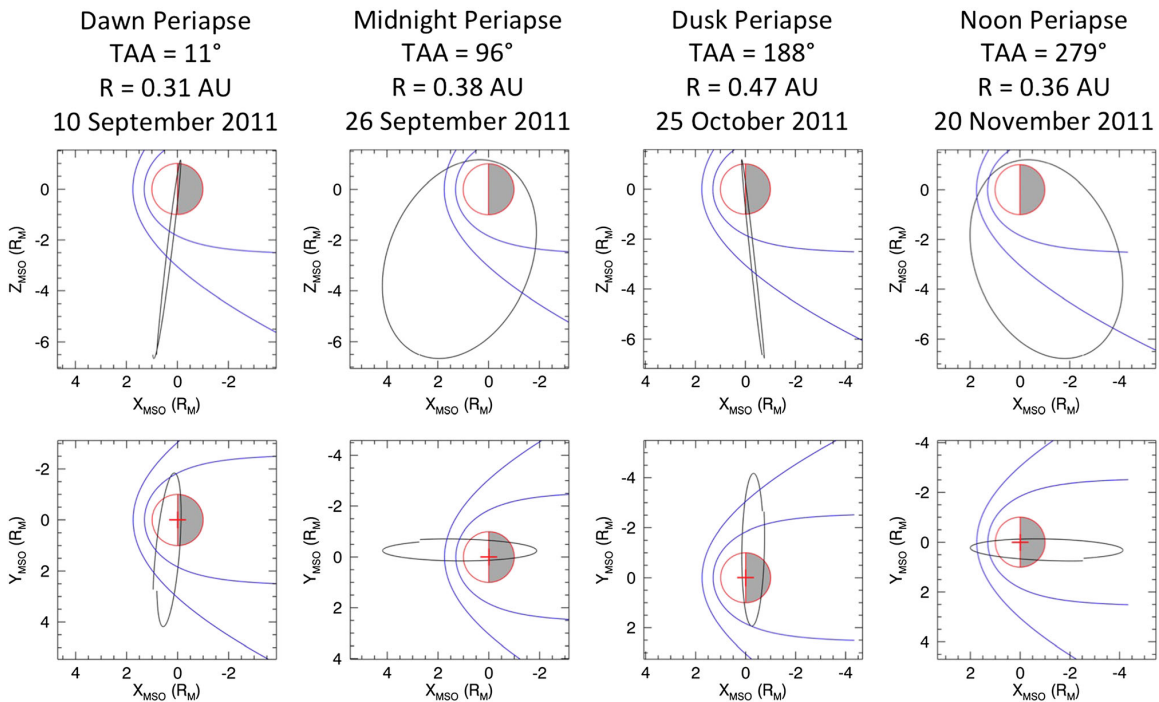


Figure 2.5: Selected MESSENGER orbits during the first three Mercury years of the MESSENGER orbital mission showing periapsis at four different local times. Mercury true anomaly angle (TAA) and radial distance to the Sun (R) are also given. Figure from *Raines et al.* [2013].

MESSENGER's primary mission phase ended on 18 March 2012 and the first extended mission (XM1) began. Less than five weeks later, two orbit-correction maneuvers (OCMs) were used to decrease MESSENGER's orbital period to 8 hours. Figure 2.6 shows the transition from the primary mission orbit to the XM1 8-hour orbit that was made possible by OCM-7 and OCM-8, which slowed the spacecraft's velocity relative to Mercury. Once the maneuvers were complete, the orbit remained highly eccentric with MESSENGER traveling between a periapsis altitude of 278 km and an apoapsis altitude of 10,314 km above Mercury's surface.

A second extended mission (XM2) began on 18 March 2013, however, the orbit is planned to remain unchanged until 17 June 2014. At this point MESSENGER will undergo a final series of four periapsis-raising OCMs in order target periapsis altitudes of 25 km (for the first three OCMs) or 15 km (for the last OCM). XM2 is planned to last for two years and will end when MESSENGER impacts Mercury's surface on 28 March 2015. For more information on the primary and extended missions phases, the reader is referred to *McAdams et al.* [2014].

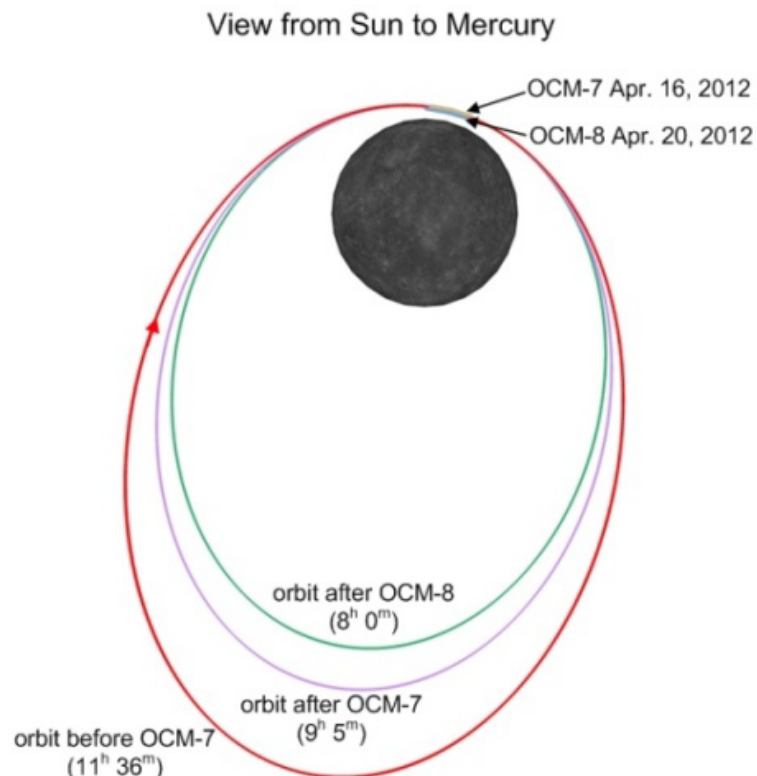


Figure 2.6: Two orbit-correction maneuvers (OCMs) provided the transition to the 8-hour extended mission. Figure from *McAdams et al.* [2012].

2.2 Magnetometer

MESSENGER's Magnetometer fulfills the measurement objectives required to answer the mission's third guiding science question regarding the nature and origin of Mercury's magnetic field [Anderson *et al.*, 2007]. Therefore, the primary science objectives of the MAG investigation are based on the structure of Mercury's magnetic field and its interaction with the solar wind. The instrument specifications were determined by the expected strength of Mercury's intrinsic field (Section 1.3), as well as any contributions due to external currents, while making efficient use of spacecraft resources. The MAG originates from an extensive heritage of magnetic field investigations of many other space missions (See Anderson *et al.* [2007] and references therein) and was assembled through a collaborative effort between NASA Goddard Space Flight Center and The Johns Hopkins Applied Physics Laboratory.

In order to reduce spacecraft field effects on the instrument measurements, the sensor of this low-noise, tri-axial, fluxgate magnetometer is mounted on a 3.6-m-long boom. The boom was deployed on 8 March 2005 and remains extended in the +*Y* direction of the spacecraft such that the MAG is directed anti-sunward during MESSENGER's orbital phase. Because the MAG sensor is extended away from the spacecraft, a conical sunshade made of a non-conducting ceramic fabric is integrated to shield the sensor from solar inputs. The Figure 2.7 illustrates the location and orientation of the Magnetometer with respect to the spacecraft. The individual components of the MAG, (i.e., sensor, electronics, and sunshade) are shown in Figure 2.8.

The instrument provides a "high" or coarse range covering $\pm 51,300$ nT with a resolution of 1.6 nT and a "low" or fine range of $\pm 1,530$ nT with a resolution of 0.047 nT. Instrument output rates range from 0.01 vectors s^{-1} to the full resolution of 20 vectors s^{-1} . In addition to playing a necessary role in the characterization of Mercury's intrinsic planetary field and its magnetosphere, this high sampling rate is particularly useful for the interpretation of plasma data provided by EPPS. The reader is referred to Anderson *et al.* [2007] for additional information on MESSENGER's Magnetometer.

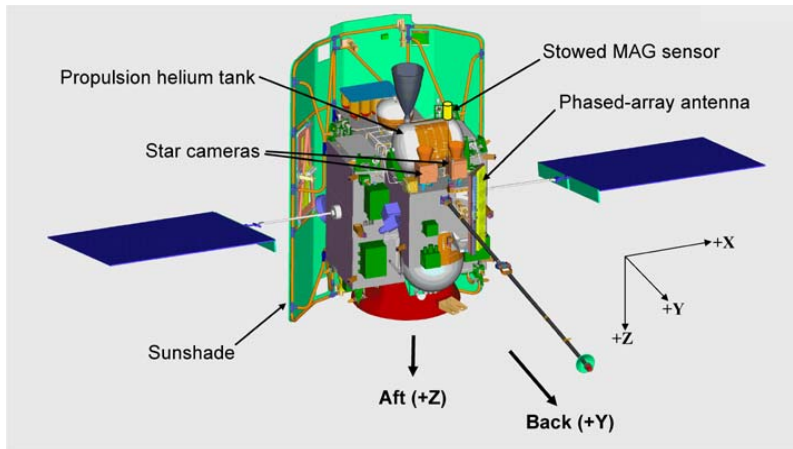


Figure 2.7: View of the MESSENGER spacecraft showing the instrument coordinates and the Magnetometer boom deployed in the $+Y$ direction, which is the anti-sunward direction during orbital operations. The MAG sensor stowed location is indicated (yellow cylinder) as are the propulsion system helium tank, the star cameras, and the phased-array antenna nearest the stowed Magnetometer sensor. The spacecraft sunshade is on the $-Y$ side of the vehicle as shown in light green. Schematic from *Anderson et al.* [2007].

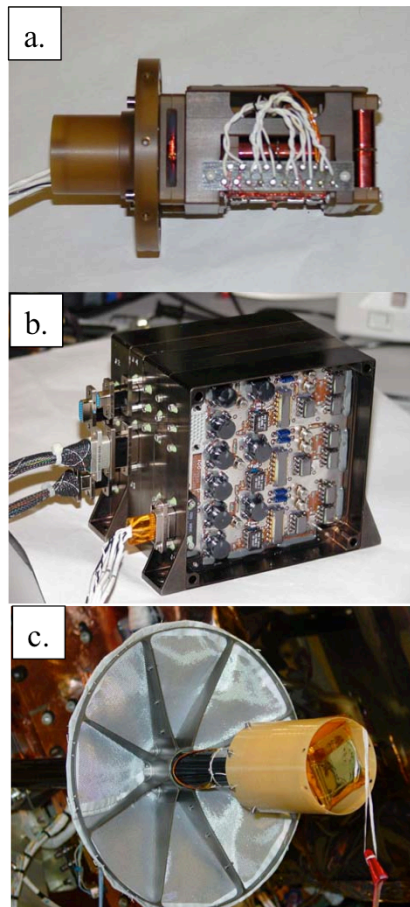


Figure 2.8: Flight MESSENGER MAG sensor (a) and electronics (b) with view of analog slice. The sensor is shown mounted to a test boom adapter flange. Sensor dimensions not including the flange are $8.1 \text{ cm} \times 4.8 \text{ cm} \times 4.6 \text{ cm}$. The electronics dimensions are 10.4 cm and 8.6 cm in cross section as shown and 13.0 cm deep. (c) Flight MESSENGER MAG sensor and sensor sunshade integrated to the boom and spacecraft prior to final thermal blanketing during deployment testing prior to installation of thermal blankets. Images from *Anderson et al.*, [2007].

2.3 Fast Imaging Plasma Spectrometer

The Fast Imaging Plasma Spectrometer (FIPS), developed at the University of Michigan, is one of two sensors that make up the Energetic Particle and Plasma Spectrometer (EPPS) package on MESSENGER [Andrews *et al.*, 2007]. Measurements provided by FIPS (Figure 2.9) are used to address both planetary and space science-based mission objectives including questions regarding the nature and origin of Mercury's magnetic field, radar-reflective materials at Mercury's poles, and sources and sinks of important volatile species on and near Mercury (See Section 2.1). In order to successfully answer the guiding science questions, FIPS surveys positively charged ions with measurements of their composition and three-dimensional distributions.

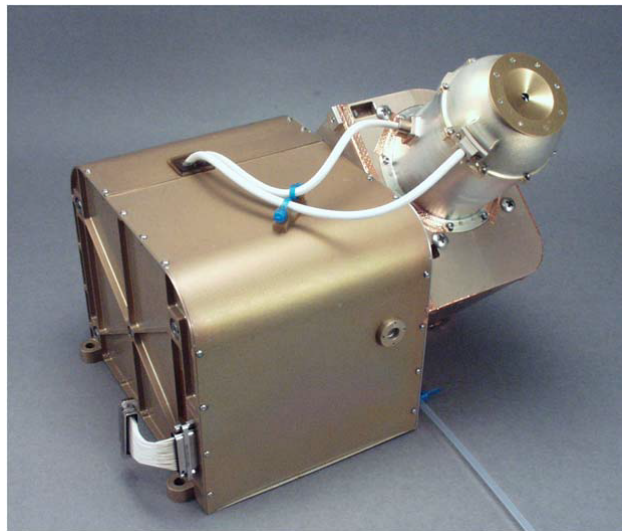


Figure 2.9: The FIPS sensor. Image from Andrews *et al.* [2007].

A cross-section diagram of the FIPS sensor is illustrated in Figure 2.10. FIPS was designed specifically for MESSENGER in order to characterize the ionized species in Mercury's environment within an energy-per-charge (E/q) range of ~ 0.05 to 13 keV/e [Zurbuchen *et al.*, 2008]. Charged particles filtered by a particular E/q based on the applied deflection voltage, ranging from $+35$ V to $+15$ kV, will enter the sensor's aperture and pass through the electrostatic analyzer (ESA). The FIPS electrostatic deflection system is an innovative design unique to FIPS that enables an instantaneous $\sim 1.4\pi$ sr field of view [Zurbuchen *et al.*, 1998]. The particles will then experience a fixed voltage post-acceleration so as to gain sufficient energy to pass through a thin carbon foil.

Secondary electrons will be ejected from the carbon foil and guided through a mirror-harp assembly in the time-of-flight (TOF) chamber onto a start micro-channel plate (MCP) detector. The ion optics of the ESA and TOF mirror-harp assembly result in a direct mapping of incident particle direction onto the start MCP with an angular resolution of $\sim 15^\circ$. The incident ion, nominally neutralized by the carbon foil, travels through the TOF chamber and hits a stop MCP. The distance traveled by the ion inside FIPS' time of flight chamber is known, as well as the TOF detected by the start and stop MCPs. This information, along with the known E/q of the particles entering the sensor is used to determine the mass-per-charge (M/q) of a given ion such as to reconstruct the distribution function for each detected species.

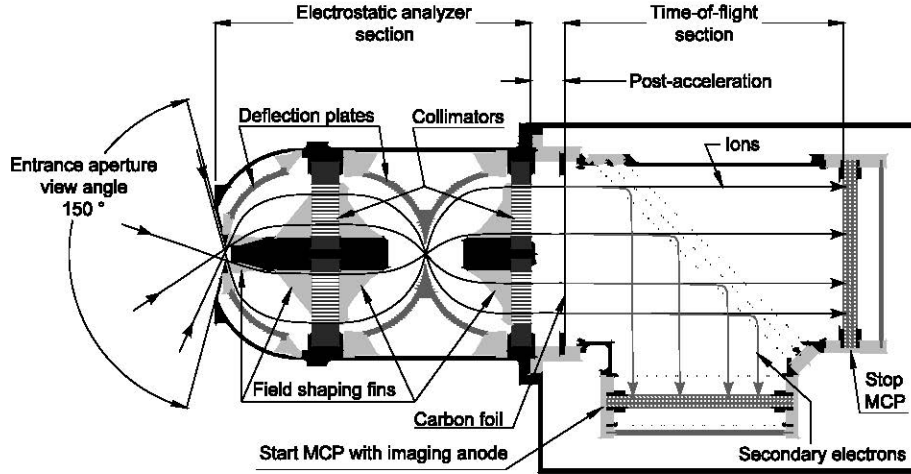


Figure 2.10: Cross-section of the FIPS sensor showing major functional components. Ions are analyzed by their energy per charge (E/q), two-dimensional position, and total time of flight. Figure from *Andrews et al.* [2007].

To determine the ionic species, the TOF forward model [*Raines et al.*, 2013] is implemented to produce tracks in E/q -TOF space for each ion analyzed by FIPS:

$$E_{tot} = q \left[\left(\frac{E}{q} \right)_{ESA} - V_{PAV} \right] - E_{loss} \quad (2.1)$$

$$v = 439 \sqrt{\left(\frac{E_{tot}}{m} \right)} \quad (2.2)$$

$$TOF = 10^4 \frac{d}{v} - \tau_e - \tau_{MCP} \quad (2.3)$$

Equation 2.1 expresses the relation between the E/q (in keV/e) value measured by the ESA, along with the additional post-acceleration energy (V_{PAV} , a negative voltage in kV) and the energy lost as the ion passes through the carbon foil (E_{loss} , in keV), to the total energy (E_{tot} , in keV). From there, equation 2.2 uses E_{tot} to calculate the velocity, v (in km s⁻¹), of an ion in the TOF chamber. Next, using this velocity and the flight distance (d in cm), the TOF (in ns) can be determined by making corrections, based on the electron's flight time (τ_e , in ns) and MCP detection times (τ_{MCP} , in ns), in equation 2.3. The forward model was used to determine tracks in E/q -TOF space for each ion analyzed by FIPS. The measured ion species can be determined using these results. Figure 2.11 shows the accumulation of orbital data with the calculated tracks overlaid in order to show the clear ion tracks in FIPS measurements.

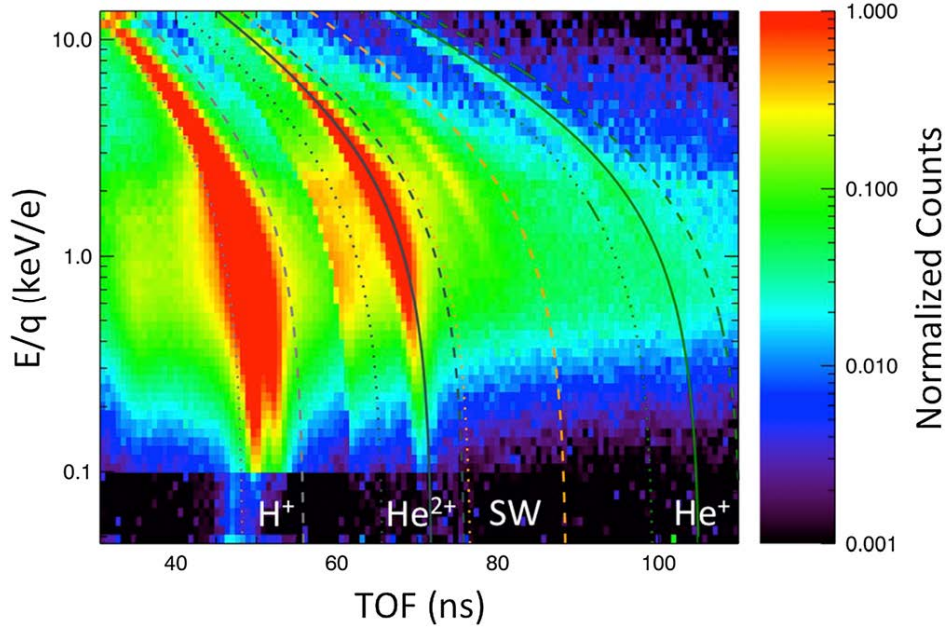


Figure 2.11: Accumulated raw FIPS event data from 25 March 2011 through 22 November 2011 together with lines showing the lower (dotted) and upper (dashed) bounds on modeled TOF as a function of E/q for each species. The modeled TOF center as a function of E/q (solid) is also shown in green for He^{2+} and He^+ . Counts are normalized to the maximum value. Background removal has not yet been completed for the data shown in this figure. The darker region below 0.1 keV/e is due to less time spent observing in this energy range. Figure from *Raines et al.* [2013].

The geometry of the ESA system enables a $\sim 1.4\pi$ sr, instantaneous field of view, though $\sim 0.25\pi$ sr is blocked due to FIPS accommodation on the spacecraft. In its survey

scan mode, the ESA provides coverage of the entire E/q range every ~ 60 s via 60 logarithmically spaced steps [Andrews *et al.*, 2007]. In its Burst mode, FIPS is able to step through the entire E/q range in ~ 10 s. The reader is referred to Andrews *et al.* [2007] and references therein for further information regarding the FIPS sensor onboard MESSENGER.

CHAPTER III

MESSENGER OBSERVATIONS OF MAGNETOPAUSE STRUCTURE AND DYNAMICS AT MERCURY

This chapter is taken from Gina A. DiBraccio, James A. Slavin, Scott A. Boardsen, Brian J. Anderson, Haje Korth, Thomas H. Zurbuchen, Jim M. Raines, Daniel N. Baker, Ralph L. McNutt Jr., and Sean C. Solomon (2013), MESSENGER observations of magnetopause structure and dynamics at Mercury, *J. Geophys. Res. Space Physics*, 118, doi:10.1002/jgra.50123.

Abstract

On 18 March 2011, MESSENGER became the first spacecraft to orbit Mercury, providing a new opportunity to study the outer boundary of the planet's magnetosphere – the magnetopause. Here we characterize Mercury's magnetopause using measurements collected by MESSENGER's Magnetometer and Fast Imaging Plasma Spectrometer. Analysis of measurements from two of MESSENGER's "hot seasons," when the orbital periapsis is on Mercury's dayside and the magnetopause crossing takes place in the subsolar region, resulted in 43 events with well-determined boundary normals. The typical duration of a magnetopause traversal was ~ 5 s. The average normal magnetic field component was ~ 20 nT, and the dimensionless reconnection rate, i.e., the ratio of the normal magnetic field component to the total field magnitude just inside the magnetopause, was 0.15 ± 0.02 . This rate is a factor of ~ 3 larger than values found during the most extensive surveys at Earth. The ratio of the reconnection rate at Mercury to that of the Earth is comparable to the ratio of the solar wind Alfvén speeds at their respective orbits. We also find that the magnetopause reconnection rate at Mercury is independent of magnetic field shear angle, but it varies inversely with plasma β , the ratio

of total thermal pressure to magnetic pressure, in the magnetosheath. These results suggest that reconnection at Mercury is not only more intense than at Earth, but also that it occurs for nearly all orientations of the interplanetary magnetic field due to the low- β nature of the solar wind in the inner heliosphere.

3.1 Introduction

On 18 March 2011, MESSENGER became the first spacecraft to orbit the planet Mercury, which possesses an intrinsic magnetic field discovered by Mariner 10 [Ness *et al.*, 1974, 1975]. MESSENGER data from three Mercury flybys and the first Mercury year in orbit (one Mercury year equals 88 Earth days) confirmed this discovery and refined the strength and orientation of the magnetic dipole. We now know that Mercury's magnetic moment is 195 ± 10 nT- R_M^3 [Anderson *et al.*, 2008, 2010; Alexeev *et al.*, 2010]. Further, the MESSENGER magnetic field data show a clear northward offset of the dipole moment from the center of the planet by 484 ± 11 km [Anderson *et al.*, 2011a], approximately 20% of the planet's radius. The interaction between the solar wind and the planetary magnetic field creates a highly dynamic magnetosphere exhibiting many of the processes observed at Earth, including magnetopause and magnetotail reconnection [Slavin *et al.*, 2008, 2009], ultra-low-frequency and Kelvin-Helmholtz waves [Boardsen *et al.*, 2009, 2010; Sundberg *et al.*, 2010], and substorm-type magnetotail loading and unloading, near-tail dipolarization, and plasmoid ejection [Slavin *et al.*, 2010, 2012a; Sundberg *et al.*, 2012b], but on much shorter temporal scales than have been observed in previously explored magnetospheric systems.

The magnetopause is arguably the most important boundary in the magnetospheric system for the reason that it controls the flux of solar wind mass, energy, and momentum into the magnetosphere. The magnetopause current sheet forms as a result of the interaction between the incident solar and planetary magnetic fields [Chapman and Ferraro, 1931]. Its location corresponds to the surface across which the pressures of the internal magnetospheric magnetic fields and charged particles are balanced by the external solar wind pressure [Spreiter *et al.*, 1966]. The pressure balance equation for the magnetopause is

$$\frac{B_{MSP}^2}{2\mu_0} + \sum_i^{MSP} n_i k T_i + n_e k T_e = \frac{B_{MSH}^2}{2\mu_0} + \sum_i^{MSH} n_i k T_i + n_e k T_e \quad (3.1)$$

where μ_0 is the magnetic field permeability of free space, $B^2/2\mu_0$ denotes the pressure of the magnetic field B , and the subscripts MSP and MSH designate the magnetosphere and magnetosheath regions, respectively. The number density and temperature of ions and electrons are represented by n_i , T_i , n_e , and T_e , respectively, where k is the Boltzmann constant, and the sums are over all ionic species.

Both Mercury and Earth have southward-directed planetary dipoles, and their average magnetopause standoff distances are $\sim 1.4 R_M$ [Ness *et al.*, 1976; Russell, 1977; Slavin *et al.*, 2010; Moldovan *et al.*, 2011] and $\sim 10 R_E$ [Fairfield, 1971], respectively. Hence, Earth occupies a much smaller volume fraction of its magnetosphere than does Mercury. By comparison, the combination of solar wind dynamic pressure falling off as $1/r^2$ with increasing Heliocentric distance, r , and stronger planetary dipole moments results in average magnetopause standoff distances of $75 R_J$ (where R_J is Jupiter's radius) and $24 R_S$ (where R_S is Saturn's radius) at Jupiter and Saturn, respectively [Joy *et al.*, 2002; Achilleos *et al.*, 2008; Went *et al.*, 2011].

Magnetic reconnection in the magnetopause current layer, between the draped IMF in the magnetosheath and the intrinsic planetary field, occurs at sites called X-lines [Dungey, 1961; Levy *et al.*, 1964]. This merging of magnetic field lines is responsible for the transfer of magnetic flux from the dayside magnetosphere into the magnetotail. Locally, such reconnection also heats the charged particles, converts magnetic energy into kinetic energy, and produces Alfvénic jets of plasma directed away from the X-line along the magnetopause [Fuselier and Lewis, 2011]. When reconnection takes place at the magnetopause, a component of the magnetic field \mathbf{B} normal to the boundary (B_N) is generated, creating a rotational discontinuity and changing the configuration into a newly opened magnetosphere. A finite B_N also enables some of the solar wind plasma to cross the magnetopause and enter the magnetospheric system [Sonnerup and Cahill, 1967; Sonnerup and Ledley, 1979; Fuselier *et al.*, 2005].

The large-scale circulation of the terrestrial magnetosphere driven by solar wind interaction with the planetary magnetic field is described as the Dungey cycle [Dungey, 1961]. This cycle, which is expected to be especially vigorous at Mercury because of the strong solar wind close to the Sun [Siscoe *et al.*, 1975], begins with the process of magnetic reconnection at the dayside magnetopause, as described above. The new field lines, with one end attached to the planet and the other in the solar wind, are pulled into the magnetotail, where they reconnect once again before convecting back to the dayside as a closed field, completing the sequence. Typical Dungey cycle times are ~ 1 h at Earth but are much shorter at Mercury, with convection times of only ~ 2 min [Siscoe *et al.*, 1975; Slavin *et al.*, 2009, 2010].

The rate of reconnection is often defined as the ratio of the reconnection inflow velocity to the speed of the Alfvénic outflow (V_{in}/V_A) [Petschek, 1964; Sonnerup, 1974]. MESSENGER is not ideally instrumented to measure these flows. However, the reconnection rate can also be expressed as the ratio of the normal magnetic field component to the total field just inside the magnetopause (B_N/B_{MP}) [Sonnerup *et al.*, 1981a] or, using measurements of the tangential electric field E_t and plasma density ρ , ($E_t \rho^{1/2}/B_{\text{MP}}^2$) [Mozer and Retinò, 2007]. At Earth, most reported values have been from case studies and do not represent a statistical survey. The results range from values on the order of 0.01 [Sonnerup and Ledley, 1979; Mozer *et al.*, 2002; Fuselier *et al.*, 2005; Fuselier *et al.*, 2010] to a maximum of ~ 0.1 [Sonnerup *et al.*, 1981a; Phan *et al.*, 2001; Vaivads *et al.*, 2004]. Further, due to the relative weakness of the normal field component compared with the background fluctuations and uncertainties in the derivation of boundary-normal coordinates, the reported B_N/B_{MP} values at Earth may be biased toward events for which B_N is large. For example, using assumptions to derive E_t , Lindqvist and Mozer [1990] reported an average reconnection rate of 0.15, but there was substantial scatter in the data. In contrast, Phan *et al.* [1996] reported a survey in which the mean V_{in}/V_A value was < 0.01 . In the most extensive statistical study at Earth to date, Mozer and Retinò [2007] calculated an average reconnection rate of 0.046 for 22 events.

Slavin and Holzer [1979] predicted high reconnection rates at Mercury's magnetopause on the basis of the low Alfvén Mach number and decreased plasma β , the ratio of total thermal pressure to magnetic pressure, in the inner solar system. With

increasing distance from the Sun, the solar wind magnetic pressure decreases more rapidly than thermal pressure [e.g., *Slavin and Holzer, 1981*]. As a result, the solar wind Mach number grows and the plasma β increases between the orbits of Mercury and Earth. These changes result in the magnetosheath at Mercury being strongly affected by magnetic stresses, whereas at Earth and the more distant planets the magnetosheath is primarily influenced by plasma pressures [*Paschman et al., 1986; Huddleston et al., 1997*]. In turn, this behavior is expected to cause the rate of reconnection between the IMF in the magnetosheath and the planetary field to decrease with distance from the Sun [*Slavin and Holzer, 1979; Scurry and Russell, 1991; Scurry et al., 1994; Mozer and Hull, 2010; Masters et al., 2012*]. An initial analysis of observations during a MESSENGER flyby magnetopause crossing with an incident magnetosheath of strong, steady southward IMF, yielded a substantial B_N/B_{MP} ratio of ~ 0.13 at Mercury [*Slavin et al., 2009*] that was larger than all but the most intense events at Earth [e.g., *Sonnerup et al., 1981a*].

In this paper we present an analysis of 43 dayside magnetopause passes, during the first three Mercury years of the MESSENGER mission orbital phase, with well-determined B_N values. MAG [*Anderson et al., 2007*] and FIPS [*Andrews et al., 2007*] measurements taken during this interval yielded a minimum of two dayside magnetopause encounters per day as a result of MESSENGER's 12-h orbit. Because the magnetopause is constantly in motion at velocities greater than the spacecraft, it is not unusual to see multiple crossings for a single encounter. Each individual crossing during this time period was systematically examined with minimum variance analysis (MVA). Our extended analysis confirms the initial MESSENGER results indicating that reconnection is frequent and intense at Mercury. Our results indicate that the low- β magnetosheath at Mercury [*Swisdak et al., 2010; Masters et al., 2012*] enables reconnection the majority of the time. Further, we observe an inverse relationship between magnetosheath plasma β and reconnection rate.

3.2 Methodology

From MESSENGER magnetic field data, with a sampling rate of 20 s^{-1} , we identified magnetopause crossings in Mercury solar magnetospheric (MSM) coordinates

as sharp discontinuities as the boundary moved past the spacecraft. In MSM coordinates, the X_{MSM} -axis is directed from Mercury's offset magnetic dipole toward the center of the Sun, the Z_{MSM} -axis is normal to Mercury's orbital plane toward the north celestial pole, and the Y_{MSM} -axis completes the right-handed system with the positive direction oriented opposite to orbital motion. As at Earth, directional rotations and a change in field magnitude serve as indicators of magnetopause crossings. At low latitudes on the dayside, the predominantly northward ($+B_z$) intrinsic field of the planet has a typical magnitude of ~ 100 nT. The transition from this stable dipole field to the more variable and somewhat weaker field of the magnetosheath IMF usually provides a distinct signature for magnetopause identification. Because of the strong IMF and low plasma β in the inner solar system, the magnetic field magnitude in Mercury's magnetosheath is often only slightly weaker than the field inside the magnetosphere. This fact makes it difficult to detect the magnetopause boundary for strongly northward IMF (i.e., low values of the shear angle θ , defined as the rotation of the magnetic field from the magnetosheath into the magnetosphere). For this reason we used the MESSENGER plasma data to assist in the accurate identification of magnetopause crossings.

FIPS measures time of flight, energy per charge (E/q), and incident angle for ions within the ranges $E/q = 0.05\text{--}13$ keV e^{-1} and $m/q = 1\text{--}60$ amu e^{-1} , where m/q is the mass per charge of detected ions. Near the magnetopause, the instrument completes one scan over the entire range of E/q values every 8 s. FIPS has a conical field of view (FOV) of $\sim 1.4\pi$ sr. The instrument's orientation with respect to the spacecraft sunshade causes $\sim 30\%$ of the FOV to be obstructed and, depending on its attitude, one of the solar panels may cause an additional FOV obstruction. The reader is referred to *Raines et al.* [2011] for further details on the FIPS FOV limitation and data analysis procedures.

The FIPS FOV direction with respect to the planet is described in spherical coordinates whereby the polar angle, θ_{FOV} , is the angle between the Z_{MSM} -axis and the FIPS boresight vector and ranges over $0\text{--}180^\circ$. The azimuthal angle, ϕ_{FOV} , is the angle between the X_{MSM} -axis and the FIPS boresight vector and ranges over $\pm 180^\circ$; the sign of ϕ_{FOV} follows the sign of Y_{MSM} . There is considerable variation in the orientation of FIPS for the magnetopause crossings in this study (Figure 3.1). These changes in spacecraft pointing are part of normal observations for other MESSENGER instruments. FIPS

orientations naturally fall into two groups, on the basis of the sign of the Y_{MSM} coordinate of the spacecraft at the time of the crossing; those groups are indicated on Figure 3.1.

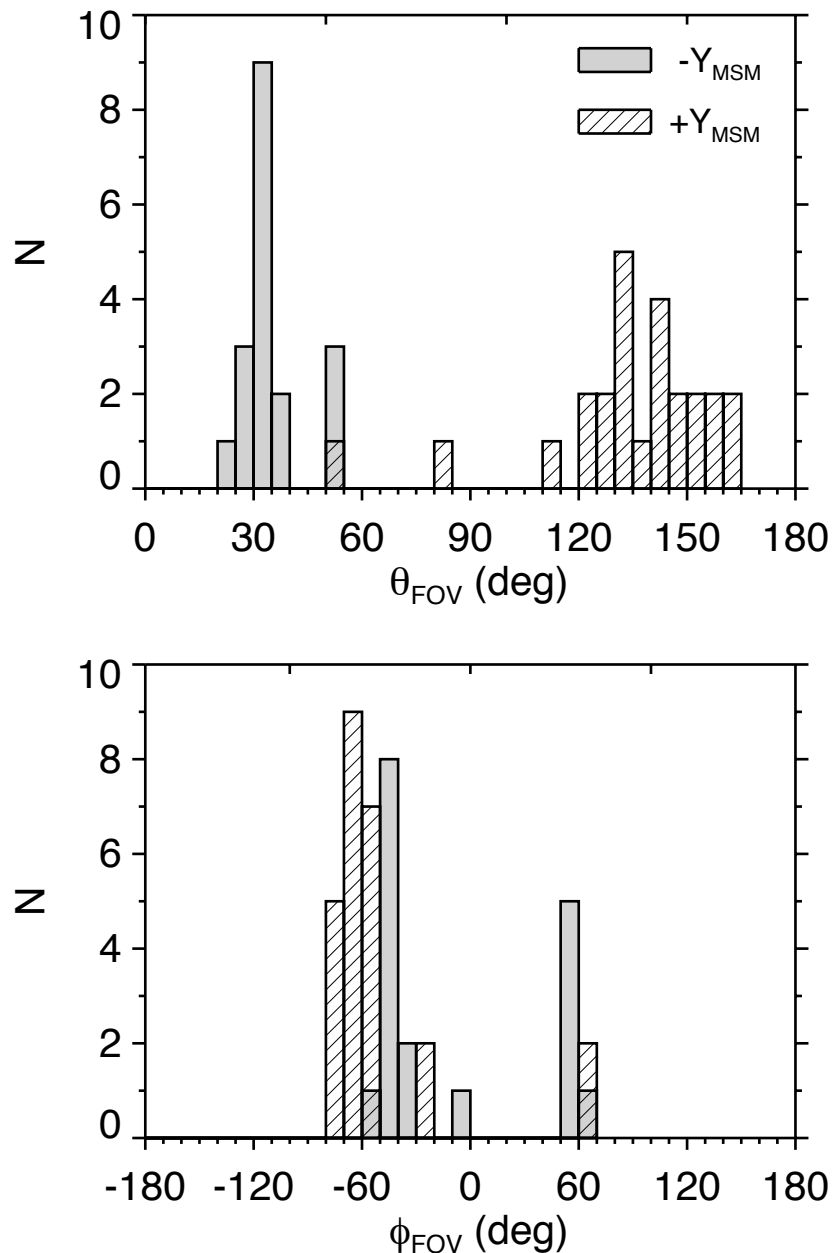


Figure 3.1: Direction of the FIPS FOV in spherical MSM coordinates for the magnetopause crossings in this study. The polar angle (θ_{FOV}) is the angle between the Z_{MSM} -axis and the FIPS boresight vector. The azimuthal angle (ϕ_{FOV}) ranges from -180 to 180° , where 0° is directed sunward along the X_{MSM} -axis and the sign of ϕ_{FOV} follows the sign of Y_{MSM} . Changes in FIPS orientation result from spacecraft maneuvers made to acquire observations with other MESSENGER instruments.

Strong decreases in the proton flux are typically observed as MESSENGER crosses the magnetopause and enters the magnetosphere. In this study, the change in flux serves as an indicator of a magnetopause crossing. Conversely, when MESSENGER exits the magnetosphere, increases in proton counts and differential energy flux signal the spacecraft's entry into the dense, hot magnetosheath. The effects of the FIPS orientation changes on the magnetopause plasma signatures are expected to be minimal because of the high contrast between the stagnant, hot plasma in the magnetosheath and the tenuous plasma inside the magnetosphere.

In order to determine the structure of Mercury's magnetopause, MVA [Sonnerup and Cahill, 1967] was used to transform the MAG measurements from MSM coordinates into boundary-normal coordinates. The MVA technique calculates the eigenvalues and associated eigenvectors of a magnetic field covariance matrix ($M_{i,j}^B$) defined by

$$M_{i,j}^B \equiv \langle B_i B_j \rangle - \langle B_i \rangle \langle B_j \rangle \quad (3.2)$$

where $i, j = 1, 2, 3$ correspond to the $B_x, B_y,$ and B_z components of \mathbf{B} in MSM coordinates and the brackets denote a temporal average. The resulting eigenvectors are orthogonal and represent the directions of minimum, intermediate, and maximum variance in the magnetic field. In the new coordinate system, the minimum variance component (B_1 , which is equivalent to B_N) is directed outward and normal to the local magnetopause surface. The directions of intermediate (B_2) and maximum (B_3) magnetic field variance lie within the plane of the magnetopause and are free to rotate in response to magnetic field variation to complete an orthogonal Cartesian system.

We utilize a discontinuity jump condition, according to which the magnetic field magnitude is discontinuous but the normal field component is continuous across the boundary, whether that component is zero in the case of a tangential discontinuity or a constant, non-zero value for the case of a rotational discontinuity [Sonnerup and Cahill, 1967; Sonnerup and Scheible, 1998]. Numerous studies have relied on the magnitude of the normal component [e.g., Sonnerup et al., 1981a] to investigate the boundary configuration, whereas others have differentiated between rotational and tangential

discontinuities on the basis of B_N/B_{tot} and $\Delta B_{\text{tot}}/B_{\text{tot}}$, where B_{tot} is the total field magnitude and ΔB_{tot} is the change in magnitude across the boundary [Lepping and Behannon, 1980; Knetter et al., 2004]. The latter method is designed to separate rotational discontinuities with a modest B_N from tangential discontinuities, but classification becomes difficult when both of these ratios are small. For this study, our interest in determining the intensity of magnetic reconnection has led us to direct our attention to the substantial B_N component prevalent at Mercury.

The accuracy of the MVA transformation is inferred from the number of vector measurements and the ratios of the eigenvalues corresponding to the directions of minimum, intermediate, and maximum variance: λ_1 , λ_2 , and λ_3 . A high ratio of intermediate to minimum eigenvalue (λ_2/λ_1) indicates a well-determined normal vector (and associated eigenvector) acquired for a particular data set. There are many approaches to determining the error associated with the MVA principal axis directions [Sonnerup, 1971; Lepping and Behannon, 1980; Hoppe et al., 1981; Kawano and Higuchi, 1995; Khrabrov and Sonnerup, 1998]. Whereas the bootstrap method performed by Kawano and Higuchi [1995] proved to quantify the amount of error more accurately than the method of Sonnerup [1971], the former technique requires considerable computational power. Khrabrov and Sonnerup [1998] developed an error estimation procedure that produces results equivalent to the bootstrap method without the associated computational requirements. Their method was further developed by Sonnerup and Scheible [1998].

We used the Sonnerup and Scheible [1998] method of error estimation here to establish a criterion for acceptable magnetopause crossings. In following this approach we required $\lambda_2/\lambda_1 \geq 5$ for crossings included in this study. Earlier MVA studies required minimum eigenvalue ratios of 1.5–3 [Sonnerup and Cahill, 1967; Collier and Lepping, 1996]. To further refine the selection we retained only those crossings with a normal field component greater than or equal twice the uncertainty in B_N , indicating a rotational discontinuity. Knetter et al. [2004] implemented a selection criterion for solar wind discontinuities using a magnetic shear angle threshold, $\theta > 60^\circ$, in order to increase the validity of the MVA results. However, reconnection rates are hypothesized to be strongly dependent on shear angle, and low-shear reconnection events are not uncommon

for interplanetary discontinuities [Gosling *et al.*, 2007], as well as for some solar wind-magnetosphere interactions [e.g., Paschmann *et al.*, 1993]. Therefore, we required a large λ_2/λ_1 , but we did not set a minimum shear angle. Additional error estimation results are discussed below, following two examples of magnetopause crossings that serve to illustrate high-shear and low-shear open magnetosphere configurations.

For this study, a magnetopause crossing interval was defined by first identifying the magnitude of the magnetic field inside both the magnetosphere (B_{MSP}) and the magnetosheath (B_{MSH}). These values served as guides to determine the initial and final points of the interval. That is, as the spacecraft exited the magnetosphere, the last measurement to equal B_{MSP} before the field rotation began was designated as the “start” and the first measurement to equal B_{MSH} was the “stop.” This designation ensured that we chose a full magnetopause crossing and avoided any partial crossings that resulted from boundary dynamics. If the magnetopause was being compressed toward the planet, causing the spacecraft to re-enter the magnetosphere as indicated by multiple crossings for a single encounter, B_{MSH} and B_{MSP} signal the beginning and end of the interval, respectively. The duration of a magnetopause crossing was calculated from the time span of the MVA intervals. The method of defining the MVA intervals ensured that the duration captured the entirety of the current sheet with a full rotation of the field.

3.3 MESSENGER Observations

3.3.1. High- and Low-Shear Magnetopause Reconnection

Trajectories of the orbits from 21 and 24 November 2011 are displayed in Figure 3.2. The outbound crossings at the dayside magnetopause occurred slightly after MESSENGER reached periapsis and were chosen as a result of their close proximity to the subsolar point. The magnetopause model [Moldovan *et al.*, 2011] was corrected for solar wind aberration due to Mercury's orbital velocity around the Sun, which varies over the planet's highly eccentric orbit.

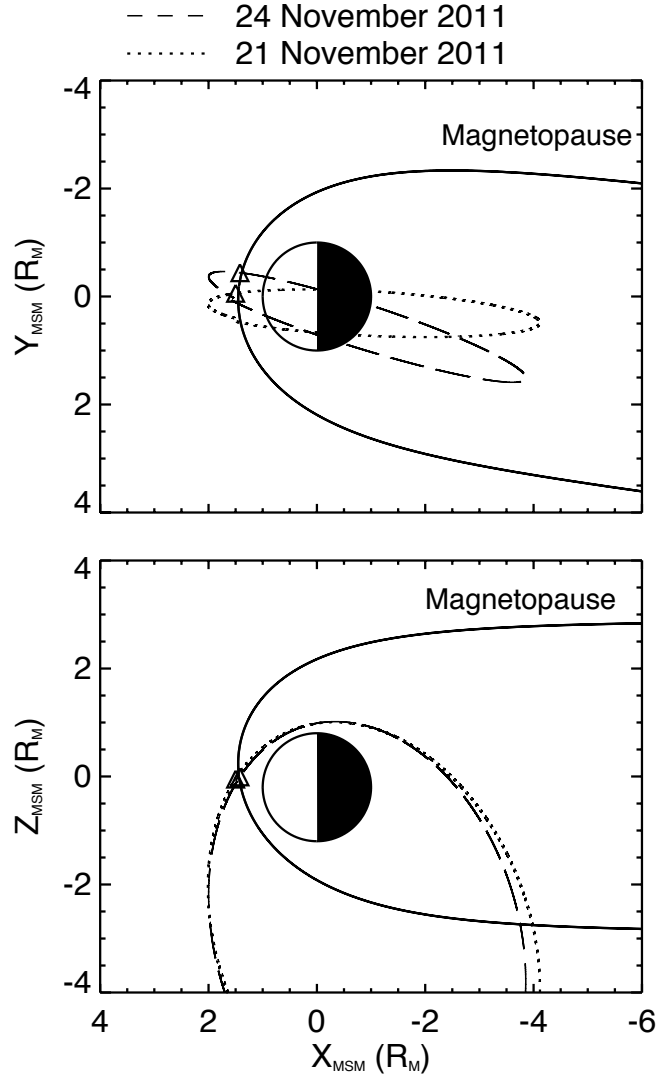


Figure 3.2: MESSENGER orbital trajectories on 21 and 24 November 2011; the magnetopause model of *Moldovan et al.* [2011] is shown in MSM coordinates. The magnetopause has been corrected for solar wind aberration for an average solar wind velocity of 400 km s^{-1} and an average orbital velocity for Mercury of 50 km s^{-1} . Observed outbound magnetopause crossings are indicated by triangles.

For the 24 November 2011 dayside pass, the magnetopause crossing was marked by a distinct shift in magnetic field data at 10:29:04.49 UTC. After applying MVA to a 2.2 s interval spanning the magnetopause crossing, the normal component of the magnetic field has a magnitude of 9.1 nT. The eigenvalue ratio indicated by the analysis, $\lambda_2/\lambda_1 = 64.24$, is well above the threshold value of 5 mentioned above, indicating that the normal direction is well determined. The error analysis reveals an uncertainty of $\pm 1 \text{ nT}$ in the magnitude of B_N , calculated from the following [Sonnerup and Scheible, 1998]:

$$|\Delta\varphi_{1j}| = \sqrt{\frac{\lambda_1}{N-1} \frac{(\lambda_1 + \lambda_j - \lambda_1)}{(\lambda_1 - \lambda_j)^2}}, j = 2, 3 \quad (3.3)$$

$$|\Delta B_N| = \sqrt{\frac{\lambda_1}{N-1} + (\Delta\varphi_{12}B_2)^2 + (\Delta\varphi_{13}B_3)^2} \quad (3.4)$$

where N is the number of measured vectors and $\Delta\varphi_{1j}$ is the expected angular uncertainty in the given normal direction, indexed by intermediate and maximum directions j . Since the non-zero magnitude of B_N is greater than twice the calculated error, this crossing was classified as a rotational discontinuity and met the criteria for this study.

The plasma and magnetic field data transformed into boundary-normal coordinates are plotted for this crossing in Figure 3.3. The minimum variance component, B_1 , is the flattest and smoothest curve, whereas the direction of maximum variance, B_3 , shows a full rotation of the field through the magnetopause. This rotation is indicated by a change from positive to negative orientation with a large shift in amplitude from $\sim +120$ nT in the magnetosphere to ~ -90 nT in the magnetosheath. The change in polarity evident in B_3 signifies a northward planetary field interacting with a southward IMF – a configuration highly conducive to dayside reconnection. The magnetopause shear angle was calculated to be 148.9° . As the spacecraft entered the magnetosheath, the plasma data showed an increase in the number of proton counts. Furthermore, high values for differential energy flux (red in Figure 3.3) spread across more of the E/q range, indicating that the plasma was hotter in the magnetosheath than inside the magnetosphere. Although this example focuses on a single magnetopause crossing, multiple crossings actually took place because of the dynamic evolution of the boundary, as identified in the figure.

In contrast, the magnetopause crossing on 21 November 2011 (Figure 3.4) is an example of a low-shear magnetopause reconnection event. A dominant northward B_Z of ~ 145 nT just inside the magnetopause is indicative of a compressed dayside magnetosphere and higher than usual solar wind pressure. The draped IMF in the magnetosheath exhibited a northward orientation for the duration of the crossing. A magnetopause crossing at 10:29:22.39 UTC was identified by a strong increase in proton count-rate over a wide range of energies accompanied by a decrease in B_3 and $|B|$.

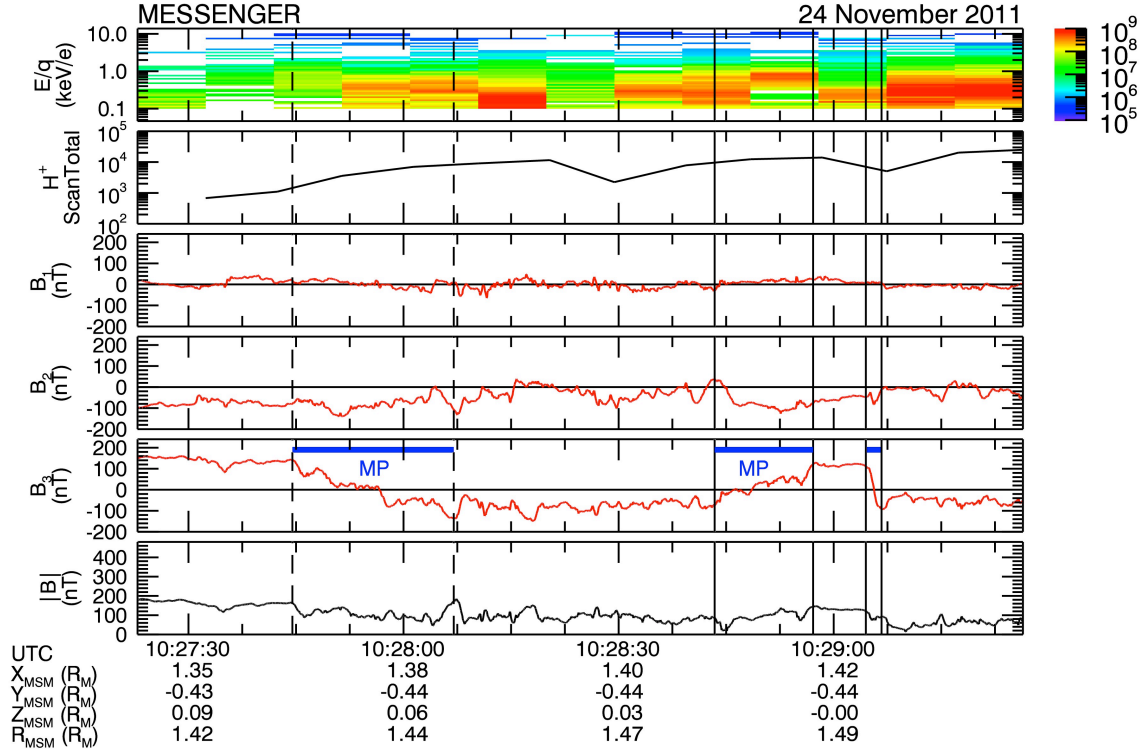


Figure 3.3: Plasma and magnetic field data in MVA coordinates transformed from the magnetopause crossing beginning at 10:29:04.49 UTC on 24 November 2011. Vertical black lines mark the accepted (solid) and rejected (dashed) magnetopause crossings (MP). The top two panels include a proton energy spectrogram with differential energy flux (color scale, in $\text{cm}^{-2} \text{s}^{-1} \text{kV}^{-1}$) and total proton counts, respectively. The next four panels are the minimum, intermediate, and maximum variance components of the magnetic field and the field magnitude, respectively. R_{MSM} is distance from the center of the planet. The minimum, intermediate, and maximum eigenvectors are $B_1 = B_N = (0.91, -0.39, 0.11)$, $B_2 = (0.40, 0.76, -0.52)$, and $B_3 = (0.12, 0.51, 0.85)$. The MVA utilized 44 magnetic field vector measurements, and the ratios of maximum to intermediate and intermediate to minimum eigenvalues are 16.51 and 64.24, respectively.

The magnetic field data transformed by the MVA results (Figure 3.4) of this 5.6 s interval show the rotation of the field as the spacecraft traversed from the magnetosphere into the magnetosheath region. The magnetopause current sheet is defined by the abrupt change of ~ 10 nT in the B_3 component, and the boundary-normal direction is well determined as indicated by a ratio of intermediate to minimum eigenvalue of 5.55. The analysis results in a normal component with a magnitude of $B_N = 6.7$ nT. The error analysis produces an uncertainty of ± 3.2 nT in the calculated magnitude of B_N , which meets our definition of a rotational discontinuity. Computing the shear between the fields of solar and planetary origin indicates an extremely low shear angle of $\theta = 1.2^\circ$ for this open magnetosphere configuration. The plasma data reinforce the crossing identification and show a sharp increase of nearly 10-fold in count rate across the interval. For low-

shear cases such as this, component reconnection results in a highly inclined, north–south X-line between the planetary and IMF fields [Sonnerup, 1974; Fuselier et al., 2011].

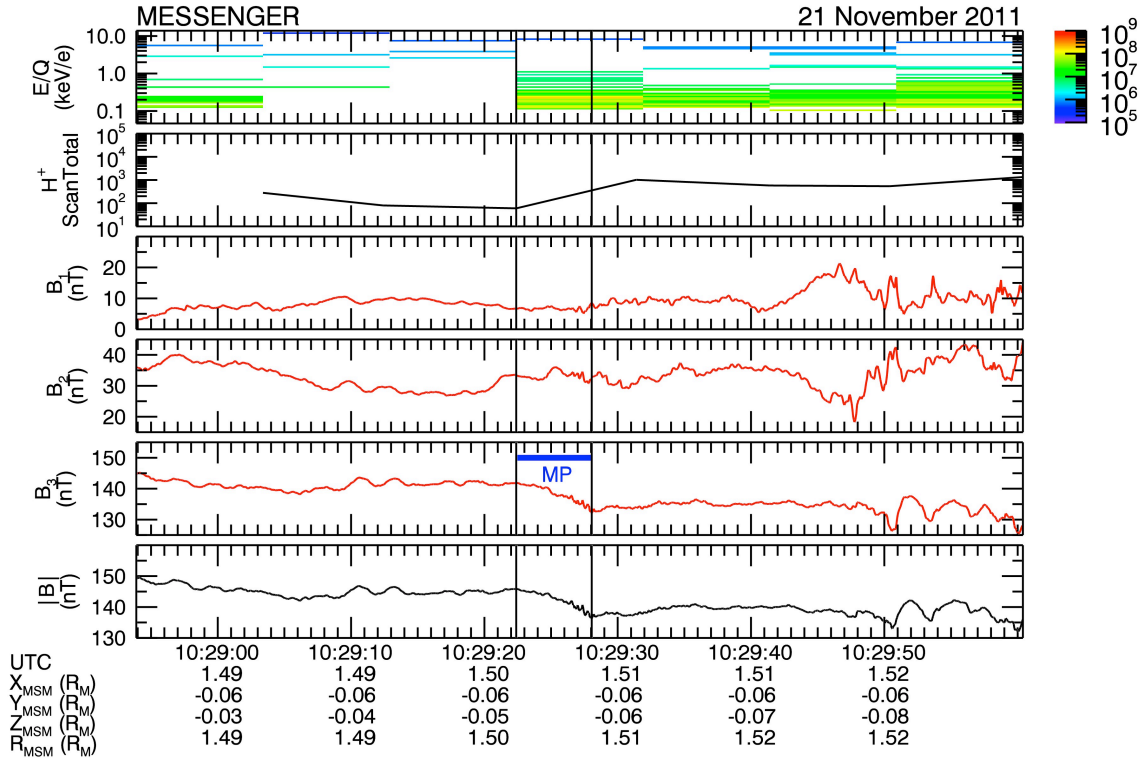


Figure 3.4: Plasma and magnetic field data in MVA coordinates transformed from the magnetopause crossing beginning at 10:29:22.39 UTC on 21 November 2011. Solid vertical lines mark the magnetopause crossing. The top two panels include a proton energy spectrogram with differential energy flux (color scale, in $\text{cm}^{-2} \text{s}^{-1} \text{keV}^{-1}$) and total proton counts. The minimum, intermediate, and maximum eigenvectors are $B_1 = (0.89, -0.46, 0.00)$, $B_2 = (0.45, 0.87, 0.22)$, and $B_3 = (-0.10, -0.20, 0.98)$. The MVA utilized 114 magnetic field vector measurements, and the ratios of maximum to intermediate and intermediate to minimum eigenvalues are 4.33 and 5.55, respectively.

3.3.2. Statistical Analysis

The MVA-based analysis procedures described above were applied to MAG and FIPS data from orbits during two of MESSENGER’s “hot seasons,” when the periapsis of the orbit was over Mercury’s subsolar region. We analyzed 15 days of magnetopause crossings during the first hot season, spanning the period 15 May – 7 June 2011, and 21 days during the third hot season, from 8 to 28 November 2011. During 10 days of the first hot season, both instruments were inoperative for the fraction of the orbit when MESSENGER passed directly in front of the planet as a precaution against excessive thermal inputs to the spacecraft. The first continuous, simultaneous measurements by

MAG and FIPS were taken during the third hot season.

For the intervals noted above, MVA was performed on every distinct dayside magnetopause crossing exhibiting a clear rotation as the field transitioned from a B_Z magnitude representative of the magnetosphere to that of the magnetosheath. Magnetopause identification was confirmed by identifying transitions in the plasma data that coincided with the field rotation, from the tenuous magnetosphere into the hot, dense plasma of the magnetosheath. A total of 89 magnetopause crossings were identified. Of these, 65 met the eigenvalue ratio criterion ($\lambda_2/\lambda_1 \geq 5$). However, nine of these crossings were eliminated because the field magnitude in the magnetosheath exceeded that of the magnetosphere. The unusual situations when $B_{MSH}/B_{MSP} > 1$ are likely the result of large, rapid changes in solar wind pressure that are incompatible with the assumptions made for our single-satellite analysis techniques. From the remaining 56 crossings, three were excluded because the error in B_N was larger than 8 nT. Finally, 10 more crossings were removed for having a normal field component that was less than twice the uncertainty in B_N . We determined that 48% of the crossings in our initial set were rotational discontinuities on the basis of these stringent requirements to account for single-spacecraft limitations. This procedure admits the possibility that some of the 49 eliminated cases were also rotational discontinuities, but their inability to meet the criteria listed above caused them to be rejected. Therefore, we cannot say how often the magnetopause is a rotational discontinuity, but our survey indicates that this configuration is not uncommon.

The locations of the 43 selected crossings fall within the confines of the subsolar region between 0800 and 1600 local time and $\pm 20^\circ$ latitude. These magnetopause crossings are compared with the boundary model of *Moldovan et al.* [2011] in Figure 3.5. The magnetopause model is projected onto the terminator plane ($X_{MSM} = 0 R_M$) in Figure 3.5b to illustrate boundary location from the perspective of the Sun. Close agreement between the location of the crossings considered here and those predicted by the model of *Moldovan et al.* [2011] is evident.

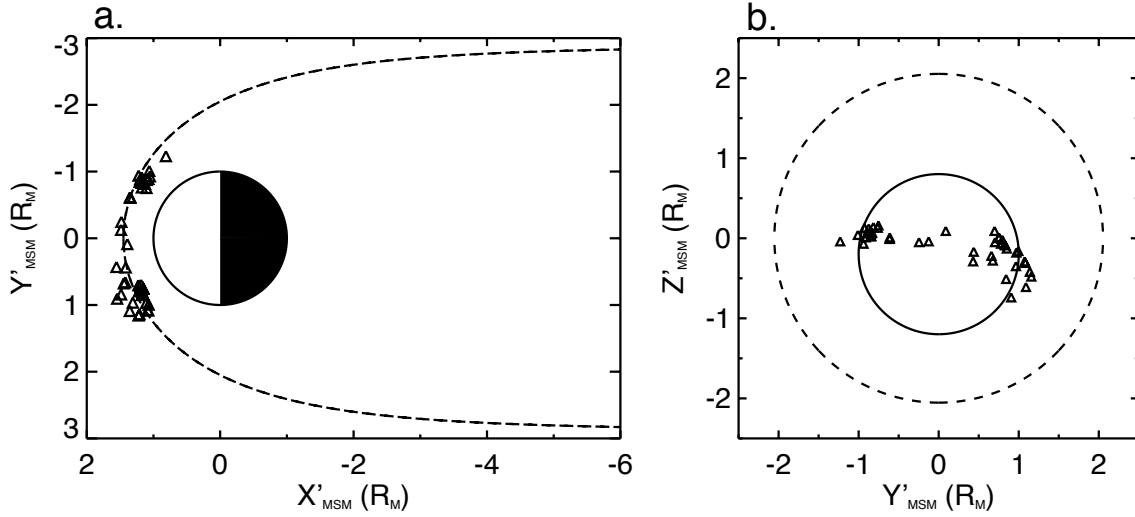


Figure 3.5: Survey of observed magnetopause crossings and the model magnetopause surface of *Moldovan et al.* [2011] in solar-wind-aberrated MSM coordinates. Triangles represent dayside magnetopause crossings. (a) Equatorial view of the crossings between local times of 0800 and 1600. (b) View from the Sun to Mercury illustrating that all crossings occur within $\pm 20^\circ$ latitude. The model magnetopause location is shown at the terminator plane.

In order to characterize the magnetopause, a statistical analysis was applied to the 43 crossings with well-determined boundary normals. Figure 3.6a displays a histogram of the ratios of intermediate to minimum eigenvalue from the surveyed dayside crossings, indicating an average value of 14 and a lower limit of 5, as predetermined by the selection criteria. This distribution strongly supports the validity of the normal directions derived from MVA. The corresponding results from the error analysis, illustrated in Figure 3.6b with an average error of 2.21 ± 0.20 nT, validate the confidence in the selected events. The standard error, in this case ± 0.20 nT, is calculated from the ratio of the standard deviation to the square root of the number of events (σ/\sqrt{N}) and is implemented for all succeeding calculations.

The distribution of the normal magnetic field component for rotational discontinuity magnetopause crossings is illustrated in Figure 3.7. The magnitude of B_N ranges from 1.31 to 91.41 nT, but most of the normal field components were smaller, with a mean of 20.1 nT.

The average duration of the magnetopause crossings was calculated from the time span of the MVA intervals, as discussed in Section 2. The mean, 5 s, is comparable to the standard deviation, 4 s, and most likely indicative of the natural variability in the

normal magnetopause velocity (V_N), which we cannot measure directly. During several longer encounters the magnetopause and the spacecraft were likely to have been moving simultaneously, causing an extended rendezvous. Figure 3.8 displays a histogram of magnetopause crossing durations.

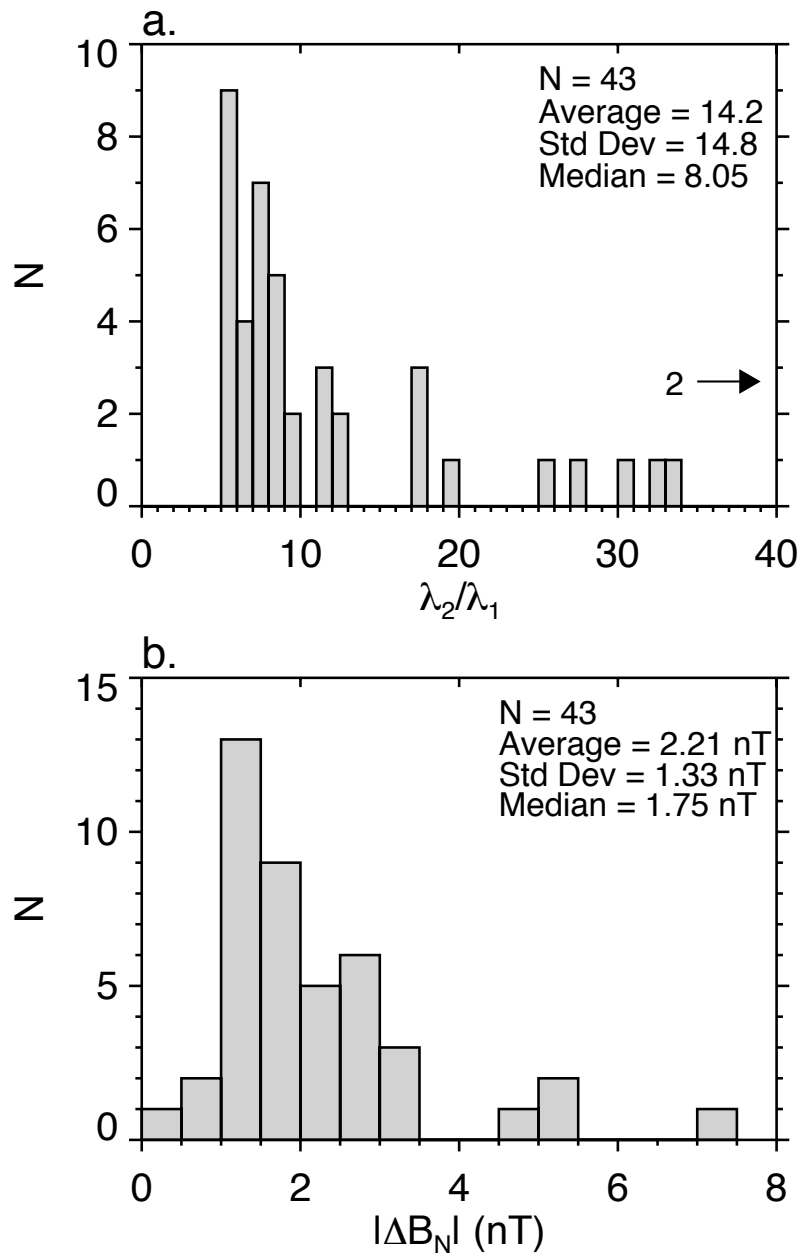


Figure 3.6: (a) Histogram of the ratios of intermediate to minimum eigenvalue for the observed dayside magnetopause crossings. Two ratios have values greater than 40 and are not shown on this graph. (b) Results of MVA error analysis (equation 3.4) derived following the method of *Sonnerup and Scheible* [1998] to describe the spread of errors in the calculated magnitude of B_N .

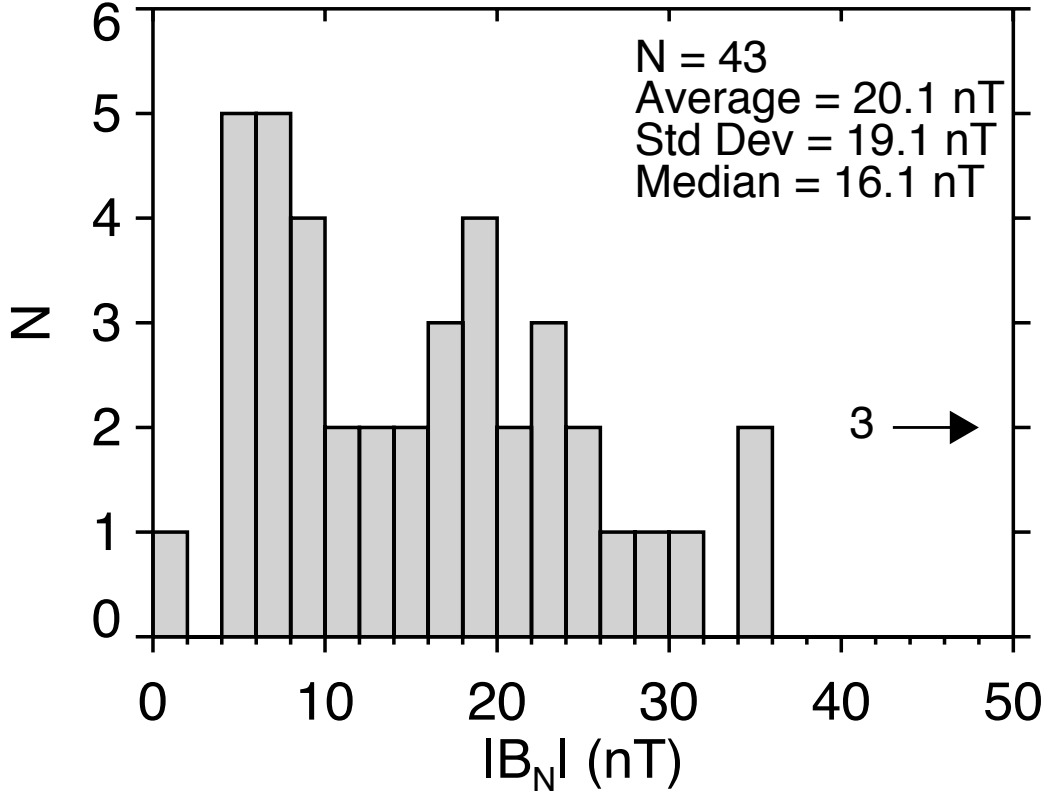


Figure 3.7: Distribution of the normal component of the magnetic field at the magnetopause calculated from MVA. Three observations have magnitudes greater than 50 nT and are not shown on the graph.

At the reconnection X-line, magnetic flux is delivered to the diffusion region at the plasma inflow speed (V_{in}). Following reconnection, the newly created open flux tubes leave the diffusion region at the outflow jet velocity, which is equal to the Alfvén speed (V_A). The rate of magnetic flux transport into the X-line, $V_{in}B_{MP}$, and the transport in the outflow region, V_AB_N , must match:

$$\dot{\Phi} = V_AB_N = V_{in}B_{MP} \quad (3.5)$$

where $\dot{\Phi}$ is the intensity or rate of reconnection. However, for many purposes it is desirable to use a dimensionless reconnection rate α [Sonnerup *et al.*, 1981a; Mozer and Retinò, 2007; Mozer and Hull, 2010]:

$$\alpha = \frac{B_N}{B_{MP}} = \frac{V_{in}}{V_A} \quad (3.6)$$

This dimensionless reconnection rate, α , removes the dependence of flux transfer rate on the strength of the magnetic field and the Alfvén speed, but not other intrinsic factors such as magnetic field shear angle or plasma β . Figure 3.9 displays the distribution of the inferred reconnection rate B_N/B_{MP} from the 43 accepted magnetopause crossings. The average ratio of 0.15 ± 0.02 is ~ 3 times larger than the best available statistical value of 0.046 at Earth [Mozer and Retinò, 2007].

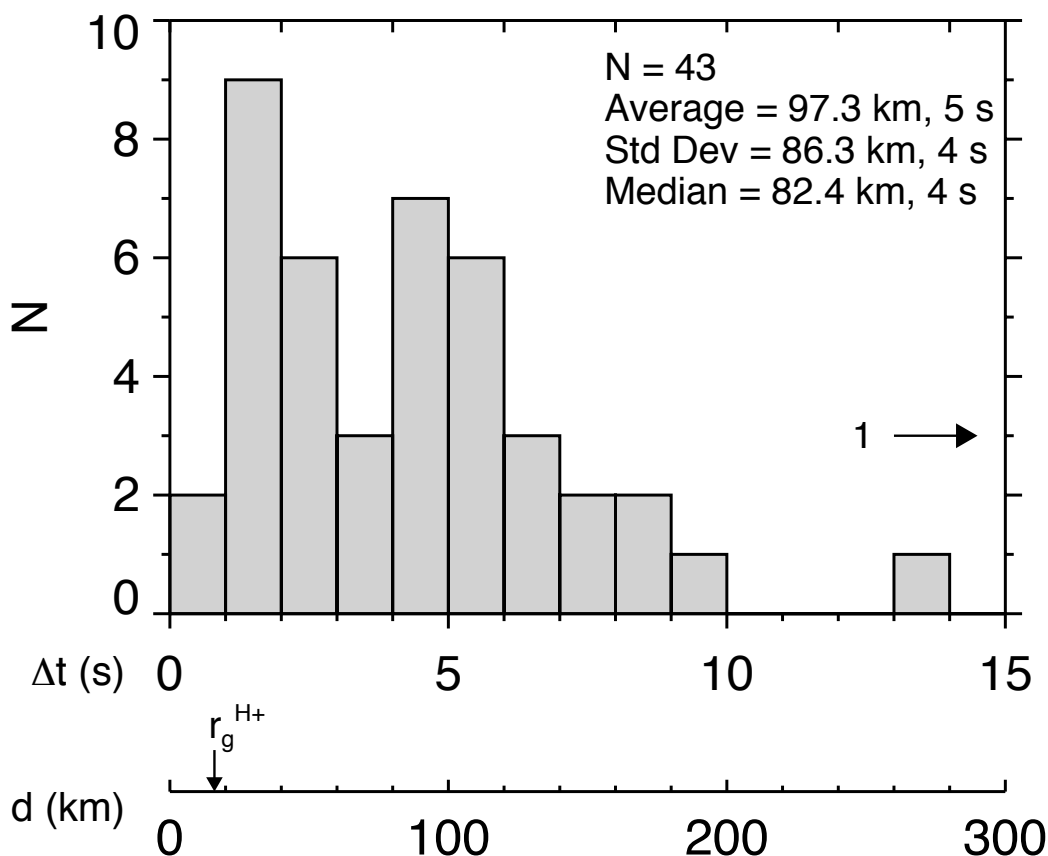


Figure 3.8: Histogram of magnetopause thickness d on the dayside magnetopause determined from measurements of the duration Δt of each magnetopause crossing and for a normal component of the magnetopause velocity of 20 km s^{-1} . The calculated gyroradius r_g of a solar wind proton (16 km) is indicated. A single crossing with duration longer than 15 s is not included on the histogram.

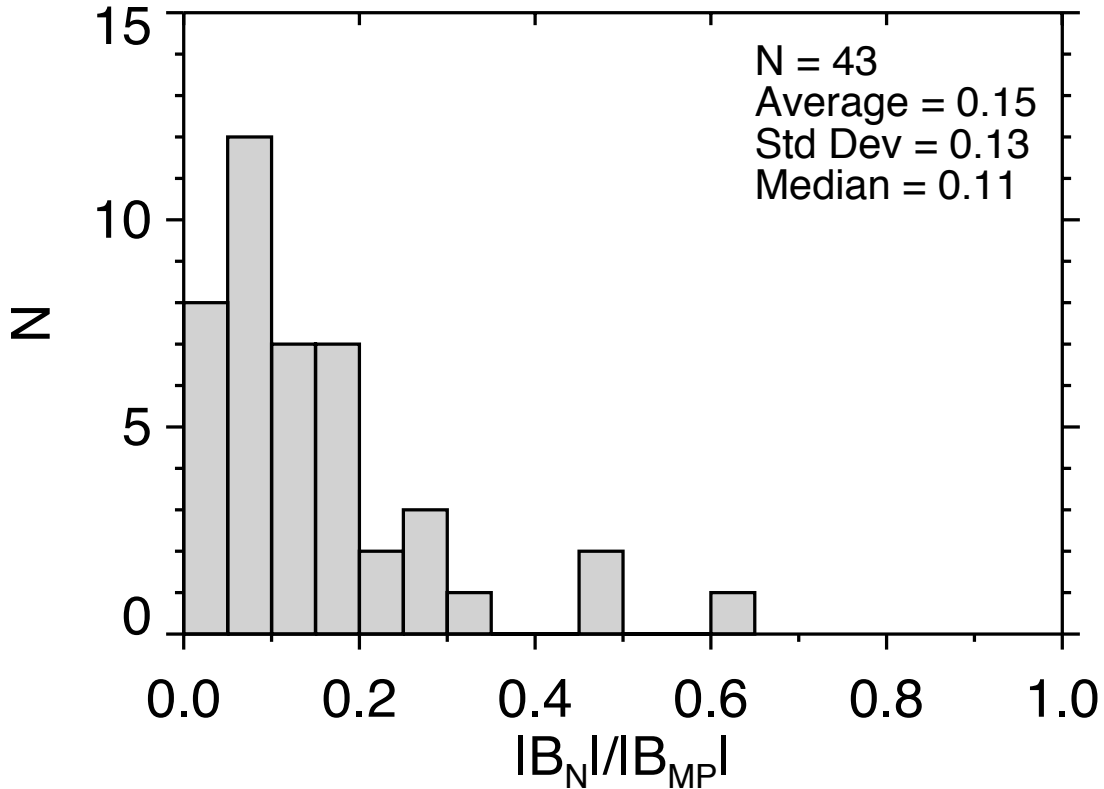


Figure 3.9: Histogram of reconnection rates calculated from the ratio of the normal component of the magnetic field determined from MVA to the magnitude of the total field just inside the magnetopause.

3.4 Discussion

In this paper, MVA has been applied to magnetic field data acquired by the MESSENGER spacecraft as it crossed the dayside magnetopause boundary. These boundaries were identified in the Magnetometer data and confirmed with FIPS plasma measurements. This procedure allowed the identification of magnetopause crossings with significant B_N , even under low-shear conditions. MVA appears well suited to the study of magnetopause reconnection at Mercury by virtue of the strong magnetic fields in the inner solar system. Just as at Earth, there are some cases for which large temporal variations or extremely large-amplitude fluctuations result in a poorly determined boundary normal. Further, if a northward IMF threads the magnetosheath such that it has a magnitude comparable to that of the planetary field, and is parallel to the field inside the magnetosphere, then the vanishing field shear and gradient can make boundary identification impossible, especially if Kelvin-Helmholtz waves are present.

ISEE and Cluster multi-spacecraft observations have shown that the magnetopause thickness at Earth is on the order of 5–10 gyroradii for a solar wind proton in the magnetosheath [Berchem and Russell, 1982; Haaland *et al.*, 2004], as predicted by single particle motion [Willis, 1975]. The gyroradii of solar wind protons (H^+) at Mercury are calculated to be 16 km for typical magnetic field strengths inside the magnetopause and a magnetosheath plasma temperature of 10^6 K. If, following Masters *et al.* [2011], we assume an average magnetopause thickness of seven proton gyroradii, the mean magnetopause thickness at Mercury is ~ 100 km. Given the observed duration of ~ 5 s in the MESSENGER observations, the calculated magnetopause velocity is 20 km s^{-1} . This value is well within the range of terrestrial multi-spacecraft observations [e.g., Russell and Elphic, 1978]. The calculated thickness of ~ 100 km for Mercury's magnetopause is much less than that of any other planet possessing an intrinsic magnetic field, e.g., ~ 400 – 1000 km for Earth [Russell and Elphic, 1978; Berchem and Russell, 1982], ~ 3500 – 5200 km at Jupiter [Sonnerup *et al.*, 1981b], and ~ 5000 km as estimated from surface waves at Saturn [Lepping *et al.*, 1981].

The normal component of the magnetic field at the magnetopause, with a mean value of 20.1 nT, is in agreement with the MESSENGER flyby results of Slavin *et al.* [2009] and supports the high rates of reconnection and ~ 2 min timescale computed for the convection of energy, plasma, and magnetic flux in Mercury's Dungey cycle. This timescale was inferred from the cross-magnetosphere electric potential drop calculated from B_N and confirmed by the direct observation of ~ 1 – 3 -min-long intervals of tail loading and unloading [Slavin *et al.*, 2010].

The dependence of the computed reconnection rate on the magnetopause shear angle is displayed in Figure 3.10. We have calculated the average reconnection rate over intervals of 30° (red) to examine the variance of the individual events from the overall average reconnection rate of 0.15. For the crossings examined in this study, the magnetopause shear angle ranges over 1 – 170° , but as indicated by the binned averages, there is minimal variation among the calculated reconnection rates. In contrast with studies of Earth's magnetopause [Fuselier and Lewis, 2011], our results indicate that the dimensionless reconnection rate at Mercury does not increase with an increase in shear angle. Instead, B_N/B_{MP} remains constrained between 0.1 and 0.3 for the majority of the

events with a mean of 0.15. Even the events with the lowest shear angle (0° to 30°) have an average reconnection rate of ~ 0.1 .

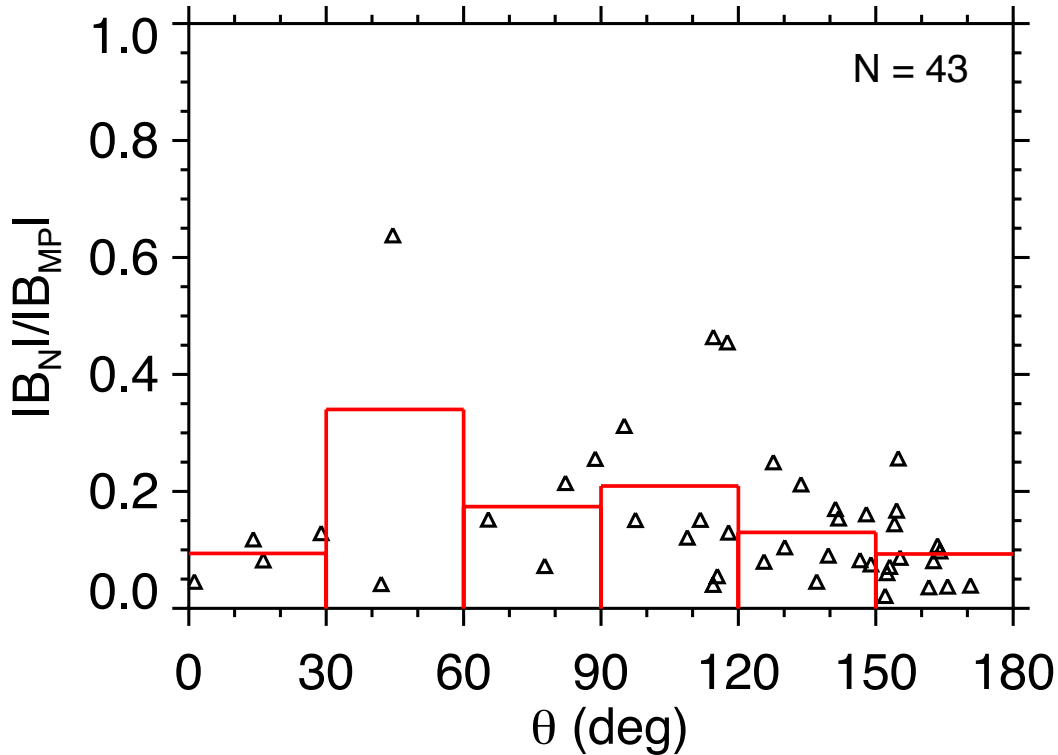


Figure 3.10: Magnetopause shear angle θ compared with the rate of reconnection for the magnetopause crossings meeting the criteria of this study. The average reconnection rate was calculated in 30° bins, as indicated by the red rectangles. Little correlation between the two quantities is evident, indicating that reconnection occurs at Mercury for a large range of shear angles.

Previous studies have explored other factors that control the occurrence and intensity of reconnection at Earth, including plasma β , solar wind Mach number, and magnetopause shear angle [Sonnerup, 1974; Scurry and Russell, 1991; Scurry et al., 1994; Trenchi et al., 2008]. Sonnerup [1974] described how reconnection is still possible when field lines are not antiparallel, but instead are positioned at only a small angle θ with respect to each other. For reconnection to occur at such low shear angles, the magnetic fields on either side of the magnetopause must have an equal field component parallel to the reconnection X-line, B_{\parallel} , known as the guide field. The perpendicular components are then oriented in the same or opposite direction. However, these conditions for low shear reconnection are best met when the magnetic fields on either side of the current sheet are similar in magnitude as, for example, occurs at the

interplanetary current sheet [Gosling *et al.*, 2007; Phan *et al.*, 2010]. This effect at Mercury was illustrated in the low-shear magnetopause reconnection example in Figure 3.4, a case for which the field magnitudes on either side of the magnetopause differed by less than 10%. We suggest that the underlying reason for the strong magnetic fields in Mercury’s magnetosheath is the low Alfvénic Mach number, $M_A \sim 3\text{--}4$, in the inner solar system [Slavin and Holzer, 1979]. Under these conditions, the electromagnetic terms in the magnetohydrodynamic (MHD) equations are more important than for high- M_A conditions. For example, as the IMF encounters the magnetopause, there is a tendency for β to decrease as the plasma is lost to flow along the draped flux tubes, which leads to the formation of a plasma depletion layer (PDL) [e.g., Anderson and Fuselier, 1993]. As first described by Zwan and Wolf [1976], the PDL is greatly enhanced for low solar wind Alfvén Mach number such as is found at Mercury, a result supported by global hybrid and MHD simulations [Trávníček *et al.*, 2010; Benna *et al.*, 2010].

A statistical survey of the terrestrial magnetopause by Scurry *et al.* [1994] showed that a low- β environment is required for low-shear reconnection. It has also been established that the frequency of reconnection is higher for both low- β and low- M_A conditions [Trenchi *et al.*, 2008], a result attributed to the fact that reconnection is possible over a wider range of shear angles under these conditions. To understand why β in the magnetosheath affects the range of shear angles at which magnetopause reconnection may occur, Swisdak *et al.* [2003] used particle-in-cell simulations to study asymmetric reconnection in collisionless plasmas. Their results showed that a diamagnetic drift, produced when a pressure gradient is present across the current sheet, prompts advection of the reconnection X-line and may inhibit reconnection when the drift velocity is super-Alfvénic ($V_* > V_A$). Swisdak *et al.* [2003] found that reconnection is more likely to be suppressed for cases of high M_A , and they established a condition on β -dependent diamagnetic effects:

$$\beta > \frac{B_{\parallel}}{B_{MP}} \frac{2L}{d_i} \quad (3.7)$$

where L represents the pressure scale length and d_i is the ion inertial length. This relation implies that magnetic reconnection is prevented at high values of β , even when a substantial guide field is present. However, in the low- β case at Mercury, we can expect a high occurrence of reconnection for a wide range of shear angles.

The condition in equation (3.7) was reformulated to relate the restriction of reconnection to the magnetic shear angle:

$$\Delta\beta > \frac{2L}{d_i} \tan\left(\frac{\theta}{2}\right) \quad (3.8)$$

where $\Delta\beta$ is the change in plasma β across the current layer [Swisdak *et al.*, 2010]. As part of a study of magnetopause reconnection at Saturn, Masters *et al.* [2012] measured the magnetized plasma conditions to explore whether the parameters satisfy the diamagnetic suppression condition (equation 3.8). With the majority of the events meeting this criterion, they determined that high- β conditions restrict reconnection at the planet.

It is possible to calculate β in the magnetosheath for our chosen magnetopause crossings by assuming that the plasma pressure inside the magnetosphere is negligible. After applying this assumption to the rotational discontinuity pressure balance given in equation (3.1), we are able to determine the magnetosheath plasma pressure:

$$P_{MSH} = \frac{B_{MSP}^2}{2\mu_0} - \frac{B_{MSH}^2}{2\mu_0} \quad (3.9)$$

This value may then be used to calculate the ratio of the plasma pressure to magnetic pressure in the magnetosheath:

$$\beta_{MSH} = \frac{P_{MSH}}{B_{MSH}^2/2\mu_0} = \frac{B_{MSP}^2 - B_{MSH}^2}{B_{MSH}^2} = \frac{B_{MSP}^2}{B_{MSH}^2} - 1 \quad (3.10)$$

where β_{MSH} is the plasma β in the magnetosheath. Since we are assuming $\beta = 0$ inside the magnetosphere, $\Delta\beta = \beta_{\text{MSH}} - \beta_{\text{MSP}} = \beta_{\text{MSH}}$.

The calculated β_{MSH} and measured shear angle are compared in Figure 3.11a using the relation of equation (3.8) for $L = d_i$. This relation separates the parameter space into two regions denoting whether reconnection is possible or suppressed. Above the curve, the diamagnetic suppression condition is not satisfied and reconnection is possible according to the necessary, but not sufficient, low- β requirement. In the region below the curve, the β -shear condition for diamagnetic suppression is satisfied and reconnection is prevented. The majority of the low- β events lie above the curve, including all crossings with reconnection rates ≥ 0.25 (red triangles), suggesting conditions that are favorable for reconnection, a result in agreement with the conclusions of *Masters et al.* [2012] for high β . Furthermore, a comparison of β_{MSH} with the reconnection rate in Figure 3.11b demonstrates that instances of high B_N/B_{MP} occur for low- β cases, in correspondence with the results of *Scurry et al.* [1994].

The total electric potential drop across the magnetosphere for a normal magnetic field B_N , a solar wind speed V_{SW} , and a dayside X-line length L is given by the expression [*Siscoe et al.*, 1975]:

$$\Phi_M = B_N V_{\text{SW}} L \quad (3.11)$$

For a magnetosheath flow velocity of 200 km s^{-1} at the terminator plane and a reconnection X-line length of $3 R_M$, values of the potential drop are as shown in Figure 3.12. The average value of 29 kV is in good agreement with the 30 kV estimate derived from measurements taken during MESSENGER's second flyby of Mercury [*Slavin et al.*, 2009]. It is also lower than typical values for the magnetospheric potential drop of about 60 kV at Earth [*Lindqvist and Mozer*, 1990], 250 kV at Jupiter, and 45 kV at Saturn [*Badman and Cowley*, 2007], consistent with the smaller magnetosphere dimensions but stronger IMF and reconnection rate at Mercury.

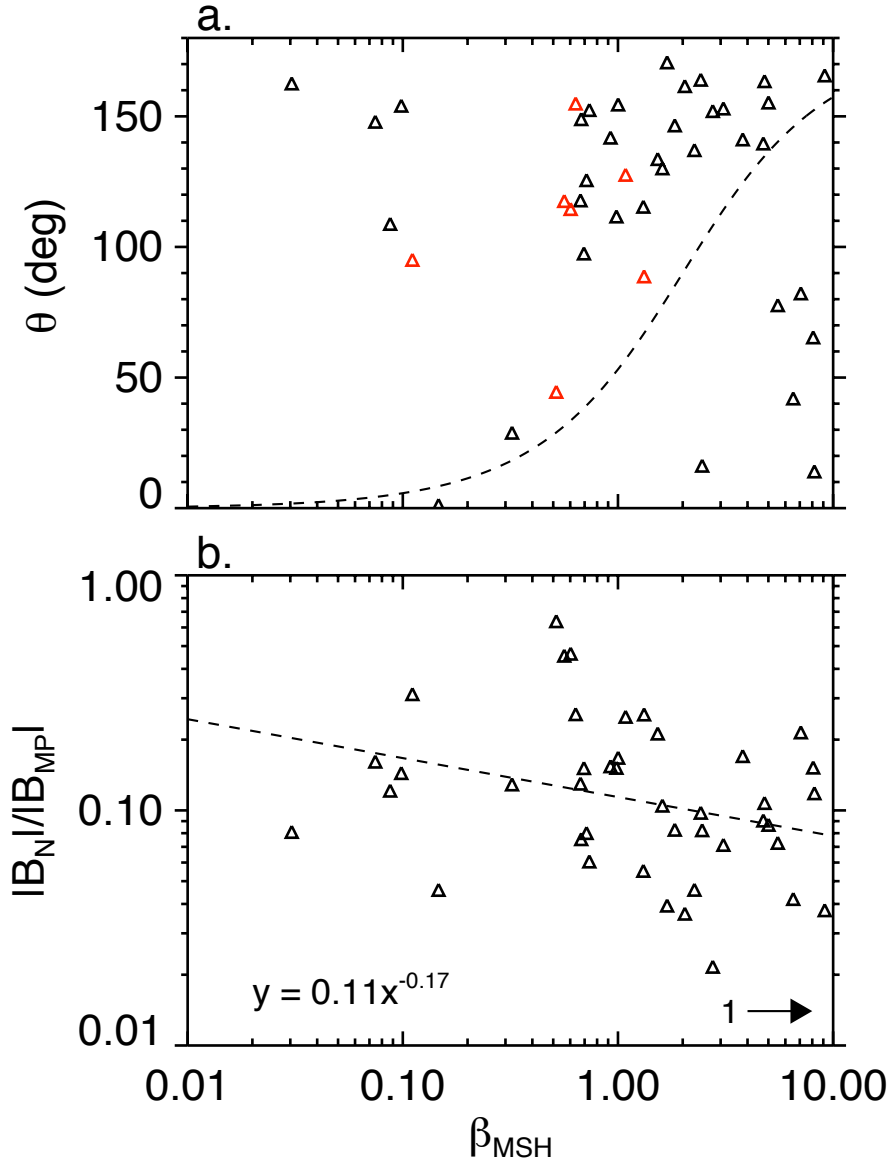


Figure 3.11: (a) Comparison of β to magnetic shear, together with the condition of *Swisdak et al.* [2010] for diamagnetic suppression of reconnection for $L = d_i$ (dashed line), to assess reconnection enhancements in the low- β environment. Black triangles are crossings with a reconnection rate < 0.25 , and red triangles show reconnection rates ≥ 0.25 . (b) Evaluation of the correlation between β and the rate of reconnection with a power-law fit (dashed line) to observations for the magnetopause crossings meeting the criteria of this study. One event with $\beta > 10$ is not shown on the plots.

We conclude that Mercury's dayside magnetopause is frequently experiencing reconnection as a result of the low- β and low- M_A conditions in the magnetosheath associated with the planet's location in the inner heliosphere. This environment facilitates reconnection over a wide range of magnetopause shear angles and contributes to a high reconnection rate and, for its small dimensions, a high magnetospheric potential.

As a result, Mercury's magnetosphere is subjected to the most intense solar wind forcing of any planet in the solar system.

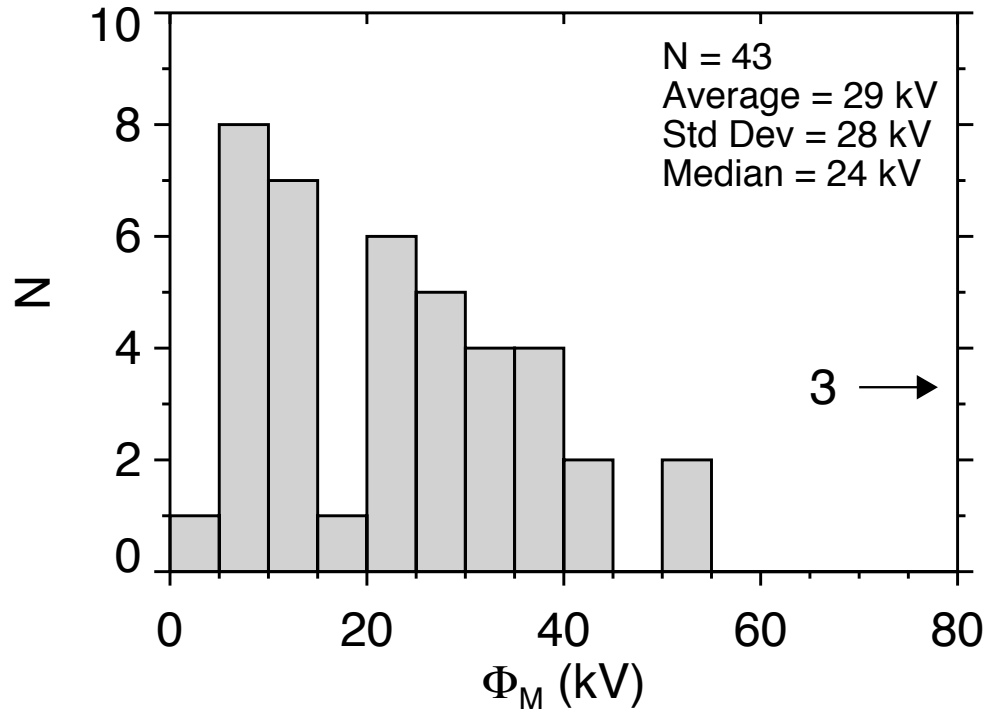


Figure 3.12: Histogram of magnetopause reconnection contribution to magnetosphere potential for a solar wind velocity of 200 km s^{-1} and an X-line length of $3 R_M$. Three magnetopause crossings for which the estimated contribution to the potential exceeds 80 kV are not included on the plot.

CHAPTER IV

MESSENGER OBSERVATIONS OF FLUX ROPES IN MERCURY'S MAGNETOAIL

This chapter is taken from Gina A. DiBraccio, James A. Slavin, Suzanne M. Imber, Daniel J. Gershman, Jim M. Raines, Caitriona M. Jackman, Scott A. Boardsen, Brian J. Anderson, Haje Korth, Thomas H. Zurbuchen, Ralph L. McNutt, Jr., and Sean C. Solomon (2014), MESSENGER observations of flux ropes in Mercury's magnetotail, manuscript in preparation.

Abstract

MESSENGER Magnetometer and Fast Imaging Plasma Spectrometer measurements during seven “hot seasons,” when the orbital periapsis is on Mercury's dayside, provide an opportunity to investigate magnetic reconnection in Mercury's magnetotail. Flux ropes are formed in the cross-tail current sheet by reconnection at two or more X-lines. We have selected 49 flux ropes observed between 1.7–2.8 R_M down the tail from the center of the planet, for which minimum variance analysis indicates that the spacecraft passed near the central axis of the structure. An average proton density of 2.55 cm^{-3} is measured in the plasma sheet surrounding these flux ropes, and the average Alfvén speed is $\sim 450 \text{ km s}^{-1}$. Under the assumption that the flux ropes move at the local Alfvén speed, we use the mean duration of $0.74 \pm 0.15 \text{ s}$ to calculate a typical diameter of $\sim 340 \text{ km}$, compared to a plasma sheet proton gyroradius of $\sim 400 \text{ km}$. We successfully fit the magnetic signatures of 16 flux ropes to a force-free model. The mean radius and core field determined in this manner were $\sim 450 \text{ km}$ and $\sim 40 \text{ nT}$, respectively. A superposed epoch analysis demonstrates that the magnetic structure of the flux ropes is similar to

those observed at Earth, including the presence of a post-plasmoid plasma sheet, filled with disconnected magnetic flux, but the timescales are 40 times shorter at Mercury. The results of this flux rope survey indicate that intense magnetic reconnection occurs frequently in the cross-tail current layer of this small but extremely dynamic magnetosphere.

4.1 Introduction

The MESSENGER spacecraft has provided continuous observations of Mercury's dynamic magnetosphere and local space environment since its orbital insertion on 18 March 2011. Prior to this, the only in situ measurements at Mercury were supplied by three flybys of the Mariner 10 spacecraft [*Ness et al.*, 1974, 1975] and three flybys from MESSENGER [*Anderson et al.*, 2008, 2010; *Slavin et al.*, 2008, 2009, 2010; *Zurbuchen et al.*, 2008; *Raines et al.*, 2011]. Mariner 10 discovered that Mercury possesses a relatively weak intrinsic magnetic field, a result that MESSENGER observations later confirmed and constrained to a magnetic dipole moment of $195 \pm 10 \text{ nT} \cdot R_M^3$ [*Anderson et al.*, 2011a]. After MESSENGER's first Mercury year in orbit (1 Mercury year = 88 Earth days), *Anderson et al.* [2011a] reported a northward offset of the nearly axial-aligned dipole moment from the center of the planet by $\sim 20\%$ of the planet's radius, or 484 ± 11 km. Mercury's magnetosphere, formed by the interaction between the solar wind and the intrinsic planetary magnetic field, is dictated by Mercury's proximity to the Sun and the small magnetic moment of the field; however, this small magnetosphere experiences many of the same processes as that of Earth.

One of these processes is magnetic reconnection, a ubiquitous phenomenon in space plasmas responsible for the explosive transfer of electromagnetic energy from magnetic fields to charged particles in the plasma. During reconnection, sheared magnetic fields are able to merge at sites called X-lines, where ions and electrons become demagnetized to form diffusion regions [e.g., *Shay et al.*, 1998; *Hesse*, 2006]. In this manner, magnetic reconnection is responsible for many of the dynamics observed in Mercury's magnetosphere.

These reconnection-driven dynamics constitute the circulation of mass, momentum, and energy throughout Mercury's magnetosphere, which is referred to as the Dungey cycle [Dungey, 1961]. At Mercury, typical Dungey cycle times are ~ 2 min, which is approximately 30 times shorter than the ~ 1 h Dungey cycle time at Earth [Siscoe *et al.*, 1975; Slavin *et al.*, 2009, 2012a]. The cycle begins with magnetic reconnection at Mercury's dayside magnetopause, which has been observed in the form of magnetic field components normal to the boundary [DiBraccio *et al.*, 2013] and as helical structures called flux transfer events [Slavin *et al.*, 2012b; Imber *et al.*, 2014]. The Dungey cycle continues in the magnetotail, where reconnection has been observed in the form of near-tail dipolarization events [Sundberg *et al.*, 2012], extreme loading and unloading events [Slavin *et al.*, 2010], and traveling compression regions (TCRs) and plasmoids [Slavin *et al.*, 2009, 2010, 2012a]. However, little is known about the characteristics of these plasmoids and their contribution to the Dungey cycle at Mercury.

Plasmoids are known to have two different magnetic structures: magnetic loops and flux ropes. Flux ropes form as a result of magnetic reconnection occurring at multiple X-lines in the plasma sheet, where the oppositely directed fields in the north and south lobes meet at the cross-tail current sheet (Figure 4.1) [Hesse and Kivelson, 1998]. The two tail lobes are sheared, with respect to one another, due to stresses imposed at the magnetopause by dayside reconnection. This shear causes a B_Y component to be generated in the current sheet [Cowley, 1981] and as a consequence, flux ropes possess a helical topology with a strong axial core field [Hughes and Sibeck, 1987]. This structure is different from conventional magnetic loops, formed by closed planetary field lines that are pinched off via reconnection at a single X-line. Once created, the plasma sheet flux ropes are ejected away from the dominant reconnection X-line, the site with the highest outflow speed, either toward or away from the planet. As they move through the magnetotail, the fields in the lobes drape around the flux rope structure and become locally compressed. These compressions, or TCRs, can be used to remotely sense a passing flux rope if it is not directly encountered. Both flux ropes and TCRs have been identified in numerous planetary magnetospheres using magnetic field measurements.

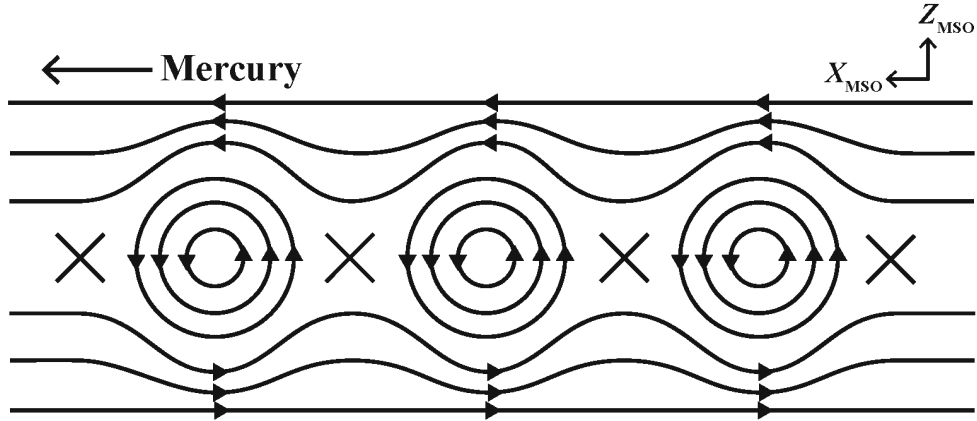


Figure 4.1: Schematic of flux ropes that are formed as a result of reconnection occurring at multiple X-lines (marked by \times) within the plasma sheet. Mercury is located to the left and the arrows indicate the opposite direction of the magnetic field within the lobes.

Hones [1977] was the first to observe plasmoids, using IMP 8 data in the Earth's magnetotail. Since their discovery, many statistical surveys have been performed to evaluate common characteristics of plasmoids at Earth [Hones *et al.*, 1983; Slavin *et al.*, 1987; Moldwin and Hughes, 1992; Nagai *et al.*, 2000; Ieda *et al.*, 1998]. For example, Ieda *et al.* [1998] surveyed Geotail particle and magnetic field data to select 824 tailward-traveling flux ropes at locations ranging from 16 to 210 R_E down the tail from the center of the planet. The average duration of these events ranged from 1.2–1.8 min. Using Geotail measurements in the near-tail plasma sheet (14 to 30 R_E away from the planet), Slavin *et al.* [2003a] identified 73 quasi-force-free flux rope events by only selecting events when the internal magnetic field variations could be well fit to the Lepping *et al.* [1990] force-free model, which allowed the dimensions and core magnetic field intensity to be determined [see Section 4.4 in this paper and Lepping *et al.*, 1990, 1995, 1996]. A superposed epoch analysis revealed that the average duration of these events was ~ 28 s for 35 planetward-traveling flux ropes and ~ 32 s for 38 tailward-moving flux ropes [Slavin *et al.*, 2003a]. These results confirmed the Ieda *et al.* [1998] findings that flux ropes are small in size, a few R_E in diameter, and generated closer to the Earth; however, for the first time, Slavin *et al.* [2003a] observed near-equal numbers of planetward- and tailward-traveling flux ropes, which strongly argues for a formation mechanism involving simultaneous reconnection at multiple X-lines. These conclusions were later supported by flux rope and TCR investigations using Cluster measurements [Slavin *et al.*, 2003b, 2005]. More recently, Imber *et al.* [2011] completed a statistical

survey of 135 flux ropes and TCRs in the near-Earth tail using data from the Time History of Events and Macroscale Interactions during Substorms (THEMIS) mission. These results demonstrated a large dawn-dusk asymmetry and many were only separated by tens of seconds, indicating once again that reconnection was occurring simultaneously at multiple X-lines.

To date, only seven plasmoid events, encountered in Mercury's magnetotail during the MESSENGER flybys, have been reported [Slavin *et al.*, 2009, 2012a]. These plasmoids appeared to have magnetic loop-like topologies with time durations of $\sim 1\text{--}3$ s, implying diameters of $\sim 0.2\text{--}0.6 R_M$. The region of extended southward B_Z , called the post-plasmoid plasma sheet, had a duration of $\sim 4\text{--}5$ s. Slavin *et al.* [2012a] suggested that a more extensive survey is necessary to confirm the trend of loop-like and flux rope-like structures in Mercury's magnetosphere. With nearly three Mercury years of MESSENGER orbital data available, this type of statistical study is now possible to understand general structure characteristics and their affect on the magnetospheric system.

In this study, we present the first statistical survey of plasma sheet flux ropes resulting from reconnection in Mercury's cross-tail current sheet. We find that flux rope-like structures are much more common than loop-like topologies and, therefore, we do not consider the latter in this investigation. We present an analysis of 122 passes through the plasma sheet at distances of $1.5\text{--}3 R_M$ down the tail from the center of the planet. Individual flux ropes encountered during these plasma sheet crossings were identified based upon their signatures in minimum variance coordinates and led to the selection of 49 plasma sheet flux ropes. The diameters, core magnetic field intensities, and magnetic flux content of these selected flux ropes are determined by fitting the magnetic field profiles to force-free flux rope models [see Lepping *et al.*, 1990, 1995, 1996; Slavin *et al.*, 2003a, 2003b; Imber *et al.*, 2014]. This survey of 49 events confirm that flux ropes frequently form in Mercury's magnetotail and the magnetic flux transport rate in the post-plasmoid plasma sheet is consistent with dayside reconnection rates and ~ 2 min Dungey cycle time determined by earlier MESSENGER investigations.

4.2 Analysis Technique

Flux ropes were identified using MESSENGER MAG data [Anderson *et al.*, 2007] with a sampling rate of 20 vectors s^{-1} , in MSM coordinates. Since the spacecraft velocity is small (e.g., $\sim 1 \text{ km s}^{-1}$) relative to typical flux rope speeds, we assume its motion to be negligible. As illustrated in Figure 4.2, a flux rope encounter is indicated in the data on the basis of: (1) A pronounced bipolar variation in the north-south (B_Z) component of the magnetic field, indicative of the outer helical wraps; (2) A local maximum in the east-west (B_Y) direction coincident with the inflection point of the B_Z bipolar perturbation, denoting the strong, axial core field; and (3) An increase in the total magnetic field magnitude ($|B|$) to reflect the enhancement in B_Y due to the core field. Based upon plasmoid studies at Earth where high resolution plasma flow measurements are available, the phase of the B_Z signature will indicate the direction that the flux rope is traveling: north-then-south (NS) for tailward traveling and south-then-north (SN) for those moving planetward [e.g., Slavin *et al.*, 2003a].

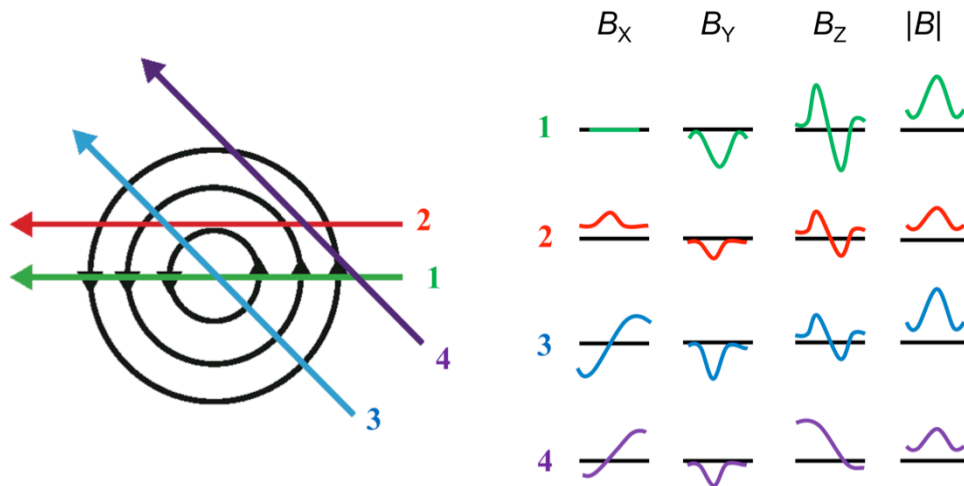


Figure 4.2: Examples of the variation in magnetic field signatures of flux ropes dependent on the trajectory at which they are encountered by the spacecraft. Flux ropes are identified on the basis of: (1) A pronounced bipolar variation in the north-south (B_Z) component of the magnetic field; (2) A local maximum in the east-west (B_Y) direction denoting the strong, axial core field; and (3) An increase in the total magnetic field magnitude ($|B|$).

It must also be noted that the spacecraft does not always encounter the middle of the flux rope structure and for this reason, the signatures described above may vary.

Figure 4.2 gives four examples of the variations in observations due to different spacecraft trajectories [cf., *Borg et al.*, 2012]. In addition to only encountering part of the structure because of trajectory effects, tail dynamics such as current sheet flapping, or tilting, may also play a role. Current sheet flapping occurs as a response to changing upstream conditions, creating a nonzero B_Z in the tail lobes adjacent to the plasma sheet. This causes a net shift in the data of the north-south component that will affect the plasmoid B_Z bipolar signatures. Depending on the spacecraft trajectory in these scenarios, the bipolar signature may not be symmetric or might not even cross through $B_Z = 0$ altogether.

Due to the aforementioned biases that may be present in the data, we have implemented a minimum variance analysis (MVA) [*Sonnerup and Cahill*, 1967] to determine the orientation and structure of each flux rope. MVA was originally implemented over magnetopause crossings in order to define the normal direction of the boundary, however, others began applying this method to flux ropes [*Sibeck et al.*, 1984; *Elphic et al.*, 1986; *Slavin et al.*, 1989; *Moldwin and Hughes*, 1991] and it has proven to be advantageous in analyzing their structure. To begin, the magnetic field data was corrected for solar wind aberration (denoted by a prime symbol) using Mercury's orbital velocity at the time of each orbit ($\sim 44\text{--}55 \text{ km s}^{-1}$) and assuming a solar wind speed of 425 km s^{-1} . MVA was performed on each individual event to transform the magnetic field data from MSM' coordinates to principal axis coordinates. In this new coordinate system, we expect the direction of minimum variance (B_1) to be mostly in the X'_{MSM} direction, intermediate variance (B_2) will lie parallel to the enhancement due to flux rope's core field, or Y'_{MSM} , and the direction of maximum (B_3) variance will align with the bipolar signature in Z'_{MSM} . The B_1 component will indicate the spacecraft's proximity to the center of the flux rope at the time of the encounter. For an ideal traversal through the middle of a flux rope (trajectory 1 in Figure 4.2), B_1 should remain constant around zero (e.g., see discussion of MVA analysis in *Briggs et al.*, 2011).

After examining a flux rope in MVA coordinates we decide to accept or reject the events based on whether it displays the inherent flux rope signatures. A strong core field enhancement coincident to the bipolar perturbation of the helical magnetic structure was necessary for the flux rope to be included in this study.

Proceeding the identification and acceptance of flux ropes in the MAG data, we examined the FIPS data [Andrews *et al.*, 2007] for each chosen event. FIPS measures the time of flight and E/q within the range of 0.05-13 keV e^{-1} for ions with mass per charge (m/q) up to 40 amu/e. FIPS has a conical field of view of $\sim 1.4\pi$ sr, completing one scan over the entire E/q range in ~ 10 s.

In the plasma sheet, one minute-average plasma data was used to examine the environment adjacent to the chosen plasmoids. As described by Gershman *et al.* [2014], FIPS measurements can generally be used to infer density and temperature, but not flow velocity in the plasma sheet. FIPS data was not available for every event in this study. Here we utilize measurements of proton density and temperature in order to calculate plasma parameters such as β , local Alfvén speed (V_A), and proton gyroradius ($r_g^{H^+}$). The resulting parameters will be discussed further in Section 4.3.2.

4.3 MESSENGER Observations

Using MESSENGER magnetic field data, we surveyed current sheet crossings in Mercury’s magnetotail during “hot season” orbits, when the orbital periapsis is on Mercury’s dayside, in search of the flux rope signatures described in Section 2. These particular orbits were of interest for two reasons: they are near the noon-midnight meridian and they take the most distant current sheet measurements, between $X_{MSM} \sim -1.7$ and $-3 R_M$, where reconnection is expected to occur at the near-Mercury neutral line (NMNL). The prediction of the NMNL location is based on a scaling factor of ~ 8 that has been found to map spatial magnetosphere structures from Mercury to Earth [Russell *et al.*, 1968] where the corresponding near-Earth neutral line (NENL) is located between -20 to $-30 R_E$ [Nagai *et al.*, 2000]. Observations from the second and third MESSENGER flybys implied the NMNL location to be $X'_{MSM} = -2.8 R_M$ and $-1.8 R_M$, respectively [Slavin *et al.*, 2012a]. Figure 4.3a shows an example of a typical “hot season” orbit. MESSENGER “warm season” orbits, when periapsis is near local midnight, intercepts the tail current sheet much closer to the planet – around $1.3 R_M$ – at a distance that is typically within the closed planetary field lines and therefore not conducive for flux rope formation.

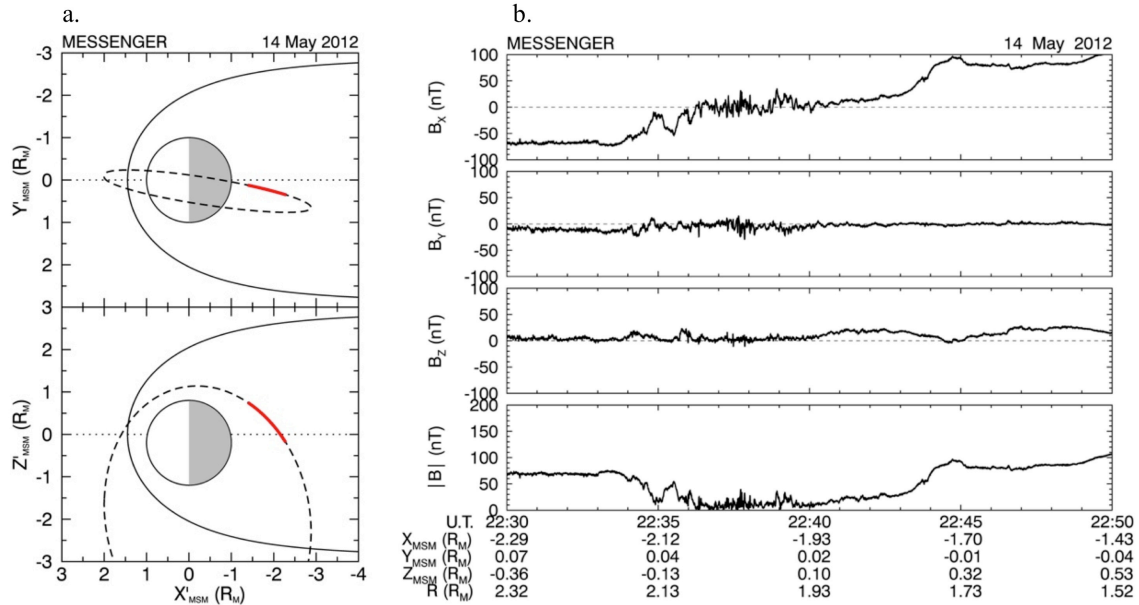


Figure 4.3: (a) MESSENGER “hot season” orbit on 14 May 2012. The portion of the orbit highlight in red indicates the location of the spacecraft as it encountered the current sheet. (b) A 20 min interval of MESSENGER MAG data during the current sheet crossing on 14 May 2012.

We have surveyed current sheet crossings during seven hot seasons, three of which MESSENGER was in a 12-h orbit and four more during the extended mission phase where the spacecraft orbit was reduced to an 8-h period. We constrained our survey to only include hot season orbits with current sheet crossings within $\pm 0.5 R_M$ in the Y'_{MSM} direction. We apply this spatial Y constraint to avoid confusion in identification between plasma sheet flux ropes generated in the cross-tail current sheet with the large flux transfer events (FTEs) that are created at the dayside and observed to compress Mercury’s small magnetotail as they travel around the flanks [Slavin *et al.*, 2012b; Imber *et al.*, 2014]. Current sheet crossings are recognized by a change of polarity in the B_X component from the tailward directed field ($-B_X$) of the southern lobe to the oppositely directed planetward field ($+B_X$) in the northern lobe. Using the orbits that met the current sheet criteria, we proceeded by examining plasma sheet encounters for the flux rope signatures described above. The plasma sheet is characterized as the region of weak, highly variable magnetic fields with roughly an order of magnitude increase in plasma density surrounding the current sheet compared to the tail lobes [Gershman *et al.*, 2014]. In the magnetic field data, the plasma sheet is represented by a diamagnetic depression

exhibited as a 50% decrease or greater in the field magnitude as plasma pressure becomes greater, increasing the plasma β .

Figure 4.3b shows MAG data from a MESSENGER current sheet crossing examined in this study. The red line along the orbit in Figure 4.3a indicates the trajectory during this data interval. The magnetic field remains stable in the B_X direction with a magnitude of ~ -70 nT from 22:30–22:34 UTC, indicating that MESSENGER was located in the southern lobe. From 22:34 to 22:45 UTC, the field rotates from $B_X = -70$ nT to $B_X = +90$ nT as the spacecraft crosses the current sheet and enters the northern lobe. At the same time, MESSENGER encounters the plasma sheet indicated by a decrease in $|B|$ from 70 nT to < 10 nT at 22:34 UTC and then increasing up to ~ 100 nT at 22:45 UTC. Throughout this interval, B_Y and B_Z remain mostly constant. The field fluctuations evident in all magnetic field components between 22:37 and 22:40 UTC at the center of the plasma sheet, are signatures of multiple flux ropes.

It is in the field depression of the plasma sheet that we survey the MAG data for flux ropes. For every orbit, we perform a MVA on each possible flux rope encounter within the plasma sheet.

4.3.1 Flux Rope Example

During the current sheet crossing on 14 May 2012 described in the previous section (Figure 4.3b), a tailward-traveling flux rope was encountered slightly after 22:37:50 UTC when MESSENGER was $2.02 R_M$ down the tail from the planet (Figure 4.4). The MAG data reveals a NS bipolar signature in the B_Z component with a peak-to-peak amplitude of ~ 20 nT. An enhancement of ~ 30 nT in the B_Y direction is indicative of the strong flux rope core field and this is also exhibited by an increase in the total magnetic field magnitude. Further supporting the conclusion that this is a flux rope, the increase in B_Y and $|B|$ are coincident with the inflection of the B_Z bipolar signature (vertical solid line). The magnetic field signatures of this flux rope are identical to trajectory 2 in Figure 4.2, suggesting that the spacecraft passed off-axis as it encountered the flux rope.

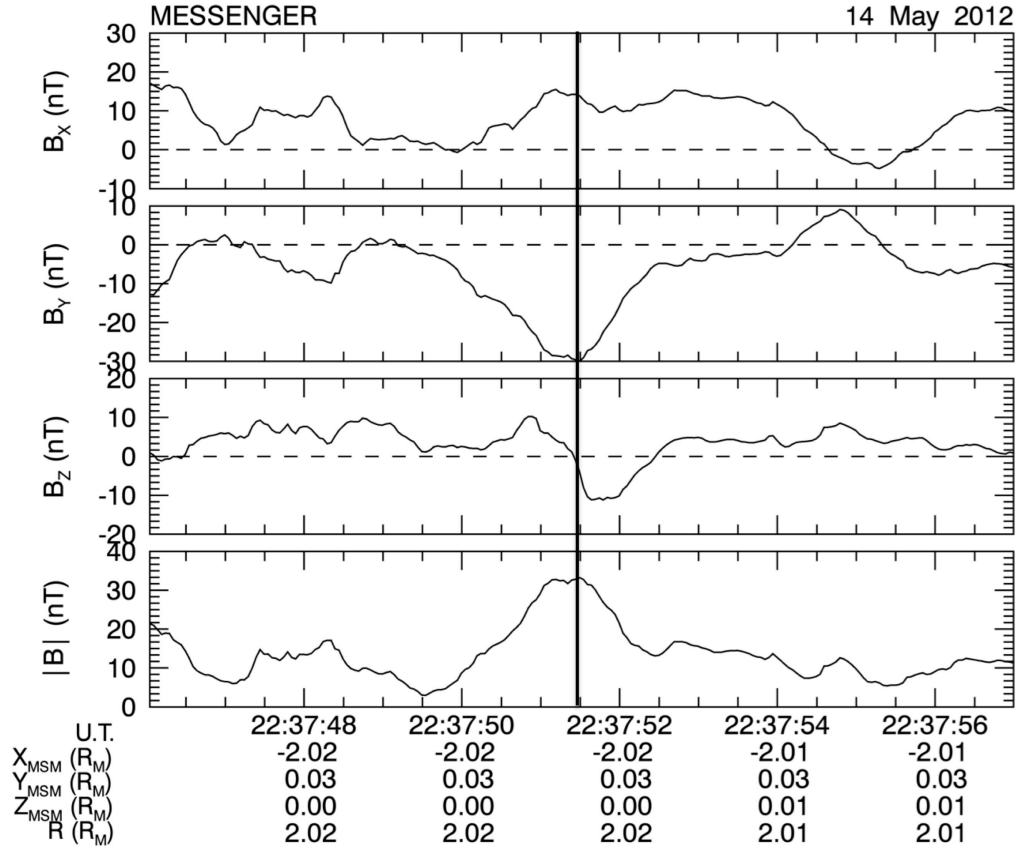


Figure 4.4: MESSENGER MAG observations, in MSM coordinates, of a tailward traveling flux rope encountered in Mercury’s cross-tail current sheet on 14 May 2012. A north-then-south bipolar signature is evident in B_z and a peak in B_y and $|B|$ occur at the inflection point of this B_z perturbation.

MVA is applied over the flux rope structure in order to understand its orientation with respect to Mercury. The MVA interval is short in duration (< 2 s) and the results are plotted in Figure 4.5. The intermediate-to-minimum (λ_2/λ_1) and maximum-to-intermediate (λ_3/λ_2) eigenvalue ratios are 50.99 and 5.96, respectively, and suggest that the new coordinate system is well determined. The corresponding eigenvectors are: $\mathbf{B}_1 = (-0.85, -0.53, 0.01)$, $\mathbf{B}_2 = (0.53, -0.85, -0.05)$, and $\mathbf{B}_3 = (0.01, 0.05, 0.99)$. This indicates that the minimum variance direction lies mostly in the X_{MSM} direction but skewed slightly in the $X_{\text{MSM}}-Y_{\text{MSM}}$ plane. Looking at Figure 4.5a, the reader should notice that the B_1 curve remains mostly constant around +3 nT, which confirms that the spacecraft did not pass through the center of the flux rope. The core field enhancement is evident in the B_2 direction, which is mostly in the Y_{MSM} direction, as expected. The helical outer wraps of the flux rope are indicated by the bipolar perturbation in B_3 as the field rotates from a northward configuration of ~ 10 nT to a southward field of ~ 15 nT. Once again, this NS

signature, in the Z_{MSM} direction based on the B_3 eigenvector, implies that the flux rope is traveling away from the planet. Additionally, two hodograms are included (Figure 4.5b and c) to further illustrate the flux rope topology of the plasmoid in this example. The main rotation of the field through the flux rope, which is $\geq 180^\circ$, is easily identified in the plot of B_2 versus B_3 in Figure 4.5c.

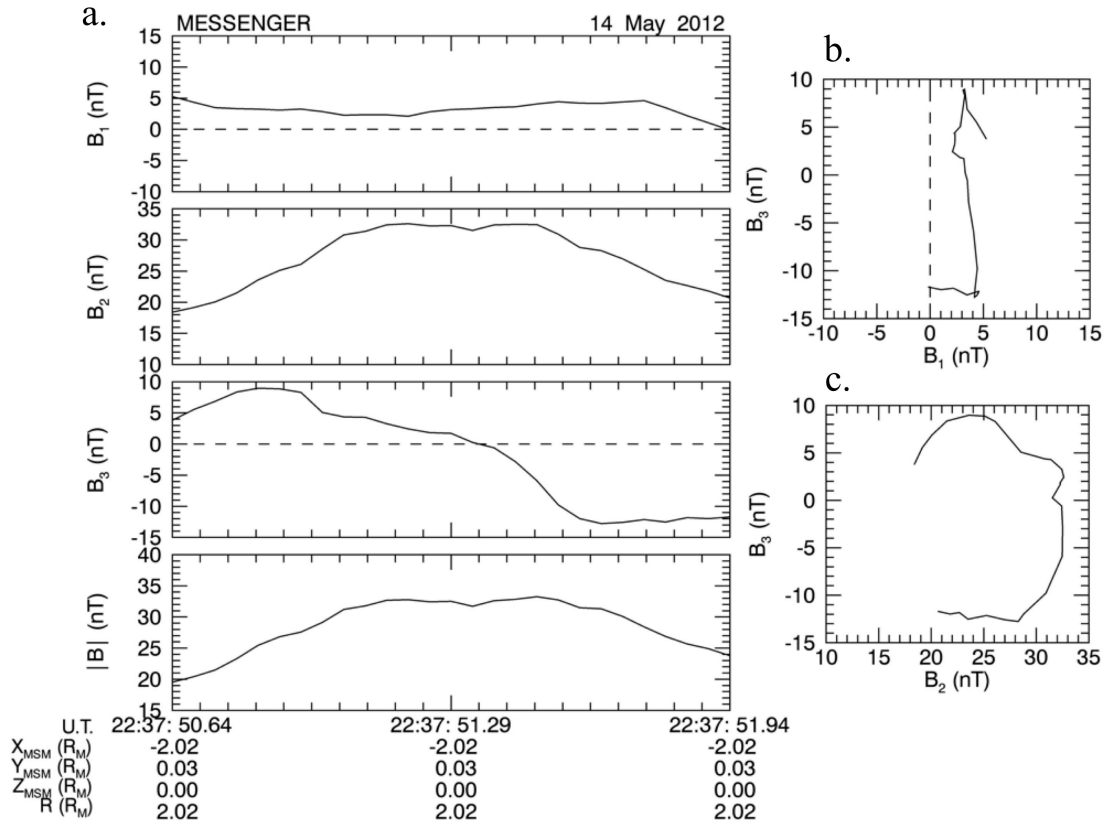


Figure 4.5: Results of minimum variance analysis (MVA) for the example flux rope encounter on 14 May 2012. (a) The magnetic field measurements transformed into MVA coordinates where B_1 , B_2 , and B_3 are the minimum, intermediate, and maximum variance directions, respectively. (b and c) Hodograms of the magnetic field data in MVA coordinates are used to illustrate the rotation of the field during the flux rope encounter.

4.3.2 Statistics

The examination of 122 current sheet crossings during seven hot seasons resulted in the selection of 103 plasma sheet flux ropes located within Mercury's plasma sheet. The events were almost evenly distributed with 52 tailward (NS) and 51 planetward (SN) traveling flux ropes. Following the examination of flux rope MVA results the set was restricted to flux ropes with a $\langle B_1 \rangle$, the time series average, ≤ 10 nT. This restriction eliminated cases when MESSENGER only crossed through the outer edge of the flux

rope. As stated earlier, if the spacecraft were to cross directly through the center of the flux rope, B_1 would measure close to 0 nT. This constraint decreased the number of selected events to 57. Finally, to avoid any TCR signatures that may have been included and ensure that our measurements are located within the flux rope proper we limit the spatial location of our measurements to $-0.25 R_M \leq Z'_{\text{MSM}} \leq +0.25 R_M$. The end result is a selection of 49 pristine plasmoid-like flux ropes that exhibit a bipolar variation in B_Z (either NS or SN), a strong axial core in B_Y , and a peak in $|B|$.

Figure 4.6 displays the distribution of the intermediate-to-minimum (λ_2/λ_1) and maximum-to-intermediate (λ_3/λ_2) eigenvalue ratios resulting from the MVA with average values of 51 and 5, respectively. The ratios describe the level of accuracy in the MVA-coordinate directions; therefore, a high ratio is desired and studies will typically set a threshold requirement to ensure this. After examining at the statistical values of the events, we find that the results are not changed by limiting these eigenvalue ratios and for this reason we have decided to maintain the larger set of events without setting a lower limit on the ratios.

The locations of the selected flux ropes are plotted in MSM' coordinates in Figure 4.7 with 23 NS events (orange circles) and 26 SN events (black circles). Although we find that they are located within the ranges of $-2.8 R_M \leq X'_{\text{MSM}} \leq -1.7 R_M$, $-0.50 R_M \leq Y'_{\text{MSM}} \leq +0.63 R_M$, and $-0.24 R_M \leq Z'_{\text{MSM}} \leq +0.17 R_M$, it should be noted that it is possible for flux ropes to exist outside of these bounds. It is important to keep in mind that the location of our results is constrained due to the implemented limitations in order to select only plasmoid signatures. These restrictions included a limit in X'_{MSM} due to orbital constraints, Y'_{MSM} to avoid confusion with FTE encounters, and Z'_{MSM} to ensure that we are crossing through the flux rope proper and avoid TCR observations. Also, although we limit the Y'_{MSM} direction, we do have several events located outside of this range because we have surveyed the adjacent plasma sheet, which does expand outside of the $\pm 0.5 R_M$ boundary.

An orbital bias is evident in Figure 4.7a as the 8-h orbits cross the current sheet slightly closer to the planet than the 12-h orbits. However, the majority of the SN events were identified during the 8-h orbits and the NS events in the 12-h orbits. Therefore, we are able to deduce that the NMNL is indeed located within the predicted range of ~ 2 - 3

R_M based on the spatial separation between the NS and SN observations. This result is in agreement with observations of the NMNL during the second and third MESSENGER flybys [Slavin *et al.*, 2012a]. The dawn-dusk distribution of the events (Figure 4.7b) is relatively symmetric with 20 on the duskside ($Y' \geq 0$), 28 on the dawnside ($Y' \leq 0$), and 1 event identified at $Y' = 0$.

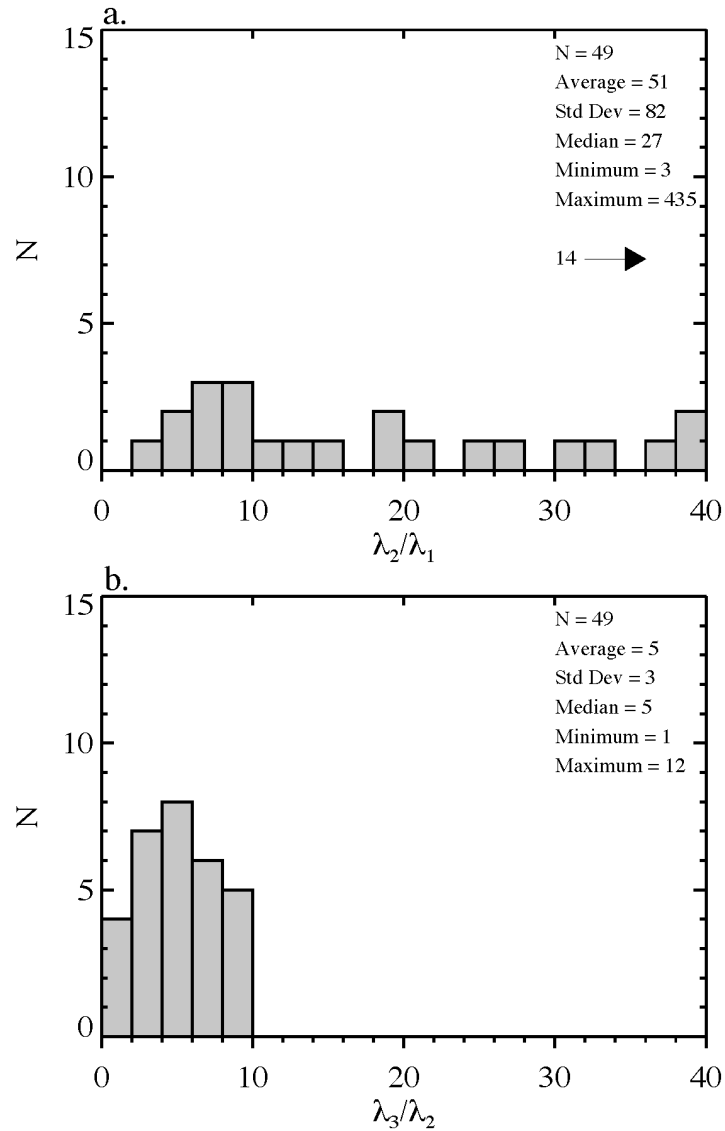


Figure 4.6: Histograms showing the distribution of the ratios of (a) intermediate to minimum eigenvalue and (b) maximum to intermediate eigenvalue resulting from minimum variance analysis (MVA) for the observed flux ropes. A higher ratio means the MVA-coordinate directions are well-determined.

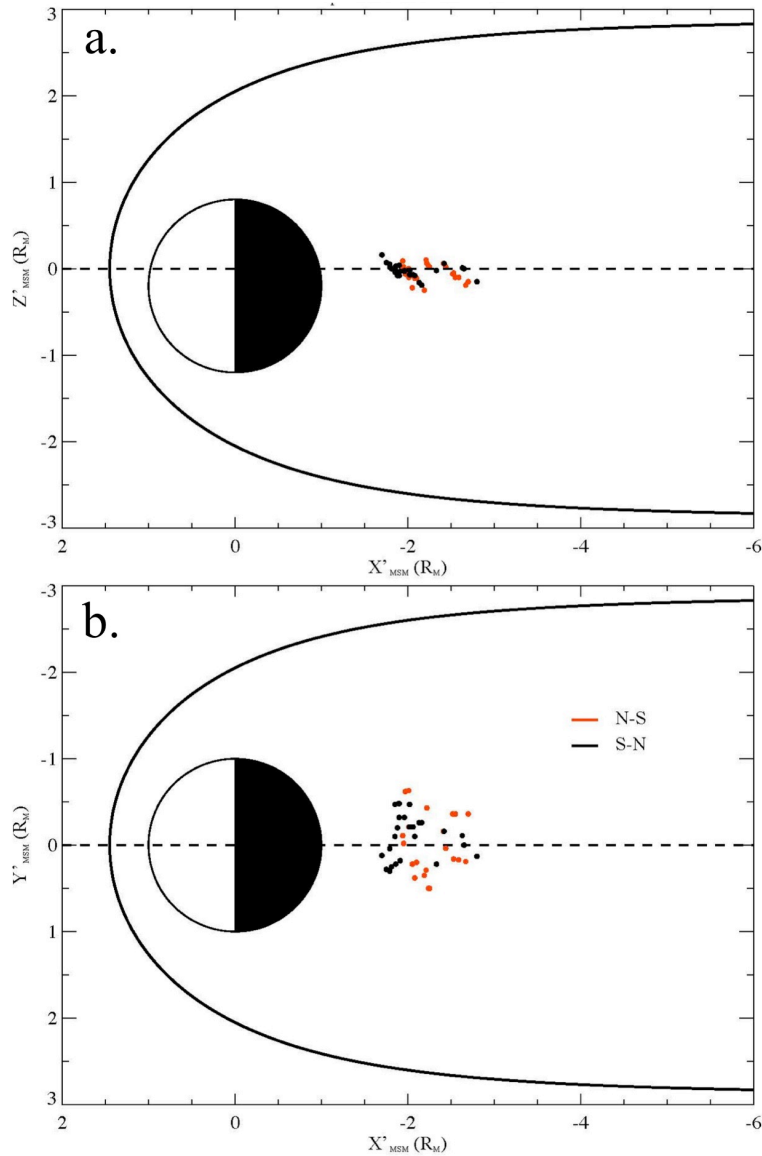


Figure 4.7: Location of the 49 selected flux ropes in aberrated MSM coordinates with a view from the (a) meridional and (b) equatorial plane. Orange circles represent NS flux ropes that are traveling away from the planet while black circles indicate SN flux ropes traveling planetward. The Sun is located to the left.

MVA eigenvector projections are displayed along with flux rope location in MSM' coordinates in Figure 4.8. B_1 is aligned in the X'_{MSM} direction for the majority of the events in Figure 4.8a. This is expected since the B_X component remains nearly constant as the flux rope moves over the spacecraft. The intermediate vector projection (Figure 4.8b) is predominately in the Y'_{MSM} direction, in agreement with the core field signatures present in B_Y . This vector is important because it lies along the central axis of

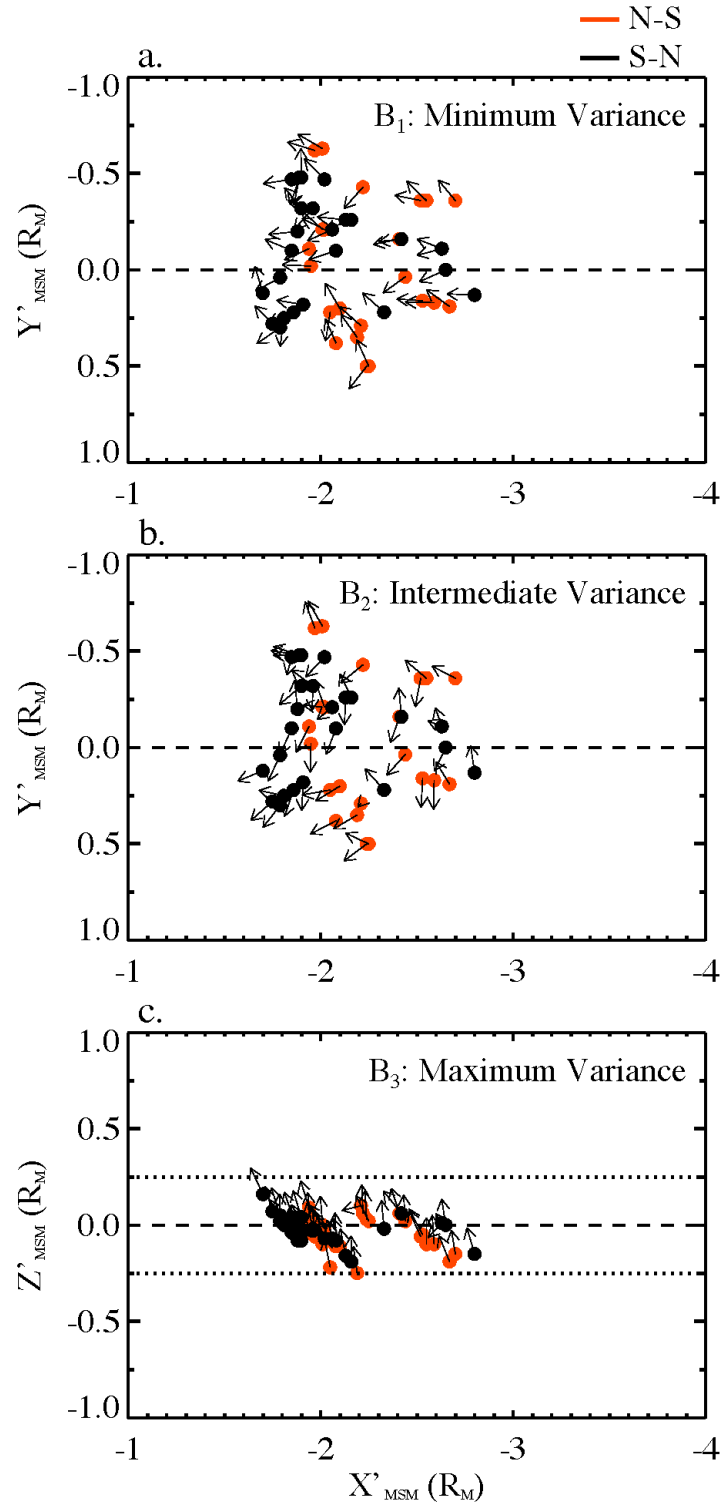


Figure 4.8: Location of plasmoids in aberrated MSM coordinates with the eigenvectors resulting from MVA projected onto the plane in each plot. (a) Projection of \mathbf{B}_1 onto the $X'-Y'$ plane. (b) Projection of \mathbf{B}_2 onto the $X'-Y'$ plane. (c) Projection of \mathbf{B}_3 onto the $X'-Z'$ plane.

the flux rope and therefore provides information of whether the flux rope is tilted as it travels through the tail. Several of the B_1 and B_2 vectors appear to be skewed in the $X'-Y'$ plane, possibly suggesting that the flux ropes are propagating through the tail at an angle or one end is released before the other [Moldwin and Hughes, 1992]. This result is not unusual and has been identified in previous studies at Earth [Hughes and Sibeck, 1987; Slavin et al., 2003a]. The bipolar signature in the maximum variance direction is confirmed by the fact that the B_3 eigenvectors are primarily in Z'_{MSM} . It should be noted that the polarity of the vectors, whether north or south in the respective coordinate, is arbitrary and may be adjusted as long as the entire eigenvector matrix is multiplied by -1 to maintain a right-handed coordinate system.

As explained in the example in Section 3.1, the local extrema in the B_Z bipolar signature associated with the flux rope was used to estimate the duration. The distribution of these time durations is exhibited in the histogram of Figure 4.9. Only two events had intervals > 3 s and the majority of the encounters lasted < 1 s with an average of 0.74 s. The short time scales suggest that the MAG resolution of 20 Hz would not be fast enough to resolve smaller flux ropes that may exist in the tail.

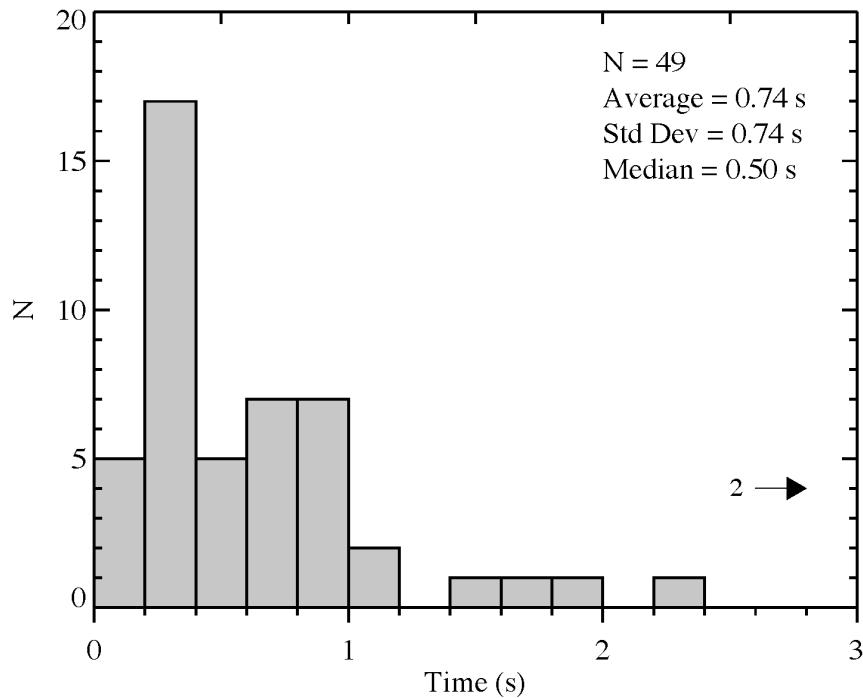


Figure 4.9: Duration of flux ropes calculated from peak-to-peak in bipolar B_Z signature.

Plasma measurements provided by FIPS were available for 31 of the 49 accepted flux ropes. These data provide 1 min average measurements of proton density and temperature of the local plasma sheet adjacent to the flux ropes from which we calculate β and the local Alfvén speeds. Distributions of each parameter are displayed in Figure 4.10. The average density of the plasma sheet surrounding the flux ropes is 2.55 cm^{-3} , a value much larger than what is found in the tail lobes, which are typically void of plasma

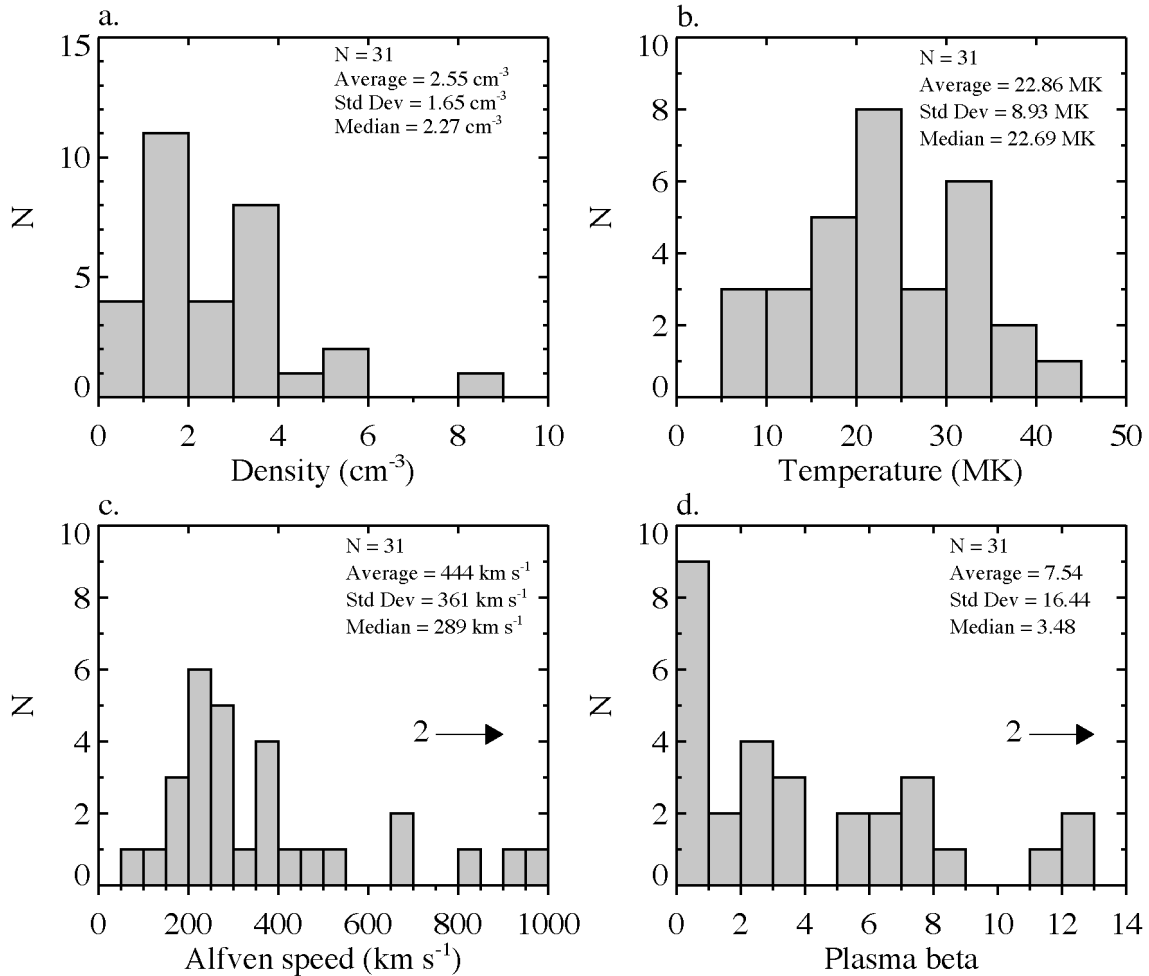


Figure 4.10: Plasma parameters of the plasma sheet directly adjacent to the encountered flux ropes determined from one minute-averaged FIPS data: (a) Proton density; (b) Proton temperature; (c) Alfvén speed; and (d) Plasma β , ratio of plasma pressure to magnetic pressure, calculated using one minute-averaged MAG data to determine the magnetic pressure; and (d) plasma beta.

and defined by the open planetary field lines. In Figure 4.10b, the temperature in the plasma sheet ranges between 7.09–41.12 MK with an average of 22.86 MK. These of proton densities and temperatures are in agreement with the plasma sheet survey by

Gershman et al. [2014]. Incorporating 1 min averaged MAG data with the plasma measurements, we calculated the plasma β (Figure 4.10c) and Alfvén speed (V_A) (Figure 4.10d) of the adjacent plasma sheet. The average plasma sheet β is ~ 7.5 , which is much greater than the lobes where $\beta \ll 1$. The average V_A is $\sim 450 \text{ km s}^{-1}$, which is likely a lower limit. If reconnection continued at a given X-line in the current sheet, the plasma depleted field lines would eventually supply the reconnection, driving up the local Alfvén speed.

4.4 Flux Rope Modeling

We have implemented a model that assumes the flux ropes are force-free structures to better estimate not only their size but also the strength of the core field and the spacecraft’s proximity to the center of the plasmoid as it passed through, known as the impact parameter. A force-free flux rope is self-balancing due to the small internal pressure gradients and $\mathbf{J} \times \mathbf{B}$ forces, and therefore, is in its lowest energy state. That is, the high outward magnetic pressure ($B^2/2\mu_0$) exerted by the strong axially aligned core field is balanced by the inward magnetic tension force ($B^2/2R_c$) of the small pitch angle field lines in the outer layers of the flux rope, where R_c is the radius of curvature of the helical fields. Assuming that a force-free flux rope is cylindrically symmetric, *Lundqvist* [1950] and *Lepping et al.* [1990, 1995, 1996] showed that the magnetic field could be expressed in cylindrical coordinates using the Bessel functions of the first kind in order to model the flux rope signatures:

$$\begin{aligned} B_A &= J_0(\alpha r') B_0 \\ B_T &= J_1(\alpha r') B_0 H \\ B_R &= 0 \end{aligned} \tag{4.1}$$

In these equations, B_A , B_T , and B_R are the axial, tangential, and radial components of the magnetic field with respect to the central axis of the flux rope. $J_0(\alpha r')$ and $J_1(\alpha r')$ are the zeroth and first order Bessel functions, B_0 is the magnetic field magnitude of the flux rope’s core field, and H is the handedness of the helicity. The Bessel functions are

dependent on r' , the radial distance from the center of the flux rope, and α , taken to be constant at 2.4048. This allows us to model a flux rope with a completely axial field ($B_T = 0$) at the center and a completely azimuthal field ($B_A = 0$) at the edge. This technique has been applied to flux ropes at Earth [e.g., *Lepping et al.*, 1990, 1995, 1996; *Slavin et al.*, 2003a, 2003b] and also to large amplitude FTEs at Mercury's magnetopause [*Imber et al.*, 2014].

We have applied this fitting technique to all 49 events in this study and implemented a least squares minimization [*Lepping et al.*, 1990] between the model results and the data to select a radius that produces a best fit for each event:

$$\chi^2 = \frac{\sum \left[(B_{A_DATA} - B_{A_MODEL})^2 + (B_{T_DATA} - B_{T_MODEL})^2 \right]}{N} \quad (4.2)$$

where B_{A_DATA} and B_{T_DATA} are the normalized axial and tangential components of the MAG data, B_{A_MODEL} and B_{T_MODEL} are the normalized axial and tangential magnetic fields resulting from the force-free model, and N is the number of data points. Figure 4.11 shows a histogram of the minimized χ^2 from all events. We set a threshold of $\chi^2 \leq 0.01$ to accept the results as good fits. This criterion enables the acceptance of 16 events. Once the best-fit radius is known, we can use the normalized modeled field to determine B_0 . We do this by scaling B_{A_MODEL} to the maximum value observed in the unnormalized axial field (B_A). Further details on this force-free flux rope modeled are provided in Appendix I.

Figure 4.12a shows a plot of the varying radii used to model the fields versus the χ^2 minimization results for the fitting of the flux rope example from Section 4.3.1. The vertical line indicates where the minimization occurs and the corresponding flux rope radius is ~ 500 km. Figure 4.12b shows an example of a good fit resulting from the minimization illustrated in Figure 4.12a. The normalized axial and tangential fields are plotted where the red line is the data and the black line is the model result. After varying the model flux rope radius between $0-1 R_M$, we find that the best-fit corresponds to a minimum $\chi^2 = 0.003$, where the radius of the flux rope is ~ 500 km, or $0.2 R_M$. The impact parameter is 0.145, which indicates that MESSENGER passed close to the center of the

flux rope but was slightly off-axis. From these model results we were able to estimate that the core field strength was ~ 33.2 nT.

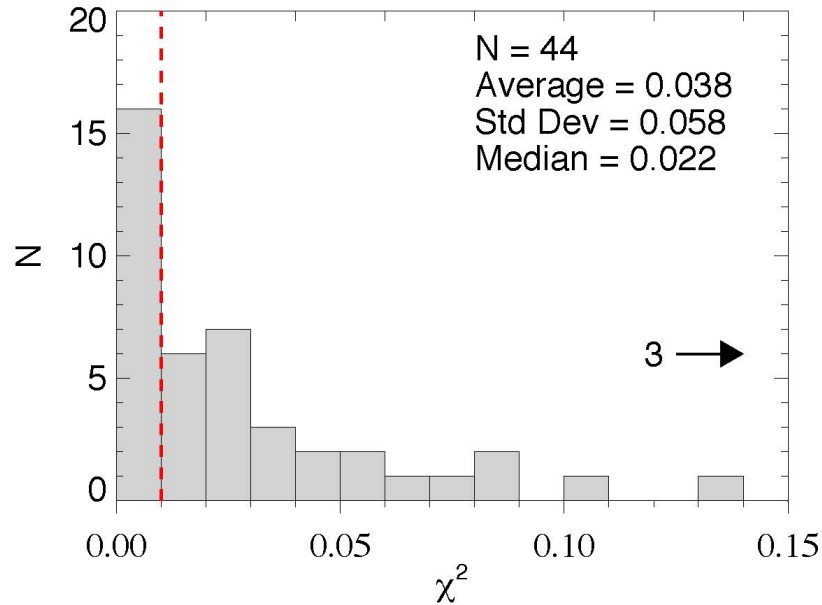


Figure 4.11: Histogram of the minimized χ^2 values resulting from the flux rope fitting. The vertical dashed red line marks the upper limit threshold of 0.01 implemented in order to accept a flux rope fitting.

Histograms of the radius (R_0), core field magnitude (B_0), and impact parameter (Y_0/R_0) for the accepted flux rope fittings are shown in Figure 4.13, where Y_0 is the distance from the spacecraft to the center of the flux rope at closest approach. The average radius is determined to be ~ 450 km, or $\sim 0.18 R_M$. Figure 4.13b displays the distribution of B_0 , which has a mean magnitude of 41 nT. The final histogram in Figure 4.13 shows the average impact parameter, or the proximity of the spacecraft trajectory to the flux rope center, was ~ 0.116 . This value indicates that MESSENGER typically crossed slightly off-axis for these encounters. Our earlier criterion of constraining the Z'_{MSM} direction for accepted crossings most likely contributed to this low average impact parameter.

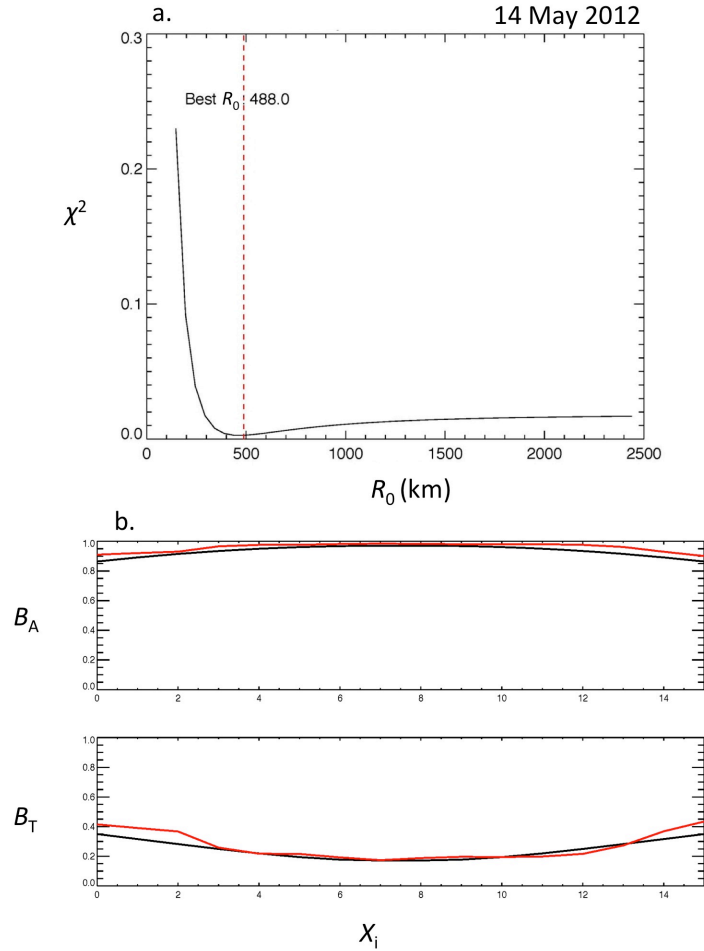


Figure 4.12: (a) The correlation between R_0 and χ^2 illustrates the least squares minimization for the 14 May 2012 flux rope example. The vertical dashed red line illustrated the point at which χ^2 is at its minimum value. This corresponds to a modeled radius of 488 km. (b) Example of the best-fit resulting from flux rope fitting for an event on 14 May 2012. Normalized magnetic field axial, B_A and tangential, B_T components are plotted to compare the data (red lines) and modeled (black lines) results. The minimized χ^2 value for this example is 0.003.

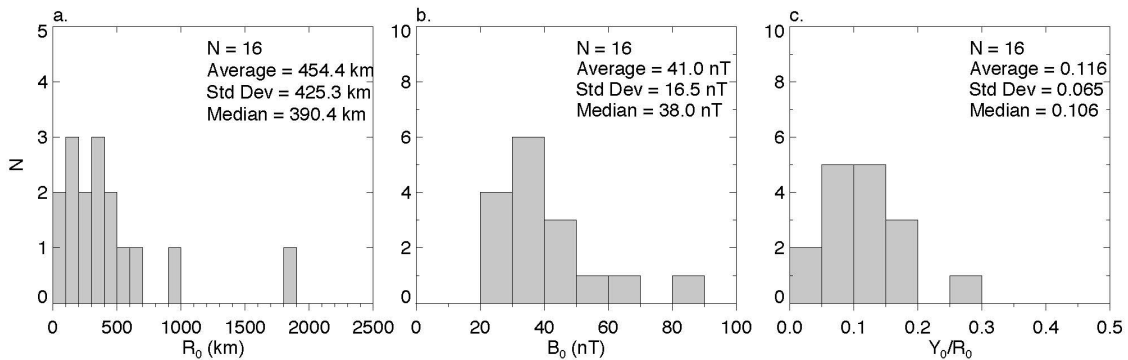


Figure 4.13: Histograms of the 16 accepted fits, with $\chi^2 \geq 0.01$ resulting from the flux rope fitting. (a) Flux rope radius, R_0 , determined using the χ^2 minimization technique. (b) Magnetic field magnitude of the flux rope core field, B_0 . (c) Impact parameter, Y_0/R_0 , describes the proximity of the spacecraft's trajectory to the center of the flux rope during the encounter.

4.5 Discussion

In this paper, we have identified and analyzed 49 plasma sheet flux ropes in Mercury's magnetotail. MVA has been applied to magnetic field measurements taken by the MESSENGER spacecraft as it crossed the current sheet between the north and south lobes of the tail. These flux ropes were identified in the MAG data and the ambient plasma sheet characteristics were determined with FIPS plasma measurements. A force-free flux rope fitting technique was implemented to model the flux rope magnetic fields using Bessel functions to estimate their size. This procedure enabled the identification of characteristic time and length scales of the recurring plasmoids in Mercury's magnetotail to be determined.

The size of flux ropes is estimated using the average duration of a flux rope encounter, 0.74 s (Figure 4.9), and the mean Alfvén speed determined from FIPS measurements, $\sim 450 \text{ km s}^{-1}$ (Figure 4.10d). By multiplying these values together, we calculate an average flux rope diameter of $\sim 330 \text{ km}$, or $\sim 0.13 R_M$. However, this result is most likely a lower limit on the size of flux ropes in Mercury's magnetotail for two reasons. First, the calculation assumes that the spacecraft has crossed directly through the center of the flux rope, which is not likely to be the case. This implies that the average duration is a lower limit estimate. Second, as stated earlier, the Alfvén speed is also a lower limit because as reconnection continues the plasma depleted field lines of the lobes will increase the outflow speed. For these reasons we conclude that the radius, R_0 , determined by the flux rope fittings (Figure 4.13a) to be a better estimate of size. The average R_0 is $\sim 450 \text{ km}$, or $0.18 R_M$. We compare this value to a proton gyroradius in the plasma sheet using the average proton temperature, 22.86 MK, and the typical magnetic field magnitude, 20 nT, in the plasma sheet. In Mercury's plasma sheet, a proton gyroradius is $\sim 400 \text{ km}$. Therefore, these plasma sheet flux ropes have radii that are on the order of one proton gyroradius.

At Earth, a superposed epoch analysis of the magnetic field signatures associated with tail flux ropes has been used to study the average phase and timescales of these events [e.g., *Imber et al.*, 2011; *Slavin et al.*, 2003a]. By implementing this analysis on Geotail data, *Slavin et al.* [2003a] determined the amplitude of the change in B_X , B_Y , and

B_Z components to be ~ 2 nT, 8 nT, and 11 nT, respectively, over a time domain of ± 120 s. Here, we perform a superposed epoch analysis on both NS and SN-type flux ropes. The results of this analysis are shown in Figure 4.14 where the inflection point of the B_Z perturbation was taken to be the epoch. This B_Z midpoint often corresponds to the peaks in the other field components and is therefore an easily reproducible technique. The time domains for both analyses at Mercury were ± 3 s, which is 40 times faster than the results at Earth.

Figure 4.14b displays the superpose epoch of 23 NS events with an enhancement in $|B_X|$, $|B_Y|$, and $|B|$ all coinciding with the bipolar B_Z signature and the midpoint is aligned with the 0 nT crossing. The peaks in $|B_X|$, $|B_Y|$, and $|B|$ measure to be ~ 9 nT, 8 nT, and 10 nT, respectively. The peak-to-peak amplitude in B_Z is ~ 20 nT and the duration measured between the local maxima is ~ 0.6 s. The background field of the plasma sheet, adjacent to the NS flux ropes, has a magnitude that is slightly less than 30 nT.

The extended southward ($-B_Z$) magnetic field following the NS flux ropes in the superposed epoch analysis (Figure 4.14b), known as the post-plasmoid plasma sheet (PPPS) [Richardson and Cowley, 1985; Richardson *et al.*, 1987], is the signature of continual reconnection between the open fields of the tail lobes after the plasmoid has been formed. This observation makes it possible to calculate the amount of lobe magnetic flux that has been detached and transported down the tail via reconnection. We compute this by integrating over the time it takes for the field to recover from the extended southward state back to $B_Z \sim 0$ nT:

$$\Phi_{PPPS}/L_Y = \int V B_Z dt \quad (4.3)$$

where Φ_{PPPS} is the total lobe flux per unit distance across the width of tail within the PPPS that has been reconnected preceding plasmoid release. L_Y is the length of the reconnection X-line in the cross-tail current sheet and V is the reconnection outflow speed. We measure a change of ~ 9 nT in B_Z magnitude between the active and recovered states. The interval is ~ 2.6 s in duration and we assume the reconnection outflow speed to be equivalent to the Alfvén speed, 450 km s^{-1} , determined from plasma measurements

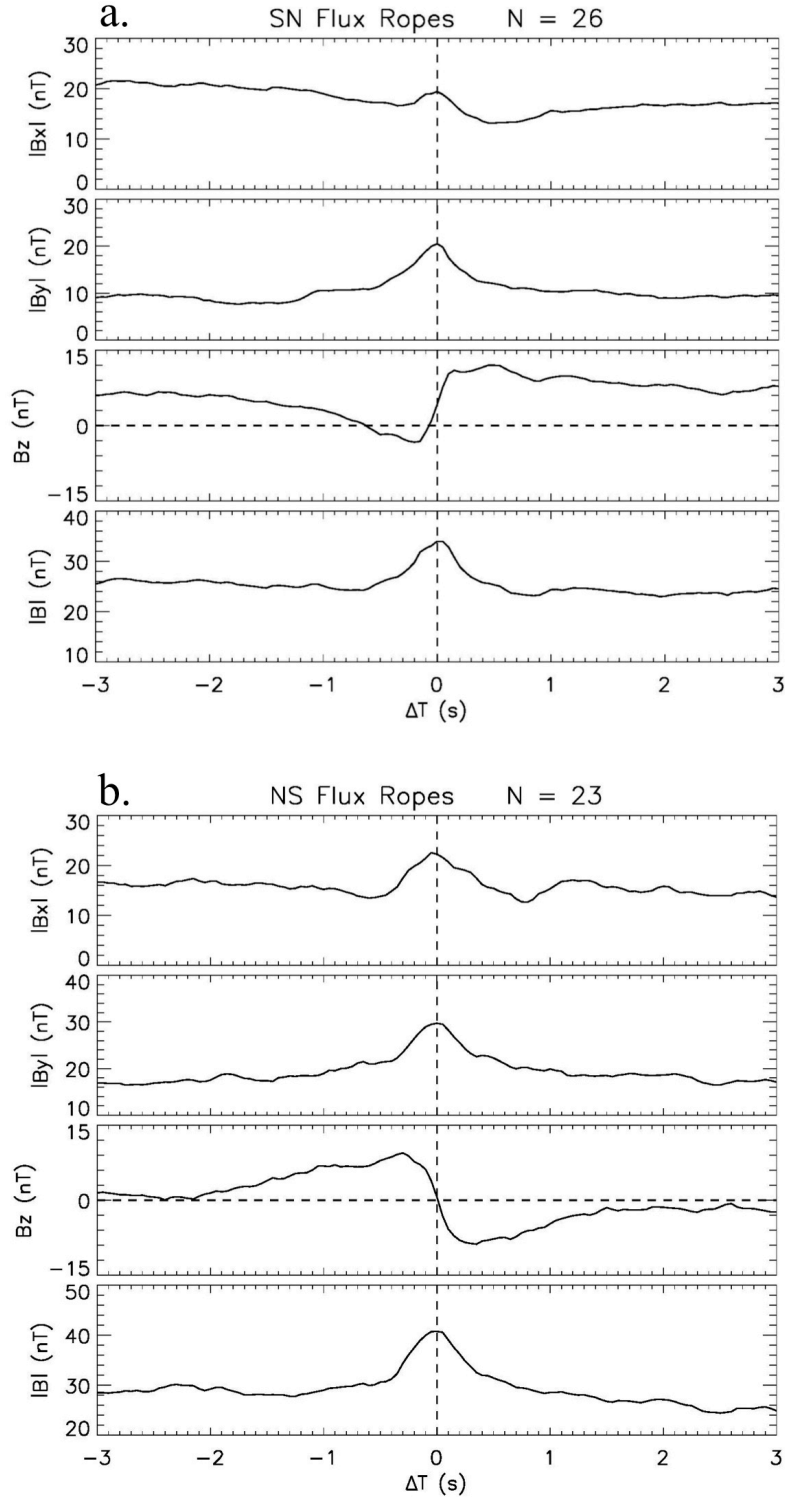


Figure 4.14: A superposed epoch analysis for (a) 26 SN planetward traveling flux ropes and (b) 23 NS tailward traveling flux ropes. The epoch is taken to be at the inflection point in the B_z bipolar signature.

(Figure 4.10d). Using Equation 4.3, we calculate Φ_{PPPS} to be ~ 0.011 MWb/m, or 0.026 MWb/ R_M . Assuming an X-line length of $3 R_M$ across the width of the tail, we conclude

that, on average, $\Phi_{\text{PPPS}} = 0.078$ MWb per plasmoid event. *Jackman et al.* [2011] performed this calculation on the PPPS in Saturn’s magnetotail and determined this value to range between 0.094–0.484 MWb/m. At Jupiter, *Vogt et al.* [2014] calculated the amount of flux in the PPPS to range from 1.24–1.60 Wb/m.

It is also possible to calculate the magnetic flux content inside these structures by utilizing the flux rope fitting results (Figure 4.13). Based on Faraday’s Law, the flux content is calculated by:

$$\Phi_{FR} = \left(\frac{1}{\alpha}\right) 2\pi B_0 R_0^2 J_1(\alpha) \quad (4.4)$$

where Φ_{FR} is the total flux content inside the plasmoid. B_0 is the magnitude of the core field and R_0 is the flux rope radius, both calculated by the fitting technique in Section 4. Using results from the 16 best-fit events, we calculated Φ_{FR} using Equation 4.4 and found the average flux content to be only ~ 0.002 MWb. The event with the largest amount of flux content measured to be ~ 0.011 MWb, only a fraction of the flux measured in the dayside FTEs by *Imber et al.* [2014]. Also, when comparing this value to the average Φ_{PPPS} we find that Φ_{FR} is negligible when describing the loss of flux via magnetotail reconnection.

It has been predicted that the direction of the flux rope core field ($\pm B_Y$) and the upstream IMF B_Y should be directly correlated [*Hughes and Sibeck*, 1987]. This theory suggests that as the tail lobes become sheared during periods of strong IMF B_Y , a B_Y component is generated in the current sheet [*Cowley*, 1981; *Sibeck et al.*, 1985], which will dictate the formation of the flux rope. *Moldwin and Hughes* [1992] tested this prediction using ISEE 3 magnetometer data and found that both the direction and strength of the B_Y components in the core field and IMF are strongly correlated. We have attempted to find a correlation between the directions of the core fields in our 49 events with the upstream IMF using 30 s average of the magnetic field just upstream of the magnetopause in the magnetosheath and upstream of the bow shock in the solar wind. A comparison revealed that there was no correlation between the core field B_Y and the upstream IMF B_Y both in the magnetosheath and solar wind. However, during hot season orbits the time between MESSENGER’s current sheet crossing and exiting the dayside

magnetosphere is ~ 1 h. Mercury’s Dungey cycle of ~ 2 min is much faster than this time scale and therefore, it is likely that the system has already responded to changing upstream IMF conditions making it difficult to measure any correlation between the IMF and flux rope core fields.

We conclude that frequent signatures of plasma sheet flux ropes indicate reconnection is often occurring at multiple X-lines in Mercury’s cross-tail current sheet. While they have a similar magnetic structure to flux ropes found at Earth, they exist on much shorter timescales. These durations are in agreement with Mercury’s Dungey cycle and intense dayside reconnection observations. As a result, the continual supply of plasma sheet flux ropes by reconnection contributes to the removal and circulation of flux in Mercury’s small, but extremely dynamic, magnetosphere.

4.6 Conclusions and Summary

MESSENGER observations provide an opportunity to investigate magnetic reconnection in the cross-tail current sheet of Mercury’s magnetotail. We use measurements collected by MAG FIPS during “hot seasons,” when the orbital periapsis is on Mercury’s dayside and MESSENGER crosses the plasma sheet at distances of ~ 1.5 to $3 R_M$. In the cross-tail current sheet, which separates the north and south lobes of the magnetotail, flux ropes are formed by reconnection at two or more X-lines and are then transported either toward or away from the planet by the Alfvénic flow emanating from the X-lines. A survey of the MAG measurements during seven MESSENGER hot seasons yielded 49 flux ropes, for which minimum variance analysis indicates that the spacecraft passed near the central axis of the structure. The flux ropes were observed between 1.7 and $2.8 R_M$ down the tail from the center of the planet. They are nearly evenly distributed between events with a north-then-south, NS (23 events), and south-then-north, SN (26 events), B_Z variation. Just as at the Earth, southward (northward) magnetic fields in the post-plasmoid plasma sheet following NS (SN) flux ropes indicative of anti-sunward (sunward) motion. The FIPS measurements indicated an average proton density of 2.55 cm^{-3} in the plasma sheet surrounding these flux ropes, implying an Alfvén speed of $\sim 450 \text{ km s}^{-1}$. Under the assumption that the flux ropes are

moving at the local Alfvén speed, we used the mean duration of 0.74 ± 0.15 s to calculate a typical diameter of $\sim 0.14 R_M$, or ~ 340 km. This compares with a proton gyroradius of ~ 400 km for the 22.86 MK mean temperature determined from FIPS. We have fit the magnetic signatures of the flux ropes with a force-free model in order to infer flux rope size, core field strength, and MESSENGER's proximity to the central axis. Good fits to the force-free model were found in 16 cases, which produced a mean flux rope radius of 450 km, or $0.18 R_M$, and core magnetic field of ~ 40 nT. A superposed epoch analysis demonstrates that the magnetic structure of the flux ropes is similar to what is observed at Earth, but the timescales are 40 times shorter at Mercury. The results of this flux rope survey indicate that intense magnetic reconnection occurs frequently in the cross-tail current layer of this small, but extremely dynamic magnetosphere. Similar to Earth, these structures play a significant role in the Dungey Cycle and may prove to have an even greater impact on the circulation of flux in Mercury's magnetospheric system.

CHAPTER V

FIRST OBSERVATIONS OF MERCURY'S PLASMA MANTLE AS SEEN BY MESSENGER

This chapter is taken from Gina A. DiBraccio, James A. Slavin, Jim M. Raines, Daniel J. Gershman, Patrick J. Tracy, Scott A. Boardsen, Thomas H. Zurbuchen, Brian J. Anderson, Haje Korth, R. L. McNutt Jr., and Sean C. Solomon (2014), First observations of Mercury's plasma mantle as seen by MESSENGER, manuscript in preparation.

Abstract

We present the first observations of Mercury's plasma mantle, a main source for solar wind entry into the planet's magnetosphere, located in the high-latitude magnetotail. The plasma mantle is created as reconnected fields, populated with solar wind plasma, convect downstream of the planet and rejoin the magnetosphere as part of the Dungey cycle. MESSENGER Fast Imaging Plasma Spectrometer (FIPS) and Magnetometer observations are analyzed for two orbits when a dense population of solar wind protons is detected just inside the tail magnetopause. Frequent flux transfer events are observed through the magnetosheath, cusp, and into the magnetosphere, suggesting that these magnetic structures are responsible for transporting solar wind plasma into Mercury's magnetosphere just as at Earth. The main plasma mantle features are: (1) decreasing plasma density as MESSENGER moves from the magnetopause deeper into the tail lobes and (2) a clear dispersion in the proton energy distribution observed by FIPS, indicating that low-energy protons are transported much deeper into the magnetosphere than the higher energy particles, which escape to large downtail distances before they can $E \times B$

drift deeper toward the plasma sheet. Using three-dimensional plasma distributions, protons are observed flowing antisunward with weighted average energies of 0.27 and 0.28 keV, corresponding to velocities of $\sim 230 \text{ km s}^{-1}$. Diamagnetic depressions, due to the presence of plasma, are observed in the magnetic field data and the field magnitude increases throughout the plasma mantle as the plasma disperses. The proton energy dispersion is used to infer a cross-magnetosphere electric potential of $\sim 20\text{-}30 \text{ kV}$, which supports the estimates made from the measurement of magnetopause structure [DiBraccio *et al.*, 2013].

5.1 Introduction

As the supersonic, super-Alfvénic solar wind streaming from the Sun interacts with Mercury’s intrinsic magnetic field, a magnetosphere is formed. Prior to the arrival of MESSENGER, which became the first spacecraft to orbit Mercury on 18 March 2011, our understanding of Mercury’s magnetosphere was restricted to *in situ* measurements from three flybys of the Mariner 10 spacecraft and limited ground-based observations [Ness *et al.*, 1974, 1975; Ogilvie *et al.*, 1974, 1977; Simpson *et al.*, 1974; Potter and Morgan, 1985, 1986]. Initially it appeared that Mercury’s magnetosphere is not unlike the Earth’s, operating with many of the same processes; however, MESSENGER observations continue to indicate that the magnetosphere of this planet is anything but ordinary. In order to understand why Mercury’s magnetosphere is unique, it is first important to recognize which factors dictate the overall structure and dynamics. The three main aspects that influence the properties of a planetary magnetosphere are: (1) the planet’s location with respect to the Sun, which sets the parameters of the ambient solar wind; (2) the strength and orientation of the intrinsic planetary magnetic field, which works to stand off the impinging solar wind; and (3) the attributes of the magnetospheric plasma environment, which dictate the time and length scales of the system. These characteristics have now been constrained at Mercury using MESSENGER observations:

(1) *Implications of the planet’s location with respect to the Sun:* As the closest planet to the Sun, Mercury is subjected to an extreme solar wind environment that varies over the course of its highly eccentric orbit, ranging between distances of 0.31–0.47 AU

away from the Sun. Mercury's proximity to the Sun leads to a local space environment of low plasma β , the ratio of plasma to magnetic pressure, and low Alfvénic Mach number (M_A), the ratio of the plasma's bulk speed to the local Alfvén speed. *Slavin and Holzer* [1979] predicted that these plasma parameters would enhance the erosion of flux by magnetic reconnection at the dayside magnetosphere. MESSENGER observations have confirmed that Mercury's low- β , low- M_A environment in the inner heliosphere promotes the formation of thick plasma depletion layers (PDLs) in the magnetosheath [*Gershman et al.*, 2013], which facilitates the frequent occurrence of magnetic reconnection for nearly all orientations of the IMF [*DiBraccio et al.*, 2013].

(2) *Strength and orientation of the intrinsic planetary magnetic field:* Measurements provided by the MESSENGER MAG [*Anderson et al.*, 2007] have indicated that Mercury's intrinsic magnetic field is nearly axial-aligned with a southward dipole moment of $195 \pm 10 \text{ nT} \cdot R_M^3$ (where R_M is Mercury's radius, or 2440 km) [*Anderson et al.*, 2011a]. This relatively weak field is able to shield the planet from the upstream solar wind with an average subsolar magnetopause standoff distance of $1.45 R_M$ [*Winslow et al.*, 2013]. With the magnetopause located only ~ 1000 km above Mercury's surface, the planet occupies a large volume of its magnetosphere, which has important implications for space weathering [see *Kabin et al.*, 2000; *Kallio et al.*, 2003, 2008; *Leblanc and Johnson*, 2003; *Massetti et al.*, 2003; *Leblanc et al.*, 2010]. Additionally, a northward offset of the planetary dipole by $\sim 0.2 R_M$ creates a north-south asymmetry in the magnetosphere [*Anderson et al.*, 2011a].

(3) *Attributes of the magnetospheric plasma environment:* Mercury lacks a substantial atmosphere; instead, it has only a surface-bounded exosphere. Because it is collisionless, Mercury's exosphere co-exists and overlaps spatially with the local space environment. In fact, the inner boundary of Mercury's magnetosphere is essentially the planetary surface itself. Planetary ions in Mercury's plasma environment primarily originate through interactions of solar wind ions with exospheric neutrals and the planetary surface [*Domingue et al.*, 2007; *Lammer et al.*, 2003]. Observations from MESSENGER's FIPS sensor [*Andrews et al.*, 2007] have shown that these planetary ions are most abundant near the surface but extend beyond the dayside bow shock [*Zurbuchen et al.*, 2008]. Although solar wind ions (i.e., H^+ and He^{2+}) account for more than 97% of

the ions seen by the FIPS sensor, an extensive examination of FIPS measurements indicates that the dominant planetary ions are Na⁺-group ions, grouped into mass-per-charge (m/q) ranges to improve signal to noise (Na⁺ group is $m/q = 21\text{--}30$ amu/e, including Na⁺, Mg⁺, and Si⁺) [Raines *et al.*, 2013]. Furthermore, recovered proton densities and temperatures in regions throughout the magnetosphere are consistent with expected values when scaled from Earth [Raines *et al.*, 2011].

The presence of solar wind ions in Mercury's magnetosphere has a substantial impact on the system and its dynamics. However, the means by which the solar wind is able to access Mercury's magnetosphere is a topic that has yet to be explored directly. The combination of Mercury's proximity to the Sun, weak intrinsic field that is frequently undergoing reconnection, and lack of a conducting ionosphere leads to a rapid circulation of plasma and magnetic flux [Hill *et al.*, 1976]. This large-scale magnetosphere convection, termed the Dungey cycle, provides several gateways by which solar wind plasma may enter the magnetosphere. A typical Dungey cycle takes only ~ 2 min at Mercury whereas this process is on the order of 1 h at Earth [Siscoe *et al.*, 1975; Slavin *et al.*, 2009, 2010], implying that plasma, both of solar and planetary origins, is constantly cycled through Mercury's system.

The Dungey cycle begins with the occurrence of magnetic reconnection at the dayside magnetopause where the sheared IMF and planetary field lines merge. This results in an open magnetic field with one end attached to the planet, through which planetary and solar wind plasmas may be exchanged. As the cycle continues the open field is convected around the magnetosphere by the anti-sunward magnetosheath flow until it eventually rejoins the magnetosphere in the tail. At this point, any solar wind plasma present on the field feels the cross-magnetosphere dawn-to-dusk electric field and begins to $\mathbf{E} \times \mathbf{B}$ drift towards the equatorial central plasma sheet. Therefore, the Dungey cycle provides two, albeit linked, channels for which the solar wind may enter into the magnetosphere: (1) promptly by flowing down newly open flux tubes directly into the cusps after reconnection has occurred between the IMF and the planetary field and (2) the transfer of open field lines, populated with both planetary and solar wind plasma, into the magnetotail.

As the open field lines are added to the high-latitude regions of the tail, solar wind plasma accumulates just inside the magnetotail, adjacent to the magnetopause. This boundary layer, known as the plasma mantle, is observed as a thick region of magnetosheath-like plasma flowing anti-sunward inside the high latitude magnetotail (Figure 5.1) [Rosenbauer *et al.*, 1975]. These charged particles follow trajectories that are the sum of this tailward, field-aligned flow and the $\mathbf{E} \times \mathbf{B}$ drift due to the cross-tail electric field. These particles all move toward the mid-plane of the tail, but the particles with the lowest field-aligned velocity will reach the plasma sheet closer to the Earth while those with higher tailward speeds will not do so before reaching much greater down tail distances. For example, at the Earth the plasma mantle particles with the lowest anti-sunward speeds may arrive in the plasma sheet at distances of only a 30 to 40 R_E downstream of the terminator plane while those with higher field-aligned speeds may not do so until $\sim 100 R_E$ or more [Rosenbauer *et al.*, 1975; Pilipp and Morfill, 1978; Sckopke and Paschmann, 1978; Slavin *et al.*, 1985]. The distance at which these mantle particles reach the plasma sheet is important because reconnection sites form in the plasma at ~ 20 to $30 R_E$ down the tail, especially during magnetospheric storms and substorms. The mantle plasma that reaches the plasma sheet Earthward of these reconnection X-lines will be convected back into the inner magnetosphere while those reaching the plasma sheet beyond these reconnection sites will continue to move down the tail to rejoin the solar wind [Cowley, 1980]. Of the particles that remain in the magnetosphere creating the plasma mantle, those with a higher parallel speed will reach farther distances down the tail than those with lower speeds. This particle dispersion causes the plasma mantle to expand with increasing distance down the tail, as shown in Figure 5.1. Based on this characteristic, studies using magnetohydrodynamic models tend to characterize the plasma mantle as a “slow-mode expansion fan” [e.g., Siscoe and Sanchez, 1987].

At Earth, the presence of a dense plasma mantle is correlated with southward IMF, confirming that it is reconnection-dependent, and vanishes during extended periods of northward IMF orientations [Sckopke, 1976; Sckopke and Paschmann, 1978]. Sibeck and Siscoe [1984] argued that FTEs are an important source of plasma for the mantle. FTEs are discrete helical bundles of magnetic flux produced as a result of simultaneous

reconnection occurring at multiple X-lines along the dayside magnetopause. FTEs are a vehicle for plasma exchange as they facilitate the mixing of magnetosheath and magnetospheric particles [Russell and Elphic, 1978, 1979; Daly et al., 1981]. Once a flux rope is formed, magnetosheath plasma may enter the magnetosphere while magnetospheric plasma can escape the system. Therefore, plasma characteristics inside these FTEs are observed to have values between the densities and temperatures of the adjacent magnetosphere and magnetosheath regions [e.g., Paschmann et al., 1982; Le et al., 2008]. As the FTEs circulate with one end attached to the planet, following the circulation of the Dungey cycle, this mixture of plasma will populate new regions of the magnetosphere.

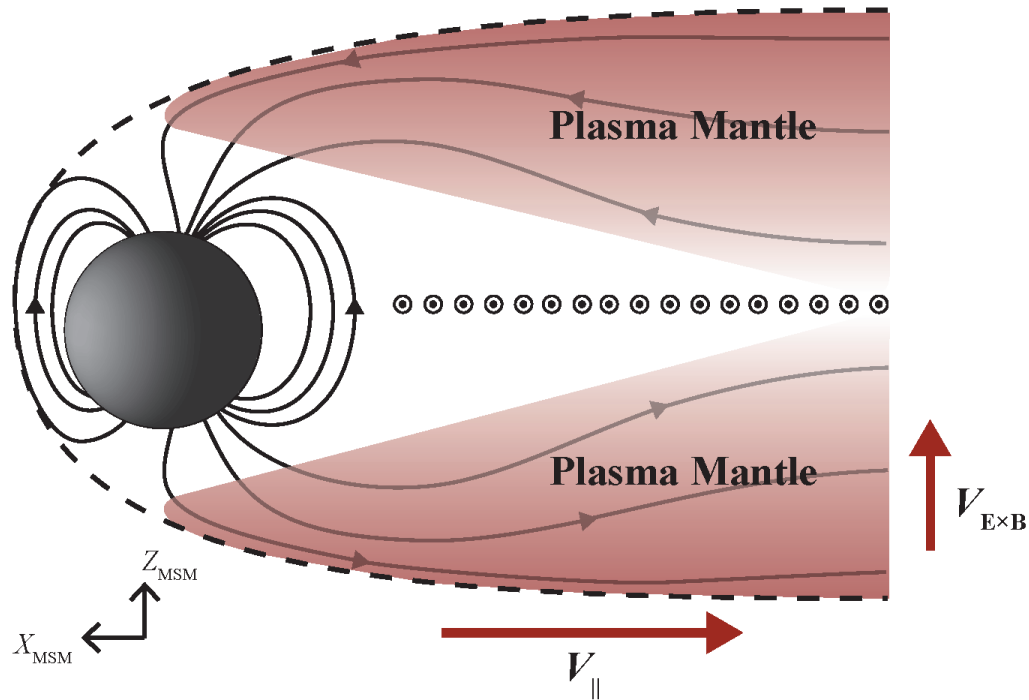


Figure 5.1: Schematic of Mercury's magnetosphere with the plasma mantle located in the high-latitude magnetotail (red shaded region). The planetary magnetic field and its orientation are represented indicated by black lines and arrows, along with the magnetopause boundary (dashed line) and the cross-tail current sheet (\odot). Solar wind particles enter along open field lines near the dayside with a velocity parallel to the magnetic field (V_{\parallel}). As the particles feel the effects of the cross-tail electric field they will $E \times B$ drift toward the central plasma sheet, surrounding the current sheet, at a velocity of $V_{E \times B}$. The particles disperse as low-energy particles drift deeper into the magnetosphere and higher energy particles flow further downstream.

FTEs were identified during the MESSENGER flybys of Mercury [Slavin et al., 2008, 2009, 2010] and they are undoubtedly playing a crucial role in the dynamics of

Mercury's magnetosphere. *Slavin et al.* [2012] reported observations of "FTE showers" which include ~ 25 min intervals of continuous flux rope encounters as the structures, originating on the dayside, circulate around the planet and make their way down the magnetotail. In this study, the FTE durations lasted only $\sim 2\text{--}3$ s with $\sim 8\text{--}10$ s separations between each individual event [*Slavin et al.*, 2012]. This direct observation of frequent FTEs moving down Mercury's tail suggests that they may have an important affect on plasma transport and circulation in Mercury's magnetosphere.

Mercury's plasma mantle has yet to be explored; however, understanding this region, which is comprised of solar wind plasma that has accessed Mercury's magnetosphere, is crucial. Solar wind entry has significant implications for both the generation of planetary ions, produced as solar wind particles interact with Mercury's exosphere and surface, as well as the time and length scales of processes occurring in the system (e.g., reconnection). Fortunately, MESSENGER's nearly-polar orbit (discussed in Section 5.3) is ideal for studying this high-latitude boundary layer in Mercury's magnetotail.

We present the first observations of Mercury's plasma mantle using plasma and magnetic field measurements provided by MESSENGER. The analysis of two successive orbits on 10 November 2012 confirm the existence of a robust plasma mantle based on the identification of a dense population of solar wind protons inside the high-latitude magnetotail. The duration of these two events were 16 and 21 min and a clear dispersion in the energy distribution, representing the slow mode expansion fan, is observed. Additionally, frequent FTEs are identified throughout the magnetosheath and plasma mantle for both cases, suggesting that the occurrence of intense dayside reconnection encourages the generation of the plasma mantle. In the subsequent sections we describe the instrumentation and data used to analyze these events, followed by an overview of the orbits on 10 November 2012 and a detailed description of both plasma mantle encounters. Finally, we discuss the conclusions and inferences determined from these initial plasma mantle observations, which help us to better understand Mercury's dynamic magnetosphere.

5.2 Instrumentation and Data

MESSENGER plasma and magnetic field observations from FIPS and MAG have been analyzed to assess the first observations of Mercury's plasma mantle. In this study we are utilizing FIPS proton observations at the full 10 s resolution. To complement the plasma measurements and further character Mercury's plasma mantle, MAG data was analyzed at its maximum resolution of 20 vectors per second.

FIPS measures ions with an E/q ratio between 0.046–13.3 keV/e and m/q up to 60 amu/e. The time required for a scan through the entire E/q range is ~ 10 s. Roughly 0.25π sr of FIPS' 1.4π sr instantaneous FOV is blocked due to its position behind MESSENGER's sunshade. The sensor has an approximate angular resolution of 15° . We refer the reader to *Raines et al.* [2011, 2013] and *Gershman et al.* [2013] for further details regarding FIPS plasma measurements and instrument constraints.

In order to evaluate plasma dynamics and characteristics in Mercury's plasma mantle, we analyze the three-dimensional observed angular and energy distributions of protons, provided by FIPS measurements. The proton energy spectrogram (in units of flux: counts $s^{-1} cm^{-2} sr^{-1} kV^{-1}$) is used to determine when MESSENGER has crossed the magnetopause, exiting the magnetosheath and entering the magnetosphere, as well as identify the extent of the plasma mantle boundary layer. We also provide calculations of the pitch angle distribution (PAD), determined from the angle between the velocity and magnetic field vectors.

In order to create an all-sky map view of proton flow direction histograms we transform the FIPS observations into a discretized non-detector-based coordinate system. However, after re-binning the histograms in the new coordinate system, it is not guaranteed that each bin was sampled for the same duration. To adjust for this inconsistency, a bin-dependent time normalization, based on the total accumulation time of each visible pixel on the FIPS detector, is applied to the histograms [*Raines et al.*, 2014; *Gershman et al.*, 2014].

For the orbits of interest on 10 November 2012, MESSENGER was located in the pre-midnight sector as it moved through the magnetotail (discussed in Section 5.3). A rotation of the MESSENGER spacecraft oriented FIPS such that it was able to observe

plasma flowing antisunward and duskward, which is ideal for plasma mantle flows in this pre-midnight region.

5.3 Plasma Mantle Observations

The two plasma mantle events reported in this study were observed on 10 November 2012. At this time, Mercury was located 0.34 AU from the Sun and was approaching orbital periapsis. Using the planet’s orbital velocity of $\sim 54 \text{ km s}^{-1}$ at this point along its highly eccentric orbit, we are able to estimate a solar wind aberration angle of 7.2° by assuming a typical solar wind speed of 425 km s^{-1} .

The two events took place during MESSENGER’s extended mission when the orbital period was 8 h, reduced from the original 12-h orbit of the primary mission. These 8-h orbits on 10 November 2012 occurred during a MESSENGER “hot season,” when orbital periapsis is on Mercury’s dayside and the spacecraft experiences high thermal inputs from the planet. During these hot-season orbits, MESSENGER first crosses the bow shock and enters the magnetosheath downstream of the planet. The spacecraft then enters the magnetosphere at distances of several R_M behind the planet before continuing through the southern lobe of the tail as it approaches the plasma sheet. Therefore, hot season orbits are useful when identifying Mercury’s plasma mantle for two main reasons: they provide the most distant measurements in the magnetotail and they survey the high-latitude tail region where the plasma mantle is expected to form.

Figure 5.2 displays the part of the orbit trajectories on 10 November 2012, along with the average magnetopause location from *Winslow et al.* [2013], in aberrated Mercury solar magnetospheric (MSM’) coordinates. In this coordinate system, where the prime symbol indicates a correction for solar wind aberration, the X'_{MSM} axis is directed from Mercury’s offset magnetic dipole toward the center of the Sun, the Z'_{MSM} axis is normal to Mercury’s orbital plane, and the Y'_{MSM} axis is positive in the direction opposite orbit motion and completes the right-handed system.

Figure 5.2a provides a view from the Sun in the $Y'_{\text{MSM}}-Z'_{\text{MSM}}$ plane, which shows that MESSENGER is measuring the pre-midnight and pre-noon regions of the

magnetosphere. For this particular day, periapsis was located near 07:30 LT. A meridional view in Figure 5.2b illustrates that MESSENGER is expected to enter the magnetosphere at a distance $< 2 R_M$ down the tail in the X'_{MSM} direction. Roughly 90 min later, the spacecraft will exit the magnetosphere at latitudes above the subsolar point. The exact locations where MESSENGER enters and exits Mercury's magnetosphere for each orbit will vary depending on conditions in the magnetosheath because the magnetopause will adjust according to changes in solar wind pressures.

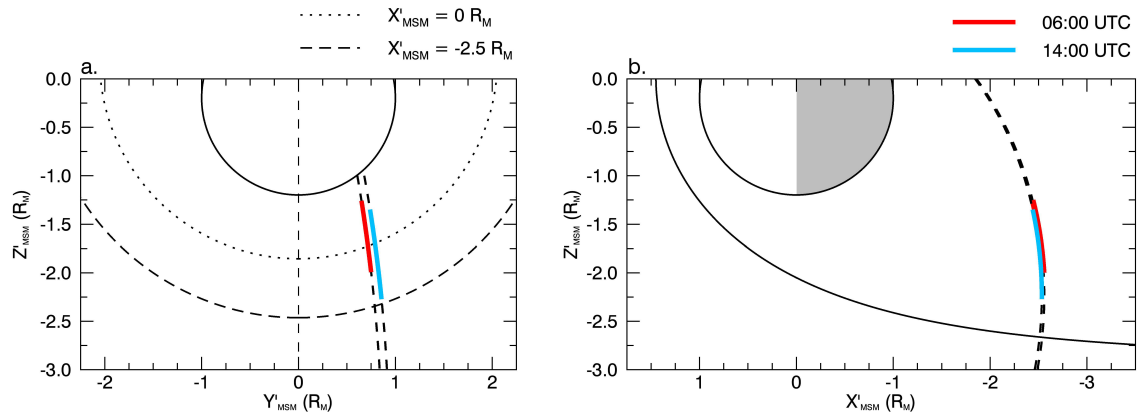


Figure 5.2: MESSENGER orbit and plasma mantle observations are shown in aberrated MSM coordinates. (a) The view from the Sun where the model magnetopause is indicated at the terminator, $X'_{MSM} = 0 R_M$, (dotted line) and at $X'_{MSM} = -2.5 R_M$ (dashed line). (b) The meridional view where the model magnetopause location is indicated by the solid line. In both plots, the thick dashed lines display MESSENGER orbits on 10 November 2012. The extent of the orbit when the plasma mantle was observed is highlighted in red for the 06:00 UTC orbit and blue for the 14:00 UTC orbit.

The locations where MESSENGER encountered the plasma mantle in Mercury's southern tail lobe for the 06:00 (red) and 14:00 (blue) orbits on 10 November 2012 are displayed in Figure 5.2. The top panel (Figure 5.2a) gives a perspective looking from the Sun to Mercury, in aberrated MSM coordinates, where the average magnetopause location is shown for the terminator plane, or $X'_{MSM} = 0 R_M$ (dotted line), and at $X'_{MSM} = -2.5 R_M$ (dashed line). Figure 5.2b shows the location of the mean magnetopause and the identified boundary crossings in cylindrical MSM' coordinates. For these two orbits, the magnetosphere is observed to be slightly compressed compared to the average location of the magnetopause, which indicates a higher solar wind pressure in the magnetosheath.

5.3.1 10 November 2012: 0600 UTC Orbit

During the first orbit on 10 November 2012, MESSENGER crossed the tail bow shock at ~05:09 UTC at a radial distance of $4.89 R_M$ away from the planet. As the orbit progressed through the magnetosheath, a series of FTEs were observed as high fluctuations in the magnetic field data. The magnetopause was encountered ~90 min after the bow shock crossing at 06:33:35 UTC when the spacecraft was located at a radial distance of $3.30 R_M$ away from the planet. Figure 5.3 provides a 30-min overview of the magnetic field and plasma observations spanning from the tail magnetosheath into Mercury's southern lobe. From the top panel down, this figure displays FIPS measurements of differential flux (in units of $(\text{cm}^2 \text{ s sr keV})^{-1}$), calculated PAD, and observed proton counts. The next three panels show the magnetic field components measured by MAG, and the bottom panel is the magnetic field magnitude. PADs are plotted in 15° bins, which is comparable to the angular resolution of FIPS; however, this measurement provides limited information due to the ~10 s scan time of FIPS compared with the magnetic field fluctuations, largely due to FTEs [see *Slavin et al.*, 2009, 2012] occurring on the order of 1 s or less. The white lines plotted in the energy and PAD spectrums represent the weighted averages, which have been smoothed in order to identify trends in the plasma mantle. The vertical dashed red lines mark the beginning and end of the plasma mantle. Note that the plasma mantle begins at the magnetopause.

From 06:25 UTC until MESSENGER encountered the magnetopause, the IMF in the magnetosheath was predominant in the $-B_X$ and $+B_Y$ directions with a magnitude of ~46 nT. The high-frequency variations in the magnetic field are FTEs that were formed at the dayside magnetopause via multiple X-line reconnection [*Slavin et al.*, 2012; *Imber et al.*, 2014] and pulled into the tail by the solar wind as part of the Dungey cycle convection. These variations in the data were confirmed to be FTEs based on their bipolar signatures, signifying a helical field topology, coincident with a peak in field magnitude that is indicative of a strong axial core field. FIPS measurements in the magnetosheath show a constant spread in proton energies with the peak energy of 0.39 keV, illustrated by the weighted average in the E/q spectrum (white line), corresponds to a solar wind velocity of $\sim 275 \text{ km s}^{-1}$. Throughout the magnetosheath the PADs vary due

to the magnetic field, which is constantly changing direction. The total proton counts remain relatively constant, measuring above 100 counts per scan.

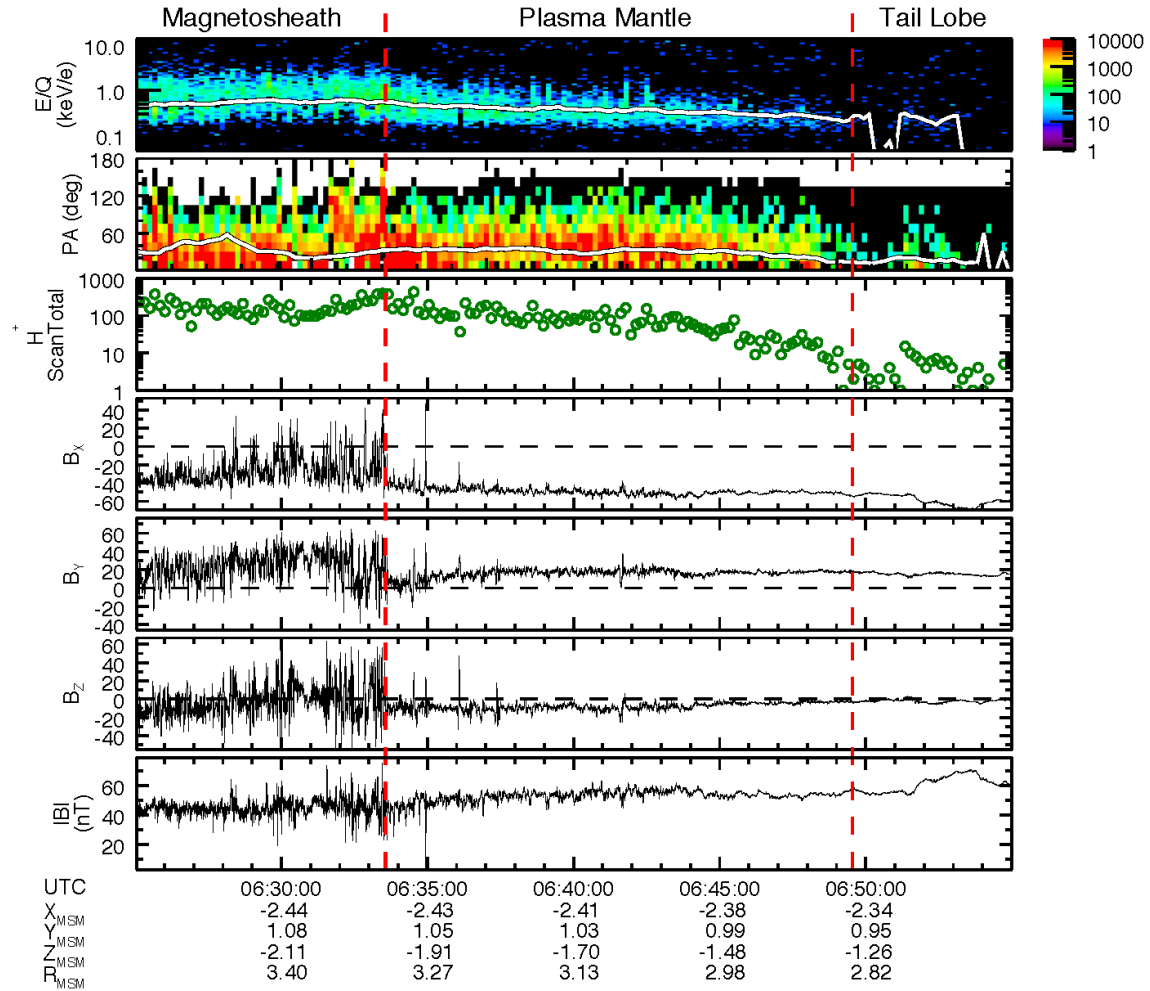


Figure 5.3: MESSENGER FIPS and MAG measurements taken during the inbound magnetopause crossing during the 06:00 orbit on 10 November 2012. The vertical red dashed lines represent the beginning and end of the plasma mantle. The beginning of the plasma mantle (first vertical red dashed line) is also the magnetopause crossing. The magnetosheath, plasma mantle, and tail lobe regions are labeled at the top. Shown from top to bottom is the: proton energy spectrogram in units of flux ($\text{counts s}^{-1} \text{cm}^{-2} \text{sr}^{-1} \text{kV}^{-1}$); proton pitch angle distribution (normalized units); total proton counts; magnetic field components B_x , B_y , B_z ; and total field magnitude. The white line in the top two panels represent the running weighted averages of the proton energy (top panel) and calculated pitch angle (second panel from the top).

MESSENGER crossed the tail magnetopause and entered the magnetosphere at 06:33:35 UTC, which is identified by a rotation in all three field components along with an overall reduction in FTE activity (vertical red line Figure 5.3). The total magnitude of the field, however, remained relatively constant across the boundary, indicating that

plasma and magnetic field pressures did not change drastically. A shift in the plasma energy distribution and a slow decrease in observed proton counts confirm that MESSENGER crossed the magnetopause. Despite these shifts observed in the FIPS data, the plasma observed remains continuous and has similar characteristics compared to the population in the magnetosheath; therefore, we are observing solar wind that has entered into the magnetosphere.

The 16 min interval between the vertical red lines in Figure 5.3, from 06:33:35 – 06:49:33 UTC, marks the region just inside Mercury’s tail magnetopause where solar wind plasma is observed. This is Mercury’s plasma mantle observed by MESSENGER as it traversed from a radial distance of $3.30 R_M$ to $2.83 R_M$ moving deeper into Mercury’s tail. Throughout the plasma mantle we observe high proton fluxes with characteristics intermediate to magnetosheath and magnetospheric values. The mantle’s main feature is the dispersion in proton energy, which confirms the plasma transition from a plasma population with characteristics that are reminiscent of the hot, nearly supersonic magnetosheath solar wind to a magnetosphere-like plasma with lower energy, temperature, and flux. Additionally, the proton counts, shown in the third panel from the top in Figure 5.3, are observed to steadily decrease from values >100 counts per scan, analogous to magnetosheath observations, down to $\sim 1-10$ counts which is typical of the magnetospheric tail lobe and matches the measurements observed in the tail lobe region of Figure 5.3. This transition of the solar wind plasma with distance from the magnetopause is due to the $\mathbf{E} \times \mathbf{B}$ drift of the protons toward the central plasma sheet while the hotter protons are able to escape further down the tail. Therefore, the less energetic particles will penetrate further into the magnetosphere at a given downtail distance and are observed as the spacecraft continues along its trajectory.

Throughout the plasma mantle, the magnetic field magnitude increases from $\sim 46-60$ nT as the plasma disperses. The field orientation is dominantly in the $-B_X$ direction, indicative of the antisunward-directed field in the southern lobe, which is confirmed by the relatively constant distribution of the pitch angles between $\sim 20-40^\circ$ (second panel from the top in Figure 5.3). Once again, we must take care when assessing the PADs as the calculations are limited by the 15° angular resolution of FIPS. FTE signatures are identified along the extent of this boundary layer as they provide a mechanism for the

solar wind to access the magnetosphere. Passing FTEs are also detected indirectly by the presence of lobe fields that are locally compressed as they drape around a FTE moving down the tail, known as traveling compression regions (TCRs) [see *Slavin et al.*, 2012]. TCRs exhibit a bipolar fluctuation in the magnetic field data, reminiscent to that of the FTEs; however, the transition is typically smoother with a subtle peak in the field magnitude.

In order to assess the average proton kinetic properties within this region, we examine the plasma flow direction and the energy distribution. Figure 5.4 displays the accumulation of three-dimensional FIPS proton measurements in the plasma mantle between 06:33:35 – 06:49:33 UTC. The all-sky map in Figure 5.4a presents a histogram of proton flow direction divided into 10° angular bins, which is the digital resolution measured by FIPS, with units of integrated flux ($\text{cm}^{-2} \text{s}^{-1} \text{sr}^{-1}$). In this frame, a translation has been applied to the MSM coordinate system such that it is centered on the FIPS instrument (aperture) rather than the planetary dipole but its orientation remains the same. Therefore, this all-sky map represents the view from the Sun along the $-X_{\text{MSM}}$ direction. As demonstrated by the white bins in the map that indicate regions that were not sampled, the FIPS FOV is partially obstructed by the spacecraft and its sunshade. To account for the coordinate system translation and any sampling biases, these plots are normalized for viewing time and projection effects. The average direction of the magnetic field during this interval is indicated by the pink \times symbol. Figure 5.4b shows energy distribution slices of the protons integrated over the duration of the plasma mantle. *Raines et al.* [2014] and *Gershman et al.* [2014] provide further details regarding the all-sky map and energy distribution analysis techniques.

The magnetic field was located at the edge of the FIPS FOV during this plasma mantle encounter; however, assuming gyrotropy, the proton distribution in Figure 5.4a peaks around the magnetic field confirming that the plasma is field-aligned and flowing in an antisunward direction. This type of flow pattern is expected for solar wind plasma that has entered the magnetosphere along the open field lines in the tail. The energy distribution slices show a peak in the plasma mantle proton energy at 0.28 keV, indicating a speed of $\sim 230 \text{ km s}^{-1}$ during this period.

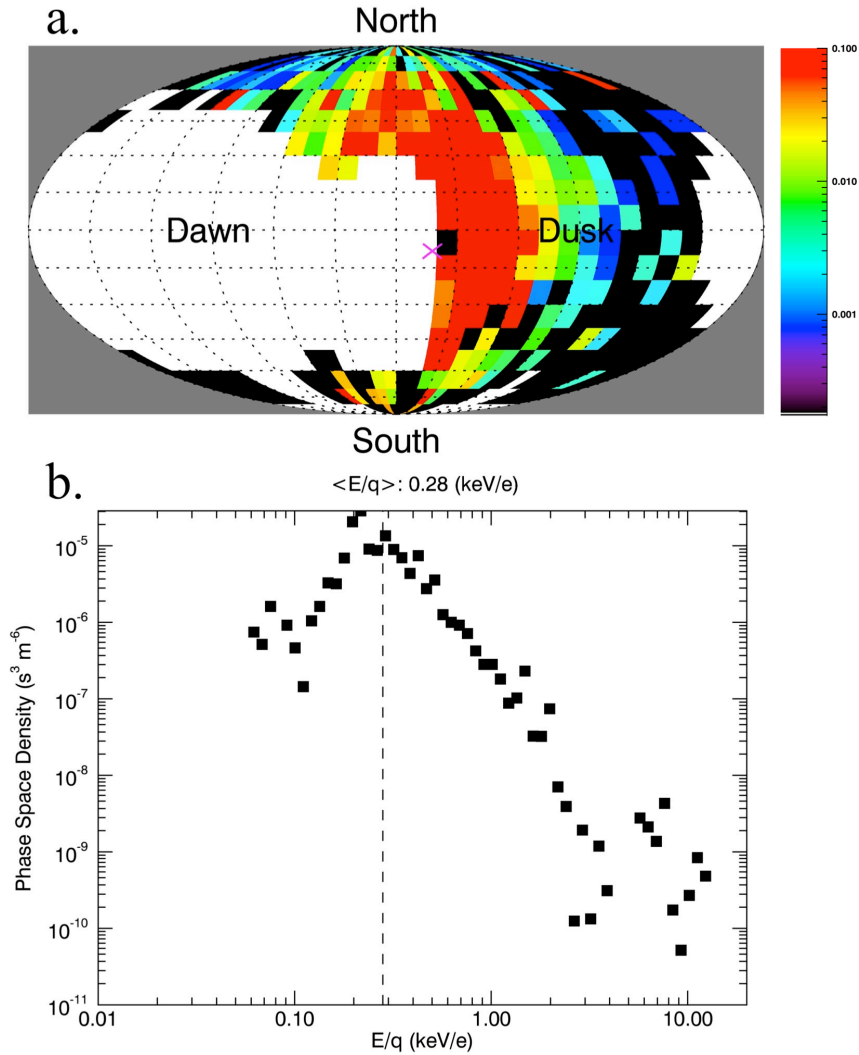


Figure 5.4: Kinetic properties of protons within the plasma mantle for the 06:00 UTC orbit on 10 November 2012. (a) The angular flux distribution map, in units of integrated flux ($cm^{-2} s^{-1} sr^{-1}$), indicates flow direction for protons. The average direction of the magnetic field during the plasma mantle encounter is indicated by the pink \times symbol. On this map, the white bins are unobserved and black bins are no measurements. Integrated flux has been normalized to 1. (b) Phase space density as a function of energy per charge (E/q). The vertical dashed line marks the weight average energy of the observed protons. See text for details.

The plasma mantle diminished by 06:49:33 UTC (second vertical red line) when MESSENGER was well within the southern lobe located at a radial distance of $2.83 R_M$ away from the planet. Only very low fluxes of protons are detected, which is typical of the low- β tail lobes, and the magnetic field is quiet without the presence of FTEs. The dominant B_X component measures ~ 50 nT, with a slight influence of ~ 15 nT in the B_Y direction while B_Z approaches zero.

5.3.2 10 November 2012: 1400 UTC Orbit

MESSENGER encountered the tail bow shock at $\sim 13:36$ UTC, during the second orbit on 10 November 2012, when the spacecraft was positioned $4.52 R_M$ away from the planet. Similar to the previous orbit, the magnetosheath is heavily populated by FTEs that have made their way down the tail after being formed by dayside magnetopause reconnection. A 35-minute overview of MAG and FIPS measurements beginning during the magnetosheath traversal is displayed in Figure 5.5. At the beginning of this interval until the magnetopause crossing at $14:26:41$ UTC, the solar wind proton energies in the magnetosheath have a weighted average of ~ 0.45 keV (white line in E/q spectrogram), which corresponds to a velocity of ~ 295 km s $^{-1}$. The proton number of protons detected by FIPS remain around ~ 100 counts per scan throughout the magnetosheath. The IMF was orientated primarily in the $-B_X$ direction, with a slight tilt in the $+B_Y$ and $-B_Z$ directions and an average magnitude of ~ 34 nT.

A dense proton population forming the plasma mantle is present for an interval of 21 min succeeding the magnetopause crossing. Resembling the signatures from the previous orbit, the energy distribution of the solar wind inside the high-latitude magnetotail begins to disperse with distance from the magnetopause. At the beginning of the plasma mantle (first vertical red line on Figure 5.5), proton energies are measured to be identical to the magnetosheath solar wind. However, as the measurements progress away from the magnetopause and closer to the plasma sheet, a clear dispersion in the proton energy is observed. The lower limit of the energy distribution remains constant as these low-energy protons $\mathbf{E} \times \mathbf{B}$ drift toward the center of tail. The upper limit of the observed energies steadily decreases as the high-energy protons have escaped further down the tail along the lobe fields. Therefore, the plasma population measured throughout the plasma mantle becomes cooler throughout this dispersion. The PADs appear to slightly increase with time, which may be an indicator of the low-energy particles drifting toward the central magnetotail; however, resolution constraints make it difficult to draw a conclusion based on this observation.

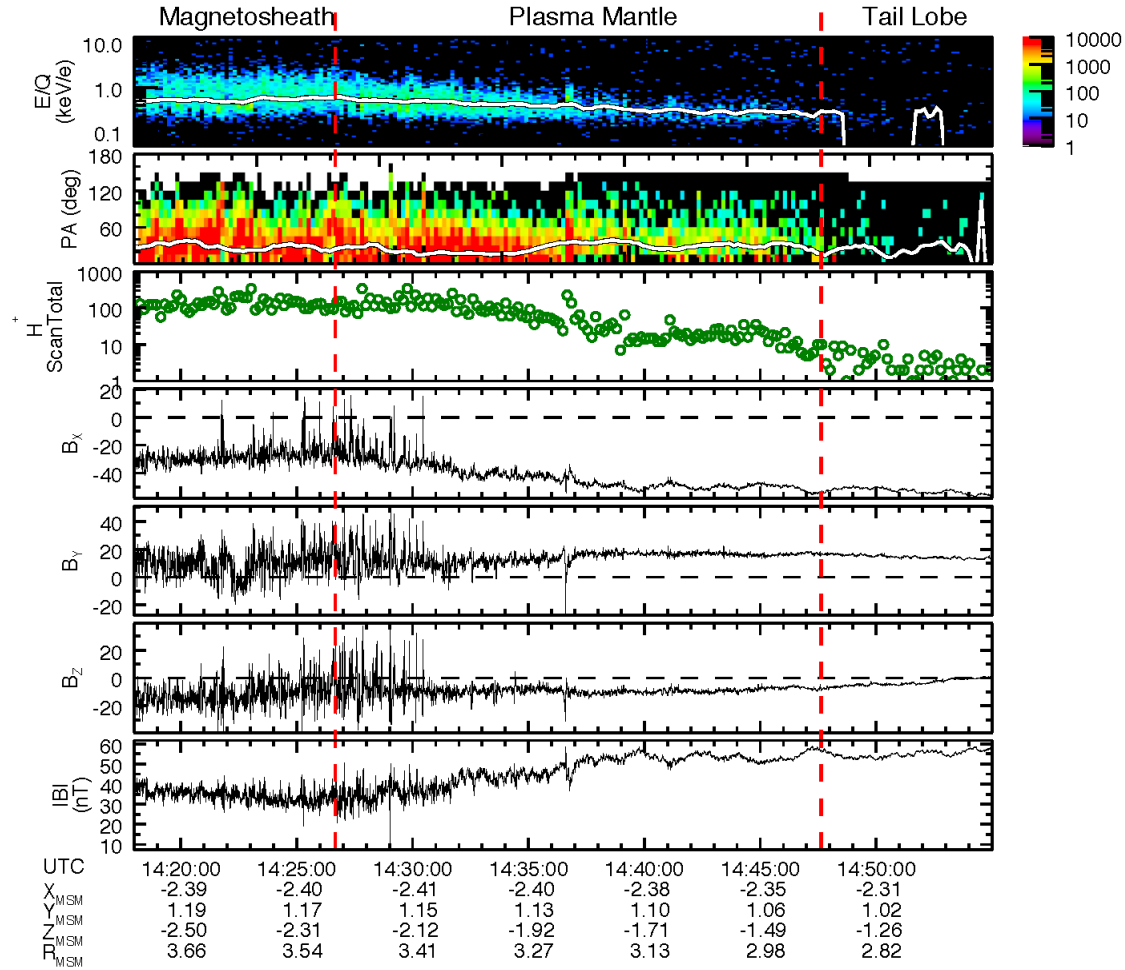


Figure 5.5: MESSENGER FIPS and MAG measurements taken during the inbound magnetopause crossing during the 14:00 orbit on 10 November 2012. The vertical red dashed lines represent the beginning and end of the plasma mantle. The beginning of the plasma mantle (first vertical red dashed line) is also the magnetopause crossing. The magnetosheath, plasma mantle, and tail lobe regions are labeled at the top. Shown from top to bottom is the: proton energy spectrogram in units of flux ($\text{counts s}^{-1} \text{cm}^{-2} \text{sr}^{-1} \text{keV}^{-1}$); proton pitch angle distribution (normalized units); total proton counts; magnetic field components B_x , B_y , B_z ; and total field magnitude. The white line in the top two panels represent the running weighted averages of the proton energy (top panel) and calculated pitch angle (second panel from the top).

The proton counts (third panel from the top in Figure 5.5) show a clear decrease as MESSENGER moves through the mantle toward lower latitudes. Initially, the measured counts are equivalent to magnetosheath values but these values decrease as the plasma disperses until the count rates are comparable to tail lobe measurements. This weakening plasma pressure means that the plasma's diamagnetic effect also diminishes, which causes the field magnitude to simultaneously increase. The field measures to be ~ 34 nT just inside the magnetopause and continues to increase to ~ 57 nT until it becomes relatively constant. FTEs are prevalent throughout the extent of the plasma

mantle, suggesting that these structures are supplying the region with solar wind plasma. The large-amplitude FTE signatures continue through the plasma mantle until $\sim 14:30:30$ UTC. At this time, we observe bipolar signatures of lower magnitude, which are the TCR signatures of locally compressed lobe fields as FTEs pass by.

The average proton kinetic properties measured by FIPS during the plasma mantle encounter between 14:26:41 – 14:47:39 UTC are presented in Figure 5.6. Using three-dimensional FIPS measurements, a histogram of plasma flow direction is projected onto

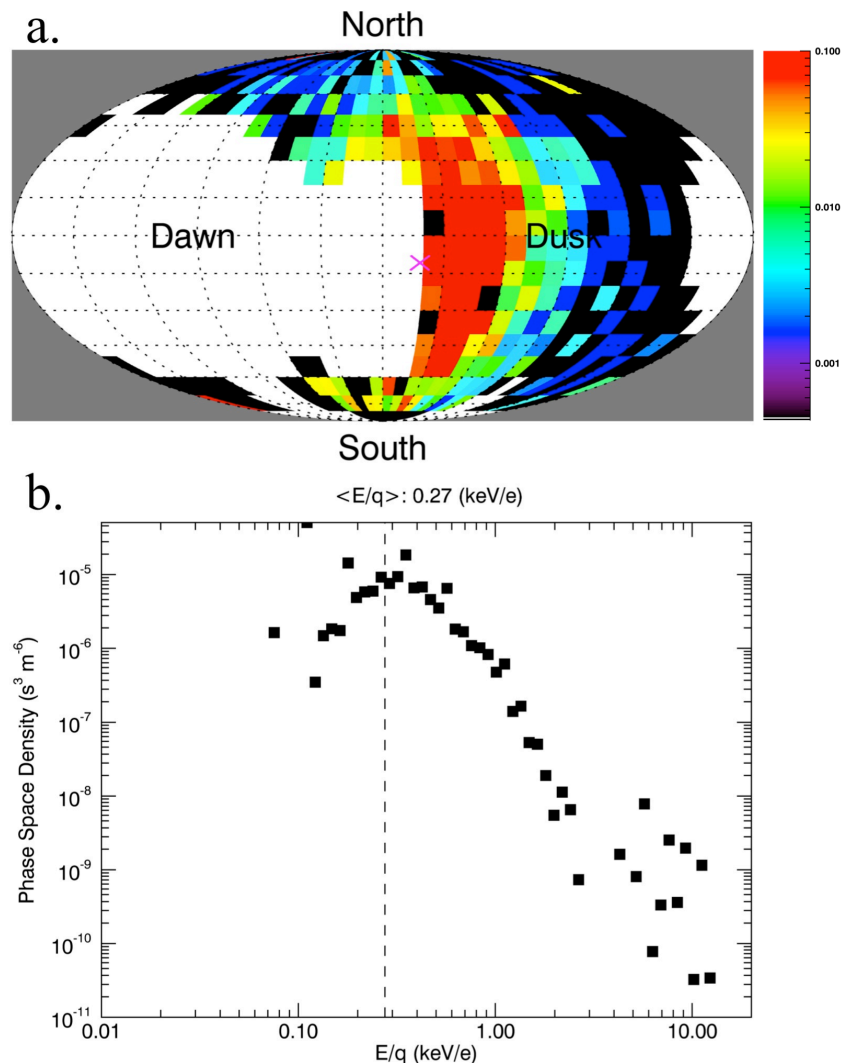


Figure 5.6: Kinetic properties of protons within the plasma mantle for the 14:00 UTC orbit on 10 November 2012. (a) The angular flux distribution map, in units of integrated flux ($\text{cm}^{-2} \text{s}^{-1} \text{sr}^{-1}$), indicates flow direction for protons. The average direction of the magnetic field during the plasma mantle encounter is indicated by the pink \times symbol. On this map, the white bins are unobserved and black bins are no measurements. Integrated flux has been normalized to 1. (b) Phase space density as a function of energy per charge (E/q). The vertical dashed line marks the weight average energy of the observed protons. See text for details.

the all-sky map, using 10° angular bins, in Figure 5.6a. This projection corresponds to the point of view from the Sun along the $-X_{\text{MSM}}$ direction and the white bins were outside of the FIPS FOV during this period. The average magnetic field direction, indicated by a pink \times , was once again on the edge of the FOV. Analogous to the previous orbit, the proton distribution appears to peak around the magnetic field, with the gyrotropic distribution assumption, which verifies a field-aligned flow moving antisunward. This bulk motion of solar wind plasma inside the high-latitude magnetotail, flowing away from the planet, is representative of the plasma mantle. Figure 5.6b shows the slices through the energy distributions for the plasma sheet protons with a peak at 0.27 keV, correlating to a velocity of $\sim 230 \text{ km s}^{-1}$.

The proton flux is substantially reduced as the boundary layer diffuses and MESSENGER reaches the tail lobe at 14:47:39 UTC (second red line Figure 5.5). In the lobe, the field magnitude remains constant between $\sim 55\text{--}60 \text{ nT}$ where it is directed in the antisunward direction ($-B_x$) and only a slightly skewed toward dusk ($+B_y$). Here the field fluctuations are minimal since the level of activity is considerably decreased without the presence of plasma.

5.4 Cross-magnetosphere Electric Potential

The bulk motion of the plasma toward the central plasma sheet can provide an estimate of the cross-magnetosphere electric potential (Φ_{Tail}), providing a measurement of solar wind transferred into the magnetosphere. This is accomplished by first estimating the convective electric field E_{conv} , based on the $\mathbf{E} \times \mathbf{B}$ drift motion of the particles. We determine E_{conv} from our measurements using two different approaches. In the first method, we use the frozen-in flux condition, $E_{\text{conv}} = -V_{\text{E} \times \text{B}} \times B$, where $V_{\text{E} \times \text{B}}$ is the velocity component of the particle drift toward the plasma sheet ($V_{\text{E} \times \text{B}}$ in Figure 5.1) and B is the average magnetic field measured throughout the plasma mantle. To determine the magnitude of $V_{\text{E} \times \text{B}}$, we start with the total velocity of the particles, v , calculated from the observed weighted average proton energy distribution. The magnitude of $V_{\text{E} \times \text{B}}$ is determined using the angle of particle motion, α , with respect to the background magnetic field. FIPS offers measurements of pitch angle distributions (shown in Figures 5.3 and

5.5); however, the angular resolution of the FIPS sensor is only $\sim 15^\circ$ and this creates a large uncertainty in this calculation of the $\mathbf{E} \times \mathbf{B}$ speed. Therefore, based on the PAD analysis we determine $V_{\mathbf{E} \times \mathbf{B}}$ by assuming α to be 10° and 15° in order to calculate a possible range of drift speeds.

In the 06:00 and 14:00 UTC orbits we determined the weighted average energy distribution of the protons in the plasma mantle to be 0.28 keV and 0.27 keV, respectively, which correspond to a velocity of $v \sim 230 \text{ km s}^{-1}$. Using $\alpha = 10^\circ$ and $\alpha = 15^\circ$ we calculate $V_{\mathbf{E} \times \mathbf{B}}$ from the relation $V_{\mathbf{E} \times \mathbf{B}} = v \cdot \sin(\alpha)$ and determine the drift speeds to be $V_{\mathbf{E} \times \mathbf{B}}(10^\circ) \approx 40 \text{ km s}^{-1}$ and $V_{\mathbf{E} \times \mathbf{B}}(15^\circ) \approx 60 \text{ km s}^{-1}$. The average magnetic field magnitude over the duration of the plasma mantle was measured to be 54 nT for the 06:00 UTC. Using the calculated values of $V_{\mathbf{E} \times \mathbf{B}}$ above along with the average field strength, we determine E_{conv} to be between 2.2 mV/m and 3.22 mV/m, assuming pitch angles of 10° – 15° , respectively. In order to calculate Φ_{Tail} , we assume a tail width of $5 R_M$ and determine the cross-tail potential to range from 26 kV to 39 kV. For the second orbit at 14:00 UTC, the average field magnitude was 47 nT, resulting in E_{conv} estimates of 1.9 mV/m and 2.8 mV/m for $\alpha = 10^\circ$ and $\alpha = 15^\circ$, respectively. Again, assuming tail width of $5 R_M$, we estimate Φ_{Tail} to be 23 kV and 34 kV.

Table 5.1 provides a summary of the plasma mantle characteristics and calculations. The results show that the calculation of Φ_{Tail} is sensitive to the assumed value of α and the width of the tail. Because of the level uncertainty associated with the angular resolution determined by FIPS we have assumed values for α that are representative of an antisunward flow as the particles are expected to remain relatively field-aligned. Additionally, the assumed tail width of $5 R_M$ is consistent with average values determined by *Winslow et al.* [2013].

The second method for determining Φ_{Tail} uses the observed spatial extent of the plasma dispersion throughout the mantle. From measurements of the plasma mantle location and the plasma velocity in the magnetosheath we can determine $V_{\mathbf{E} \times \mathbf{B}}$. For this approach we must assume an entry point of the solar wind particles so that we may estimate the observed length of the plasma mantle. That is, we assume that the plasma has entered near the magnetic cusps and take the origination of the mantle to be at the terminator $X'_{\text{MSM}} = 0$. With this assumption we know the distance, d , that the plasma has

traveled from the terminator to the location where the MESSENGER entered the plasma mantle. Also, from MESSENGER's nearly-polar orbit we can assume the spacecraft was moving orthogonal to the magnetopause and plasma sheet, so we can estimate the thickness of the plasma mantle, δ , from the change in Z'_{MSM} between the beginning and end of the plasma mantle observations. We know that the ratio δ/d is equal to the ratio of the $\mathbf{E} \times \mathbf{B}$ drift velocity to the velocity in the magnetosheath (V_{\parallel} in Figure 5.1), or $V_{\mathbf{E} \times \mathbf{B}}/V_{\parallel}$. From FIPS measurements we have determined V_{\parallel} to be 275 km s^{-1} and 295 km s^{-1} for the 0600 and 1400 UTC orbits, respectively. Using this information, along with the ratio of the spatial dimensions, it is possible to calculate $V_{\mathbf{E} \times \mathbf{B}}$.

Time (UTC)	Location ($X'_{\text{MSM}}, Y'_{\text{MSM}}, Z'_{\text{MSM}}$)	$\langle E \rangle$ (keV/e)	$\langle B_{\text{PM}} \rangle$ (nT)	α ($^{\circ}$)	E_{conv} (mV/m)	Φ_{Tail} (kV)
06:33:35 – 06:49:33	(-2.55, 0.75, -1.96)	0.28	54	10	2.2	26
				15	3.2	39
14:26:41 – 14:47:39	(-2.53, 0.85, -2.24)	0.27	47	10	1.9	23
				15	2.8	34

Table 5.1: Plasma mantle properties from the 06:00 and 14:00 UTC orbits on 10 November 2012. The location listed in the table marks the position where MESSENGER first entered the plasma mantle as it crossed the magnetopause. E_{conv} and Φ_{Tail} calculations are determined using the first method described in Section 4.

During the 0600 UTC orbit, $\delta = 0.69 R_{\text{M}}$ and $d = 2.55 R_{\text{M}}$ resulting in a ratio of $\delta/d = 0.27$. Using $V_{\parallel} = 275 \text{ km s}^{-1}$ we find an $\mathbf{E} \times \mathbf{B}$ drift velocity of $V_{\mathbf{E} \times \mathbf{B}} \sim 74 \text{ km s}^{-1}$. In order to calculate E_{conv} , we multiply this value by the average field strength in the plasma mantle (54 nT) and find $E_{\text{conv}} \sim 4.0 \text{ mV/m}$. Once again, taking the tail width to be $5 R_{\text{M}}$ we determine a cross-tail electric field potential of $\Phi_{\text{Tail}} \sim 49 \text{ kV}$.

Performing the same calculation for the 1400 UTC orbit, we find a spatial ratio of $\delta/d = 0.88/2.53 = 0.35$. From this, we use $V_{\parallel} = 295 \text{ km s}^{-1}$ to calculate an $\mathbf{E} \times \mathbf{B}$ drift velocity of $V_{\mathbf{E} \times \mathbf{B}} \sim 103 \text{ km s}^{-1}$. We determine E_{conv} to be 4.8 mV/m using the average field magnitude of 47 nT in the plasma mantle region. From this we determine a value of $\Phi_{\text{Tail}} \sim 59 \text{ kV}$.

Table 5.2 provides a summary of the plasma mantle characteristics and calculations. The cross-magnetosphere potentials determined by this second method are about a factor of 2 greater than the results determined in the first approach. This

difference is likely due to many levels of uncertainty associated with the parameters used to determine Φ_{Tail} . The point at which the solar wind plasma enters the magnetosphere is unknown and most likely occurs upstream of the terminator when reconnection takes place at the dayside magnetopause. Mercury’s magnetosphere is constantly responding to changing upstream solar wind conditions and therefore, the actual width of the magnetotail is not known. Due to FOV constraints, FIPS is only measuring a fraction of the plasma distribution, assumed to be ~ 0.5 in our calculation of magnetosheath speeds. If this fraction is smaller than ~ 0.3 , the actual flow speed will be higher than the one measured. Additionally, there is no way of determining the rate of reconnection at the dayside magnetopause at the time of the plasma mantle encounter. If reconnection is occurring at a high rate for these particular orbits, which is suggested by the level of FTE activity, then magnetospheric convection may be increased.

Time (UTC)	Location ($X'_{\text{MSM}}, Y'_{\text{MSM}}, Z'_{\text{MSM}}$)	d (R_{M})	δ (R_{M})	E_{conv} (mV/m)	Φ_{Tail} (kV)
06:33:35 – 06:49:33	(-2.55, 0.75, -1.96)	2.55	0.69	4.0	49
14:26:41 – 14:47:39	(-2.53, 0.85, -2.24)	2.53	0.88	4.8	59

Table 5.2: Plasma mantle properties from the 06:00 and 14:00 UTC orbits on 10 November 2012. The location listed in the table marks the position where MESSENGER first entered the plasma mantle as it crossed the magnetopause. E_{conv} and Φ_{Tail} calculations are determined using the second method described in Section 4.

5.5 Discussion and Conclusions

In this work we have presented the first observations of Mercury’s plasma mantle using MESSENGER measurements from two hot-season orbits on 10 November 2012. FIPS measurements revealed a continuous population of solar wind plasma as the spacecraft crossed from the magnetosheath into the magnetosphere, which represents the plasma mantle. The plasma mantle was observed for intervals of 16 and 21 min during the 06:00 and 14:00 UTC orbits, respectively. A distinct dispersion in the proton energy distribution is observed with increasing distance from the magnetopause. This occurs because the low-energy particles $\mathbf{E} \times \mathbf{B}$ drift toward the central plasma sheet while the protons of higher energies proceed further down the tail. As the particle flux in the

plasma mantle decreases, we observe a steady increase in the field magnitude in order to maintain a pressure balance.

It is expected that magnetosheath ions travel along reconnected field lines and enter the magnetosphere through the magnetic cusp where they will eventually mirror and move back out towards the magnetopause [see *Raines et al.*, 2014]. Depending on their parallel velocity and the strength of the magnetic field the particles will either be lost to the surface or they will mirror at the cusp and begin streaming in the opposite direction away from the planet. As the particles stream away from the planet the field continues its convection pattern and returns to the magnetotail, bringing the mirrored solar wind plasma with it.

We have identified signatures related to magnetic reconnection in both plasma mantle events based on the recurrence of large-scale fluctuations throughout the extent of the magnetosheath and the plasma mantle. These high-amplitude signatures are FTEs that were formed at the dayside magnetopause and then circulated around the planet to enter the magnetotail. These observations are analogous to the “FTE showers” in the downstream magnetosheath reported by *Slavin et al.* [2012].

The extent to which FTEs contribute to the existence of the plasma mantle has only been briefly explored at Earth. As FTEs form, they facilitate the mixing of solar wind and planetary plasmas and provide a gateway for the solar wind plasma to enter the magnetosphere. The plasma mantle formation model presented by *Sibeck and Siscoe* [1984] implies that FTEs may have an even greater effect on magnetospheric dynamics than once thought. Their significance in any given magnetosphere is determined by the amount of flux they are transporting. At Earth, FTEs only contribute to ~2% of the total flux transported [e.g., *Huang et al.*, 2009]; however in Mercury’s magnetosphere, these flux ropes contribute at least 30% of the total flux circulated throughout the Dungey cycle [*Imber et al.*, 2014]. Furthermore, given the short convection times at Mercury, FTEs are able to move from the dayside, where they are generated, back into the magnetotail in only a matter of minutes. It is plausible that they are the source of the plasma mantle in Mercury’s magnetosphere, although a more extensive analysis must be performed to examine this.

The calculated values of Φ_{Tail} from both orbits range from 23–59 kV (Tables 5.1 and 5.2). Calculations of the electric potential drop in Mercury’s magnetosphere have been performed using several different techniques in the past. After MESSENGER’s second flyby of Mercury, *Slavin et al.* [2009] determined an electric potential of 30 kV using the magnetic field component normal to the magnetopause, B_N , generated by reconnection. *DiBraccio et al.* [2013] performed an extensive survey of B_N measurements at the dayside magnetopause and found an average magnetosphere potential of 29 kV. After determining the flux content of FTEs in Mercury’s magnetosphere, *Imber et al.* [2014] applied their short transit times to calculate a cross-polar-cap potential of 25 kV. Although our resulting values of Φ_{Tail} vary by a factor of ~ 2 , they are found to be of the same order as previous measurements, which is supportive of the initial estimate of Mercury’s convection electric field of ~ 2.0 mV/m by *Slavin et al.* [2009] used to calculate the short ~ 2 min Dungey cycle.

We have reported the first observations of Mercury’s plasma mantle using magnetic field and plasma measurements collected during two MESSENGER orbits. The observed plasma energy dispersion provides a new method for inferring the cross-magnetosphere electric field. The presence of frequent FTEs throughout these encounters is supportive of the high reconnection rates measured at Mercury. Observations of Mercury’s plasma mantle provide further evidence that this small magnetosphere is constantly circulating plasma and magnetic flux as it is driven by the intense solar wind forcing of the inner heliosphere.

CHAPTER VI

MESSENGER OBSERVATIONS MERCURY'S DAYSIDE MAGNETOSPHERE UNDER EXTREME SOLAR WIND CONDITIONS

This chapter is taken from James A. Slavin, Gina A. DiBraccio, Daniel J. Gershman, Suzanne M. Imber, Gang Kai Poh, Jim M. Raines, Thomas H. Zurbuchen, Xianzhe Jia, Daniel N. Baker, Karl-Heinz Glassmeier, Stefano Livi, Scott A. Boardsen, Timothy A. Cassidy, Menelaos Sarantos, Torbjorn Sundberg, Adam Masters, Catherine L. Johnson, Reka M. Winslow, Brian J. Anderson, Haje Korth, Ralph L. McNutt, Jr., and Sean C. Solomon (2014), MESSENGER observations of Mercury's dayside magnetosphere under extreme solar wind conditions, manuscript in preparation. I performed the analysis of magnetic field data resulting in Figures 6.1, 6.3, 6.4, 6.5, 6.6, 6.10, 6.12, 6.14, 6.18, 6.19, and 6.20 as well as Tables 6.1 and 6.2. I also made significant contributions to the writing and manuscript preparation.

Abstract

MESSENGER observations of Mercury's dayside magnetosphere are presented during three extreme solar wind dynamic pressure events. Two were due to coronal mass ejections (CMEs) and one due to a high-speed stream (HSS). The inferred pressures for these events are ~ 45 to 65 nPa. The CME events produced thick, low- β (ratio of thermal to magnetic pressure) plasma depletion layers and high reconnection rates of $0.1 - 0.2$, despite small magnetic shears across the magnetopause of only 27 to 60° . For one of the CME events brief, $\sim 1 - 2$ s - long diamagnetic decreases, which we term cusp plasma filaments, are observed within and adjacent to the cusp. These filaments may map magnetically to flux transfer events at the magnetopause. The HSS event produced a

high- β magnetosheath with no plasma depletion layer and large magnetic shear angles of 148 to 166°, but low reconnection rates of 0.03 to 0.1. These results confirm that magnetic reconnection at Mercury is very intense and its rate is primarily controlled by plasma β in the adjacent magnetosheath. The distance to the subsolar magnetopause is reduced during these events from its mean of 1.45 R_M to between 1.03 and 1.12 R_M . The shielding provided by induction currents in Mercury’s interior, which temporarily increases Mercury’s magnetic moment, was negated by reconnection-driven magnetic flux erosion.

6.1 Introduction

The MESSENGER measurements show that Mercury’s magnetic field is highly dipolar, closely aligned with the planet’s rotation axis, and has the same polarity as at Earth, but with an offset northward from the planetary center of $\sim 0.2 R_M$ [Anderson *et al.*, 2008; 2010; 2011a; 2012; Alexeev *et al.*, 2008; 2010; Johnson *et al.*, 2012]. Figure 6.1a displays the low altitude portion of MESSENGER’s orbit against an illustration of Mercury’s dayside magnetic field. The MESSENGER trajectory is representative of the intervals considered in this paper with periapsis on the dayside and the orbital plane near the noon – midnight plane. These are termed “hot seasons” because MESSENGER experiences its highest thermal input from the planet during such orbits. The mean distance from Mercury’s offset dipole to the subsolar magnetopause (represented here approximately by the outermost closed magnetic flux tube) based upon the Mariner 10 and MESSENGER observations is $\sim 1.45 R_M$ [Ness *et al.*, 1976; Slavin *et al.*, 2010; Winslow *et al.*, 2013].

Figure 6.1b–e display MESSENGER MAG observations [Anderson *et al.*, 2007] from a rather quiet pass that occurred late on 23 November 2011 (after one of the extreme events analyzed in this paper). Full resolution (20 vectors s^{-1}) MAG measurements are displayed in MSM coordinates [Anderson *et al.*, 2012]. The interval displayed begins with MESSENGER exiting the plasma sheet and moving into the northern lobe of the near tail and beginning its periapsis pass. The total magnetic field smoothly increases as MESSENGER travels toward Mercury’s north magnetic pole reaching a maximum

magnetic field strength of 341 nT at 22:08:24 UTC when the altitude was 450 km. The polarity of B_x reverses very near the maximum in the total field magnitude and the southward (i.e., inward) B_z .

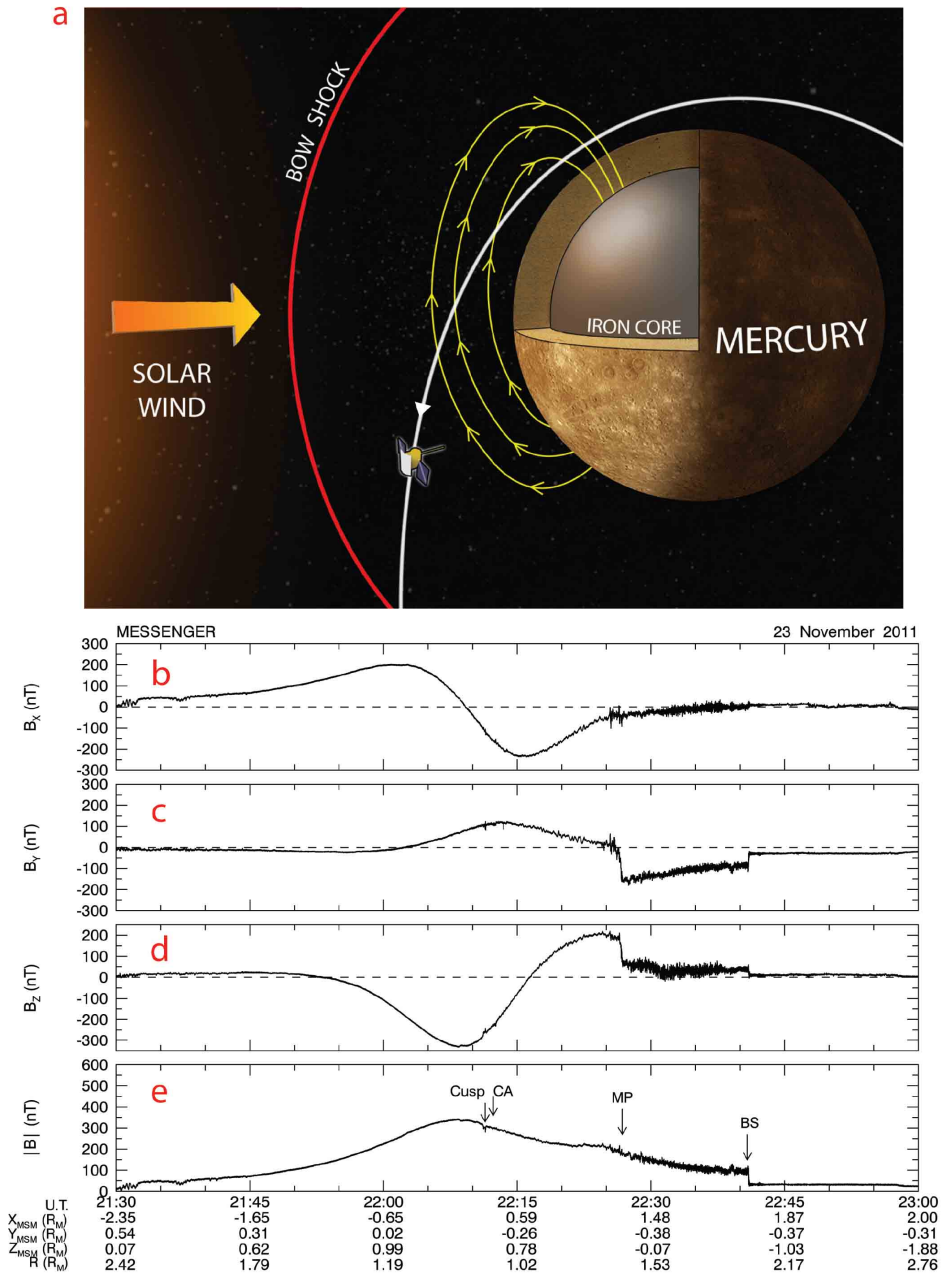


Figure 6.1: (a) Mercury’s bow shock, some dayside magnetic field lines, and large iron core are displayed. The outermost dipolar field line (yellow) lies at a distance of $\sim 1.4\text{--}1.5 R_M$ sunward of the planetary rotation axis while the nose of the bow shock (red) is at $\sim 1.9\text{--}2.0 R_M$ [Winslow *et al.*, 2013]. The MESSENGER spacecraft orbit has periapsis ranging from 200 to 500 km at a latitude of $\sim 60^\circ$ and an inclination of $\sim 82.5^\circ$ is shown (white). (b-e) Magnetic field measurements (sampling rate: 20 s^{-1}) taken during a typical MESSENGER periapsis pass.

The northern magnetospheric cusp (see Figure 6.1e), as expected, occurs over the dayside hemisphere at high latitudes. On this occasion it is encountered just prior to MESSENGER's closest approach (CA) to the surface at an altitude of 402 km. The cusp is identified by the diamagnetic effect of the solar wind plasma entering directly from the magnetosheath [Winslow *et al.*, 2012]. The cusp, ~ 22:11:20 UTC, is barely discernable due to the weakness of the diamagnetic decrease in total magnetic field intensity. As reported by Winslow *et al.* [2012] and Raines *et al.* [2013, 2014] the amount of plasma in the cusp region and, hence, its diamagnetic effect are highly variable.

The magnetopause at 22:26:40 is apparent in the rotation of the magnetic field from its dipole configuration to the draped interplanetary magnetic field orientation in the magnetosheath. In contrast with the Earth and the outer planets, the magnetosheath at Mercury is usually a low β (i.e., ratio of plasma thermal to magnetic field pressure) environment with the PDL adjacent to the magnetopause [Gershman *et al.*, 2013]. This is reflected in the very modest decrease in magnetic field intensity as MESSENGER passes from the magnetosphere into the subsolar magnetosheath in Figure 6.1. At Mercury the magnetopause is mostly readily identified by the rotation of the magnetic field from a magnetospheric to magnetosheath orientation as the spacecraft crosses the current sheet. MESSENGER then exited the magnetosheath through the bow shock (BS) at 22:40:57 UTC.

Siscoe and Christopher [1975] were the first to take a long time series of solar wind ram pressure measurements collected at 1 AU, scale it by $1/r^2$ inward to Mercury's orbit to take into account the increase in solar wind density with decreasing heliocentric distance, and then use the Mariner 10 planetary dipole moment [Ness *et al.*, 1974] to compute the distribution of solar wind standoff distances for the nose of the magnetopause. They found that for almost all solar wind pressure conditions the magnetopause stood off from Mercury's surface. However, the Siscoe and Christopher [1975] analysis only considered the effect of solar wind dynamic pressure and planetary dipole strength, but not the effects of dayside magnetic reconnection or electromagnetic induction in the planetary interior.

Earth observations have shown that magnetic reconnection removes magnetic flux from the dayside magnetosphere and transfers it to the magnetotail thereby eroding the

dimensions of the forward magnetosphere [Aubry *et al.*, 1971; Holzer and Slavin, 1978; Sibeck *et al.*, 1991]. The magnetic flux transferred to the nightside magnetosphere may immediately undergo reconnection or be stored, and later returned to the dayside in an intense episode of reconnection in the tail [Caan *et al.*, 1977; Holzer and Slavin, 1979; Milan *et al.*, 2004]. Such tail loading – unloading events are termed magnetospheric substorms [McPherron *et al.*, 1973; Baker *et al.*, 1996]. Empirically, the time-scale for substorms corresponds approximately to one complete circulation cycle of plasma and magnetic flux from the reconnection site at the dayside magnetopause to the reconnection site in the nightside cross-tail current sheet, and back to the forward magnetosphere. This reconnection-driven circulation is called the Dungey cycle [Dungey, 1961] and has a time-scale of ~ 1 to 3 hr for the Earth [Tanskanen *et al.*, 2009], but only ~ 1 to 3 min at Mercury [Siscoe *et al.*, 1975; Slavin *et al.*, 2009; 2010; DiBraccio *et al.*, 2013]. At other times, especially when solar wind conditions produce intense, but steady reconnection at the dayside magnetopause, the circulation or convection of magnetic flux and plasma in the Earth’s magnetosphere occurs in a relatively continuous manner. This is termed steady magnetospheric convection (SMC) [Sergeev *et al.*, 1996; Tanskanen *et al.*, 2005]. Evidence for both modes of convection, substorms and SMCs have been reported for various intervals of Mercury observations [Slavin *et al.*, 2009; 2010; 2012; Sundberg *et al.*, 2012].

Low-latitude reconnection at Earth is strongly controlled by the magnetic shear angle across the magnetopause with the highest rates being observed for the largest shear angles when the IMF has a strong southward component [Reiff and Luhmann, 1986; Mozer and Retino, 2007; Fuselier and Lewis, 2011]. This is called the “half-wave rectifier effect” [Burton *et al.*, 1975]. The ultimate reason that reconnection at Earth requires large shear angles, ~ 90 to 270° , is the high average Alfvénic Mach number at 1 AU, i.e., $\sim 6 - 12$ [Slavin *et al.*, 1984; Sarantos *et al.*, 2007]. These high Mach numbers result in a high- β magnetosheath and, generally, thin, weak PDLs adjacent to the magnetopause [Zwan and Wolf, 1976; Crooker *et al.*, 1979]. Even when solar wind conditions produce a well developed layer of plasma depleted flux tubes draped about the dayside magnetopause at Earth, the onset of reconnection often leads to PDL dissipation due to the high flux transfer rates that ensue [Anderson *et al.*, 1997]. The typically high- β

magnetosheaths at the Earth cause the magnetic fields on either side of the magnetopause to differ greatly in magnitude. Under these circumstances, reconnection is only possible for large shear angles, typically greater than 90° [see *Sonnerup*, 1974]. In contrast, the presence of a strong PDL in the inner magnetosheath naturally leads to magnetic fields of similar magnitude on either side of the magnetopause. For low- β magnetosheaths and well developed PDL's observed at Mercury [*Gershman et al.*, 2013], the near equality of the magnetic field on either side of the magnetopause (see Figure 6.1) will allow reconnection to occur for arbitrarily low shear angles such as observed, for example, across heliospheric current sheets where the magnetic fields are also nearly equal on both sides [*Gosling et al.*, 2005; *Phan et al.*, 2005].

Slavin and Holzer [1979] was the first to consider the effect of erosion on Mercury's magnetosphere. They assumed the terrestrial-style half-wave rectifier reconnection model, but they increased the efficiency (i.e., the fraction of the flux of southward IMF incident upon the dayside magnetopause that undergoes reconnection) from the Earth value by a factor of ~ 3 to account for the enhanced Alfvén speeds in the inner solar system. It was argued that these high Alfvén speeds would ultimately lead to correspondingly higher absolute inflow speeds to the diffusion region, and, hence, higher reconnection rates, and an overall increase in the fraction of the incident IMF flux that reconnects with the planetary magnetic field. Further, the expected low electrical conductance of the planetary regolith will greatly reduce the retarding effects of line-tying, i.e., field-aligned currents that limit the cross-magnetospheric electric potential drop and the rate of magnetospheric convection [*Hill et al.*, 1976]. In this manner they estimated that erosion could reduce the altitude of the dayside magnetopause at Mercury by several tenths of a Mercury radius. Given the mean subsolar magnetopause altitude of only $\sim 0.4\text{--}0.5 R_M$, *Slavin and Holzer* [1979] concluded that reconnection, especially during intervals of enhanced solar wind pressure, might erode the magnetopause down to the surface.

Mercury is the densest planetary body in our solar system due to its very large, ~ 2000 km radius, iron-rich, highly electrically conducting core [*Smith et al.*, 2012]. As a result, changes in the external magnetic field are estimated to take of order 10^{4-5} years to diffuse to the center of the planet [*Glassmeier*, 2001]. Given the short time scales for

solar wind pressure increases, i.e., durations of several minutes to days, Mercury’s core will react as a perfectly electrically conducting sphere with respect to all changes in solar wind pressure. Changes in the magnetic field normal to the surface of the large conducting core will generate currents according to Faraday’s law that oppose the change in the magnetic field as shown in Figure 6.2a [Hood and Schubert, 1979; Suess and Goldstein, 1979; Glassmeier et al., 2007]. The magnetic flux sandwiched between the magnetopause and the surface of the core can still be compressed, but it will diffuse into the core only on very long time scales. The Hood and Schubert [1979], Suess and Goldstein [1979], and Glassmeier et al. [2007] models predict that the subsolar magnetopause altitude will remain at or above $\sim 0.2 R_M$ for even the highest anticipated solar wind dynamic pressures at Mercury.

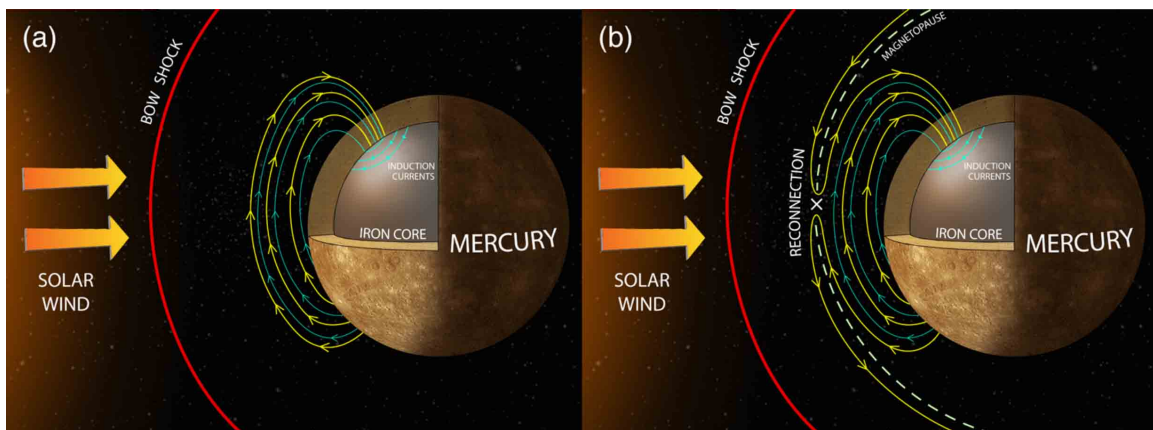


Figure 6.2: (a) Increases in solar wind pressure drive induction currents on the surface of Mercury’s large iron core (green loops). The senses of these currents is to oppose the compression of the intrinsic magnetic field (yellow) by generating additional magnetic flux (green field lines) which, when added to the intrinsic flux, acts to balance the increased solar wind pressure. (b) Magnetic reconnection between the interplanetary magnetic field and the intrinsic planetary magnetic field opposes the effectiveness of induction by removing magnetic flux from the dayside magnetosphere and transporting it into the tail.

We have surveyed the MESSENGER “hot-season” orbits in 2011 and 2012 for which the outbound magnetopause crossing(s) occurs within 1 hr of local noon to identify intervals when Mercury’s magnetosphere was subjected to extremely high solar wind dynamic pressure. For these hot-season orbits the spacecraft passes through the nightside plasma sheet, the northern cusp and the subsolar magnetopause just before and during each periapsis pass (see Figure 6.1a). Only three passes were identified for which the magnetic field just inside the magnetopause exceeded 300 nT. We analyze the

MESSENGER measurements for these events to infer the upstream dynamic pressure, the response of the dayside magnetosphere, and to assess the relative roles of magnetic reconnection and currents induced in the interior of the planet to standing-off the solar wind under these extreme conditions. The choice of 300 nT is somewhat arbitrary, but it is 2 to 3 times the typical intensity of the magnetic field in the subsolar magnetosphere [DiBraccio *et al.*, 2013; Winslow *et al.*, 2013], implying solar wind ram pressures that are 4 to 9 times normal. The results confirm that magnetic reconnection at Mercury is very intense and that its rate is primarily controlled by plasma β in the adjacent magnetosheath. The additional shielding provided by the induction currents, which effectively increase the magnetic moment of Mercury when solar wind pressure increases, is found to be largely negated by reconnection-driven erosion. Indeed, an average magnetopause surface passing through the lowest altitude magnetopause crossing, which had the highest inferred solar wind pressure and reconnection rate, intersected the planetary surface in the southern hemisphere where the surface magnetic field is weakest. The results of our analyses indicate that not only high-intensity reconnection, but also magnetosphere – core coupling must be included in global models of Mercury’s magnetosphere during extreme solar wind pressure conditions.

6.2 Extreme Solar Wind Event Overviews

The MESSENGER spacecraft entered orbit about Mercury on 18 March 2011 [Solomon *et al.*, 2007]. MESSENGER remained in this 82° inclination, highly eccentric (~200 × 15,000 km altitude) orbit until 16 April 2012 when the apoapsis was decreased and the orbital period reduced to 8 hr. For our purposes, the primary difference between these two orbits is that the 12 hr orbit crossed the dayside magnetopause at lower latitudes and the plasma sheet farther down the tail than the 8 hr orbit. We have surveyed MESSENGER magnetopause crossings in the magnetic field measurements [Anderson *et al.*, 2007] during hot season orbits (i.e., periapsis on the dayside, see Figure 6.1) that occurred within 1 hr of local noon from the start of the orbital phase through the end of 2012.

Typical values of the magnetic field just inside the dayside magnetopause are ~ 150 nT [DiBraccio *et al.*, 2013; Winslow *et al.*, 2013] corresponding to solar wind ram pressures of ~ 10 nPa. For the extreme solar wind events identified for this study we require that the magnetic field just inside the subsolar magnetopause exceed 300 nT implying a minimum solar wind pressure of ~ 36 nPa. As discussed earlier, this threshold is arbitrary, but it is the highest pressure for which multiple orbits could be found when MESSENGER was near the desired noon – midnight plane and taking measurements in the key regions of the magnetosphere. Indeed, only three MESSENGER periapsis passes through Mercury’s subsolar region met this requirement. They occurred on 23 November 2011, 8 May 2012 and 11 May 2012. Figure 6.3 graphs the MESSENGER orbits and the average location of the magnetopause from Winslow *et al.* [2013] in MSM' coordinates. A prime on the axes labels indicates that they have been aberrated according to Mercury’s orbital velocity so that a 400 km/s solar wind directed radially outward from the Sun moves in the $-X'_{\text{MSM}}$ direction. As expected for such high dynamic pressures, the magnetopause crossings for these days are all displaced significantly inward from its mean boundary model and very close to Mercury’s surface. The effect of the northward offset in Mercury’s dipole magnetic field is clearly evident in the closeness of the model magnetopause to the surface, especially in the southern hemisphere where the planetary field is weakest. We discuss the possible compression of the magnetopause to the surface in the southern hemisphere in Section 6.6.

An ideal magnetohydrodynamic simulation called ENLIL [Toth and Odstrcil, 1996; Odstrcil *et al.*, 2004] provides global context for these extreme pressure events. It is based upon the Wang-Sheeley-Arge (WSA) model of the coronal magnetic field derived by ground-based observations of the photospheric magnetic field gathered over a solar rotation [Arge *et al.*, 2004]. Details of the WSA-ENLIL model as applied to the inner heliosphere in support of MESSENGER can be found in Baker *et al.* [2009, 2013]. CMEs are included by means of the “cone model” wherein the CME is usually assumed to start near 21.5 solar radii and then propagate outward with a constant angular extent and radial velocity. The properties of a specific CME, and its “cone”, are determined based upon remote observations, usually from the STEREO coronal imagers [Xie *et al.*, 2004].

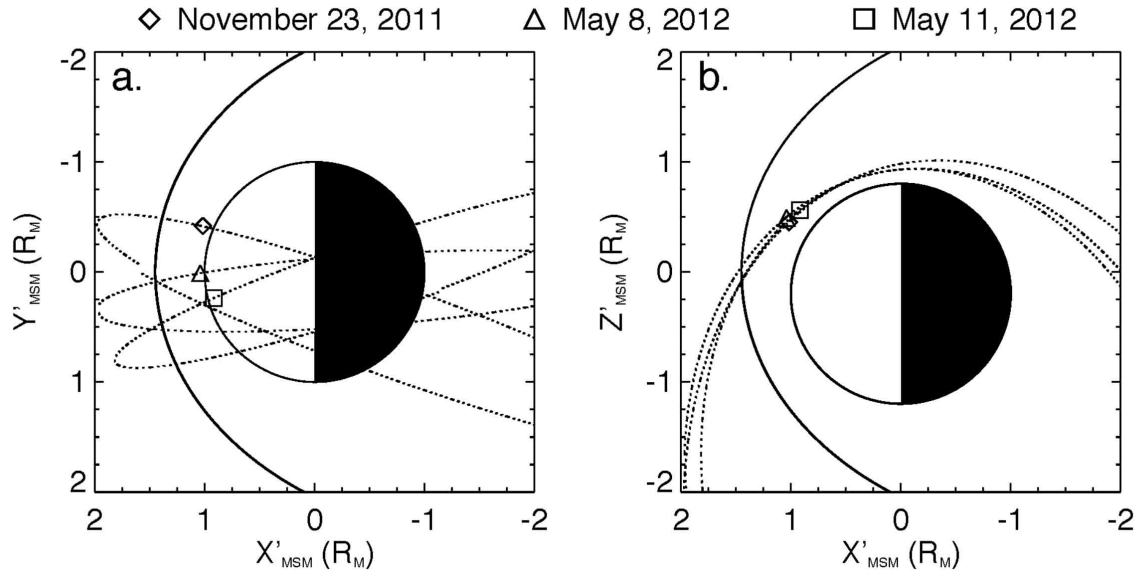


Figure 6.3: MESSENGER orbits projected into the aberrated MSM (a) Y' - X' and (b) Z' - X' planes relative to Mercury (dotted line) and its average magnetopause location (solid line) [Winslow *et al.*, 2013]. Note the displacement of the magnetopause relative to the planet due to the northward offset of the magnetic dipole by $\sim 0.2 R_M$. The extreme compression of the dayside magnetosphere on these passes is evident in the very low altitudes of the magnetopause crossings on 23 November 2011, 8 May 2012, and 12 May 2012 (diamonds, squares and triangles, respectively). The 23 November 2011 (DOY 327) orbit is before the reduction in orbital period from 12 hr to 8 hr, while the other two are afterwards. Note: The 23 November 2011 trajectory arcs farther downstream to intersect the mid-plane of the tail at greater distances than the 8 hr orbits.

On 23 November 2011 MESSENGER started its first periapsis pass of the day moving northward and sunward to cross the downstream bow shock and pass from the solar wind into the magnetosheath at 05:03:54 UTC. Shortly thereafter an interplanetary shock wave passed over MESSENGER at 05:19:40 UTC. After passing through periapsis and exiting the magnetosphere through the dayside magnetopause and the bow shock, MESSENGER measured an IMF that was oriented largely in the $+Y_{MSM}$ direction; $B_X = 7.65$ nT, $B_Y = 92.0$ nT, $B_Z = 31.9$ nT, and $B_{total} = 98.2$ nT (Table 6.1). This IMF direction represents a 20 min average, but the magnetic field draping pattern in the near-Mercury magnetosheath appears to have been relatively stable during this event. An upstream solar wind speed of 450 km s^{-1} (Table 6.1) was derived from the FIPS measurements using methodology detailed in Gershman *et al.* [2012], but density could not be recovered. The state of compression of the dayside magnetosphere can be analyzed to infer solar wind dynamic pressure, as will be described shortly.

Table 6.1: Extreme solar wind events.

Yr	DOY	IMF ^a	B'_{XMSM}	B'_{YMSM}	B'_{ZMSM}	V_{sw} ^b	P_{sw} ^c
			(nT)			(km/s)	(nPa)
2011	327		(7.66, 92.0, 31.9)			450	51.0
2012	129		(-2.01, 20.1, -9.50)			500	65.1
2012	132 ^d		(13.0, -9.51, -0.20)			425	53.0
							48.8
							48.6
							44.1
							44.3

^aIMF averaged over 20 min upstream of outbound bow shock

^bFIPS measurement immediately upstream of bow shock

^cDetermined from equation (6.1)

^dPressure determined for 5 of the multiple magnetopause crossings

Figures 6.4a-b display equatorial views of the solar wind velocity and the density, the latter multiplied by the square of radial distance (in units of AU) from the center of the Sun to de-trend for the decrease in density with increasing distance. The views are snapshots at 24:00 UT on 23 November 2011 after the CME passed over Mercury. The solar wind speed (6.4a) shows the CME near the trailing edge of a higher speed stream. The solar wind density (6.4b) depicts the expected interaction region compression signatures where the higher speed stream overtakes the slower solar wind. The CME does not stand out in the velocity display because its speed is only $\sim 450 \text{ km s}^{-1}$, but it is very clear in the density display due to the high density compression signature as it overtakes the slower upstream solar wind.

The magnetic field measured by MESSENGER over a 90 min interval beginning on 23 November 2011 is displayed in Figure 6.4c-f. It begins with MESSENGER just north of the plasma sheet ($X_{MSM} = -2.4$, $Y_{MSM} = 0.44$, $Z_{MSM} = 0.07 R_M$), then passing over the northern polar region. After passing through periapsis near Mercury's north pole, MESSENGER heads southward, first traversing a broad magnetospheric cusp within which the total field highly variable and is often depressed by more than 100 nT, the

2011-11-23 24:00

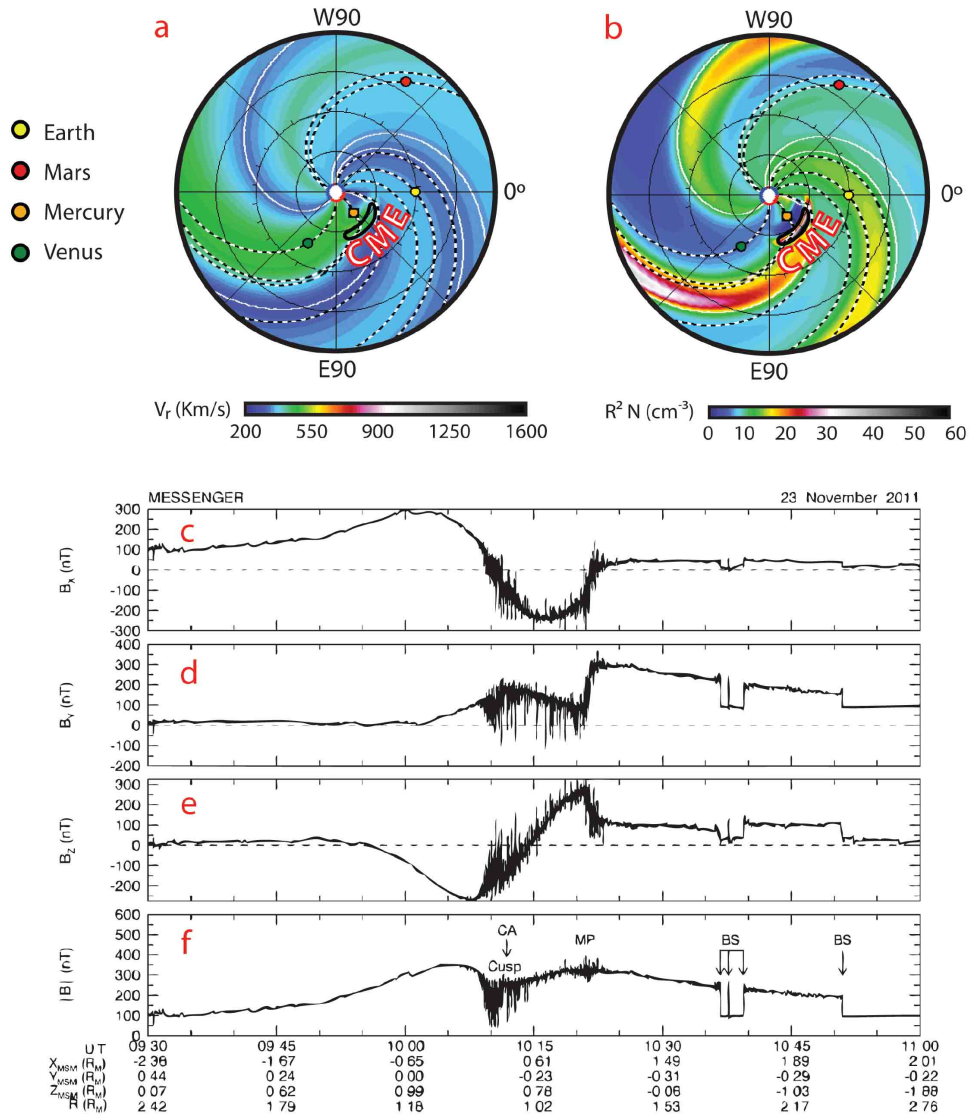


Figure 6.4: ENLIL-WSA models of the (a) solar wind speed and (b) solar wind density multiplied by the square of distance from the Sun in AU for 23 November 23 at 24:00 UT. The center of a coronal mass ejection impacted Mercury and its magnetosphere (yellow circle). The locations of Earth, Venus, and Mercury are all indicated by small colored dots. The inner domain of the model (where WSA is utilized) is denoted by the white central circle. Magnetic field measurements (sampled at a rate of 20 s^{-1}) taken during a CME-driven compressed magnetosphere pass on 23 November 2011 are displayed in MSM coordinates. The locations of the northern cusp, the magnetopause (MP), and the bow shock (BS) are labeled.

magnetopause, and multiple bow shock crossings. The magnetic field intensity at the magnetopause is 321 nT. Starting just poleward of the cusp and continuing through the high altitude dayside magnetosphere, the magnetic field exhibits large amplitude perturbations due to a new phenomenon, which we term cusp plasma filaments, and flux transfer events, as will be discussed later. The outward motion of the bow shock appears

due to be due to a decreasing upstream Mach number. The decreasing Mach number is reflected in the declining magnetic field jumps across each succeeding shock crossing. The low upstream Mach number is also reflected in the near-constant magnetic field intensity across the magnetopause indicative of a strong plasma depletion layer [Zwan and Wolf, 1976; Gershman et al., 2013]. Low solar wind Mach number conditions are especially common during CMEs [e.g., Farrugia et al., 1995; Lavraud and Borovsky, 2008; Sarantos et al., 2009].

The WSA-ENLIL simulation results for 12:00 UT on 8 May 2012 are shown in Figure 6.5. Again, a CME is shown passing over Mercury, as was the situation for the extreme solar wind pressure on 23 November 2011. However, in this case the simulation indicates that the CME did not pass directly over Mercury, but rather the planet encountered its eastern flank. This event is remarkable in that MESSENGER appears to have remained inside of the bow shock from the inbound encounter at $\sim 18:12$ UTC during the previous periapsis pass on 7 May 2012, the day before, until after the following periapsis pass with extreme pressure and an outbound bow shock encounter at $\sim 07:58$ UTC. The mean, a 20 min average, IMF upstream of the bow shock was $B_X = -2.01$ nT, $B_Y = 20.1$ nT, $B_Z = -9.50$ nT and $B_{\text{total}} = 27.0$ nT (Table 6.2). The IMF draping pattern in the magnetosheath was stable after a strong field rotation at $\sim 7:25$ UTC just upstream of the magnetopause. Figure 6.5 shows that this CME is predicted to have had a speed near 800 km/s and a density similar to or greater than the 23 November 2011 event. The solar wind speed measured by FIPS upstream of the outbound bow shock was only ~ 500 km s⁻¹ (Table 6.1) as compared with the forecast 800 km s⁻¹. This is likely due to Mercury having passed through the flank region of this CME. As we will show later, this event had the highest dynamic pressure of the three considered here. The fact that MESSENGER never emerged into the upstream solar wind between the last periapsis pass on 7 May 2012 and the outbound leg of the first periapsis pass on 8 May 2012 indicates that Alfvénic Mach number was extremely low and the bow shock unusually weak and distant.

Table 6.2: Magnetopause analysis.

Yr	DOY	UTC	X'_{MSM} Y'_{MSM} Z'_{MSM} (R_{M})	$N_{\text{MP}}/ N $	B'_{N} (nT)	Shear Angle ($^{\circ}$)	α^{a}	$\beta_{\text{MSH}}^{\text{b}}$
2011	327	10:21:18	(1.07, -0.14, 0.46)	(0.95, -0.09, 0.30)	31.9	59.6	0.10	0.06
2012	129	07:19:11	(0.83, 0.45, 0.56)	(0.86, 0.31, 0.39)	70.3	27.3	0.22	0.74
2012	132	23:21:07	(1.01, 0.26, 0.50)	(0.93, 0.17, 0.33)	26.1	148	0.082	0.70
2012	132	23:21:14	(1.02, 0.26, 0.49)	(0.93, 0.17, 0.32)	29.4	157	0.096	0.58
2012	132	23:21:20	(1.02, 0.26, 0.48)	(0.93, 0.17, 0.32)	29.4	159	0.096	1.82
2012	132	23:21:25	(1.02, 0.27, 0.48)	(0.93, 0.18, 0.31)	9.7	160	0.033	1.56
2012	132	23:21:32	(1.03, 0.28, 0.48)	(0.93, 0.18, 0.31)	22.5	166	0.077	8.67

^aDimensionless reconnection rate $\alpha = B'_{\text{N}}/B_{\text{MP}}$

^bDetermined from equation (6.2)

The magnetic field measurements for the first periapsis pass on 8 May 2012 are displayed in Figure 6.5c-f. The geometry of this hot season pass is quite similar to the 23 November 2011 event (cf. Figure 6.3). The 90 min interval starts with MESSENGER in the plasma sheet on the nightside ($X_{\text{MSM}} = -2.0$, $Y_{\text{MSM}} = -1.0$, $Z_{\text{MSM}} = -0.3 R_{\text{M}}$). As with the previous event, this pass over the northern polar cap shows another very broad, deep magnetic cusp with multiple short deep magnetic depressions, and a peak field intensity of 328 nT just inside the magnetopause. The bow shock is, again, weak, and located unusually far from the planet [cf. *Winslow et al.*, 2013]. The IMF for this event is extremely disturbed and variable. As with the 23 November 2011 event, the magnetic field decreases only slightly across the magnetopause indicating a strong PDL, but with a slightly higher plasma beta magnetosheath than for the previous event (see Table 6.2).

2012-05-08 12:00

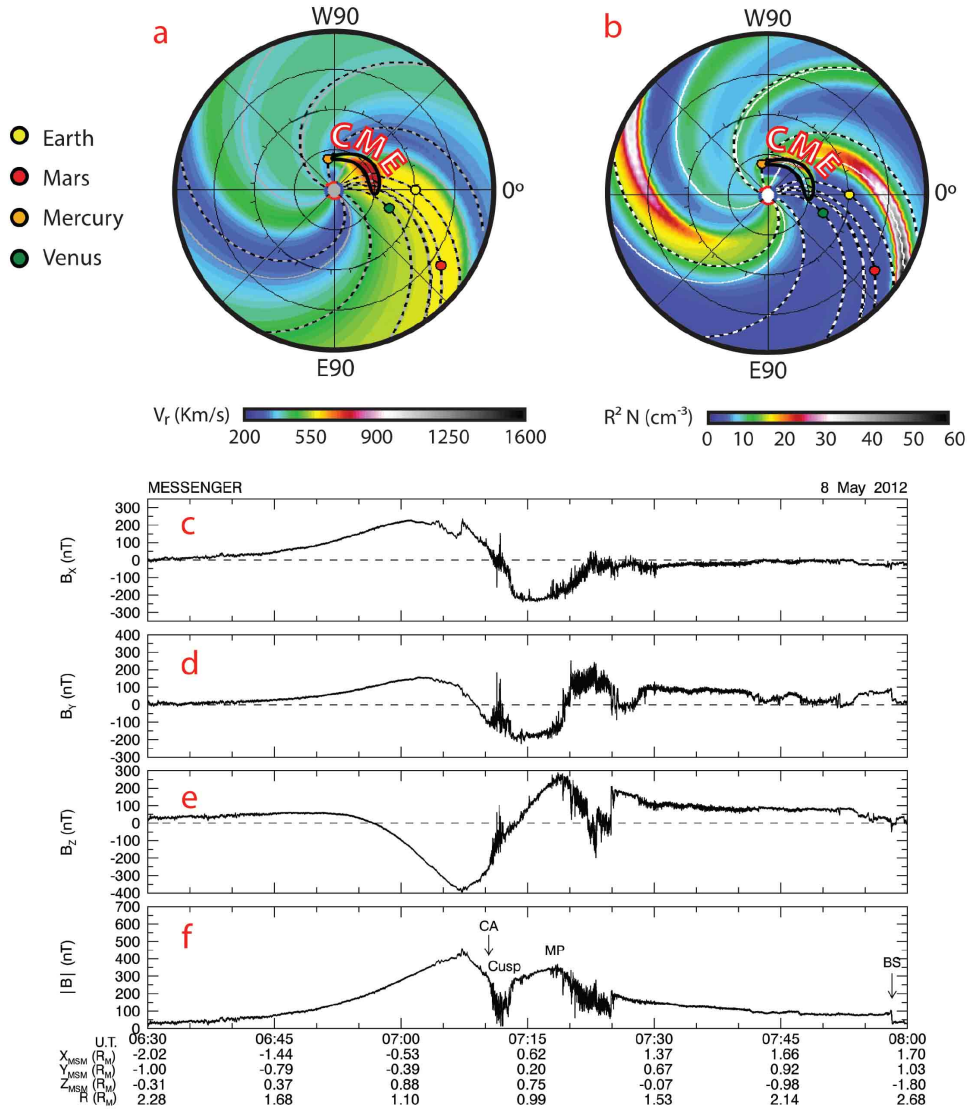


Figure 6.5: ENLIL-WSA models of the (a) solar wind speed and (b) density multiplied by the square of distance from the Sun in AU on 8 May 2012 at 12:00 UT. As shown, the edge of a coronal mass ejection moves over Mercury as it moves radially away from the Sun. Magnetic field measurements (sampled at a rate of 20 s^{-1}) taken during a CME-driven compressed magnetosphere pass on 8 May 2012 are displayed in MSM coordinates. The locations of the northern cusp, the magnetopause (MP), and the bow shock (BS) are labeled.

The WSA-ENLIL simulation results for 24:00 UT on 11 May 2012 displayed in Figure 6.6 show a different type of solar wind than for the previous two extreme solar wind pressure events. On this occasion Mercury appears to have encountered the inward edge of a co-rotating interaction region (CIR) caused by the collision between a high-speed stream, $\sim 600 \text{ km s}^{-1}$, with slower solar wind ahead of it. The FIPS measurements upstream of the bow shock for this periapsis pass showed a speed of only $\sim 425 \text{ km s}^{-1}$

(Table 6.1), again supporting the WSA-ENLIL simulation which shows that Mercury only encountered the edge of the CIR. No evidence for an interplanetary shock is present in the magnetic field measurements, consistent with expectations for a CIR in the inner solar system. Further, the IMF decreased in strength between MESSENGER's inbound bow shock crossing for this periapsis pass and the outbound bow shock where the 20 min averaged IMF was $B_X = 13.0$ nT, $B_Y = -9.51$ nT, $B_Z = -0.20$ nT and $B_{\text{total}} = 24.6$ nT. Further, the IMF draping pattern in the forward magnetosheath is variable with several rotations in the field direction. The magnetic field measurements in Figure 6.6c – f show that the bow shock is much stronger and closer than for the two events associated with CMEs. The bow shock crossings also exhibit significant overshoots indicative of high Mach numbers at Mercury [Masters *et al.*, 2013].

The magnetic field measurements displayed in Figure 6.6c-f start with MESSENGER moving north to exit the southern lobe of the tail ($X_{\text{MSM}} = -2.6$, $Y_{\text{MSM}} = -0.5$, $Z_{\text{MSM}} = -1.0 R_M$). In contrast with the other two extreme events, this pass over the northern polar cap shows a shallower magnetic cusp. For this event a series of magnetopause crossings were observed as the spacecraft moved away from Mercury toward the south. The magnetic field intensity just inside the initial magnetopause crossing was 318 nT and it decreased with each succeeding crossing as would be expected if the underlying cause of the multiple encounters was a slow, continuous decrease in solar wind pressure. As mentioned earlier, the bow shock is clearly standing in a higher Mach number solar wind than the two earlier events as evidenced by the much thinner magnetosheath and the larger jumps in the magnetic field across the shock. For this 11 May 2012 event the magnetic field decreases strongly across the magnetopause and no significant PDL was present. Accordingly, the magnetosheath was a much higher β than for the 23 November 2011 or 8 May 2012 events. Although some perturbations are present in the magnetospheric magnetic field measurements between the cusp and the magnetopause, the FTE signatures are limited to the region around the magnetopause.

2012-05-11 24:00

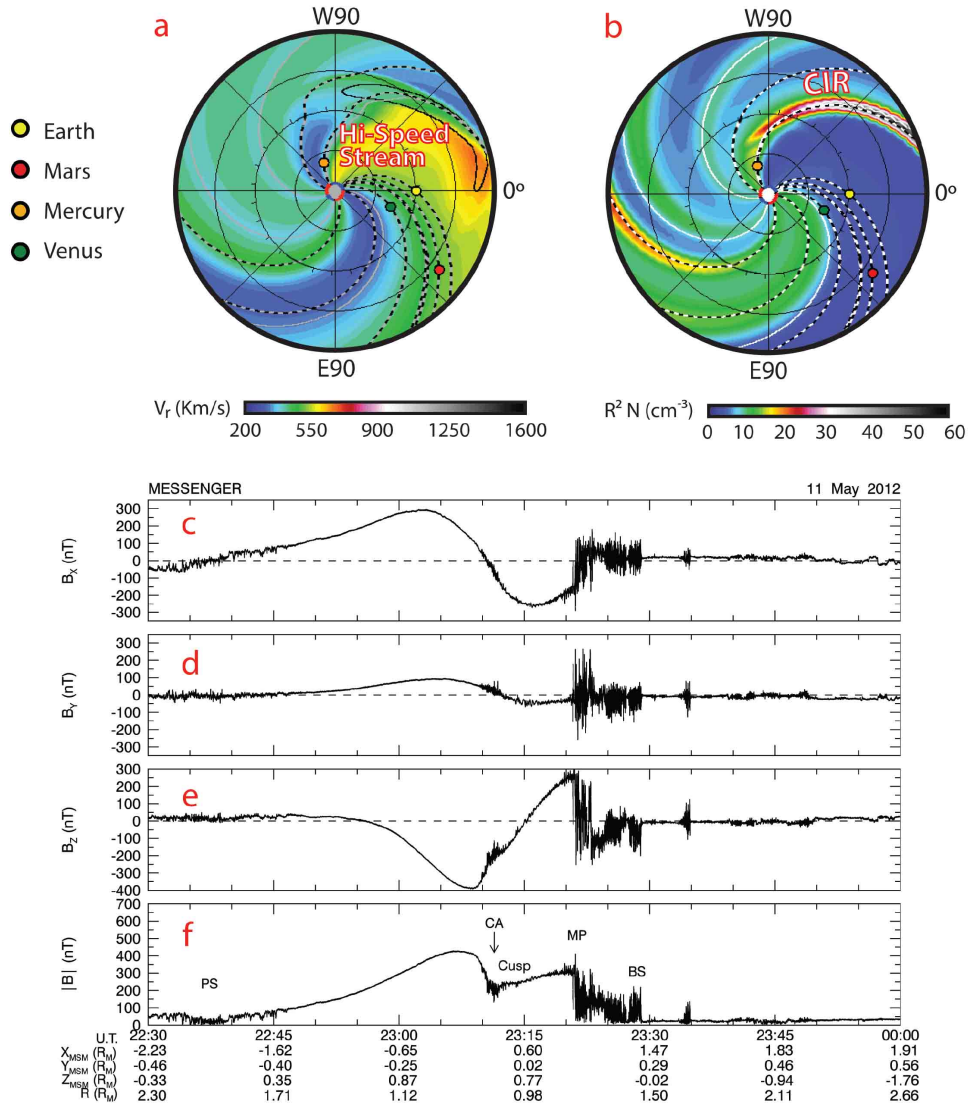


Figure 6.6: ENLIL-WSA models of the (a) solar wind speed and (b) density multiplied by the square of distance from the Sun in AU on 11 May 2012 at 24:00 UT. As shown, the edge of a co-rotating interaction region driven by a high-speed stream passes over Mercury and compresses its magnetosphere. Magnetic field measurements (sampled at a rate of 20 s^{-1}) taken during a high-speed stream interval on 11 May 2012 are displayed in MSM coordinates. The locations of the northern cusp, the magnetopause (MP), and the bow shock (BS) are labeled.

6.3 Magnetopause Analysis

MVA [Sonnerup and Cahill, 1967] was performed on each dayside magnetopause crossing during the three extreme solar wind intervals considered here. Large normal magnetic field components B_N were determined for all of the magnetopause crossings

during these events. However, for these extreme interval magnetopause crossings the eigenvalue ratios were marginal (e.g., see discussion of MVA analysis in *DiBraccio et al.*, 2013) due to the presence of large amplitude fluctuations, especially those associated with flux transfer events, in the magnetopause current layer. Further, the magnitudes of the magnetic fields normal to the magnetopause determined in this manner were found to be sensitive to the choice of analysis interval, again indicative of high levels of fluctuations and/or rapid temporal variations in orientation of the magnetopause.

For these reasons, we have used the normal vectors to the magnetopause surface determined from the average magnetopause model of *Winslow et al.* [2013]. This study assumed the functional form of the *Shue et al.* [1997] model, which has been shown to closely fit the Earth's magnetopause:

$$r = (X'_{\text{MSM}}{}^2 + Y'_{\text{MSM}}{}^2 + Z'_{\text{MSM}}{}^2)^{0.5} = R_{\text{ss}} [2/(1 + \cos \theta)]^\alpha \quad (6.1)$$

where $\theta = \tan^{-1} [(Y'_{\text{MSM}}{}^2 + Z'_{\text{MSM}}{}^2)^{0.5} / X'_{\text{MSM}}]$, the subsolar standoff distance, R_{ss} , is the distance from the offset planetary magnetic dipole to the nose of the magnetopause, and α is the magnetopause flaring parameter. *Winslow et al.* [2013] found a best fit to three Mercury years of MESSENGER magnetopause crossings for $R_{\text{ss}} = 1.45 R_{\text{M}}$ and $\alpha = 0.5$.

Using the normal direction at the point of the magnetopause crossing derived from the *Winslow et al.* [2013] model surface, the magnetic field data in the vicinity of each magnetopause has been rotated into the boundary normal coordinates (L, M, N) [see *Berchem and Russell*, 1982]. In this system N is normal to the magnetopause, L is perpendicular to N and lies in the plane defined by N and Z_{MSM} , and M completes the right-handed system. The magnetic field component normal to each magnetopause was computed by averaging the B_{N} magnetic field across the width of the magnetopause current layer. The magnetic field shear angle, or rotation, across the magnetopause current layer and the dimensionless reconnection rate, $B_{\text{N}}/B_{\text{MP}}$ [*Sonnerup et al.*, 1981; *DiBraccio et al.*, 2013] were also computed and are displayed in Table 6.2.

6.3.1 23 November 2011

The normal magnetic field direction derived from the mean magnetopause model of *Winslow et al.* [2013], in aberrated MSM coordinates, for the 23 November 2011 magnetopause is $\hat{B}_N = (0.95, -0.09, 0.30)$. It occurred at an altitude of only 685 km, or $0.28 R_M$, as shown in Figure 6.3. Two minutes of magnetometer measurements are displayed in boundary normal coordinates in Figure 6.7. The start and stop times for the magnetic field rotation across the magnetopause current layer are marked by red vertical dashed lines and the horizontal red bar. For the first minute of the interval MESSENGER was inside the magnetosphere as evidenced by the $B_L \sim +300$ nT and $B_M \sim 0$ nT magnetic fields. The magnetic field in the magnetosheath after exiting the magnetopause current layer is $B_L \sim 200$ nT and $B_M \sim 250$ nT. This magnetopause crossing occurred at magnetic latitude of 25.4° and is just slightly pre-noon (Figure 6.3). The magnetic shear angle θ , defined as the angle between the field vectors in the magnetosheath and magnetosphere adjacent to the magnetopause, was calculated to be 59.6° . The normal component to the magnetopause is strongly negative at the beginning of the 2 min interval reflecting the inward orientation of the planetary dipole magnetic field at low altitude in the northern hemisphere. The direction of the normal component magnetic field beyond the magnetopause is small and slightly positive reflecting the field draping in the magnetosheath and the average IMF direction (Table 6.1). The B_N component transitions from primarily inward (negative) to outward (positive) near the outer edge of the current layer as expected for a stable rotational discontinuity northward of an extended low-latitude X-line(s) [e.g., *Paschmann et al.*, 2013]. Averaged over the full width of the current sheet $B_N = -31.9$ nT and the dimensionless reconnection rate, $B_N/B_{MP} = 0.10$, which is typical of the values reported earlier for MESSENGER magnetopause crossings [*Slavin, et al.*, 2009; *DiBraccio et al.*, 2013]. For Earth and Mercury the mean dimensionless reconnection rate values are ~ 0.05 [*Mozer and Retino*, 2007] and 0.15 [*DiBraccio et al.*, 2013], respectively. Uncertainties in the normal magnetic field component and the reconnection rate are difficult to estimate, but they are believed to be in the $\sim 10\text{--}30\%$ range [*DiBraccio et al.*, 2013]. Hence, the reconnection rate for this magnetopause is high relative to the mean for Earth, but somewhat less than the average at Mercury.

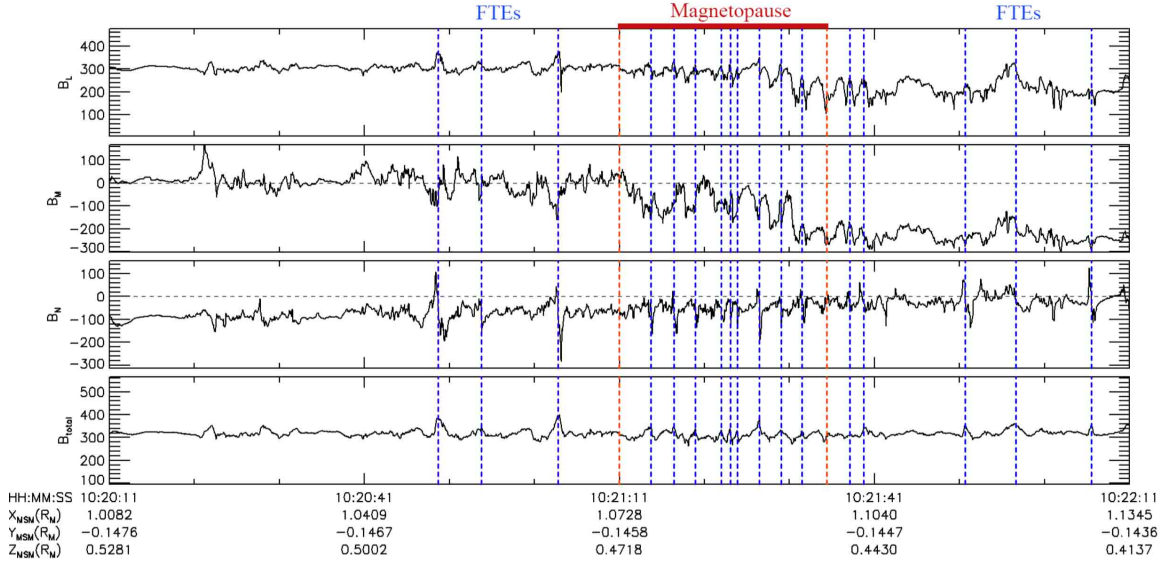


Figure 6.7: Magnetic field measurements in boundary normal coordinates across the dayside magnetopause on 23 November 2011. The magnetopause normal used here was determined from the average magnetopause of *Winslow et al.* [2013]. The start and stop times for the main magnetopause current layer and the occurrence of flux transfer events are indicated with a red bar and vertical dashed lines.

Following the methodology of *DiBraccio et al.* [2013], we calculate the ratio of thermal to magnetic pressure in the magnetosheath, β_{MSH} , from the magnetic field intensities just inside the magnetopause, B_{MP} , and in the adjacent magnetosheath, B_{MSH} :

$$\beta_{MSH} = (B_{MP}/B_{MSH})^2 - 1 \quad (6.2)$$

yielding $\beta_{MSH} = 0.06$. We confirm the assumption of negligible plasma pressure just inside the magnetopause by using the magnetosheath thermal pressure estimated from the FIPS data to determine that β_{MSH} of order 10^{-2} .

Assuming that the magnetic pressure dominates the plasma pressure just inside the magnetopause, which appears justified based upon the FIPS measurements (Figure 6.10), the subsolar point and the solar wind ram pressure, P_{sw} , may be inferred using the Newtonian pressure balance [*Spreiter et al.*, 1966] by taking into account the angle, ψ , of the magnetopause normal to the solar wind direction (assumed to be radial in MSM' coordinates):

$$P_{\text{sw}} = (B_{\text{MP}}^2/2\mu_0)/(0.88 \cos^2 \psi) \quad (6.3)$$

The total magnetic field magnitude, $|\mathbf{B}|$, inside the magnetopause was observed to be $B_{\text{MP}} \sim 319$ nT and the solar wind dynamic pressure for $\psi = 18.5^\circ$ angle of incidence, i.e., the upstream solar wind is 51.0 nPa (Tables 6.1 and 6.2).

Just upstream of the 23 November 2011 bow shock, the FIPS measurements indicate a solar wind speed of ~ 450 km/s, but solar wind density cannot be directly determined [see *Gershman et al.*, 2013]. However, in the subsonic region just behind the bow shock the FIPS measurements show $n_p \sim 350 \text{ cm}^{-3}$ and $T_p \sim 2.5$ MK. Given the factor of 2.5 jump in magnetic field intensity and, therefore, plasma density across this quasi-perpendicular bow shock, we estimate an upstream solar wind density of $\sim 140 \text{ cm}^{-3}$. Combined with the direct measurement of solar wind speed, the upstream M_A is ~ 2.5 , and the solar wind dynamic pressure is ~ 47 nPa. The calculated solar wind dynamic pressure matches the magnetic pressure measured inside the near-subsolar magnetopause extremely well, supporting the robustness of the technique and the assumption that plasma pressure just inside of the magnetopause may be neglected. The low upstream M_A value and quasi-perpendicular shock geometry produce a large-scale plasma depletion layer resulting in the low- β value at the magnetopause [*Gershman et al.*, 2013]. Such large-scale flux pile-up was observed at Earth for CME events with low upstream M_A [*Farrugia et al.*, 1995].

6.3.2 8 May 2012

The model-based normal magnetic field direction for 8 May 2012 magnetopause crossing in aberrated MSM coordinates, is $\hat{B}_N = (0.86, 0.31, 0.39)$. It occurred at an altitude of only 535 km and magnetic latitude of 26.7° , as shown in Figure 6.3. Two minutes of magnetometer measurements are displayed in boundary normal coordinates in Figure 6.8. As with the previous event, the start and stop times for the rotation of the magnetic field across the magnetopause current layer are marked by the red vertical bar and dashed lines. As will be shown shortly, FIPS observes the magnetosheath plasma flux drop to extremely low values inside of this current sheet. It is also the boundary above which the magnetic field begins to show the high levels of fluctuations

characteristic of the magnetosheath. However, this traversal of the magnetosphere – magnetosheath interface has significant similarities to the “double magnetopause” observed during the first MESSENGER flyby of Mercury [Slavin *et al.*, 2008]. As described by Slavin *et al.* [2008], and in more detailed analyses by Anderson *et al.* [2011b] and Raines *et al.* [2011], the complete transition from magnetosphere to magnetosheath took the form of two current sheets separated by a boundary layer region. For the first minute of the interval MESSENGER is inside the magnetosphere as evidenced by the $B_L \sim +320$ nT and $B_M \sim 0$ nT magnetic fields. The magnetic field in the boundary layer region, which ended with a second magnetopause like rotation in the magnetic field and the observation of two FTEs (see vertical blue dashed lines), is at $\sim 07:20:04:10$ UTC. In the magnetosheath upstream of this second magnetopause-like current we observe (see Figure 6.8) $B_L \sim 100$ nT and $B_M \sim 160$ nT. The normal magnetic field component, B_N , has a mean value of -70.3 nT across the inner magnetopause current layer, becomes steadily less negative across the boundary layer before fluctuating about zero upstream of the second magnetopause. The magnetic shear angle was only 27.3° . The dimensionless reconnection rate, B_N/B_{MP} is therefore 0.21, which is largest of

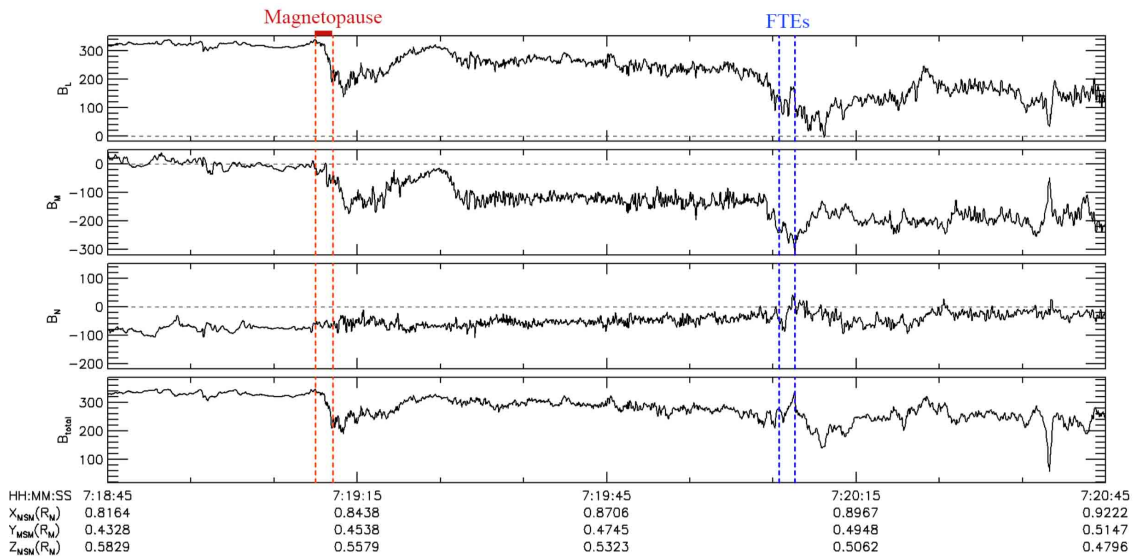


Figure 6.8: Magnetic field measurements in boundary normal coordinates across the dayside magnetopause on 8 May 2012. The magnetopause normal used here was determined from the average magnetopause of Winslow *et al.* [2013].

any of the magnetopause crossings during these extreme intervals. It is also greater than the mean of ~ 0.15 found by analysis of a large number of Mercury magnetopause crossings [DiBraccio *et al.*, 2013]. The magnetosheath β calculation method of DiBraccio *et al.* [2013] results in $\beta_{\text{MSH}} \sim 0.74$. This low value is consistent with a value of $\beta_{\text{MSH}} \sim 0.5$ calculated from the FIPS and MAG measurements. The total magnetic field magnitude, $|\mathbf{B}|$, inside the magnetopause was observed to be $B_{\text{MP}} \sim 328$ nT. Following the same approach as for the previous event, the solar wind dynamic pressure inferred from our magnetopause analysis is 61 nPa (Table 6.1).

6.3.3 11 May 2012

On 11 May 2012 the first magnetopause crossing occurred at 23:21:07 UTC at 26.4° MLAT and an altitude of 615 km, as shown in Figure 6.3. Two minutes of magnetometer measurements are displayed in boundary normal coordinates in Figure 6.9. As shown, there were at least 5 distinct magnetopause crossings at altitudes between ~ 615 and 640 km with other partial, less clear encounters both slightly before and after this interval. As with the previous events, the start and stop times for the rotation of the magnetic field across the magnetopause current layer is marked by the red bar and vertical dashed lines. Four additional complete magnetopause crossings occur over the next ~ 30 s. The vertical dashed lines in Figure 6.9 indicate a large number of FTEs, but as will be discussed later, and unlike the 23 November 2011 event, the 11 May 2012 FTEs are all confined to the vicinity of the low latitude magnetopause encounters. The mean time between the FTEs is ~ 4 s and many good examples of FTE-type flux ropes are present, such as the very large amplitude FTE observed in the magnetopause current layer at 23:21:32 UTC. In addition to the FTEs for which MESSENGER penetrates into the structure and observes the characteristic helical magnetic field structure, there are also many FTE-type TCRs in the magnetic field measurements. These TCR signatures are produced when FTE-type flux ropes are pushed against the magnetopause and compress the internal magnetic field as the solar wind drags them downstream [see Zhang *et al.*, 2008; Slavin *et al.*, 2012].

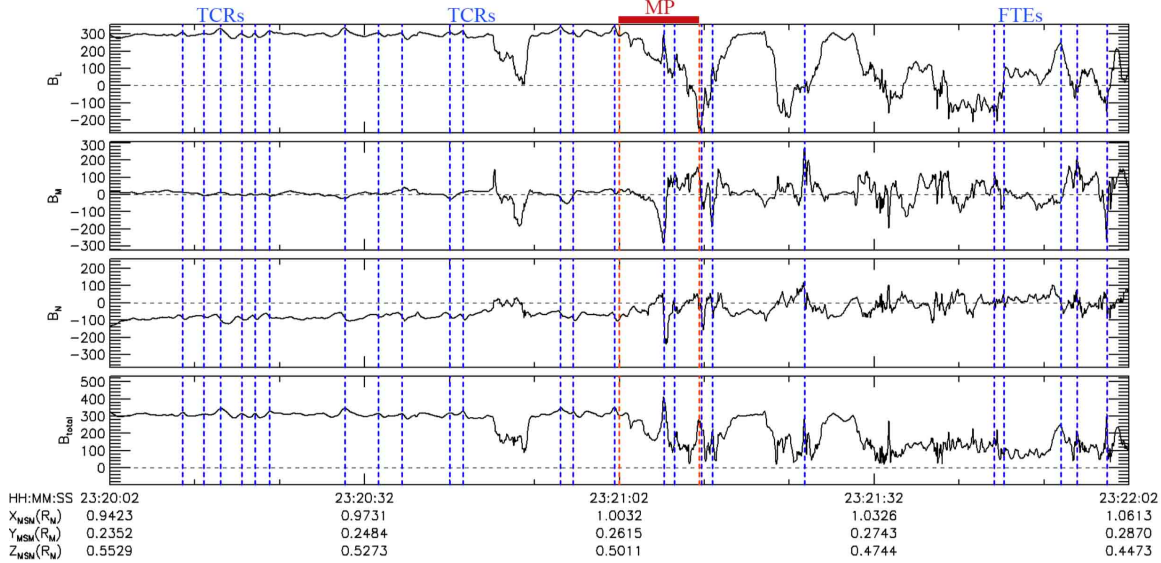


Figure 6.9: Magnetic field measurements in boundary normal coordinates across the dayside magnetopause on 11 May 2012. The magnetopause normal used here was determined from the average magnetopause of *Winslow et al.* [2013].

The IMF in the magnetosheath on 11 May 2012 is variable, but always with a southward component. The magnetic shear angle rotations across these magnetopause crossings were all large and varied from 148 to 166°. The aberrated model normal for the first magnetopause crossing was $\hat{B}_N = (0.93, 0.17, 0.33)$. The negative B_L is observed after this innermost magnetopause crossing and each to follow while B_M is near zero throughout the interval graphed in Figure 6.9. The normal component, B_N , transitions from positive to negative across each of the magnetopause crossings with an average normal field magnitude across the innermost magnetopause current layer of - 26.1 nT. For the later magnetopause current layers the normal magnetic field components ranged from - 9.7 to - 29.4 nT (Table 6.2). The dimensionless reconnection rate resulting from this first magnetopause crossing is $B_N/B_{MP} \sim 0.08$ and the later crossings range from 0.03 to 0.1 with a mean of 0.08.

These reconnection rates are on average about half of the average rate determined by *Slavin et al.* [2009] and *DiBraccio et al.* [2013] and they are the lowest reconnection rates inferred for the three extreme events considered in this study. These low reconnection rates are despite the strongly southward IMF and the very large shear angles. The reason for the very low reconnection rates in comparison with the 23 November 2011 and 8 May 2012 events appears to be the generally high magnetosheath plasma β

values inferred from the magnetic field of up to 8.7 for these magnetopause crossings (Table 6.2). An inverse correlation between magnetopause reconnection rate and magnetosheath β has been known for some time at Earth [Scurry *et al.*, 1994; Anderson *et al.*, 1997; Phan *et al.*, 2010] and was recently found for Mercury [DiBraccio *et al.*, 2013]. The low reconnection rate and high- β magnetosheath found during this high-speed stream event stands in contrast with the two CME events with their higher reconnection rates and low- β magnetosheaths.

The magnetic field intensities just inside these magnetopause crossings range from 318 nT for the first, to 292 nT for the last complete crossing. Using the same technique applied to the 23 November 2011 and 8 May 2012 events, the solar wind dynamic pressure inferred from the first magnetopause crossing on 11 May 2012 is 53 nPa. The solar wind dynamic pressures decrease for each succeeding magnetopause crossing until a value of 44.3 nPa is reached for the fifth and final complete crossing (Table 6.2), consistent with an outward expansion of the magnetopause that overtook MESSENGER multiple times as it moved away from the planet.

6.4 Northern Cusp Observations

Winslow et al. [2012] conducted the first investigation of Mercury's northern magnetospheric cusp. They found that the mean extent of the cusp is 4.5 hrs in local time and 11° in latitude. The equatorward boundary of the cusp is defined as the locus of the most poleward closed field lines in the forward magnetosphere. As reconnection changes the relative amounts of closed and open magnetic flux in the low and high latitude magnetosphere, respectively, the cusp is expected to move in latitude. At Earth the cusp moves equatorward (poleward) with southward (northward) IMF [Burch, 1973; Zhou and Russell, 1997]. The range of latitude over which *Winslow et al.* [2012] found the cusp to be encountered by MESSENGER was $\sim 28^\circ$, but no clear correlation with IMF B_z could be found. However, they did find that the depth of the diamagnetic decrease in the northern cusp magnetic field increases with negative IMF B_x and increasing solar wind ram pressure. Negative B_x is expected, and has been observed to produce strong reconnection at the anti-sunward boundary of Mercury's northern cusp, including "FTE

showers” [Slavin *et al.*, 2012]. While this type of reconnection does not affect the balance between closed and open magnetic flux, it does inject solar wind plasma directly into the cusp and enhances the diamagnetic decrease. Here we examine the northern cusp in the MAG and FIPS measurements that were taken during the three extreme solar wind passes identified in this study. From Figure 6.3 it can be seen that these perigee passes all go through the region where Winslow *et al.* [2012] most frequently observed the cusp.

6.4.1 23 November 2011

The MAG and FIPS measurements collected during the MESSENGER crossing of the northern cusp on 23 November 2011 are displayed in Figure 6.10. As observed by Winslow *et al.* [2012], the poleward boundary of the cusp is marked by enhanced fluctuations and a general decrease in the magnetic field intensity beginning at approximately 10:08:40 UTC and magnetic latitude 80.3° . The minimum in the large wavelength magnetic field strength in the cusp was ~ 150 nT at $\sim 10:10:30$ and magnetic latitude 72.7° . However, the cusp is seen here to be composed of narrow, few sec – long field decreases in which the field strength is reduced to values as low as ~ 50 nT. The larger scale length magnetic field recovers to ~ 250 nT by 10:11:00 UTC with MESSENGER at 70.3° magnetic latitude. But, the narrow, discrete decreases in magnetic field intensity, which began poleward of the cusp proper and exceed 100 nT in depth, continue until 10:14:15 UTC and 54.3° magnetic latitude. This point is over 15° farther equatorward than where the large-scale decrease in the cusp magnetic field ends. We call these several second long discrete diamagnetic decreases “cusp plasma filaments” reflecting their spatial association with the cusp. We use the term filament to reflect the presumed diamagnetic origin of the field decrease implying columns of enhanced plasma density aligned with the local magnetic field. The total latitudinal extent of the 23 November 2011 cusp crossing based upon the large-scale magnetic field decrease was $\sim 10^\circ$ and the maximum diamagnetic decrease was ~ 200 nT or 16 nPa of equivalent plasma pressure. These values compare with the typical cusp values of $\sim 11^\circ$ and thermal plasma pressures of 2 to 3 nPa [Winslow *et al.*, 2012]. This suggests that the major differences between this extreme solar wind pressure event and the more typical cusp is the great depth of the diamagnetic decrease and the presence of these isolated cusp

filaments that begin poleward of the cusp and extend to latitudes at least as low as 54° magnetic latitude. Below this latitude the fluctuations in the magnetic field continue, but they correspond to flux transfer events. In the next section both the cusp filaments and the FTEs observed during this event will be further examined.

FIPS proton differential energy flux measured during this periapsis pass is displayed in Figure 6.10a. Consistent with the earlier surveys of the FIPS plasma data [Zurbuchen *et al.*, 2008; Raines *et al.*, 2014] high fluxes of ~ 100 eV to ~ 3 keV protons are measured during the cusp pass. FIPS Na^+ ions counts are displayed in Figure 6.10b.

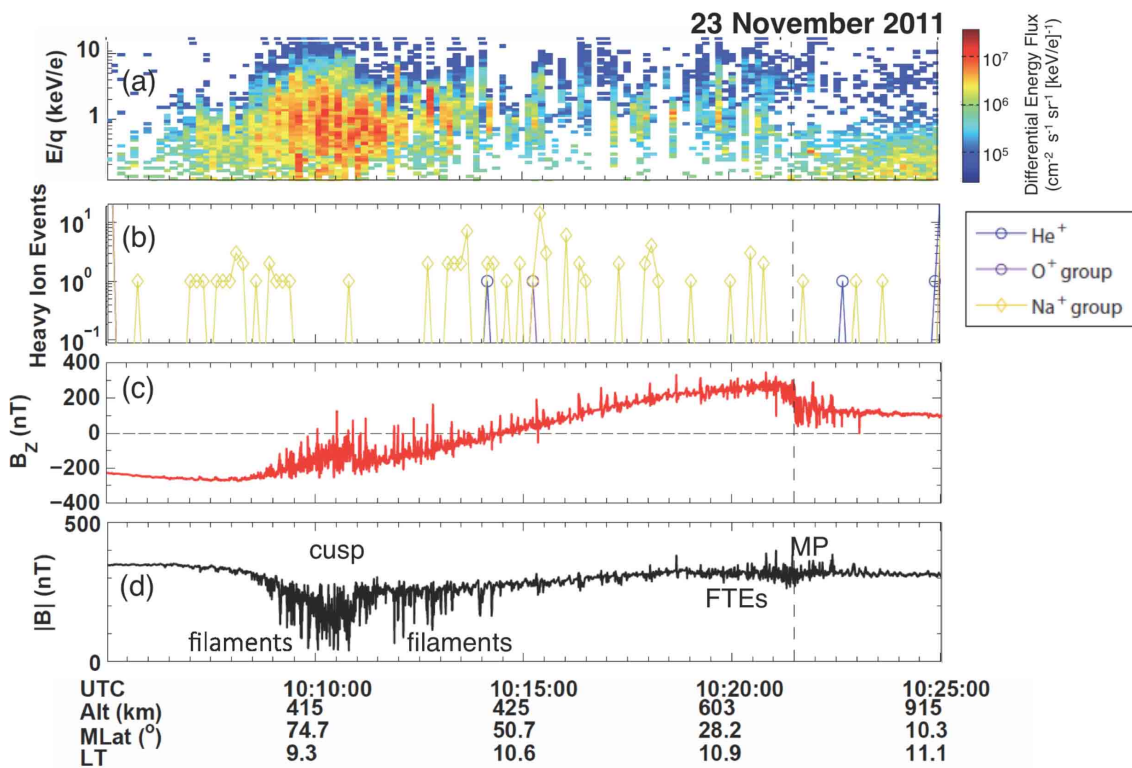


Figure 6.10: (a) Proton differential energy flux as a function of UTC for the 23 November 2011 periapsis pass. (b) Heavy ion counts binned by three composition types: He^+ , O^+ group ($m/q = 14-20$), and Na^+ group ($m/q = 21-0$). (c) B_z component of the magnetic field in MSM coordinates and (d) total magnetic field intensity plotted versus UTC. The locations of the cusp and magnetopause are labeled.

Na^+ was observed at a moderately constant count rate across the full periapsis pass. Short-lived enhancements in the proton flux near 1 keV are observed at the poleward edge of the cusp all the way down to the magnetopause at $\sim 25.4^\circ$ magnetic latitude. It will be shown that at higher latitudes these single energy-scan proton flux enhancements are generally correlated with the narrow cusp filaments while at lower latitudes these

peaks in the proton flux are frequently coincident with FTE signatures in the magnetic field data.

The near-constant magnetic field intensity across the magnetopause on 23 November 2011 indicates that a strong plasma depletion layer is present in the adjacent magnetopause. Figure 6.11 presents the FIPS proton measurements just upstream of the

Plasma Depletion Layer UTC 10:23:00-10:25:30, 23 November 2011

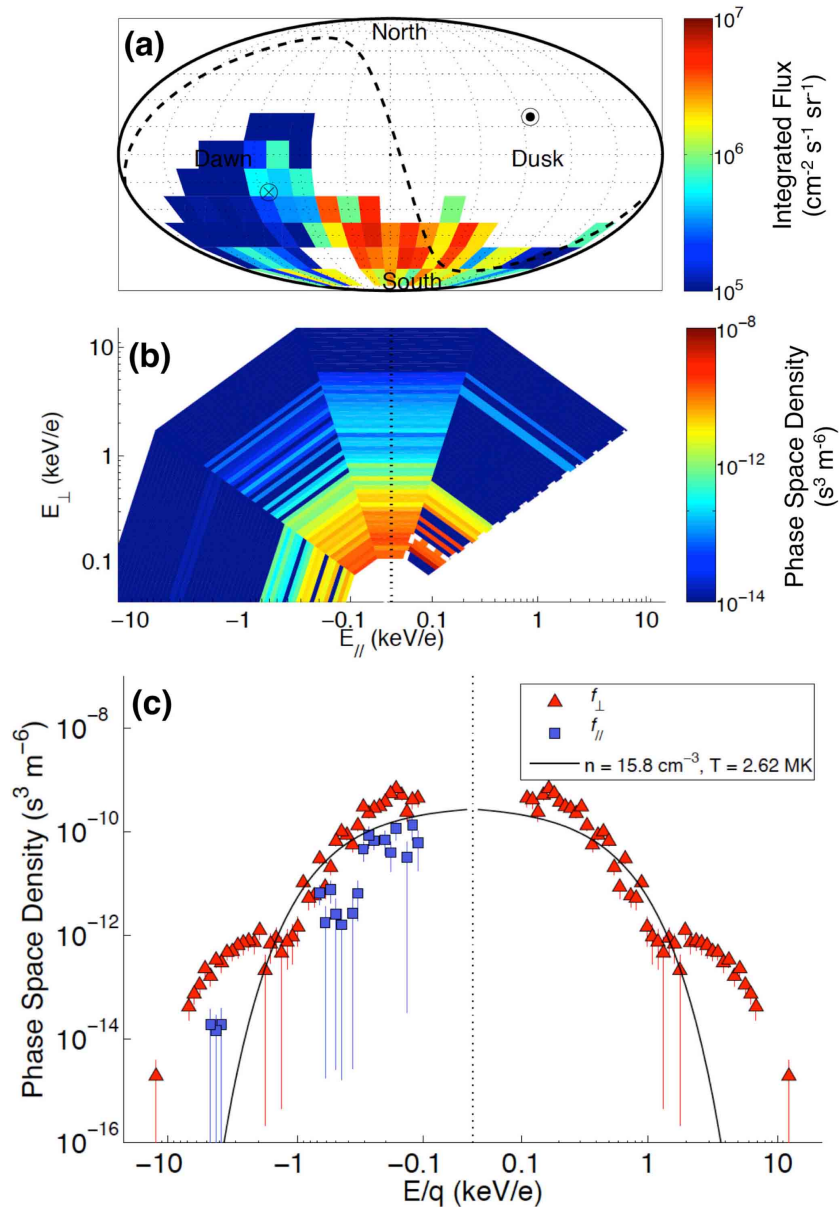


Figure 6.11: (a) All-sky map of integrated proton flux in the plasma depletion layer on 23 November 2011 with the north and south poles and the dawn and dusk directions indicated. (b) Proton phase space distribution. (c) Single temperature fit to the proton distribution function.

magnetopause between 10:23:00 – 10:25:30 UTC. The unobstructed field-of-view available to FIPS is limited, as shown in Figure 6.11a. Hence, assuming gyrotropy, most of the distribution function can be imaged as displayed (Figure 6.11b). Moment-based calculations of density and a single isotropic temperature yield values of 15.4 cm^{-3} and $2.62 \times 10^6 \text{ K}$ (Figure 6.11c). When separate temperatures parallel and perpendicular to the local magnetic field are allowed, the resulting values are $\sim 1 \times 10^6$ and $3 \times 10^6 \text{ K}$, respectively, consistent with the expected perpendicular heating in the PDL due to compression by the pressure of the upstream solar wind [Zwan and Wolf, 1975; Gershman et al., 2013]. Given the $\sim 315 \text{ nT}$ magnetic field magnitude, the plasma β in the PDL based upon a single isotropic temperature is only 2×10^{-3} , consistent with the lack of any change in magnetic field magnitude across the magnetopause.

6.4.2 8 May 2012

The MAG and FIPS measurements for the 8 May 2012 periapsis pass from the poleward side of the cusp through the dayside subsolar magnetopause crossing are shown in Figure 6.12. The FIPS measurements for 8 May 2012 are similar in many respects to the 23 November 2011 extreme cusp. The planetary ions are present from poleward of the cusp down through the magnetopause at magnetic latitude $\sim 26.7^\circ$. However, in the proton data it is clear that the field of view is much more favorable than for the previous extreme event and the overall flux levels are significantly higher. The high-latitude boundary of the cusp based upon the onset of the large diamagnetic decrease in the total magnetic field intensity occurs at 07:10:50 UTC when MESSENGER was at 70.5° magnetic latitude. The center of the large-scale diamagnetic decrease was at $\sim 07:12:00$ UTC which corresponds to 64.7° magnetic latitude. Short-duration diamagnetic decreases in the cusp magnetic field intensity are present as during the 23 November 2011 event, but somewhat deeper with minimum magnetic field intensities of less than 20 nT. The equatorward edge of the cusp in the large-scale diamagnetic signature on 8 May 2012 is at $\sim 07:13:00$ UTC which occurred at a magnetic latitude of $\sim 57.9^\circ$. Unlike the 23 November 2011 extreme cusp, there are no further deep diamagnetic decreases south of the equatorward edge of the main diamagnetic decrease, and the FTE activity is limited to the region immediately adjacent to the magnetopause. Close inspection of the

Figure 6.12a proton spectra also shows the clear signature of the boundary layer between the two magnetopause-like magnetic field rotations, which are marked with vertical dashed lines, as discussed earlier.

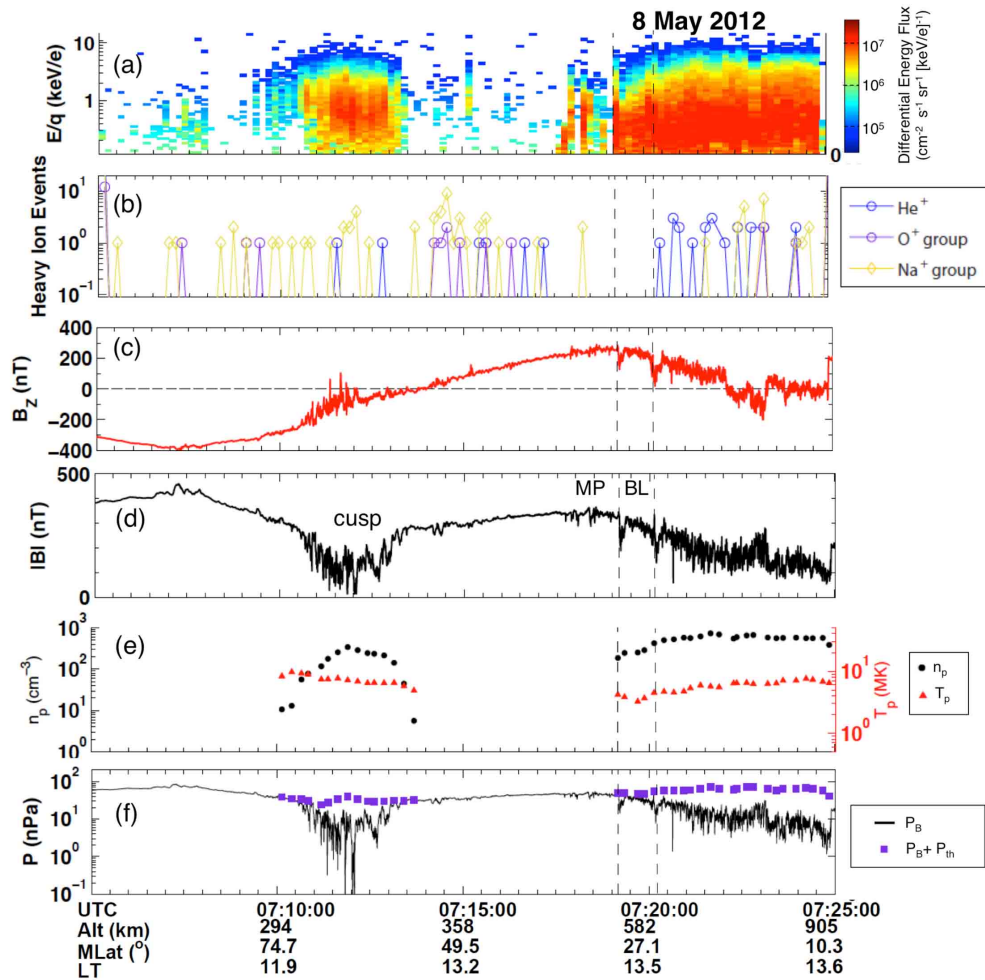


Figure 6.12: (a) Proton differential energy flux as a function of UTC for the 8 May 2012 periapsis pass. (b) Heavy ion counts binned by three composition types: He^+ , O^+ group, and Na^+ group. (c) B_z component of the magnetic field in MSM coordinates, (d) total magnetic field intensity plotted versus UTC, (e) proton density and temperature, and (f) magnetic and proton thermal pressure. The locations of the cusp and magnetopause are shown.

The proton density and temperature for individual FIPS energy-scans are displayed in Figure 6.12e, enabled by the higher overall flux in this cusp. In the cusp region the correlation between the hot, dense proton population and the large-scale diamagnetic decrease in the total magnetic field is very clear as expected from previous studies [Winslow *et al.*, 2012; Raines *et al.*, 2014]. In the magnetosheath, the density and

temperature increase away from the magnetopause toward the bow shock consistent with a plasma depletion layer [Gershman *et al.*, 2013], albeit not so depleted as on 23 November 2011 when no change in magnetic field intensity was evident across the magnetopause. Figure 6.10f shows that the proton densities and temperatures determined from the FIPS measurements produce thermal pressures that match the diamagnetic decreases in the cusp and bring the magnetic and plasma pressures across the magnetopause into approximate balance. Figure 6.13c displays the proton distribution

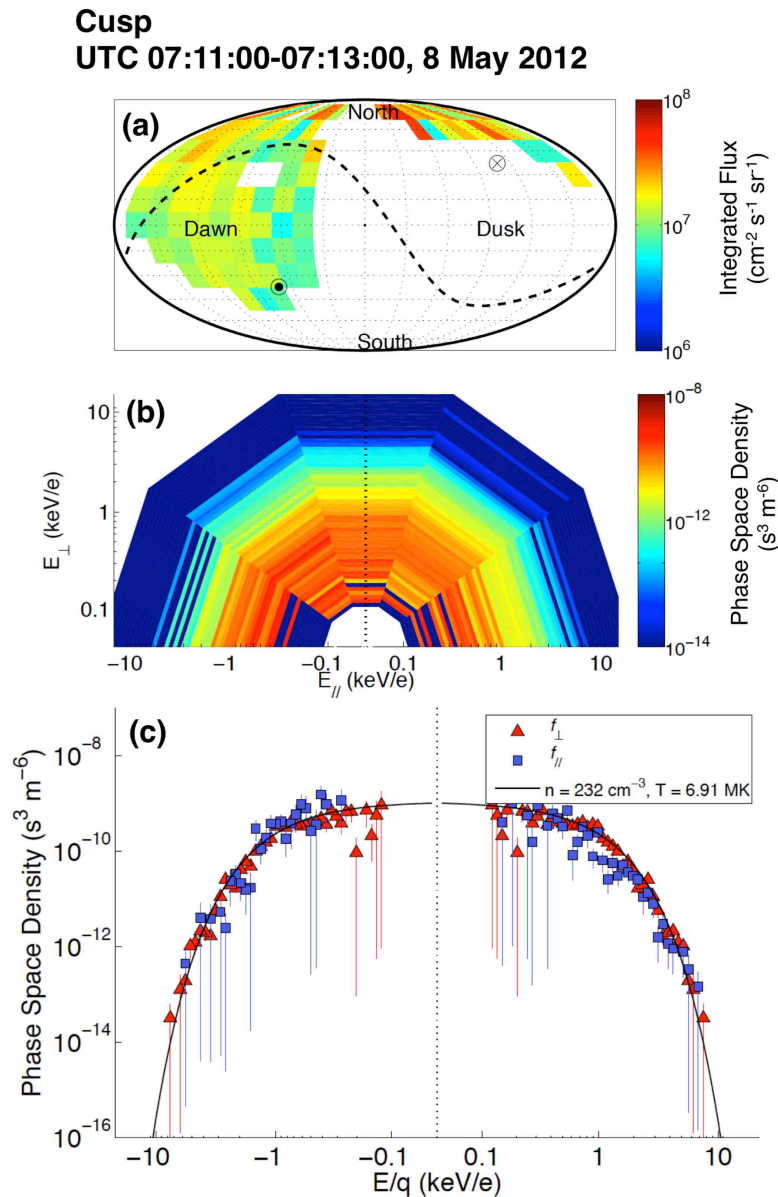


Figure 6.13: (a) All-sky map of integrated proton flux in the northern cusp on 8 May 2012 with the north and south poles and the dawn and dusk directions indicated. (b) Proton phase space distribution. (c) Single temperature fits to the proton distribution function.

integrated over the cusp interval along with the field-of-view and moment-derived equivalent Maxwellian for the cusp data [Gershman *et al.*, 2013; Raines *et al.*, 2014]. The distribution function is clearly much more isotropic than for the previous event, as evidenced by comparing the various angular bins in Figure 6.13b. The parallel and perpendicular slices of the distribution function also agree very well with the modeled Maxwellian (black line). Taking moments of this distribution, summed over the entire cusp, yields $n_p = 232 \text{ cm}^{-3}$ and $T_p = 6.9 \times 10^6 \text{ K}$.

6.4.3 11 May 2012

The 11 May 2012 MAG and FIPS measurements from the poleward side of the cusp through the dayside subsolar magnetopause crossing are shown in Figure 6.14. The high-latitude boundary of the cusp based upon the onset of the large-scale diamagnetic decrease in the total magnetic field intensity occurs at 23:09:54 UTC when MESSENGER was at 77.8° magnetic latitude. The center of the large-scale diamagnetic

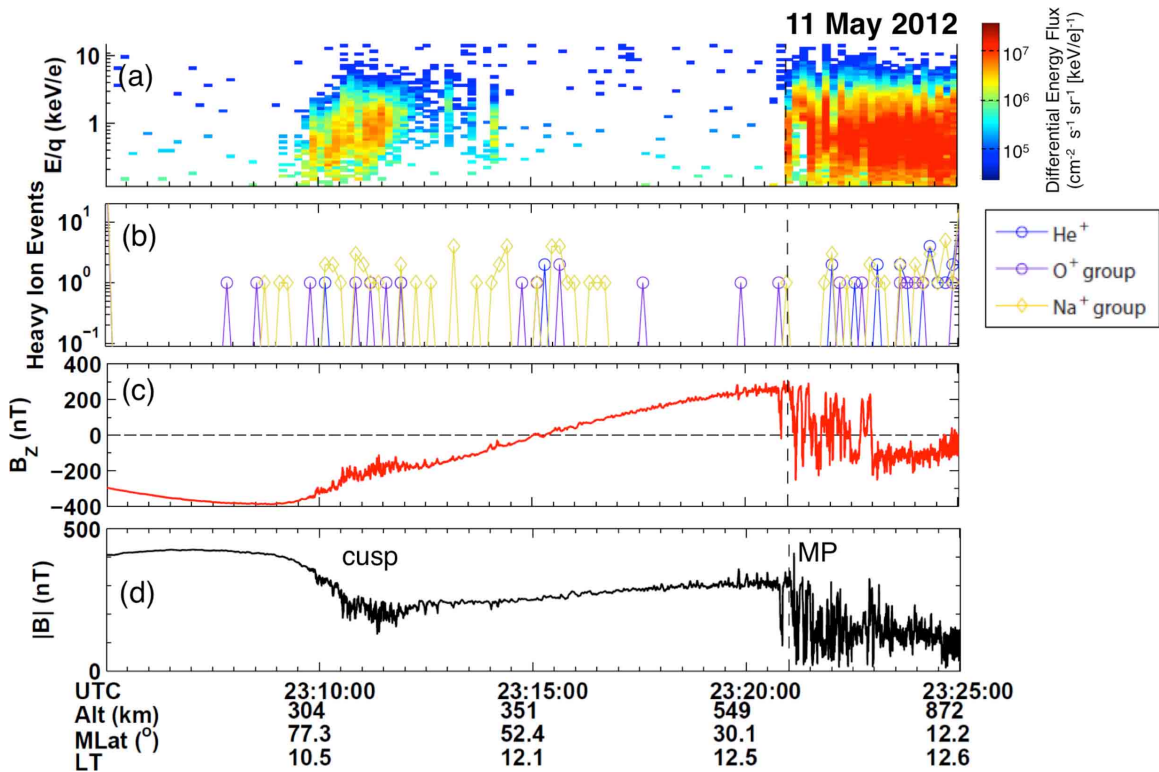


Figure 6.14: (a) Proton differential energy flux as a function of UTC for the 11 May 2012 periapsis pass. (b) Heavy ion counts binned by three composition types: He^+ , O^+ group, and Na^+ group. (c) B_z component of the magnetic field in MSM coordinates and (d) total magnetic field intensity plotted versus UTC. The locations of the cusp and magnetopause are shown.

decrease was at 23:11:08 UTC which corresponds to 71.9° magnetic latitude with MESSENGER at an altitude of 300 km. The diamagnetic decreases in the total cusp magnetic field intensity are less structured than the 23 November 2011 and 8 May 2012 extreme event, and the overall decrease in the magnetic field intensities is much less with the magnetic field not falling below 150 nT except for two short duration excursions to ~ 120 nT. The equatorward edge of the cusp on 11 May 2012 in the diamagnetic signature is at 23:12:47 UTC which occurred at a magnetic latitude of $\sim 63.7^\circ$. Unlike the 23 November 2011 extreme cusp, there are only two further weak diamagnetic decreases south of the equatorward edge of the main diamagnetic decrease. In contrast with the 23 November 2011 event, but like the 8 May 2012, the FTE activity is limited to the region adjacent to the magnetopause.

The FIPS proton differential energy flux spectra are shown in Figure 6.14a. The FOV and look directions for this pass are, like 8 May 2012, favorable and hot proton distributions with energies up to $\sim 1 - 2$ keV are present in the cusp and the magnetosheath adjacent to the magnetopause. Planetary Na^+ and O^+ ions are present during the pass, but primarily closer to the cusp and in the magnetosheath. The proton distribution function and Maxwellian fits to the data are inter-compared in Figure 6.15. As shown the fits to the integrated proton distribution yield $n_p = 69.1 \text{ cm}^{-3}$ and $T_p = 7.5 \times 10^6 \text{ K}$. Two-dimensional fits for the temperature give $T_{\text{para}} = 4 \times 10^6 \text{ K}$ and $T_{\text{perp}} = 7 \times 10^6 \text{ K}$, consistent with the apparent anisotropy in the distribution (Figure 6.15b-c). While these proton temperatures are similar, the density is only $\sim 30\%$ of that during the 8 May 2012 cusp crossing.

6.5 Cusp Plasma Filaments and Flux Transfer Events

Two minutes of MAG and FIPS measurements taken just after and equatorward of the magnetospheric cusp encounter on 23 November 2011 are shown in Figure 6.16. The top panel displays the proton differential energy spectra for each integration period. FIPS steps through energy per charge (E/q) steps sequentially, from 13.3 keV to 46 eV, with ~ 150 ms between steps. The next panel contains the same proton data, but with the time of the individual E/q steps displayed. The proton flux per E/q step profiles are

Cusp
UTC 23:10:00-23:12:00, 11 May 2012

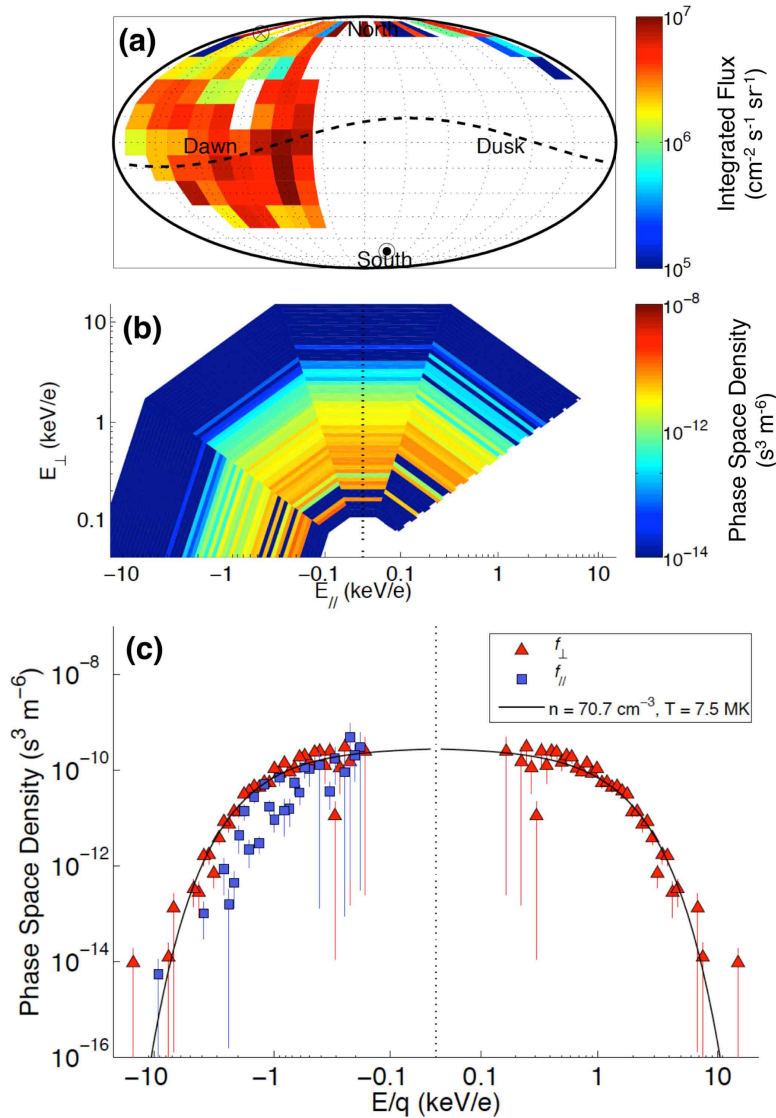


Figure 6.15: (a) All-sky map of integrated proton flux in the northern cusp on 23 November 2011 with the north and south poles and the dawn and dusk directions indicated. (b) Proton phase space distribution. (c) Single temperature fit to the proton distribution function.

plotted over the total magnetic field. Figure 6.16c shows the B_z component of the magnetic field. Vertical dashed lines mark the brief decreases in field magnitude that identify them as cusp filaments. Because the cusp plasma filaments are only $\sim 1 - 2$ s in duration, the individual 8-s energy spectra in Figure 6.16a show peak differential flux only at the E/q step that was being measured at the time that the filament swept over MESSENGER. However, it is clear that strong increases in proton flux are observed whenever FIPS was making measurements near 1 keV for protons, which is close to their

mean energy in the magnetosheath, during traversals of these cusp filaments. Lower fluxes are observed when FIPS is making measurements at higher or lower energies as the filament moves over MESSENGER.

Two minutes of MAG and FIPS measurements taken as MESSENGER approached the magnetopause on 23 November 2011 are shown in Figure 6.17 in the same format as the previous figure. Vertical dashed lines mark bipolar $\pm \Delta B_Z$ variations in the magnetic field that are correlated with peaks in the total field. As already discussed relative to Figure 6.7, which displayed the 23 November 2011 outbound magnetopause crossing in boundary normal coordinates, these are FTE perturbations due to the motion of flux ropes formed at the magnetopause by pulses of reconnection at multiple X-lines [Russell and Elphic, 1978; Rijnbeek et al., 1984; Lee and Fu, 1985; Wang et al., 2005].

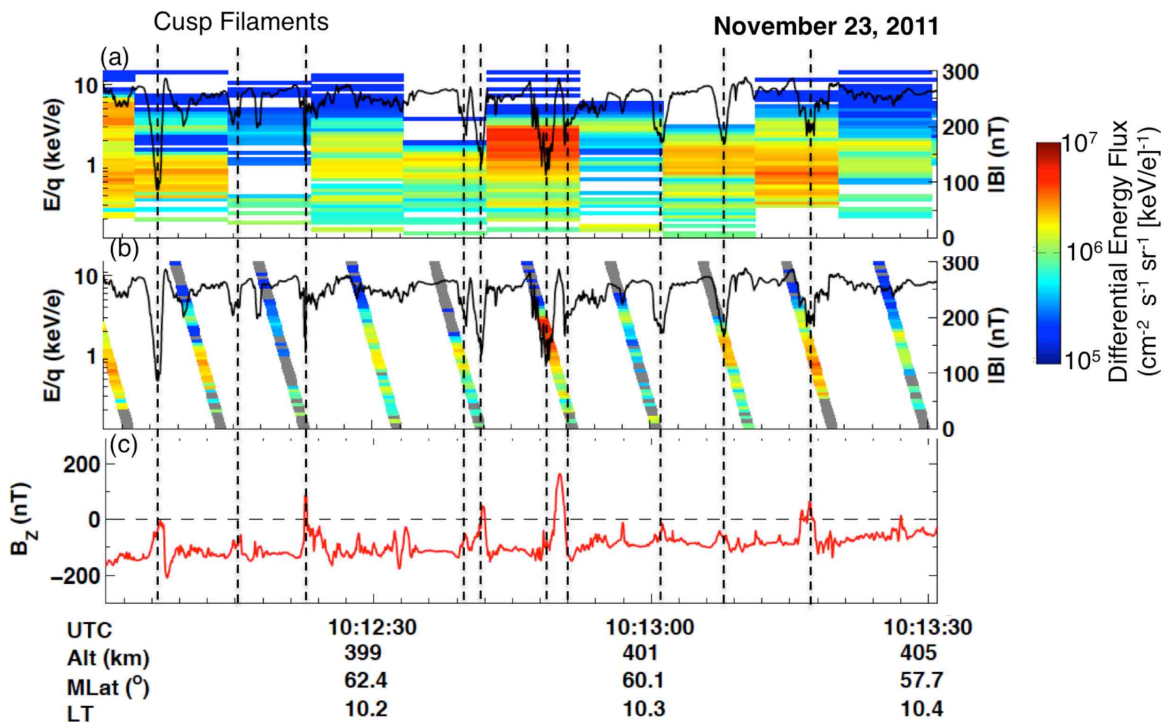


Figure 6.16: (a) Proton differential energy flux over plotted versus UTC. The intensity of the magnetic field is shown in black. (b) Differential flux plotted versus energy along gray diagonal bands depicting energy step as function of UTC. The intensity of the magnetic field is shown in black. (c) B_z is displayed in MSM coordinates. Vertical dashed lines indicate cusp filament events.

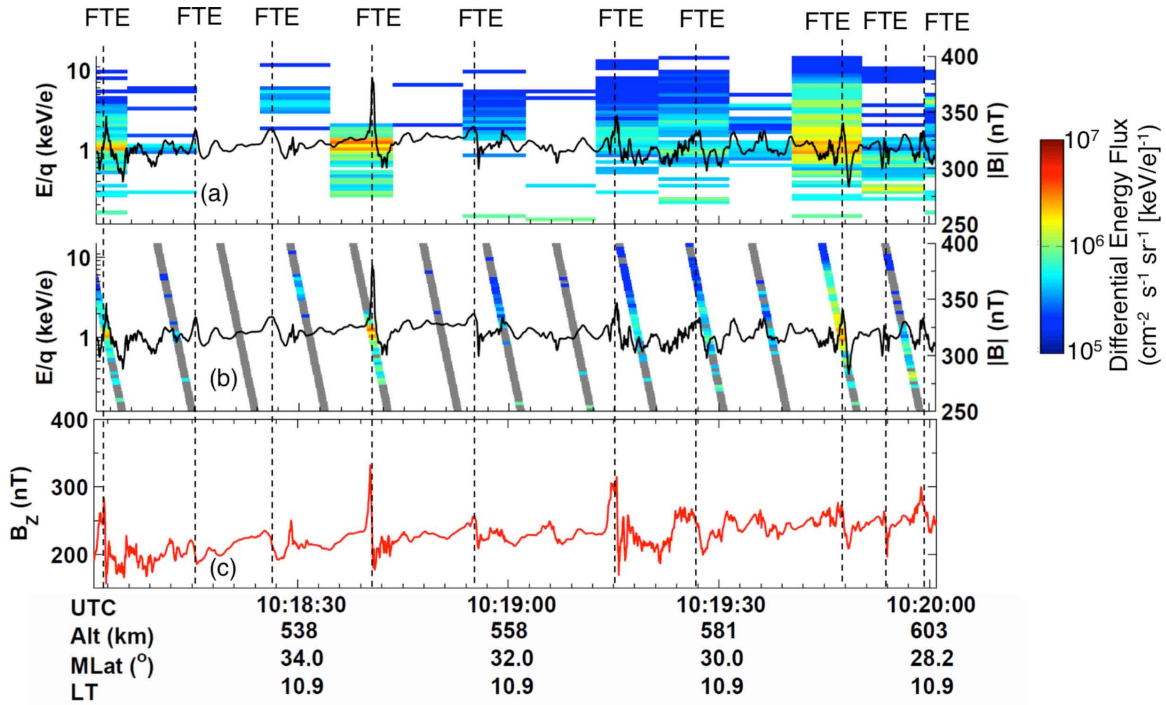


Figure 6.17: (a) Proton differential energy flux over plotted versus UTC. The intensity of the magnetic field is shown in black. (b) Differential flux plotted versus energy along gray diagonal bands depicting energy step as function of UTC. The intensity of the magnetic field is shown in black. (c) B_z is displayed in MSM coordinates. Vertical dashed lines indicate flux transfer events.

6.6 Magnetopause Altitude vs. Solar Wind Pressure

The locations of the magnetopause with respect to Mercury during the three extreme solar wind intervals investigated here are examined in Figure 6.18. Solar wind aberrated, cylindrical MSM coordinates are used and the magnetopause is assumed to always have the mean shape determined by *Winslow et al.* [2013]. Their fit to a large ensemble of magnetopause crossings with its mean solar wind standoff distance of $1.45 R_M$ is shown as the outermost dashed surface. Mercury's surface north and south of the magnetic equator, which is located at $Z'_{MSM} \sim 0.2 R_M$, are graphed separately in these coordinates to call attention to the strong effect of dipole offset on magnetopause altitude (see also Figure 6.3).

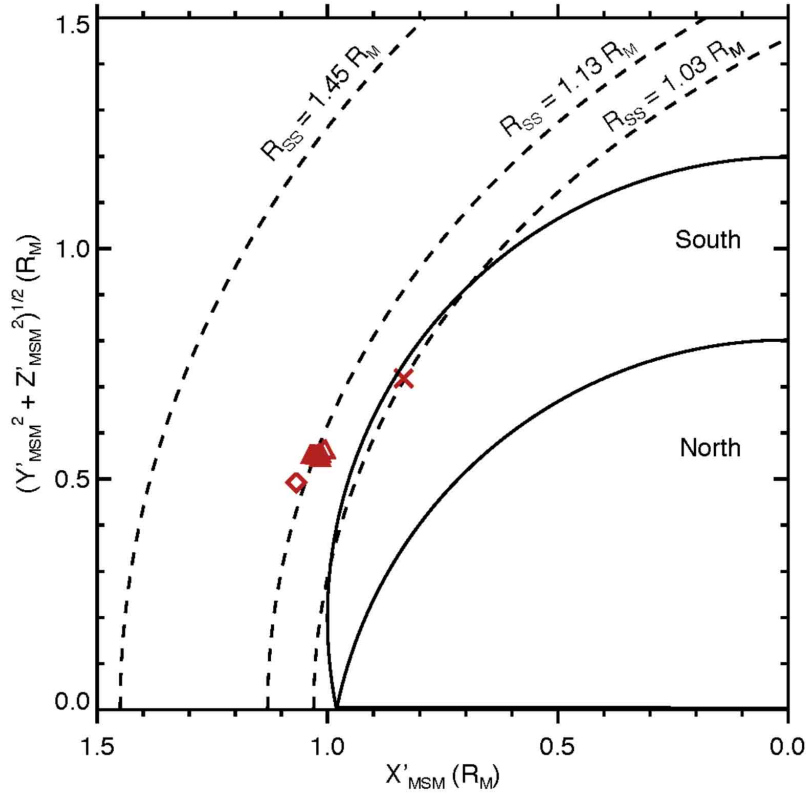


Figure 6.18: The *Winslow et al.* [2013] magnetopause model surface is displayed in aberrated cylindrical coordinates for mean, $R_{SS} = 1.45 R_M$, and extreme $R_{SS} = 1.05 R_M$, solar wind pressure conditions. The 23 November 2011, 8 May 2012, and 11 May 2012 magnetopause crossings are indicated with diamonds, x's, and triangle symbols.

The 23 November 2011 and 11 May 2012 magnetopause crossings cluster together and, as shown, suggest a solar wind standoff distance of $1.13 R_M$. The upstream solar wind dynamic pressures inferred from the analyses of these magnetopause crossings range from 44.3 to 53 nPa (Table 6.1). The reconnection rates determined from the magnetic field variations across the magnetopause range between 0.03 and 0.10 (Table 6.2). However, the 8 May 2012 magnetopause is located much closer to the planet with a standoff of only $1.03 R_M$. The upstream solar wind pressure and the reconnection rates determined for this magnetopause crossing are 65 nPa and 0.22, respectively. As shown in the Figure 6.18 the combined effect of this extremely high solar wind dynamic pressure and high dayside reconnection rate appear sufficient to bring the magnetopause into contact with the surface of Mercury at middle magnetic latitudes in the southern hemisphere.

In Figure 6.19 the solar wind ram pressure at the subsolar point, P_{ss} , is plotted against the magnetopause solar wind standoff distance, R_{ss} . Using a large data set of MESSENGER magnetopause crossings collected during solar wind pressures between ~ 5 and 15 nPa, *Winslow et al.* [2013] determined a sixth-root relationship between P_{ss} and R_{ss} displayed in Figure 6.19 with thin dashed line. Absent other effects, this earth-like relationship between upstream solar wind pressure and solar wind stand-off distance implies that the magnetopause would be compressed down to the subsolar magnetic equator of Mercury when the upstream pressure reaches ~ 90 nPa.

However, Mercury is known to have a very large, highly conducting iron core that has a radius of ~ 2000 km [*Smith et al.*, 2012] compared with Mercury's radius of 2440 km. As discussed earlier, and illustrated in Figure 6.2, the compression of the dayside magnetosphere will induce electric currents in the outermost layers of Mercury's core that add to the closed magnetic flux in dayside magnetosphere and temporarily increase the magnetic moment of Mercury [*Hood and Schubert*, 1979; *Suess and Goldstein*, 1979]. The bold dashed curve in Figure 6.19 is the predicted relationship between solar wind ram pressure and magnetopause standoff distance with the effects of induction included [*Glassmeier et al.*, 2007]. The models of the effect of induction on solar wind stand-off distance at Mercury all predict that R_{ss} will only be compressed below $\sim 1.2 R_M$ for solar wind pressures greater than ~ 90 nPa. However, as shown, MESSENGER observes individual magnetopause during the extreme solar wind pressure events studied here to be located at distances as small as $1.03 R_M$ for pressures of only ~ 65 nPa.

The most likely reason for the closeness of the magnetopause to Mercury's surface during these events is the effect of reconnection and its transfer of magnetic flux into the tail [*Slavin and Holzer*, 1979]. In effect, dayside magnetic reconnection appears to be negating much of the shielding effect of the dayside induction currents during these extreme events. Indeed, the magnetopause crossings observed during the extreme solar wind events considered here fall roughly along this sixth-root, Chapman-Ferraro-type pressure balance curve (short dashes) with the higher and lower reconnection rate crossings lying $\sim 0.2 - 0.3 R_M$ closer and farther, respectively, from the offset dipole. These variations in magnetopause altitude suggest that, on average, the effects of erosion [*Slavin and Holzer*, 1979] and induction [*Hood and Schubert*, 1979] are in approximate

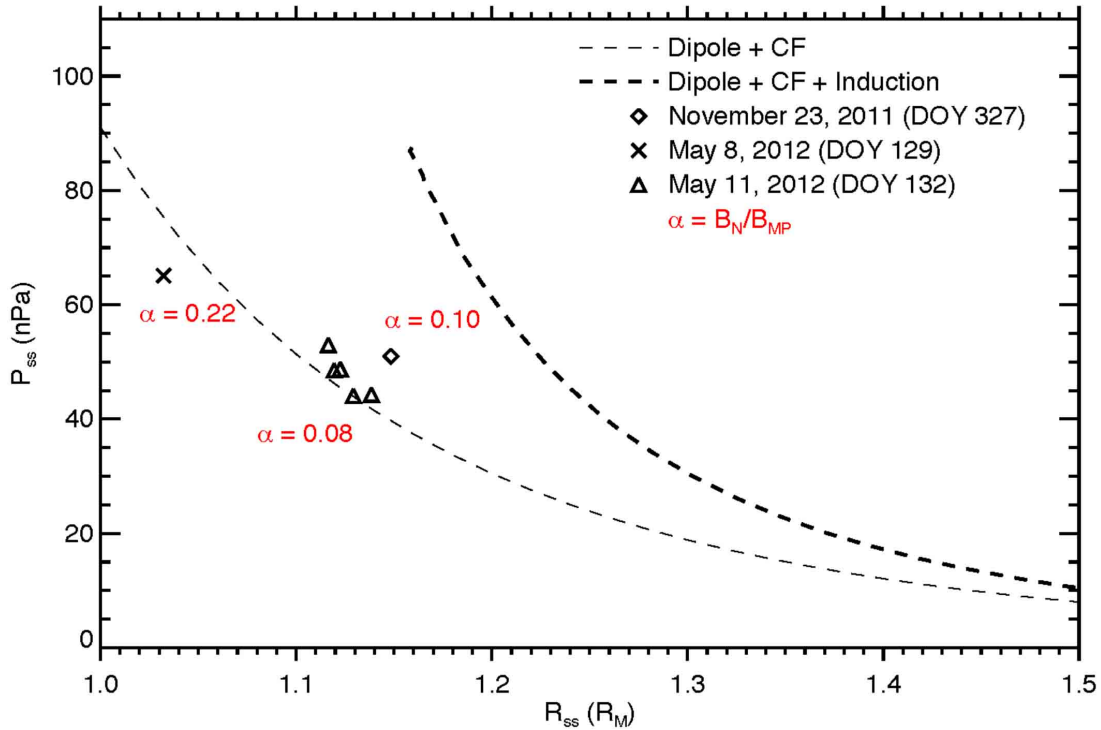


Figure 6.19: (a) The subsolar solar wind ram pressure, P_{ss} , is plotted against the extrapolated magnetopause stand-off distance for the magnetopause crossings observed during the three extreme solar wind events, $P_{ss} \sim 45$ to 65 nPa, are shown as diamonds, X's and triangle. The sixth-root relationship determined by *Winslow et al.* [2013] (short dashes) determined from a large dataset of MESSENGER magnetopause encounters at typical upstream pressures of ~ 5 to 15 nPa is shown as a dashed line. A theoretical model that includes the effects of induction in Mercury's interior developed by *Glassmeier et al.* [2007] is graphed as bold dashes.

balance. In this context the magnetopause displacement to lower altitudes due to magnetic reconnection compensates for the increased planetary moment due to induction that acts to displace the magnetopause to higher altitudes. The induction still occurs, consistent with the high ram pressures, and still contributes to an enhanced planetary magnetic moment, but the location of the magnetopause for these extreme pressure events with strong magnetic reconnection is at lower altitudes than would be expected for induction alone.

6.7 Discussion

MESSENGER observations taken during three extreme solar wind dynamic pressure events have been presented and analyzed. Two were due to CMEs and one to a

high-speed stream. The strength of the bow shock for the CME events was markedly weaker than for the high-speed stream event. The locations of the bow shock for the CME events were also more distant from Mercury than was the case for the high-speed stream event. These facts strongly argue that the solar wind Mach numbers for the CME events were much lower than for the high-speed stream event. The CME events also produced thick, low- β plasma depletion layers in the inner magnetosheath adjacent to the subsolar magnetosheath. These PDLs are apparent in the low plasma densities and high temperatures measured by FIPS just outside of the magnetopause [see Figure 6.9; *Gershman et al.*, 2013]. The high-speed stream event, in contrast, produced a high- β magnetosheath and no plasma depletion layer. This is reflected in both the large decrease in magnetic field intensity across the magnetopause and the high plasma densities measured by FIPS in the adjacent magnetosheath. The inferred solar wind pressures for all of these events are extreme, ~ 44 to 65 nPa as compared to the mean value of 14.3 nPa for the MESSENGER mission [*Winslow et al.*, 2013].

When strong PDLs are present, such as is the case for the CME events studied here, the magnetic field intensity becomes nearly equal on both sides of the magnetopause. Under these conditions reconnection is allowed for all non-zero magnetic shear angles with the X-line bisecting the planetary field inside of the magnetopause and the draped IMF in the external magnetosheath [*Sonnerup*, 1974; *Anderson et al.*, 1997; *Eastwood et al.*, 2013]. This situation is shown qualitatively for the two low- β , small-to-moderate shear events observed on 23 November 2011 and 8 May 2012 in Figure 6.20a-b. The draped IMF field lines (red) reconnect with the planetary field to create new merged field lines with the resultant “kink” being 90° or less. In this case the flow away from the extended X-line is as much or more in the east and west direction as in the north and south directions. In contrast, the reconnected flux in the high- β , high-shear conditions associated with the high-speed stream on 11 May 2012 is much more kinked and the flow away from the X-line is largely in the north and south directions, as depicted in Figure 6.20c.

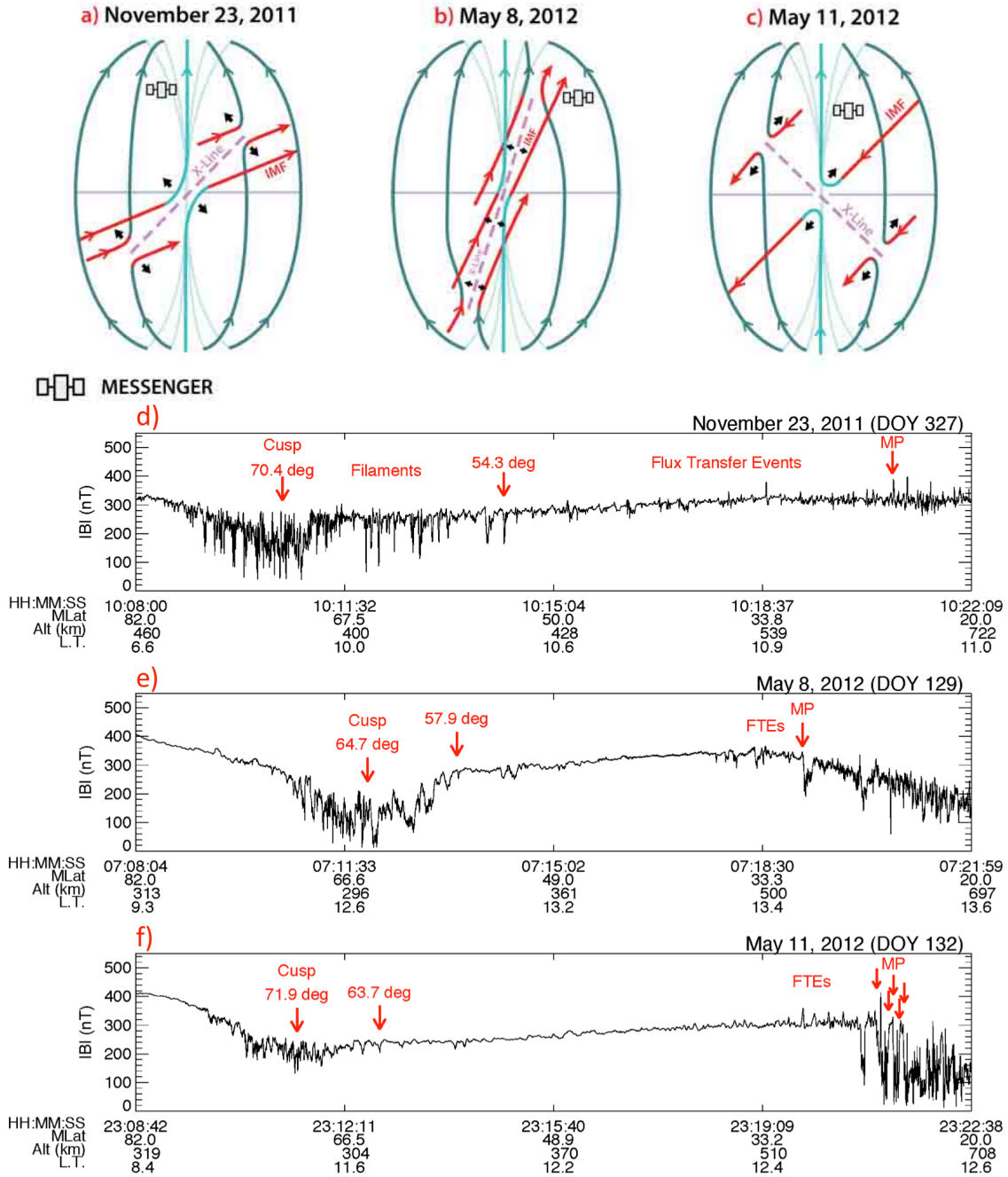


Figure 6.20: Total magnetic field intensity is displayed versus UTC for each of the extreme solar wind passes when MESSENGER was between magnetic latitudes between 82° and 20° . The center of the central magnetic cusp depression in $|B|$ and the lowest latitude where the narrow magnetic field depressions associated with plasma filaments are observed. The occurrence of flux transfer events and magnetopause crossings and the dimensionless reconnection rates, measured at the magnetopause, are also called out.

The reconnection rates determined from the normal magnetic field to the magnetopause, i.e., 0.1–0.2, for the two CME events, 23 November 2011 and 8 May 2012, were comparable to or greater than the mean Mercury reconnection rates measured

by *DiBraccio et al.* [2013]. They are also significantly greater than the 0.03 – 0.10 measured for the high-speed stream event. These results at Mercury regarding the relationship between low M_A , plasma- β , magnetic shear angle, and reconnection rate observed here for these extreme events not only support other recent Mercury studies [*DiBraccio et al.*, 2013; *Gershman et al.*, 2013], but they are paralleling the latest developments regarding PDL formation under low M_A [*Lavraud et al.*, 2013] and reconnection as a function of plasma- β [*Phan et al.*, 2013]. At Earth the magnetosheath is typically high- β and this often limits fast reconnection to IMF orientations that have a southward component, i.e., magnetic shear angles across the magnetopause greater than 90° (i.e., the half-wave rectifier effect).

MESSENGER's observations of the northern cusp of Mercury during these three extreme solar wind perigee passes are displayed in Figure 6.20d-f. During all of these extreme events the northern cusp became unusually deep with the average cusp magnetic field intensity dropping from ~ 300 nT to ~ 100 nT at MESSENGER altitudes due to the inflow of solar wind plasma from the magnetosheath. In the bottom panels of Figure 6.20 the magnitude of the magnetic field is plotted versus UTC with the start and stop times selected so that they begin at 82.0° and end at 20.0° MLAT. The 23 November 2011 and 11 May 2012 cusps have similar poleward edges and centers, $80 - 78^\circ$ and $73 - 72^\circ$ MLAT, respectively. The 8 May 2012 periapsis pass cusp is at significantly lower latitudes, beginning at 70.5° , and an equatorward edge at 57.9° . The center of the central diamagnetic depression is at 64.7° . The depth of the large-scale magnetic field decrease during the 8 May 2012 cusp crossing is much greater than for the 23 November 2011 and 11 May 2012 diamagnetic decreases with the minima for 8 May 2012 being less than ~ 20 nT.

At Earth the depth and latitudinal breadth of the cusp diamagnetic decreases is controlled by the rate of reconnection at the dayside magnetopause and just tailward of the cusp and the dynamic pressure of the solar wind [*Reiff et al.*, 1977; *Newell and Meng*, 1987; *Zhou et al.*, 2000]. The fact that the cusp diamagnetic signatures recorded during these extreme events are much larger than the average values reported by *Winslow et al.* [2012] suggests that Mercury's cusp responds to increasing solar wind pressure in much the same manner as at the Earth. The broadest and deepest of the three extreme cusps

considered here is the 8 May 2012 event (see Figure 6.20d-f). In agreement with expectations based upon observations at Earth, the 8 May 2012 extreme event had the highest solar wind pressure and the highest reconnection rate at the dayside magnetopause. At Earth equatorward displacements of the cusp are strongly correlated with southward IMF [Burch, 1973] and other predictors of dayside reconnection and energy input to the magnetosphere [Newell *et al.*, 2006]. Winslow *et al.* [2012] did not observe a correlation between the north-south component of the IMF and the latitude of Mercury’s cusp. However, it was later found by DiBraccio *et al.* [2013], and supported by the extreme events analyzed in this study, that the intensity of dayside reconnection at Mercury is primarily determined by M_A and the formation of low- β plasma depletion layers and not the north – south component of the upstream IMF. Hence, the fact that the 8 May 2012 event, which had the highest dayside reconnection rate of the three extreme events, occurs at the lowest magnetic latitude is in agreement with the Earth result that dayside reconnection transfers magnetic flux to the magnetotail and reduces the latitude of the cusp. Raines *et al.* [2014] concluded that large fluxes of protons and planetary ions measured between the equatorward edge of the cusp and the magnetopause crossing were associated with dayside reconnection. The 23 November 2011 and 8 May 2012, events in this study had the highest reconnection rates and contained the largest fluxes of ions below the cusp in latitude, in agreement with their results.

Flux transfer events are observed at most MESSENGER magnetopause crossings [Slavin *et al.*, 2009; 2010b; 2012], and this is the case for the three extreme solar wind intervals in Figure 6.20d-f. However, the 23 November 2011 event stands out in that FTEs begin to be observed at magnetic latitude $\sim 50^\circ$ and continue until the magnetopause is crossed at 25.4° . The ~ 4 to 10 s quasi-periodicity of these events (see Figure 6.17) is very similar to the “FTE shower” events that Slavin *et al.* [2012] reported tailward of the southern cusp. These FTEs move in response to Maxwell stress as the newly reconnected flux tubes move toward a new equilibrium at the local Alfvén speed [Cowley and Owen, 1989]. Depending upon the direction of the IMF and the location and extent of the region where the FTEs are being formed by reconnection, MESSENGER may or may not be well positioned to observe them [Cooling *et al.*, 2001]. In the case of the three extreme events considered here, the schematic diagrams of X-line

location, based upon IMF orientation, and spacecraft location in Figure 6.20a-c indicate that MESSENGER was properly positioned for observing FTEs moving away from extended low latitude X-line(s) on 23 November 2011 and 11 May 2012. Indeed, these are the two events for which FTE activity is the most widespread in Figure 6.20d-f with more and larger amplitude FTEs being observed for the 23 November 2011 event for which the reconnection rate at the magnetopause was measured to be greater. In contrast, the 8 May 2012 event, which had the highest magnetopause reconnection rate of the three, produced the fewest FTEs and they were localized near the magnetopause crossing. However, inspection of Figure 6.20b shows that MESSENGER was not located in the central outflow region for tilted X-line(s) passing through or near the sub-solar point, and, therefore, much less likely to encounter FTEs.

The 23 November 2011 event also revealed a new observational phenomenon, which we have termed cusp filaments. As shown in Figure 6.16, these $\sim 1 - 2$ s – long decreases in magnetic field intensity are located adjacent to and within the cusp proper where the magnetic field can drop from ~ 250 nT to ~ 20 nT during these brief events. However, these filaments are observed with decreasing amplitude as MESSENGER moved southward through the dayside magnetosphere gradually gaining altitude until it passed through the magnetopause (Figures 6.3 and 6.10). A detailed analysis of these new structures is beyond the scope of this study, but we must note the qualitative similarities between our observations at Mercury and models developed to explain how plasma is injected into the cusp at the Earth. In particular, the similarities between the the 8 min repeat time of FTEs observed at the low-latitude magnetopause at Earth and dynamic changes in cusp auroral emissions and charged particle precipitation have been used to develop detailed models of ion acceleration and transport into the cusp by FTEs [Menietti and Burch, 1988; Smith and Lockwood, 1990]. The time resolution of the MESSENGER plasma measurements do not appear to be sufficient to test the predictions of these Earth-based models of cusp plasma injection at Mercury. However, the Earth models support our suggestion that the high-plasma β filaments observed by MESSENGER near the cusp at Mercury may be due to FTE-associated injections of plasma.

Based on the large-scale diamagnetic decrease in magnetic field during these

events, the ion flux to the surface at the cusps should during the CME and HSS events considered here be an order of magnitude larger than quiet conditions described by *Winslow et al.* [2012]. This could result in an increased source rate to the exosphere via source processes that respond to ion flux. The best known of these is ion sputtering, the ejection of atoms and molecules from a surface following ion impact [*Sarantos et al.*, 2007; *Killen et al.*, 2010; *Wurz et al.*, 2010]. Ions can also contribute to the exosphere indirectly via two processes: chemical sputtering [*Potter*, 1995] and ion-enhanced diffusion [*Killen et al.*, 2001]. Both of these processes aid in freeing atoms from the crystal lattice so that they may be ejected by other processes, usually thermal desorption or UV photon-stimulated desorption. Recent modeling suggests that these indirect processes dominate over ion sputtering for the sodium exosphere [*Mura et al.*, 2009; *Burger et al.*, 2010; *Schmidt et al.*, 2012].

The exosphere is regularly observed by MESSENGER's Mercury Atmospheric and Surface Composition Spectrometer (MASCS) UltraViolet and Visible Spectrometer (UVVS); however, exospheric observations during these extreme solar wind events are severely compromised by increased instrumental backgrounds induced by penetrating energetic particle flux. Further analysis is needed to determine if any signature of an exospheric response to these events can be reliably isolated from these large and variable backgrounds. Before MESSENGER orbital operations began observers regularly inferred that the exosphere responds to ion flux even during periods of relatively quiet space weather [*Potter et al.*, 1990; *McClintock et al.*, 2008; *Leblanc et al.*, 2009; *Vervack et al.*, 2010; *Benna et al.*, 2010; *Burger et al.*, 2010]. The orbital observations analyzed so far have not shown the variability expected if the exosphere responded promptly to changes in ion flux. For example, *Winslow et al.* [2012] and *Raines et al.* [2013, 2014] reported a highly variable cusp and magnetosphere, but *Burger et al.* [2014] and *Cassidy et al.* [2014] found the exosphere to be highly stable as inferred from the lack of year-to-year variation in observations. Such works suggest that there is no simple correspondence between the exospheric and magnetospheric activity, but much of the MESSENGER dataset has not been analyzed and the search for exospheric responses to magnetospheric activity is ongoing.

The three extreme solar wind intervals with solar wind pressures of ~ 44 to 65

nPa, as compared with the typical range of $\sim 5 - 20$ nPa [*Baker et al.*, 2009, 2012; *Winslow et al.*, 2013], examined here reinforce the emerging picture of magnetospheric structure and dynamics at Mercury presented above. Two were due to coronal mass ejections (CMEs) and one to a high-speed stream. The inferred solar ram pressures are ~ 44 to 65 nPa. CMEs typically produce low M_A conditions, at least within their interior regions, and, indeed, strong plasma depletion layers were observed for both the two CME events analyzed here. Further examination of magnetopause structure for these two events (23 November 2011 and 8 May 2012) revealed high reconnection rates, 0.1 – 0.2, despite the small magnetic shear angles of only ~ 27 to 60° across the magnetopause. The high-speed stream produced a more Earth-like high- β magnetosheath and the large magnetic shear angles, ~ 148 to 166° , that would be expected to produce strong reconnection and very possibly a major geomagnetic storm at Earth. However, only low reconnection rates, ~ 0.03 to 0.1, were determined based upon the magnetopause normal magnetic fields most likely due to the high plasma β in the magnetosheath. The relatively modest depth of the large-scale diamagnetic decrease in the cusp region supports our determination that the reconnection rate was lowest for the 11 May 2012 event.

The distance to the subsolar magnetopause is reduced during these events from its mean of $1.45 R_M$ to 1.03 to $1.12 R_M$, with the lowest altitude associated with the CME event with the greatest solar wind pressure and highest reconnection rate (8 May 2012). Despite the effects of induction currents in Mercury’s interior, reconnection-driven erosion lowered the magnetopause to the point where the magnetopause in the southern hemisphere, where the magnetic field is weakest, was at or below the surface.

6.8 Conclusions

This first study of Mercury’s dayside magnetosphere during extreme solar wind conditions has revealed a number of important new processes and facets to its system response: (1) Coronal mass ejections produce very strong plasma depletion layers which support high rates of magnetopause reconnection independent of IMF orientation in agreement with the results of *DiBraccio et al.* [2013] and *Gershman et al.* [2013]. (2) The magnetospheric cusps are observed to become very deep and broad during these

events, relative to the average conditions determined by *Winslow et al.* [2012] and *Raines et al.* [2014], presumably due to the high rate of dayside reconnection and the extreme solar wind pressure. (3) During one of these extreme events quasi-periodic, large amplitude FTEs were observed that strongly resemble the FTE showers events along the high-latitude magnetopause reported by *Slavin et al.* [2012]. (4) A new phenomenon, cusp plasma filaments, was observed adjacent to and in the cusp proper; their cause is not clear, but may be due to the same pulses of magnetopause reconnection that produce FTEs. (5) The subsolar magnetopause was observed at much lower altitudes during these extreme solar wind intervals than predicted by models that include the effects of induction in Mercury's interior [*Hood and Schubert, 1979; Glassmeier et al., 2007*]. We suggest that this is most likely due to the effects of strong dayside reconnection and the reduction in magnetopause altitude that comes as a result of magnetic flux transfer to the magnetotail [*Slavin and Holzer, 1979*]. (6) For the 8 May 2012 event, which occurred during the largest solar wind pressure and exhibited the highest dayside reconnection rate, the magnetopause may have intersected the planetary surface in the southern hemisphere where Mercury's magnetic field is weakest.

CHAPTER VII

CONCLUSIONS

7.1 Summary of Guiding Science Questions

At this time, we revisit the discussion from Section 1.6, outlining the guiding science questions motivating this work, in order to highlight the advancements that have been made with respect to the analyses and results presented in the preceding chapters:

Q1. What impact does magnetic reconnection have on Mercury's magnetosphere?

We have characterized magnetic reconnection in Mercury's magnetosphere using observations of the normal magnetic field component generated at the magnetopause and through the identification of magnetic flux ropes in the cross-tail current sheet. With these measurements we have observed high reconnection rates and determined this rate to be a function of the low- β plasma in Mercury's local space environment, confirming the predictions of *Slavin and Holzer* [1979]. The measured rates were determined to be at least 3 times greater than reconnection rates measured at Earth. This reconnection dependency on plasma β has implications for the dynamics of planetary magnetospheres throughout the heliosphere as solar wind parameters vary with distance from the Sun.

We have demonstrated the influence of reconnection on Mercury's magnetosphere in several additional ways. The high reconnection rates are supported by the short-duration flux ropes observed in the cross-tail current sheet and along the magnetopause. Also, we examined the impact of extreme solar events with varying plasma β and found that the low- β events produce higher

rates of reconnection. We conclude that Mercury's proximity to the Sun creates an environment with conditions favorable for reconnection; therefore, this small magnetosphere experiences high rates of reconnection, which is responsible for the short Dungey cycle.

Q2. What dynamics are associated with solar wind plasma entry and flux circulation throughout Mercury's magnetosphere?

Here, we have characterized three separate regions where the solar wind is able to enter Mercury's magnetosphere: (1) At the dayside magnetopause when the boundary is a rotational discontinuity, thus creating an open magnetosphere configuration and promoting the exchange of plasma between the magnetosheath and the magnetosphere; (2) In the magnetic cusp, observed in the form of "cusp plasma filaments," which are diamagnetic decreases indicating the presence of plasma that has entered along open magnetic field lines; and (3) At the high-latitude magnetotail where we have presented the first observations of Mercury's plasma mantle, characterized as a dense solar wind population, transported into the magnetosphere along convecting field lines, drifting toward the central plasma sheet. Each of these solar wind-entry sites directly results from the magnetosphere-solar wind coupling by magnetic reconnection. In every case, reconnection has made it possible for the solar wind plasma to populate open field lines and enter the system at multiple locations throughout the magnetosphere. This finding reinforces the importance of magnetic reconnection and its role in magnetospheric dynamics at Mercury.

Once the solar wind has accessed the magnetosphere, its presence has direct consequences on the length and time scales throughout the system. We have found the average magnetopause thickness and typical flux rope diameters to be on the order of a solar wind proton gyroradius. Additionally, the local Alfvén speed, a parameter that is dependent on plasma density, is affected by the presence of solar wind plasma. Because reconnection rates are determined by the Alfvén speed, the presence of solar wind plasma will directly affect reconnection in the magnetosphere. Also, measurements of the plasma mantle provide a new

insight to magnetospheric circulation. That is, the reported observations of solar wind plasma entering in the magnetotail and drifting toward the plasma sheet offer an independent measurement of the cross-tail electric field. Quantifying this electric field is critical for the understanding of Mercury's solar wind-driven magnetosphere because it is a direct measure of solar wind momentum being transferred into Mercury's system. The cross-magnetosphere electric potential controls two very important magnetospheric characteristics: (1) the amount of energy particles gain as they move across the magnetosphere and (2) Dungey cycle circulation times.

Q3. How does Mercury's magnetosphere respond to changing upstream solar wind conditions?

We investigate the response of Mercury's magnetosphere by identifying the upstream conditions during magnetopause reconnection events. From this we have determined that reconnection occurs at Mercury's magnetopause independent of magnetic shear between the IMF and the planetary field. Since reconnection is not restricted by IMF orientation, favorable conditions for reconnection are easily met. This result is unique to Mercury because magnetic reconnection is observed to be limited to high-shear, or antiparallel, conditions at Earth and other planetary magnetospheres.

In order to truly understand the impact of solar wind conditions, we have examined the effects of extreme solar events on Mercury's magnetic field to determine whether the magnetic field is able to standoff solar wind bombardment. We find that under intense solar wind forcing, induction fields are generated as a result of Mercury's highly conducting core; however, these induction effects are negated by reconnection. Although we observe magnetopause erosion, as the standoff distance is located below the average position of $1.45 R_M$, Mercury's field is not observed to reach the surface at the subsolar point for these intense upstream conditions. These observations indicate the robustness of Mercury's intrinsic field, which is able to withstand extreme solar events and protect the surface from solar wind impingement. Additionally, these results provide a better

understanding of geomagnetic storms at Earth, which are initiated by the arrival of CMEs and create a low- β environment. Therefore, Mercury's magnetosphere serves as a laboratory for these conditions and our findings are directly applicable to Earth.

7.2 Future Work

Throughout this work, we have reported the initial findings of magnetic reconnection and plasma dynamics in Mercury's magnetosphere using the first orbital observations provided by MESSENGER. This availability of continuous *in situ* data has made it possible to answer key questions regarding dynamics at Mercury, which are also applicable to other magnetospheric systems. However, many aspects of Mercury's plasma and magnetic field environment have yet to be explored and unanswered questions remain.

The natural extension of this work includes the exploration of magnetopause reconnection as a random process as first suggested by *Nishida* [1979]. Mercury's high rates of reconnection make it an ideal candidate for reconnection to produce random open field lines across the magnetopause instead of the organized X-line that can be predicted from calculations of magnetic shear across the surface of the magnetopause (see *Trattner et al.*, 2004, 2007). This work can be explored using the magnetopause reconnection events from Chapter III along with additional reconnection observations as MESSENGER continues to collect data. The direction of the normal component, B_N , can provide information regarding the spacecraft's location with respect to the reconnection X-line. If we augment the number of B_N observations and analyze the location of the X-line as a function of upstream IMF direction, it will be possible to determine whether magnetic reconnection is a random process at Mercury.

In Chapter VI we presented the observed dynamics of Mercury's dayside magnetosphere during extreme solar wind conditions. The next logical step is to understand the response of Mercury's magnetotail from these events. This is important for understanding the effects of extreme solar wind forcing on the entire system. It is expected that, similar to the dayside observations, the nightside magnetosphere will

experience high reconnection rates and possibly even intense loading and unloading of magnetic flux.

One additional project that would have a great impact on the general magnetospheric community, not only to Mercury, is an extensive comparative magnetospheric exploration studying the effects of plasma β on reconnection throughout the heliosphere. Mercury is an extreme case in the sense that frequent plasma depletion layers form as a result of the low- β environment; however, Saturn offers the opposite scenario with a high- β environment and few observations of magnetopause reconnection. Additionally, Earth is a variable environment that experiences fluctuations in plasma parameters creating both Mercury- and Saturn-like cases. Although similar plasma β studies have been explored at these planets individually [i.e., *Phan et al.*, 2010; *Masters et al.*, 2012], a comparative study throughout the heliosphere with increased statistics and a wide range of plasma parameters will make it possible to truly assess the effects of local plasma β on the occurrence of reconnection in planetary magnetospheres.

APPENDIX I

FORCE-FREE FLUX ROPE FITTING TECHNIQUE

In this work, a force-free flux rope model, based on the original studies by *Lundqvist* [1950] and *Lepping et al.* [1990, 1995, 1996], has been fitted to the magnetic flux ropes identified in Mercury's cross-tail current sheet from Chapter IV.

A1.1 Background

In this force-free flux rope fitting technique, the magnetic flux rope structure is assumed to be cylindrically symmetric with the pitch angle of the helical field lines increasing with distance away from the central axis of the flux rope. More specifically, the field at the center of the flux rope is axially aligned and becomes less so with radial distance from the center. This cylindrically symmetric assumption implies that the flux ropes are force-free structures, meaning they have evolved to their lowest energy state (i.e., $\mathbf{J} \times \mathbf{B} = 0$).

The force-free magnetohydrodynamic (MHD) approximation typically occurs in tenuous plasmas where forces due to pressure gradients can be considered negligible. Under this condition, the current density \mathbf{J} becomes everywhere parallel to the magnetic field \mathbf{B} to balance the system. Assuming static equilibrium, the MHD equations simplify to

$$\mathbf{J} \times \mathbf{B} = \nabla P \tag{A1.1}$$

$$\nabla \times \mathbf{B} = \mu_0 \mathbf{J} \quad (\text{A1.2})$$

$$\nabla \cdot \mathbf{B} = 0 \quad (\text{A1.3})$$

where the plasma pressure P is taken to be isotropic, or $\nabla P = 0$. Equation A1.1 simplifies to $\mathbf{J} \times \mathbf{B} = 0$, denoting that the currents are field-aligned and no $\mathbf{J} \times \mathbf{B}$ forces exist inside the system. The current can be described as $\mathbf{J} = \alpha \mathbf{B}$ where α is a scalar function and Ampère's law (equation A1.2) is simplified such that

$$\nabla \times \mathbf{B} = \alpha \mathbf{B} \quad (\text{A1.4})$$

$$\nabla \times (\nabla \times \mathbf{B}) = \nabla \times (\alpha \mathbf{B}) \quad (\text{A1.5})$$

$$\nabla^2 \mathbf{B} = -\alpha^2 \mathbf{B} \quad (\text{A1.6})$$

By applying this argument to cylindrically symmetric flux ropes, *Lundqvist* [1950] demonstrated that one class of force-free solutions satisfying Equation A1.6 uses a magnetic field $\mathbf{B} = (B_R, B_T, B_A)$ of the form

$$B_R = 0 \quad (\text{A1.7})$$

$$B_T = J_1(\alpha r') B_0 H \quad (\text{A1.8})$$

$$B_A = J_0(\alpha r') B_0 \quad (\text{A1.9})$$

where the radial (B_R), axial (B_A), and tangential (B_T) fields, with respect to the central axis of the flux rope, are given in terms of the Bessel functions of the first kind, J_0 and J_1 . B_0 is the magnitude of the core field along the axis of flux rope, H is the handedness of the structure, and r' describes the fractional radial distance from the center of the flux rope, equal to zero at the core and one at the edge. We take α to be constant where $\alpha = 2.4048$, the value at which J_0 reaches zero. Figure A1.1 shows J_0 and J_1 as a function of $\alpha r'$ where the vertical dashed line marks $\alpha r' = 2.4048$, the edge of the modeled flux rope. At the center of the flux rope ($\alpha r' = 0$) the field is purely in the axial direction such that $J_0(0) = 1$ and $J_1(0) = 0$, where $B_A \propto J_0$ and $B_T \propto J_1$ as indicated in Equations A1.7 – A1.9; therefore, $B_A(0) = B_0$ and $B_T(0) = 0$ at this location. At the flux rope edge ($\alpha r' = 2.4048$,

marked by the vertical dashed line), $B_A(2.4048) = 0$ and the field is purely in the tangential direction.

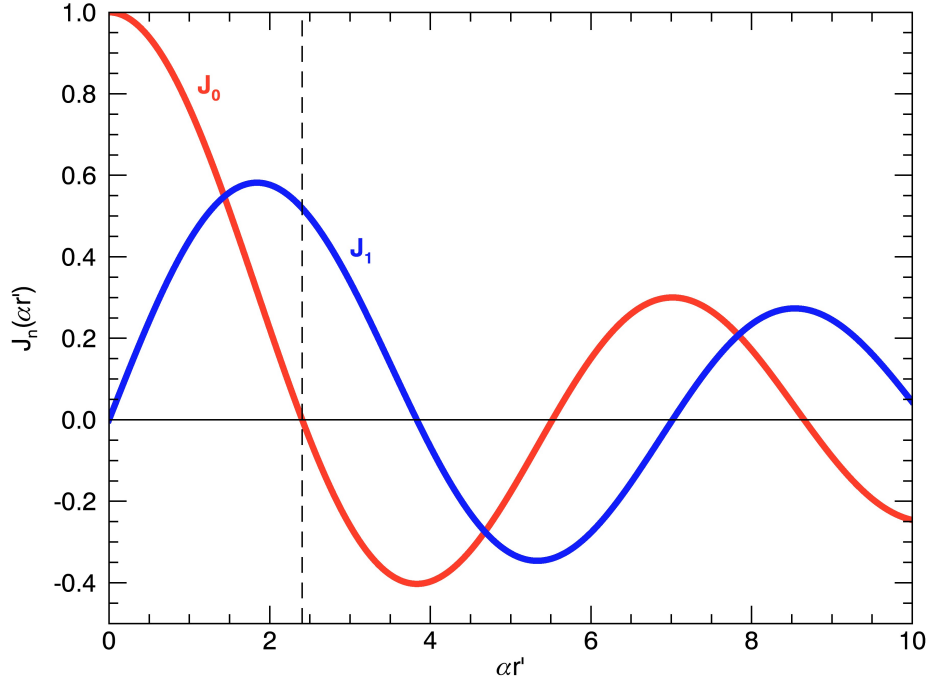


Figure A1.1: Bessel functions of the first kind, J_0 and J_1 , plotted as a function of distance from the flux rope center. Here, $\alpha = 2.4048$ and r' is the fractional radial distance. The dashed vertical line marks the flux rope edge where $\alpha r' = 2.4048$.

A1.2 Data Setup

In order to compare the modeled force-free fields (Equations A1.7–A1.9) with flux rope observations, the magnetic field measurements must be transformed from Cartesian coordinates into the cylindrical B_R - B_A - B_T coordinate system. To begin, the MAG data is in solar wind-aberrated MSM coordinates, defined in Chapter IV. A minimum variance analysis (MVA), described in Chapter III, is performed over the discrete flux rope encounter interval in order to transform the magnetic field observations into minimum (B_1), intermediate (B_2), and maximum (B_3) variance coordinates. The core field of a force-free flux rope will lie in the B_2 direction and the outer helical wraps will be detected in B_3 (see Chapter IV) enabling the observed axial (B_{A_OBS}) and tangential (B_{T_OBS}) fields to be defined from normalized MVA observations:

$$B_{A_OBS} = \frac{B_2}{|B|} \quad (A1.10)$$

$$B_{T_OBS} = \sqrt{\left(\frac{B_1}{|B|}\right)^2 + \left(\frac{B_3}{|B|}\right)^2} \quad (A1.11)$$

When a spacecraft encounters a flux rope, the trajectory does not necessarily cross through the center of the structure; therefore, the point of closest approach (CA) to the flux rope center is defined by the peak magnitude in B_{A_OBS} . Once the point of closest approach is determined, the ratio of B_{A_OBS} to B_{T_OBS} at CA is used to calculate the impact parameter, Y_0/R_0 (shown in Figure A1.2). The impact parameter is the fractional distance that the spacecraft has passed from the flux rope core at closest approach, where Y_0 is the distance from the flux rope center and R_0 is the radius of the flux rope, both of which are unknown at this point. Since $B_A \propto J_0$ and $B_T \propto J_1$ it is also true that $B_{A_OBS}/B_{T_OBS} \propto J_0/J_1$. After determining the value of B_{A_OBS}/B_{T_OBS} at CA we can use the plot in Figure A1.3 to calculate $\alpha r'$ at CA by identifying where the ratio intersects the curve and then calculating the corresponding $\alpha r'$. Then the value of r' , which is equivalent to Y_0/R_0 , is determined by making use of the fact that α is a known constant equal to 2.4048.

Next, by determining the time, t_0 , that it takes the spacecraft to traverse from CA to the edge of the flux rope, and by assuming a speed relative to the flux rope, v , we can calculate X_0 , the distance traveled during this time:

$$X_0 = vt_0 \quad (A1.12)$$

We now have values for X_0 and Y_0/R_0 , and we know that Y_0 and R_0 are constants. Figure A1.2 illustrates these parameters with respect to the flux rope. The frame is oriented such that the spacecraft's trajectory (dashed line) is parallel to the cross-sectional axis of the flux rope (solid horizontal line) in order to form a right-hand triangle (red) between X_0 , Y_0 , and R_0 .

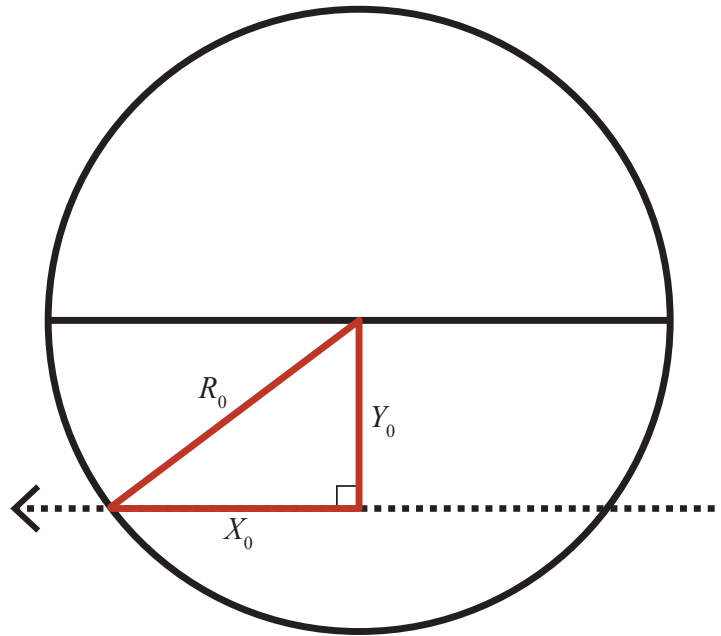


Figure A1.2: A cross-sectional view of a flux rope with an example spacecraft trajectory (dashed line). The solid black horizontal line marks the cross-sectional axis of the flux rope. The spacecraft trajectory is always parallel to the solid black line. This is useful because Y_0 , the distance from the flux rope center at closest approach, will be perpendicular to the trajectory. The distance traveled by the spacecraft from closest approach to the edge of the flux rope is X_0 and R_0 is the flux rope radius. The three parameters Y_0 , X_0 , and R_0 create a right-handed triangle.

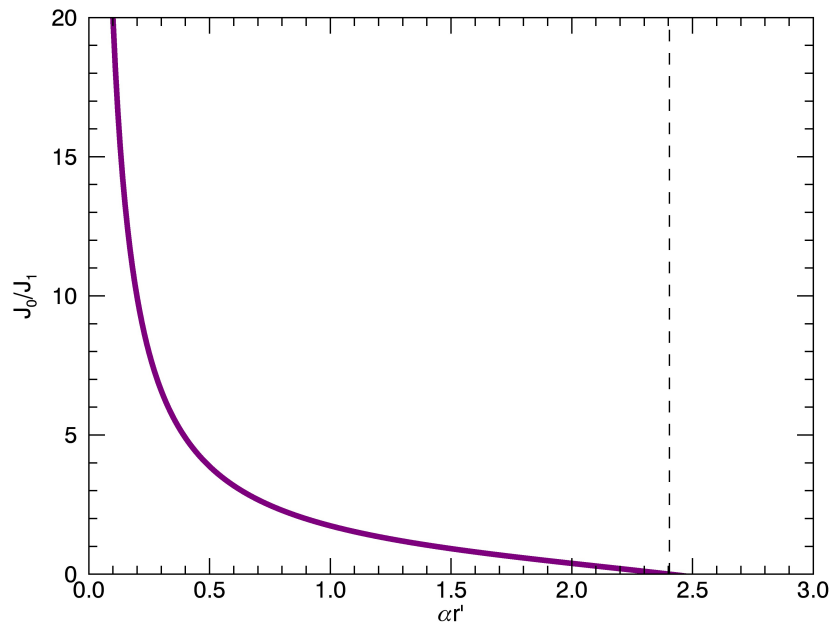


Figure A1.3: The ratio of the Bessel functions of the first kind, J_0 and J_1 , which is proportional to B_{A_OBS}/B_{T_OBS} , plotted as a function of distance from the center of the flux rope. The vertical dashed line represents the edge of the flux rope where $ar' = 2.4048$. By determining where the value of B_{A_OBS}/B_{T_OBS} at closest approach intersects the curve, the associated ar' can be calculated.

A1.3 Force-Free Flux Rope Model

In order to fit a modeled flux rope to the transformed magnetic field data, profiles of B_A and B_T are generated by stepping through the spacecraft trajectory (from Figure A1.2) in increments that are equivalent to the resolution of the data. With each additional increment, a new right-handed triangle is produced (Figure A1.4) where X_i is the distance from CA along the spacecraft's trajectory and R_i is the radial distance from the flux rope center to X_i . The value of X_i will range from zero at closest approach to X_0 at the edge of the flux rope along the spacecraft's path. In Figure A1.4, the blue triangle will have new values of R_i and X_i at each incremental step, marked by the small vertical blue lines, as the steps progress along the trajectory.

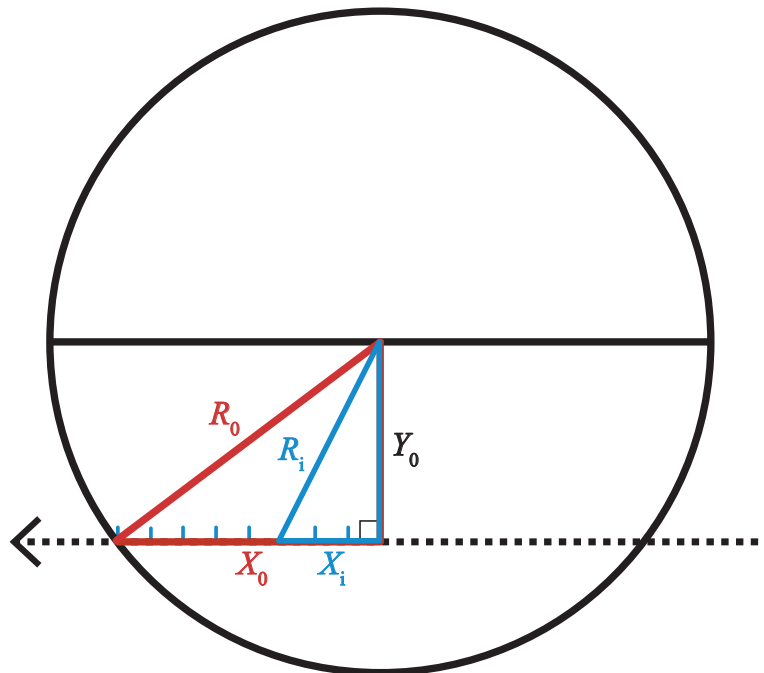


Figure A1.4: A cross-sectional view of a flux rope with an example spacecraft trajectory (dashed line). The solid black horizontal line marks the cross-sectional axis of the flux rope. This closest distance along the spacecraft trajectory to the flux rope center is Y_0 . Making up the red triangle, R_0 is the flux rope radius and X_0 is the distance from closest approach to the flux rope edge. The blue triangle varies with each incremental step set to match the resolution of the data, marked by the small vertical blue lines. X_i is the distance from closest approach to a particular incremental step and R_i is the radial distance from the flux rope center to the location along the trajectory. Both the blue and red triangles are right-handed.

We are able to implement the Pythagorean Theorem in order to relate the parameters from the red and blue triangles:

$$X_0^2 + Y_0^2 = R_0^2 \quad (\text{A1.13})$$

$$X_i^2 + Y_i^2 = R_i^2 \quad (\text{A1.14})$$

After normalizing Equation A1.14 with the flux rope radius, the fractional radial distance, r' , can be described by

$$r' = \frac{R_i}{R_0} = \sqrt{\left(\frac{Y_0}{R_0}\right)^2 + \left(\frac{X_i}{R_0}\right)^2} \quad (\text{A1.15})$$

where the impact parameter, Y_0/R_0 , and the flux rope radius, R_0 , are constants. A quick check shows that at closest approach, where $X_i = 0$, Equation A1.15 reduces to $r' = R_i/R_0 = Y_0/R_0$. After inserting Equation A1.15 into the Bessel functions from Equations A1.8 and A1.9, B_A and B_T now have the form

$$B_A = J_0 \left(\alpha \sqrt{\left(\frac{Y_0}{R_0}\right)^2 + \left(\frac{X_i}{R_0}\right)^2} \right) B_0 \quad (\text{A1.16})$$

$$B_T = J_1 \left(\alpha \sqrt{\left(\frac{Y_0}{R_0}\right)^2 + \left(\frac{X_i}{R_0}\right)^2} \right) B_0 H \quad (\text{A1.17})$$

A1.4 Data-Model Fitting

At this point, the measured axial and tangential fields may be fit to the *Lundqvist* [1950] model. For simplicity, we set B_0 equal to unity, until the actual value is

determined later, because it is simply a scaling factor. Also, we are assuming that $H = 1$. Then, for an assumed radius, R_0 , the modeled values of B_A and B_T are calculated for each step of increasing X_i , from 0 to X_0 . Once the modeled profiles of B_A and B_T are complete, a least squares minimization is implemented between the data and the model results:

$$\chi^2 = \frac{\sum \left[(B_{A_OBS} - B_A)^2 + (B_{T_OBS} - B_T)^2 \right]}{N} \quad (\text{A1.18})$$

where N is the number of data points. This process is repeated over a range of assumed flux rope radii. The radius resulting in the minimization of χ^2 represents the best fit for the force-free flux rope model. A χ^2 threshold, typically around 0.01, must be met in order to accept a given flux rope as meeting the force-free approximation.

Once a best-fit radius is deemed acceptable by the χ^2 criterion, it is possible to establish the spacecraft's proximity to the center of the flux rope (Y_0). The constant value of Y_0/R_0 , determined in Section A1.2, is simply multiplied by the best-fit radius in order to determine the absolute value of Y_0 .

It is now also possible to calculate the flux rope's core field strength, B_0 . To do this, the value of B_A at closest approach, ranging between 0–1, is scaled by a factor, C , to meet the value of B_{A_OBS} at this point, also between 0–1. We determine the scaling factor by simply taking the ratio of the observed axial field to the axial field at the center of the flux rope inferred from the model:

$$C = \frac{B_{A_OBS}}{B_A} \quad (\text{A1.19})$$

In order to solve for B_0 , the value of C is used to scale the unnormalized axial field (B_2 in Equation A1.10) at closest approach:

$$B_0 = CB_2 \quad \text{at CA} \quad (\text{A1.20})$$

Note that unless the spacecraft passes directly through the center of the flux rope, which is typically not the case, the value of B_0 will be greater than the field strength measured at the spacecraft's closest approach ($B_0 > B_2$ at CA).

A1.5 Discussion

The value of B_0 and the modeled flux rope radius R_0 can be used to determine the amount of flux being transported through the magnetosphere by a given flux rope. This is calculated by integrating around the axial magnetic field:

$$\phi = \frac{2\pi B_0 R_0^2}{\alpha} J_1(\alpha) \quad (\text{A1.21})$$

This flux, ϕ , leads to further estimates regarding the total flux rope contribution to transported flux in a planetary magnetosphere when determining the balance of flux throughout the system.

The results of this force-free flux rope model provide several useful parameters, which are otherwise impossible to calculate due to single spacecraft limitations. The implementation of a χ^2 minimization limits the number of accepted flux ropes to only those near a force-free state. This technique is both useful for magnetosphere and heliospheric applications.

REFERENCES

- Achilleos, N., C. S. Arridge, C. Bertucci, C. M. Jackman, M. K. Dougherty, K. K. Khurana, and C. T. Russell (2008), Large-scale dynamics of Saturn's magnetopause: Observations by Cassini, *J. Geophys. Res.*, *113*, A11209, 10.1029/2008JA013265.
- Alexeev, I. I., E. S. Belenkaya, J. A. Slavin, H. Korth, B. J. Anderson, D. N. Baker, S. A. Boardsen, C. L. Johnson, M. E. Purucker, M. Sarantos, and S. C. Solomon (2010), Mercury's magnetospheric magnetic field after the first two MESSENGER flybys, *Icarus*, *209*, 23–39, doi:10.1016/j.icarus.2010.01.024.
- Anderson, B. J., and S. A. Fuselier (1993), Magnetic pulsations from 0.1 to 4.0 Hz and associated plasma properties in the Earth's subsolar magnetosheath and plasma depletion layer, *J. Geophys. Res.*, *98*, 1461–1479, doi:10.1029/92JA02197.
- Anderson, B. J., T. –D. Phan, and S. A. Fuselier (1997), Relationships between plasma depletion and subsolar reconnection, *J. Geophys. Res.*, *102*, 9531.
- Anderson, B. J., M. H. Acuña, D. A. Lohr, J. Scheifele, A. Raval, H. Korth, and J. A. Slavin (2007), The Magnetometer instrument on MESSENGER, *Space Sci. Rev.*, *131*, 417–450, doi:10.1007/s11214-007-9246-7.
- Anderson, B. J., M. H. Acuña, H. Korth, M. E. Purucker, C. L. Johnson, J. A. Slavin, S. C. Solomon, and R. L. McNutt Jr. (2008), The structure of Mercury's magnetic field from MESSENGER's first flyby, *Science*, *321*, 82–85.
- Anderson, B. J., M. H. Acuña, H. Korth, J. A. Slavin, H. Uno, C. L. Johnson, M. E. Purucker, S. C. Solomon, J. M. Raines, T. H. Zurbuchen, G. Gloeckler, and R. L. McNutt Jr. (2010), The magnetic field of Mercury, *Space Sci. Rev.*, *152*, 307–339, doi:10.1007/s11214-009-9544-3.
- Anderson, B. J., C. L. Johnson, H. Korth, M. E. Purucker, R. M. Winslow, J. A. Slavin, S. C. Solomon, R. L. McNutt, Jr. J. M. Raines, and T. H. Zurbuchen (2011a), The global magnetic field of Mercury from MESSENGER orbital observations, *Science*, *333*, 1859–1862, doi:10.1126/science.1211001.
- Anderson, B. J., J. A. Slavin, H. Korth, S. A. Boardsen, T. H. Zurbuchen, J. M. Raines, G. Gloeckler, Ralph L. McNutt Jr., S. C. Solomon (2011b), The dayside

- magnetospheric boundary layer at Mercury, *Planet. Sp. Sci.*, 59, 2037.
- Anderson, B. J., C. L. Johnson, H. Korth, R. M. Winslow, J. E. Borovsky, M. E. Purucker, J. A. Slavin, S. C. Solomon, M. T. Zuber, and R. L. McNutt Jr. (2012), Low-degree structure in Mercury's planetary magnetic field, *J. Geophys. Res.*, 117, E00L12, doi:10.1029/2012JE004159.
- Andrews, G. B., T. H. Zurbuchen, B. H. Mauk, H. Malcom, L. A. Fisk, G. Gloeckler, G. C. Ho, J. S. Kelley, P. L. Koehn, T. W. LeFevre, S. S. Livi, R. A. Lundgren, and J. M. Raines (2007), The Energetic Particle and Plasma Spectrometer instrument on the MESSENGER spacecraft, *Space Sci. Rev.*, 131, 523–556, doi:10.1007/s11214-007-9272-5.
- Arge, C.N., Luhmann, J. G., Odstrcil, D., Schrijver, C. J., Li, Y. (2004), Stream structure and coronal sources of the solar wind during the May 12th, 1997 CME, *J. Atmos. Solar Terr. Phys.*, 66, 1295–1309.
- Aubry, M. P., M. G. Kivelson, and C. T. Russell (1971), Motion and structure of the magnetopause, *J. Geophys. Res.*, 76, 1673.
- Badman, S. V., and S. W. H. Cowley (2007), Significance of Dungey-cycle flows in Jupiter's and Saturn's magnetospheres, and their identification on closed equatorial field lines, *Ann. Geophys.*, 25, 941–951, doi:10.5194/angeo-25-941-2007.
- Baker, D. N., J. A. Simpson, and J. H. Eraker (1986), A model of impulsive acceleration and transport of energetic particles in Mercury's magnetosphere, *J. Geophys. Res.*, 91, 8742–8748, doi:10.1029/JA091iA08p08742.
- Baker, D. N., T. I. Pulkkinen, V. Angelopoulos, W. Baumjohann, and R. L. McPherron (1996), Neutral line model of substorms: Past results and present view, *J. Geophys. Res.*, 101, 12,975-13,010.
- Baker, D. N., D. Odstrcil, B. J. Anderson, C. N. Arge, M. Benna, G. Gloeckler, J. M. Raines, D. Schriver, J. A. Slavin, S. C. Solomon, R. M. Killen, and T. H. Zurbuchen (2009), Space environment of Mercury at the time of the first MESSENGER flyby: Solar wind and interplanetary magnetic field modeling of upstream conditions, *J. Geophys. Res.*, 114, A10101, doi:10.1029/2009JA014287.
- Baker, D. N., D. Odstrcil, B. J. Anderson, C. N. Arge, M. Benna, G. Gloeckler, H. Korth, Leslie R. Mayer, J. M. Raines, D. Schriver, J. A. Slavin, S. C. Solomon, P. M. Trávníček, and T. H. Zurbuchen (2011), The space environment of Mercury at the times of the second and third MESSENGER flybys, *Planet. Space Sci.*, 59, 2066–2074.
- Baker, D. N., et al. (2013), Solar wind forcing at Mercury: WSA-ENLIL model results, *J. Geophys. Res.*, 118, 45–57, doi:10.1029/2012JA018064.

- Benna, M., et al. (2010), Modeling of the magnetosphere of Mercury at the time of the first MESSENGER flyby, *Icarus*, 209, 3–10, doi:10.1016/j.icarus.2009.11.036.
- Berchem, J., and C. T. Russell (1982), The thickness of the magnetopause current layer: ISEE 1 and 2 observations, *J. Geophys. Res.*, 87, 2108–2114, 10.1029/JA087iA04p02108.
- Bida, T. A., R. M. Killen, and T. H. Morgan (2000), Discovery of calcium in Mercury's atmosphere, *Nature*, 404, 6774, 159–161.
- Boardsen, S. A., B. J. Anderson, M. H. Acuña, J. A. Slavin, H. Korth, and S. C. Solomon (2009), Narrow-band ultra-low-frequency wave observations by MESSENGER during its January 2008 flyby through Mercury's magnetosphere, *Geophys. Res. Lett.*, 36, L01104, doi:10.1029/2008GL036034.
- Boardsen, S. A., T. Sundberg, J. A. Slavin, B. J. Anderson, H. Korth, S. C. Solomon, and L. G. Blomberg (2010), Observations of Kelvin–Helmholtz waves along the dusk-side boundary of Mercury's magnetosphere during MESSENGER's third flyby, *Geophys. Res. Lett.*, 37, L12101, doi:10.1029/2010GL043606.
- Boardsen, S. A., J. A. Slavin, B. J. Anderson, H. Korth, D. Schriver, and S. C. Solomon (2012), Survey of coherent ~1 Hz waves in Mercury's inner magnetosphere from MESSENGER observations, *J. Geophys. Res.*, 117, A00M05, doi:10.1029/2012JA017822.
- Borg, A. L., M. G. G. T. Taylor, and J. P. Eastwood (2012), Observations of magnetic flux ropes during magnetic reconnection in the Earth's magnetotail, *Ann. Geophys.*, 30, 761–773.
- Briggs, J. A., D. A. Brain, M. L. Cartwright, J. P. Eastwood, and J. S. Halekas (2011), A statistical study of flux ropes in the Martian magnetosphere, *Planet. Space Sci.*, 59, 1498–1505.
- Broadfoot, A. L., S. Kumar, M. J. S. Belton, and M. B. McElroy (1974), Mercury's atmosphere from Mariner 10: Preliminary results, *Science*, 185, 4146, 166–169.
- Broadfoot, A. L., D. E. Shemansky, and S. Kumar (1976), Mariner 10: Mercury atmosphere, *Geophys. Res. Lett.*, 3, 10, 577–580.
- Burch, J. L. (1973), Rate of erosion of dayside magnetic flux based on a quantitative study of the dependence of polar cusp latitude on the interplanetary magnetic field, *Radio Sci.*, 8, 955.
- Burger, M. H., R. M. Killen, W. E. McClintock, A. W. Merkel, R. J. Vervack, Jr., T. A. Cassidy, M. Sarantos. Seasonal Variations in Mercury's Dayside Calcium Exosphere. *Icarus*, in press.
- Burger, M.H., et al. (2010). Monte Carlo modeling of sodium in Mercury's exosphere

- during the first two MESSENGER flybys. *Icarus*, 209, 63-74.
doi:10.1016/j.icarus.2010.05.007
- Burton, R.K., R.L. McPherron, and C.T. Russell (1975), The terrestrial magnetosphere: A half-wave rectifier of the interplanetary electric field. *Science*, 189, 717.
- Caan, M. N., R. L. McPherron, and C. T. Russell (1977), Characteristics of the association between the interplanetary magnetic field and substorm, *J. Geophys. Res.*, 82, 4837.
- Cassidy, T. A., A. W. Merkel, M. H. Burger, R. M. Killen, W. E. McClintock, R. J. Vervack, Jr., M. Sarantos. Mercury's Seasonal Sodium Exosphere: MESSENGER Observations from Mercury Orbit. in prep.
- Chapman, S., and V. C. A. Ferraro (1931), A new theory of magnetic storms: Part I – The initial phase, *Terr. Magn. Atmos. Electr.*, 36, 77–97, 171–186, and 37, 147–156, 421–429.
- Collier, M. R., and R. P. Lepping (1996), Jovian magnetopause breathing, *Planet. Space Sci.*, 44, 187–197.
- Cooling, B. M. A., Owen, C. J., and Schwartz, S. J.: Role of the magnetosheath flow in determining the motion of open flux tubes, *J. Geophys. Res.*, 106, 18 763–18 776, 2001.
- Cowley, S. W. H. (1980), Plasma Populations in a Simple Open Model Magnetosphere, *Space Sci. Rev.*, 26, 217–275.
- Cowley, S. W. H. (1981), Magnetospheric asymmetries associated with the Y-component of the IMF, *Space Sci. Rev.*, 29, 79–96.
- Cowley, S. W. H., and C. J. Owen, A simple illustrative model of open flux tube motion over the dayside magnetopause (1989), *Planet. Space Sci.*, 37, 1461– 1475.
- Cowley, S. W. H. and Lockwood, M.: Excitation and decay of solar wind-driven flows in the magnetosphere-ionosphere system (1992), *Ann. Geophys.*, 10, 103–115.
- Crooker, N. U. (1979), Dayside merging and cusp geometry, *J. Geophys. Res.*, 84, 951–959.
- Daly, P. W., D. J. Williams, C. T. Russell, and E. Keppler (1981), Particle Signature of Magnetic-Flux Transfer Events at the Magnetopause, *J. Geophys. Res.*, 86, 1628 – 1632.
- Delcourt, D. C., T. E. Moore, S. Orsini, A. Millilo, and J.-A. Sauvaud (2002), Centrifugal acceleration of ions near Mercury, *Geophys. Res. Lett.*, 29, L01591, doi:10.1029/2001GL013829.

- Delcourt, D. C., S. Grimald, F. Leblanc, J.-J. Berthelier, A. Millilo, A. Mura, S. Orsini, and T. E. Moore (2003), A quantitative model of the planetary Na⁺ contribution to Mercury's magnetosphere, *Annal. Geophys.*, *21*, 1723–1736, doi:10.5194/angeo-21-1723-2003.
- Denevi, B. W., C. M. Ernst, H. M. Meyer, M. S. Robinson, S. L. Murchie, J. L. Whitten, J. W. Head, T. R. Watters, S. C. Solomon, L. R. Ostrach, C. R. Chapman, P. K. Byrne, C. Klimczak, and P. N. Peplowski (2013), The distribution and origin of smooth plains on Mercury, *J. Geophys. Res.: Planets*, *118*, 891–907, 10.1029/2012JE002075.
- DiBraccio, G. A., J. A. Slavin, S. A. Boardsen, B. J. Anderson, H. Korth, T. H. Zurbuchen, J. M. Raines, D. N. Baker, R. L. McNutt Jr., and S. C. Solomon (2013), MESSENGER observations of magnetopause structure and dynamics at Mercury, *J. Geophys. Res. Space Physics*, *118*, doi:10.1029/2012JA018123.
- Domingue, D. L., P. L. Koehn, R. M. Killen, A. L. Sprague, M. Sarantos, A. F. Cheng, E. T. Bradley, and W. E. McClintock (2007), Mercury's atmosphere: A surface-bounded exosphere, *Space Sci. Rev.*, *131*, 161–186.
- Dungey, J. W. (1961), Interplanetary magnetic field and the auroral zones, *Phys. Rev. Lett.*, *6*, 47–48, doi:10.1103/PhysRevLett.6.47.
- Eastwood, J. P., T. D. Phan, M. Oieroset, M. A. Shay, K. Malakit, M. Swisdak, J. F. Drake, and A. Masters (2013), Influence of asymmetries and guide fields on the magnetic reconnection diffusion region in collisionless space plasmas, submitted to *Plasma Phys. Control. Fusion*.
- Elphic, R. C., C. A. Cattell, K. Takahashi, S. J. Bame, and C. T. Russell (1986), ISEE-1 and 2 observations of magnetic flux ropes in the magnetotail: FTE's in the plasma sheet?, *Geophys. Res. Lett.*, *13*, 7, 648–651.
- Evans, L. G., P. N. Peplowski, E. A. Rhodes, D. J. Lawrence, T. J. McCoy, L. R. Nittler, S. C. Solomon, A. L. Sprague, K. R. Stockstill-Cahill, R. D. Starr, S. Z. Weider, W. V. Boynton, D. K. Hamara, and J. O. Goldsten (2012), Major-element abundances on the surface of Mercury: Results from the MESSENGER Gamma-Ray Spectrometer, *J. Geophys. Res.*, *117*, E00L07, 10.1029/2012JE004178.
- Fairfield, D. H. (1971), Average and unusual locations for the Earth's magnetopause and bow shock, *J. Geophys. Res.*, *76*, 6700–6716, doi:10.1029/JA076i028p06700.
- Farrugia, C. J., N. V. Erkaev, , H. K. Biernat, and L. F. Burlaga, (1995). Anomalous magnetosheath properties during Earth passage of an interplanetary magnetic cloud. *Journal of Geophysical Research* *100*: doi: 10.1029/95JA01080. issn: 0148-0227.
- Fuselier, S. A., and W. S. Lewis (2011), Properties of near-Earth magnetic reconnection from in-situ observations, *Space Sci. Rev.*, *160*, 95–121.

- Fuselier S. A., K. J. Trattner, S. M. Petrinec, C. J. Owen, and H. Rème (2005), Computing the reconnection rate at the Earth's magnetopause using two spacecraft observations, *J. Geophys. Res.*, *110*, A06212, 10.1029/2004JA010805.
- Fuselier, S. A., S. M. Petrinec, and K. J. Trattner (2010), Antiparallel magnetic reconnection rates at the Earth's magnetopause, *J. Geophys. Res.*, *115*, A10207, doi:10.1029/2010JA015302.
- Fuselier, S. A., K. J. Trattner, and S. M. Petrinec (2011), Antiparallel and component reconnection at the dayside magnetopause, *J. Geophys. Res.*, *116*, A10227, doi:10.1029/2011JA016888.
- Gershman, D. J., J. A. Slavin, J. M. Raines, T. H. Zurbuchen, B. J. Anderson, H. Korth, D. N. Baker, and S. C. Solomon (2013), Magnetic flux pileup and plasma depletion in Mercury's subsolar magnetosheath, *J. Geophys. Res.*, *118*, doi:10.1002/2013JA019244.
- Gershman, D. J., J. A. Slavin, J. M. Raines, T. H. Zurbuchen, B. J. Anderson, H. Korth, D. N. Baker, and S. C. Solomon, Ion kinetic properties in Mercury's pre-midnight plasma sheet, in prep.
- Glassmeier, K.-H. (2000), Currents in Mercury's magnetosphere, in *Magnetospheric Current Systems*, Geophysical Monograph Series, 118, pp. 371-380, American Geophysical Union, Washington, DC.
- Glassmeier, K. -H., J. Grosser, U. Auster, D. Constantinescu, Y. Narita, and S. Stellmach (2007), Electromagnetic Induction Effects and Dynamo Action in the Hermean System, *Space Sci. Rev.*, *132*: 511–527, DOI 10.1007/s11214-007-9244-9.
- Gosling, J. T., et al. (2005), Direct evidence for magnetic reconnection in the solar wind near 1 AU, *J. Geophys. Res.*, *110*, A01107, doi:10.1029/2004JA010809.
- Gosling, J. T., T. D. Phan, R. P. Lin, and A. Szabo (2007), Prevalence of magnetic reconnection at small field shear angles in the solar wind, *Geophys. Res. Lett.*, *34*, L15110, doi:10.1029/2007GL030706.
- Haaland, S. E., B. U. Ö. Sonnerup, M. W. Dunlop, A. Balogh, E. Georgescu, H. Hasegawa, B. Klecker, G. Paschmann, P. Puhl-Quinn, H. Rème, H. Vaith, and A. Vaivads (2004), Four-spacecraft determination of magnetopause orientation, motion, and thickness: Comparison with results from single-spacecraft methods, *Ann. Geophys.*, *22*, 1347–1365, doi:10.5194/angeo-22-1347-2004.
- Hauck, S. A., II, S. C. Solomon, J. -L. Margot, F. G. Lemoine, E. Mazarico, S. J. Peale, M. E. Perry, R. J. Phillips, D. E. Smith, and M. T. Zuber (2012), Mercury's internal structure as constrained by MESSENGER observations, *Lunar Planet. Sci.*, *43*, abstract 1170.

- Hauck, S. A., II., et al. (2013), The curious case of Mercury's internal structure, *J. Geophys. Res. Planets*, *118*, 1204–1220, doi:10.1002/jgre.20091.
- Hesse, M. (2006), Dissipation in magnetic reconnection with a guide magnetic field, *Phys. Plasmas*, *13*, 122107, doi:10.1063/1.2403784.
- Hesse, M., and Kivelson, M. G. (2013), The formation and structure of flux ropes in the magnetotail, in *New Perspectives on the Earth's Magnetotail*, edited by A. Nishida, D. N. Baker, and S. W. H. Cowley, American Geophysical Union, Washington, D. C., doi:10.1029/GM105p0139.
- Hill, T. W., A. J. Dessler, and R. A. Wolf (1976), Mercury and Mars: The role of ionospheric conductivity in the acceleration of magnetospheric particles, *Geophys. Res. Lett.*, *3*, 429–432.
- Holzer, R. E., and J. A. Slavin (1978), Magnetic flux transfer associated with expansions and contractions of the dayside magnetosphere, *J. Geophys. Res.*, *83*, 3,831.
- Hood, L. L., and Schubert, G. (1979), Inhibition of solar wind impingement on Mercury by planetary induction currents, *J. Geophys. Res.* *84*, 2641-2647.
- Hones, E. W., Jr. (1977), Substorm processes in the magnetotail: Comments on "On hot tenuous plasma, fireballs, and boundary layers in the Earth's magnetotail" by L. A. Frank, K. L. Ackerson, and R. P. Lepping, *J. Geophys. Res.*, *82*, 5633.
- Hoppe, M. M., C. T. Russell, L. A. Frank, T. E. Eastman, and E. W. Greenstadt (1981), Upstream hydromagnetic waves and their association with backstreaming ion populations – ISEE 1 and 2 observations, *J. Geophys. Res.*, *86*, 4471–4492, doi:10.1029/JA086iA06p04471.
- Huang, C.-S., A. D. DeJong, and X. Cai (2009), Magnetic flux in the magnetotail and polar cap during sawteeth, isolated substorms, and steady magnetospheric convection events, *J. Geophys. Res.*, *114*, A07202, doi:10.1029/2009JA014232.
- Huddleston, D. E., C. T. Russell, G. Le, and A. Szabo (1997), Magnetopause structure and the role of reconnection at the outer planets, *J. Geophys. Res.*, *102*, 24,289–24,302.
- Hughes, W. J., and D. G. Sibeck (1987), On the 3-dimensional structure of plasmoids, *Geophys. Res. Lett.*, *14*, 6, 636–639.
- Ieda, A., S. Machida, T. Mukai, Y. Saito, T. Yamamoto, A. Nishida, T. Terasawa, and S. Kokubun (1998), Statistical analysis of the plasmoid evolution with Geotail observations, *J. Geophys. Res.*, *103*(A3), 4453–4465, doi:10.1029/97JA03240.
- Imber, S. M., J. A. Slavin, H. U. Auster, and V. Angelopoulos (2011), A THEMIS survey of flux ropes and traveling compression regions: Location of the near-Earth reconnection site during solar minimum, *J. Geophys. Res.*, *116*, A02201,

doi:10.1029/2010JA016026.

- Imber, S. M., J. A. Slavin, S. A. Boardsen, B. J. Anderson, H. Korth, R. L. McNutt Jr. and S. C. Solomon, MESSENGER observations of large dayside flux transfer events: Do they drive Mercury's substorm cycle?, *J. Geophys. Res.*, submitted.
- Izenberg, N. R., R. L. Klima, S. L. Murchie, D. T. Blewett, G. M. Holsclaw, W. E. McClintock, E. Malaret, C. Mauceri, F. Vilas, A. L. Sprague, J. Helbert, D. L. Domingue, J. W. Head III, T. A. Goudge, S. C. Solomon, C. A. Hibbitts, and M. D. Dyar (2014), The low-iron, reduced surface of Mercury as seen in spectral reflectance by MESSENGER, *Icarus*, *228*, 364–374.
- Jackman, C. M., J. A. Slavin, and S. W. H. Cowley (2011), Cassini observations of plasmoid structure and dynamics: Implications for the role of magnetic reconnection in magnetospheric circulation at Saturn, *J. Geophys. Res.*, *116*, A10212, doi:10.1029/2011JA016682.
- Jackson, D. J., and D. B. Beard (1977), The magnetic field of Mercury, *J. Geophys. Res.*, *82*, 19, 2828–2836.
- Joy, S. P., M. G. Kivelson, R. J. Walker, K. K. Khurana, C. T. Russell, and T. Ogino (2002), Probabilistic models of the Jovian magnetopause and bow shock locations, *J. Geophys. Res.*, *107*(A10), 1309, doi:10.1029/2001JA009146.
- Kabin, K., T. I. Gombosi, D. L. DeZeeuw, and K. G. Powell (2000), Interaction of Mercury with the solar wind, *Icarus*, *143*(2), 397-406.
- Kallio, E., and P. Jahunen (2003), Solar wind and magnetospheric ion impact on Mercury's surface, *Geophys. Res. Lett.*, *30*, 1877, doi:10.1029/2003GL017842.
- Kallio, E., P. Wurz, R. Killen, S. McKenna-Lawlor, A. Milillo, A. Mura, S. Massetti, S. Orsini, H. Lammer, P. Janhunen, and W.-H. Ip (2008), On the impact of multiply charged heavy solar wind ions on the surface of Mercury, the Moon and Ceres, *Planet. Space Sci.*, *56*, 1506-1516.
- Kawano, H., and T. Higuchi (1995), The bootstrap method in space physics: Error estimation for the minimum variance analysis, *Geophys. Res. Lett.*, *22*, 307–310.
- Khrabrov, A. V., and B. U. Ö. Sonnerup, (1998), Error estimates for minimum variance analysis, *J. Geophys. Res.*, *105*, 6641–6651.
- Killen, R. M., et al. (2001). Evidence for space weather at Mercury. *J. Geophys. Res.*, *106*, 20,509-20,525. doi:dx.doi.org/10.1029/2000JE001401.
- Knetter, T., F. M. Neubauer, T. Horbury, and A. Balogh (2004), Four-point discontinuity observations using Cluster magnetic field data: A statistical survey, *J. Geophys. Res.*, *109*, A06102, doi:10.1029/2003JA010099.

- Kornack, T. W., P. K. Sollins, and M. R. Brown (1998), Experimental observation of correlated magnetic reconnection and Alfvénic ion jets, *Phys. Rev. E*, *58*, R36.
- Kulsrud, R. M. (1998), Magnetic reconnection in a magnetohydrodynamic plasma, *Phys. Plasmas*, *5*, 1599.
- Kumar, S. (1976), Mercury's atmosphere: A perspective after Mariner 10, *Icarus*, *28*, 579–591.
- Kuritsyn, A., M. Yamada, S. Gerhardt, H. Ji, R. Kulsrud, and Y. Ren (2006), Measurements of the parallel and transverse Spitzer resistivities during collisional magnetic reconnection, *Phys. Plasmas*, *13*, doi: 10.1063/1.2179416.
- Lammer, H., P. Wurz, M. R. Patel, R. Killen, C. Kolb, S. Massetti, S. Orsini, and A. Milillo (2003), The variability of Mercury's exosphere by particle and radiation induced surface release processes, *Icarus*, *166*(2), 238-247.
- Lavraud, B., and J. E. Borovsky (2008), Altered solar wind – magnetosphere Interaction at low Mach numbers: Coronal mass ejections, *J. Geophys. Res.*, *113*, A00B08, doi:10.1029/2008JA013192.
- Le, G., Y. Zheng, C. T. Russell, R. F. Pfaff, J. A. Slavin, N. Lin, F. Mozer, G. Parks, M. Wilber, S. M. Petrinec, E. A. Lucek, and H. Reme (2008), Flux transfer events simultaneously observed by Polar and Cluster: Flux rope in the subsolar region and flux tube addition to the polar cusp, *J. Geophys. Res.*, *113*(A1), doi:10.1029/2007ja012377.
- Leary, J. C., et al. (2007), The MESSENGER spacecraft, *Space Sci. Rev.*, *131*(1-4), 187–217.
- Leblanc, F., and R. E. Johnson (2003), Mercury's sodium exosphere, *Icarus*, *164*(2), 261-281.
- Leblanc, F., and R. E. Johnson (2010), Mercury exosphere I. Global circulation model of its sodium component, *Icarus*, *209*(2), 280-300.
- Leblanc, F., et al. (2009). Short-term variations of Mercury's Na exosphere observed with very high spectral resolution. *Geophys. Res. Lett.* *36*, L07201. doi:dx.doi.org/10.1029/2009GL038089.
- Lee, L. C. and Fu, Z. F. (1985), A theory of magnetic flux transfer at the Earth's magnetopause, *Geophys. Res. Lett.*, *12*, 105–108.
- Lepping, R. P., J. A. Jones, L. F. Burlaga (1990), Magnetic field structure of interplanetary magnetic clouds at 1 Au, *J. Geophys. Res.*, *95* (A8), 11,957–11,965.
- Lepping, R. P., D. H. Fairfield, J. Jones, L. A. Frank, W. R. Paterson, S. Kokubun, T. Yamamoto (1995), Cross-tail magnetic flux ropes as observed by the Geotail

- spacecraft, *Geophys. Res. Lett.*, 22, 10, 1193–1196.
- Lepping, R. P., J. A. Slavin, M. Hesse, J. A. Jones, A. Szabo (1996), Analysis of magnetotail flux ropes with strong core fields: ISEE 3 observations, *J. Geomag. Geoelec.*, 48, 589–601.
- Lepping, R. P., and K. W. Behannon (1980), Magnetic field directional discontinuities: 1. Minimum variance errors, *J. Geophys. Res.*, 85, 4695–4703, doi:10.1029/JA085iA09p04695.
- Lepping, R. P., L. F. Burlaga, and L. W. Klein (1981), Surface waves on Saturn's magnetopause, *Nature*, 292, 750–753, doi:10.1038/292750a0.
- Levy, R. H., H. E. Petschek, and G. L. Siscoe (1964), Aerodynamic aspects of the magnetospheric flow, *AIAA J.*, 2, 2065–2076.
- Lindqvist, P.-A., and F. S. Mozer (1990), The average tangential electric field at the noon magnetopause, *J. Geophys. Res.*, 95, 17, 137–17, 144.
- Lundqvist, S. (1950), Magneto-hydrostatic fields, *Ark. Fys.*, 2, 4, 361–365.
- Massetti, S., S. Orsini, A. Milillo, A. Mura, E. De Angelis, H. Lammer, and P. Wurz (2003), Mapping of the cusp plasma precipitation on the surface of Mercury, *Icarus*, 166(2), 229-237.
- Masters, A., D. G. Mitchell, A. J. Coates, and M. K. Dougherty (2011), Saturn's low-latitude boundary layer 1: Properties and variability, *J. Geophys. Res.*, 116, A06210, doi:10.1029/2010A016421.
- Masters, A., J. P. Eastwood, M. Swisdak, M. F. Thomsen, C. T. Russell, N. Sergis, F. J. Crary, M. K. Dougherty, A. J. Coates, and S. M. Krimigis (2012), The importance of plasma β conditions for magnetic reconnection at Saturn's magnetopause, *Geophys. Res. Lett.*, 39, L08103, doi:10.1029/2012GL051372.
- Masters, A., J. A. Slavin, G. A. DiBraccio, T. Sundberg, R. M. Winslow, C. L. Johnson, B. J. Anderson, and H. Korth (2013), A comparison of magnetic overshoots at the bow shocks of Mercury and Saturn, *J. Geophys. Res.*, 118, doi:10.1002/jgra.50428.
- McAdams, J. V., D. W. Dunham, R. W. Farquhar, A. H. Taylor, and B. G. Williams, Trajectory design and maneuver strategy for the MESSENGER mission to Mercury, *15th Space Flight Mechanics Conference, American Astronautical Society/American Institute of Aeronautics and Astronautics*, paper AAS 05-173, 20 pp., Copper Mountain, CO, January 23-27, 2005.
- McAdams, J. V., S. C. Solomon, P. D. Bedini, E. J. Finnegan, R. L. McNutt, Jr., A. B. Calloway, D. P. Moessner, M. W. Wilson, D. T. Gallagher, C. J. Ercol, and S. H. Flanigan, MESSENGER at Mercury: From orbit insertion to first extended mission, *63rd International Astronautical Congress*, paper IAC-12-C1.5.6, 11 pp.,

Naples, Italy, October 1-5, 2012.

- McAdams, J. V., C. G. Bryan, D. P. Moessner, B. R. Page, D. R. Stanbridge, and K. E. Williams, Orbit design and navigation through the end of MESSENGER's extended mission at Mercury, *24th Space Flight Mechanics Meeting, American Astronautical Society/American Institute of Aeronautics and Astronautics*, paper AAS 14-369, 20 pp., Santa Fe, NM, January 26-30, 2014.
- McClintock, W. E., et al. (2009), MESSENGER observations of Mercury's exosphere: Detection of magnesium and distribution of constituents, *Science*, *324*, 610–613, doi:10.1126/science.1172525.
- McPherron, R. L., C. T. Russell, and M. P. Aubry (1973), Satellite studies of magnetospheric substorms on August 15, 1968: 9. Phenomenological model for substorms, *J. Geophys. Res.*, *78*, 3131–3149.
- Menietti, J. D, and J. L. Burch (1988), Spatial extent of the plasma injection region in the cusp – magnetosheath interface, *J. Geophys. Res.*, *93*, 105.
- Milan, S. E., S. W. H. Cowley, M. Lester, D. M. Wright, J. A. Slavin, M. Fillingim, C. W. Carlson, and H. J. Singer (2004), Response of the magnetotail to changes in the open flux content of the magnetosphere, *J. Geophys. Res.*, *109*, A04220, doi:10.1029/2003JA010350.
- Moldovan, R., B. J. Anderson, C. L. Johnson, J. A. Slavin, H. Korth, M. E. Purucker, and S. C. Solomon (2011), Mercury's magnetopause and bow shock from MESSENGER observations, *EPSC-DPS Joint Meeting Abstracts and Program*, abstract EPSC-DPS2011-674.
- Moldwin, M. B., and W. J. Hughes (1991), Plasmoids as magnetic flux ropes, *J. Geophys. Res.*, *96*(A8), 14,051–14,064, doi:10.1029/91ja01167.
- Moldwin, M. B., and W. J. Hughes (1992), On the formation and evolution of plasmoids: A survey of ISEE 3 Geotail Data, *J. Geophys. Res.*, *97*(A12), 19,259–19,282, doi:10.1029/92JA01598.
- Mozer, F. S., and A. Hull (2010), Scaling the energy conversion rate from magnetic field reconnection to different bodies, *Phys. Plasmas*, *17*, 102906, doi:10.1063/1.3504224.
- Mozer, F. S., and A. Retinò (2007), Quantitative estimates of magnetic field reconnection properties from electric and magnetic field measurements, *J. Geophys. Res.*, *112*, A10206, doi:10.1029/2007JA012406.
- Mozer, F. S., S. D. Bale, and T. D. Phan (2002), Evidence of diffusion regions at a subsolar magnetopause crossing, *Phys. Rev. Lett.*, *89*, A015002, doi:10.1103/PhysRevLett.89.015002.

- Mura, A., et al. (2009). The sodium exosphere of Mercury: Comparison between observations during Mercury's transit and model results, *Icarus*, 200, 1-11. DOI: <http://dx.doi.org/10.1016/j.icarus.2008.11.014>.
- Nagai, T., H. J. Singer, T. Mukai, T. Yamamoto, and S. Kokubun (2000), Development of substorms in the near-Earth tail, *Adv. Space Res.*, 25, 1651–1662.
- Ness, N. F., K. W. Behannon, R. P. Lepping, Y. C. Whang, and K. H. Schatten (1974), Magnetic field observations near mercury: Preliminary results from Mariner 10, *Science*, 185, 151–160.
- Ness, N. F., K. W. Behannon, R. P. Lepping, and Y. C. Whang (1975), Magnetic field of Mercury confirmed, *Nature*, 255, 204–205, doi:10.1038/255204a0.
- Ness, N. F., K. W. Behannon, R. P. Lepping, and Y. C. Whang (1976), Observations of Mercury's magnetic field, *Icarus*, 28, 479–488.
- Newell, P. T., and C. –I. Meng (1987), Cusp width and B_z : Observations and a conceptual model, *J. Geophys. Res.*, 92(A12), 13,673-13,678, doi:10.1029/JA092iA12p13673.
- Newell, P. T., T. Sotirelis, K. Liou, C. –I. Meng, and F. J. Rich (2006), A nearly universal solar wind-magnetosphere coupling function inferred from 10 magnetospheric state variables, *J. Geophys. Res.*, 112, A01206, doi:10.1029/2006JA012015.
- Nishida, A. (1979), Can Random Reconnection on the Magnetopause Produce the Low Latitude Boundary-Layer, *Geophys. Res. Lett.*, 16, 3, 227–230.
- Nittler, L. R., R. D. Starr, S. Z. Weider, T. J. McCoy, W. V. Boynton, D. S. Ebel, C. M. Ernst, L. G. Evans, J. O. Goldsten, D. K. Hamara, D. J. Lawrence, R. L. McNutt, Jr., C. E. Schlemm II, S. C. Solomon, and A. L. Sprague (2011), The major-element composition of Mercury's surface from MESSENGER X-ray spectrometry, *Science*, 333, 1847–1850.
- Odstroil, D., Riley, P. and Zhao, X.P. (2004). Numerical simulation of the 12 May 1997 interplanetary CME event. *J. Geophys. Res.*, 109, doi: 10.1029/2003JA010135.
- Ogilvie, K. W., J. D. Scudder, R. E. Hartle, G. L. Siscoe, H. S. Bridge, A. J. Lazarus, J. R. Asbridge, S. J. Bame, and C. M. Yeates (1974), Observations at Mercury encounter by Plasma Science Experiment on Mariner 10, *Science*, 185, 4146, 145–151.
- Ogilvie, K. W., J. D. Scudder, V. M. Vasyliunas, R. E. Hartle, and G. L. Siscoe (1977), Observations at the planet Mercury by the plasma electron experiment: Mariner 10, *J. Geophys. Res.*, 82, 13, 1807–1824.

- Ono, Y., M. Inomoto, T. Okazaki, and Y. Ueda (1997), Experimental investigation of three-component magnetic reconnection by use of merging spheromaks and tokamaks, *Phys. Plasmas*, *4*, 1953.
- Paschmann, G., G. Haerendel, I. Papamastorakis, N. Sckopke, S. J. Bame, J. T. Gosling, C. T. Russel (1982), Plasma and Magnetic-Field Characteristics of Magnetic-Flux Transfer Events, *J. Geophys. Res.*, *87*, 2159–2168.
- Paschmann, G., I. Papamastorakis, W. Baumjohann, N. Sckopke, C. W. Carlson, B. U. Ö. Sonnerup, and H. Lühr (1986), The magnetopause for large magnetic shear: AMPTE/IRM observations, *J. Geophys. Res.*, *91*, 11,099–11,115, doi:10.1029/JA091iA10p11099.
- Paschmann, G., W. Baumjohann, N. Sckopke, and T. D. Phan (1993), Structure of the dayside magnetopause for low magnetic shear, *J. Geophys. Res.*, *98*, 13,409–13,422.
- Petschek, H. E. (1964), Magnetic field annihilation, in *Symposium on the Physics of Solar Flares*, edited by W. N. Ness, *Spec. Publ. SP-50*, pp. 425–439, NASA, Washington, D.C.
- Phan, T. D., G. Paschmann, and B. U. Ö. Sonnerup (1996), Low-latitude dayside magnetopause and boundary layer for higher magnetic shear, 2. Occurrence of magnetic reconnection, *J. Geophys. Res.*, *101*, 7817–7828.
- Phan, T. D., B. U. Ö. Sonnerup, and R. P. Lin (2001), Fluid and kinetics signatures of reconnection at the dawn tail magnetopause: Wind observations, *J. Geophys. Res.*, *106*, 25,489–25,501.
- Phan, T. D., J. T. Gosling, M. S. Davis, R. M. Skoug, M. Øieroset, R. P. Lin, R. P. Lepping, D. J. McComas, C. W. Smith, H. Reme and A. Balogh (2005), A magnetic reconnection X-line extending more than 390 Earth radii in the solar wind, *Nature* *439*, 175–178 doi:10.1038/nature04393.
- Phan, T. D., J. T. Gosling, G. Paschmann, C. Pasma, J. F. Drake, M. Øieroset, D. Larson, R. P. Lin, and M. S. Davis (2010), The dependence of magnetic reconnection on plasma β and magnetic shear: Evidence from solar wind observations, *Astrophys. J.*, *719*, L199–L203.
- Pilipp, W. G., and G. Morfill (1978), Formation of plasma sheet resulting from plasma mantle dynamics, *J. Geophys. Res.*, *83*, 5670–5678.
- Potter, A., and T. Morgan (1985), Discovery of sodium in the atmosphere of Mercury, *Science*, *229*, 4714, 651–653.
- Potter, A., and T. Morgan (1986), Potassium in the atmosphere of Mercury, *Icarus*, *67*, 2, 336–340.

- Potter, A. E., T. H. Morgan (1990). Evidence for Magnetospheric Effects on the Sodium Atmosphere of Mercury. *Science*, 248, 835-838. doi:dx.doi.org/10.1126/science.248.4957.835
- Potter, A.E. (1995). Chemical sputtering could produce sodium vapor and ice on Mercury. *Geophys. Res. Lett.* 22, 3289-3292. doi:10.1029/95GL03181.
- Potter, A. E., R. M. Killen, and T. H. Morgan (2007), Solar radiation acceleration effects on Mercury sodium emission, *Icarus*, 186, 571–580, doi:10.1016/j.icarus.2006.09.025.
- Priest, E. R., and T. G. Forbes (2000), *Magnetic Reconnection: MHD Theory and Applications*, Cambridge Univ. Press, New York.
- Raines, J. M., J. A. Slavin, T. H. Zurbuchen, G. Gloeckler, B. J. Anderson, D. N. Baker, H. Korth, S. M. Krimigis, and R. L. McNutt Jr. (2011), MESSENGER observations of the plasma environment near Mercury, *Planet. Space Sci.*, 59, 2004–2015, doi:10.1016/j.pss.2011.02.004.
- Raines, J. M., D. J. Gershman, T. H. Zurbuchen, M. Sarantos, J. A. Slavin, J. A. Gilbert, H. Korth, B. J. Anderson, G. Gloeckler, S. M. Krimigis, D. N. Baker, R. L. McNutt Jr., and S. C. Solomon (2013), Distribution and compositional variations of plasma ions in Mercury’s space environment: The first three Mercury years of MESSENGER observations, *J. Geophys. Res.*, 118, 1604–1619, doi:10.1029/2012JA018073.
- Raines, J. M., D. J. Gershman, J. A. Slavin, T. H. Zurbuchen, H. Korth, B. J. Anderson, G. Gloeckler, S. C. Solomon (2014), Magnetospheric cusp structure and dynamics: MESSENGER FIPS measurements of protons and planetary ions at Mercury, *J. Geophys. Res.*, submitted.
- Reiff, P. H., T. W. Hill, and J. L. Burch (1977), Solar wind plasma injection at the dayside magnetospheric cusp, *J. Geophys. Res.*, 82(4), 479–491, doi:10.1029/JA082i004p00479.
- Reiff, P. H., and J. G. Luhmann (1986), Solar wind control of the polar-cap potential, in *Solar Wind-Magnetosphere Coupling*, edited by Y. Kamide and J. A. Slavin, p. 453, Terra Sci., Tokyo.
- Ren, Y., M. Yamada, S. Gerhardt, H. Ji, R. Kulsrud, and A. Kuritsyn (2005), Experimental Verification of the Hall Effect during Magnetic Reconnection in a Laboratory Plasma, *Phys. Rev. Lett.*, 95, 055003.
- Ren, Y., M. Yamada, H. Ji, S. Gerhardt, and R. Kulsrud (2008), Identification of the electron-diffusion region during magnetic reconnection in a laboratory plasma, *Phys. Rev. Lett.*, 101, 085003.
- Richardson, I. G., and S. W. H. Cowley (1985), Plasmoid-associated energetic ion bursts

- in the deep geomagnetic tail: Properties of the boundary layer, *J. Geophys. Res.*, *90*(A12), 12,133–12,158.
- Richardson, I. G., S. W. H. Cowley, E. W. Hones, and S. J. Bame (1987), Plasmoid-associated energetic ions bursts in the deep Geomagnetic tail: Properties of plasmoids and the postplasmoid plasma sheet, *J. Geophys. Res.*, *91*(A9), 9997–10,013, doi:10.1029/Ja092ia09p09997.
- Richardson, J. D. (2002), The magnetosheaths of the outer planets, *Planet. Sp. Sci.*, *50*, 503.
- Rijnbeek, R. P., S. W. H. Cowley, D. J. Southwood, and C. T. Russell (1984), A survey of dayside flux transfer events observed by ISEE-1 and ISEE-2 magnetometers, *J. Geophys. Res.*, *89*, 786– 800.
- Rosenbauer, H., H. Grunwaldt, M. D. Montgomery, G. Paschmann, and N. Sckopke (1975) Heos-2 plasma observations in distant polar magnetosphere – Plasma mantle, *J. Geophys. Res.*, *80*, 19, 2723–2737.
- Russell, C. T. (1977), On the relative locations of the bow shocks of the terrestrial planets, *Geophys. Res. Lett.*, *4*, 387–390.
- Russell, C. T., and R. C. Elphic (1978), Initial ISEE magnetometer results: Magnetopause observations, *Space Sci. Rev.*, *22*, 681–715.
- Russell, C. T., and R. C. Elphic (1979), Observation of Magnetic-Flux Ropes in the Venus Ionosphere, *Nature*, *279*, 616–618.
- Russell, C. T., D. N. Baker, J. A. Slavin (1968), The magnetosphere of Mercury, in *Mercury*, edited by F. Vilas, C. R. Chapman, M. S. Matthews, University of Arizona Press, Tucson, AZ, pp. 514–561.
- Sarantos, M., R. M. Killen, and D. Kim (2007), Predicting the long-term solar wind ion-sputtering source at Mercury, *Planet. Space Sci.*, *55*, 1584–1595.
- Sarantos, M., and J. A. Slavin (2009), On the possible formation of Alfvén wings at Mercury during encounters with coronal mass ejections, *Geophys. Res. Lett.*, *36*, L04107, doi:10.1029/2008GL036747.
- Schmidt, C.A., J. Baumgardner, M. Mendillo, J. K. Wilson (2012). Escape rates and variability constraints for high-energy sodium sources at Mercury. *J. Geophys. Res.*, *117*, A03301. DOI: <http://dx.doi.org/10.1029/2011JA017217>.
- Sckopke, N., and G. Paschmann (1978), Plasma mantle – Survey of magnetotail boundary layer observations, *J. Atmos. Terr. Phys.*, *40*, 3, 261–278.
- Sckopke, N., G. Paschmann, H. Rosenbauer, D. H. Fairfield (1976), Influence of Interplanetary Magnetic-Field on Occurrence and Thickness of Plasma Mantle, *J.*

- Geophys. Res.*, 81, 16, 2687–2691.
- Scurry, L., and C. T. Russell (1991), Proxy studies of energy transfer to the magnetosphere, *J. Geophys. Res.*, 96, 9541–9548, doi:10.1029/91JA00569.
- Scurry, L., C. T. Russell, and J. T. Gosling (1994), Geomagnetic activity and the beta dependence of the dayside reconnection rate, *J. Geophys. Res.*, 99, 14,811–14,814, doi:10.1029/94JA00794.
- Shay, M. A., J. F. Drake, R. E. Denton, and D. Biskamp (1998), Structure of the dissipation region during collisionless magnetic reconnection, *J. Geophys. Res.*, 103(A5), 9165–9176.
- Sergeev, V., R. J. Pellenin, and T. I. Pulkkinen (1996), Steady magnetospheric convection: A review of recent results, *Space Sci. Rev.*, 75:551–604.
- Shue, J.-H., J. K. Chao, H. C. Fu, C. T. Russell, P. Song, K. K. Khurana, and H. J. Singer (1997), A new functional form to study the solar wind control of the magnetopause size and shape, *J. Geophys. Res.*, 102(A5), 9497–9511, doi:10.1029/97JA00196, 1997.
- Sibeck, D. G., and G. L. Siscoe (1984), Downstream Properties of Magnetic-Flux Transfer Events, *J. Geophys. Res.*, 89, 709–715.
- Sibeck, D. G., G. L. Siscoe, J. A. Slavin, E. J. Smith, S. J. Bame, and F. L. Scarf (1984), Magnetotail flux ropes, *Geophys. Res. Lett.*, 11, 10, 1090–1093.
- Sibeck, D. G., G. L. Siscoe, J. A. Slavin, E. J. Smith, B. T. Tsurutani, R. P. Lepping (1985), The distant magnetotail's response to a strong interplanetary magnetic field BY: Twisting, flattening, and field line bending, *J. Geophys. Res.*, 90(A5), 4011–4019.
- Sibeck, D. G., R. E. Lopez, and E. C. Roelof (1991), Solar wind control of the magnetopause shape, location, and motion, *J. Geophys. Res.*, 96, 5489 – 5495.
- Simpson, J. A., J. H. Eraker, J. E. Lamport, and P. H. Walpole (1974) Electrons and protons accelerated in Mercury's magnetic field, *Science*, 185, 4146, 160–166.
- Siscoe, G. and Christopher, L. (1975), Variations in the solar wind stand-off distance at Mercury, *Geophys. Res. Lett.*, 2, 158.
- Siscoe, G. L., and E. Sanchez (1987), An Mhd Model for the Complete Open Magnetotail Boundary, *J. Geophys. Res.*, 92(A7), 7405–7412, Doi 10.1029/JA092ia07p07405.
- Siscoe, G. L., N. F. Ness, and C. M. Yeates (1975), Substorms on Mercury?, *J. Geophys. Res.*, 80, 4359–4363, doi:10.1029/JA080i031p04359.
- Slavin, J. A. (2004), Mercury's magnetosphere, *Adv. Space Res.*, 33, 11, 1859–1874,

doi:10.1016/J.Asr.2003.02.019.

- Slavin, J. A., and R. E. Holzer (1979), The effect of erosion of the solar wind stand-off distance at Mercury, *J. Geophys. Res.*, *84*, 2076–2082.
- Slavin, J. A., and R. E. Holzer (1981), Solar wind flow about the terrestrial planets, 1. Modeling bow shock position and shape, *J. Geophys. Res.*, *86*, 11,401–11,418, doi:10.1029/JA086iA13p11401.
- Slavin, J. A., E. J. Smith, D. G. Sibeck, D. N. Baker, R. D. Zwickl, and S. I. Akasofu (1985), An ISEE-3 study of average and substorm conditions in the distance magnetotail, *J. Geophys. Res.*, *90*, 875–895, doi:10.1029/JA090ia11p10875.
- Slavin, J. A., D. N. Baker, J. D. Cravens, R. C. Elphic, D. H. Fairfield, L. A. Frank, A. B. Galvin, W. J. Hughes, R. H. Manka, D. G. Mitchell, I. G. Richardson, T. R. Sanderson, D. J. Sibeck, E. J. Smith, and R. D. Zwickl (1989), CDAW 8 observations of plasmoid signatures in the Geomagnetic tail: An assessment, *J. Geophys. Res.*, *94*(A11), 15,153–15,175, doi:10.1029/JA094iA11p15153.
- Slavin, J. A., R. P. Lepping, J. Gjerloev, D. H. Fairfield, M. Hesse, C. J. Owen, M. B. Moldwin, T. Nagai, A. Ieda, and T. Mukai (2003a), Geotail observations of magnetic flux ropes in the plasma sheet, *J. Geophys. Res.*, *108*(A1), 1015, doi:10.1029/2002JA009557.
- Slavin, J. A., R. P. Lepping, J. Gjerloev, M. L. Goldstein, D. H. Fairfield, M. H. Acuna, A. Balogh, M. Dunlop, M. G. Kivelson, K. Khurana, A. Fazakerley, C. J. Owen, H. Reme, and J. M. Bosqued (2003b), Cluster electric current density measurements within a magnetic flux rope in the plasma sheet, *Geophys. Res. Lett.*, *30*, 7, doi:10.1029/2002GL016411.
- Slavin, J. A., E. I. Tanskanen, M. Hesse, C. J. Own, M. W. Dunlop, S. Imber, E. A. Lucek, A. Balogh, and K.-H. Glassmeier (2005), Cluster observations of traveling compression regions in the near-tail, *J. Geophys. Res.*, *110*, A06207, doi:10.1029/2004JA010878.
- Slavin, J. A., S. M. Krimigis, M. H. Acuña, B. J. Anderson, D. N. Baker, P. L. Koehn, H. Korth, S. Livi, B. H. Mauk, S. C. Solomon, and T. H. Zurbuchen (2007), MESSENGER: Exploring Mercury's magnetosphere, *Space Sci. Rev.*, *131*, 133–160, doi:10.1007/s11214-007-9154-x.
- Slavin, J. A., et al. (2008), Mercury's magnetosphere after MESSENGER's first flyby, *Science*, *321*, 85–89, doi:10.1126/science.1159040.
- Slavin, J. A., et al. (2009), MESSENGER observations of magnetic reconnection in Mercury's magnetosphere, *Science*, *324*, 606–610.
- Slavin, J. A., et al. (2010), MESSENGER observations of extreme loading and unloading of Mercury's magnetic tail, *Science*, *329*, 665–668.

- Slavin, J. A., *et al.* (2012a), MESSENGER and Mariner 10 flyby observations of magnetotail structure and dynamics at Mercury, *J. Geophys. Res.*, *117*, A01215, doi:10.1029/2011JA016900.
- Slavin, J. A., *et al.* (2012b), MESSENGER observations of a flux-transfer-event shower at Mercury, *J. Geophys. Res.*, *117*, A00M06, doi:10.1029/JA017926.
- Smith, D. E., *et al.* (2012), Gravity field and internal structure of Mercury from MESSENGER, *Science*, *336*, 214-217.
- Smith, M. F., and M. Lockwood (1990), The statistical cusp: A flux transfer event model, *Geophys. Res. Lett.*, *17*, 1069–1072.
- Solomon, S. C., R. L. McNutt Jr., R. E. Gold, and D. L. Domingue (2007), MESSENGER mission overview, *Space Sci. Rev.*, *131*, 3–39, doi:10.1007/s11214-007-9247-6.
- Sonnerup, B. U. Ö. (1971), Magnetopause structure during the magnetic storm of September 24, 1961, *J. Geophys. Res.*, *76*, 6717–6735.
- Sonnerup, B. U. Ö. (1974), Magnetopause reconnection rate, *J. Geophys. Res.*, *79*, 1546–1549, doi:10.1029/JA079i010p01546.
- Sonnerup, B. U. Ö., and L. J. Cahill Jr. (1967), Magnetopause structure and attitude from Explorer 12 observations, *J. Geophys. Res.*, *72*, 171–183.
- Sonnerup, B. U. Ö., and B. G. Ledley (1979), Ogo 5 magnetopause structure and classical reconnection, *J. Geophys. Res.*, *84*, 399–405.
- Sonnerup, B. U. Ö., and M. Scheible (1998), Minimum and maximum variance analysis, in *Analysis Methods for Multi-Spacecraft Data*, edited by G. Paschmann and P. W. Daly, ISSI Scientific Report no. SR-001, chap. 8, pp. 185–220, European Space Agency, Noordwijk, The Netherlands.
- Sonnerup, B. U. Ö., G. Paschmann, I. Papamastorakis, N. Sckopke, G. Haerendel, S. J. Bame, J. R. Asbridge, J. T. Gosling, and C. T. Russell (1981a), Evidence for reconnection at Earth's magnetopause, *J. Geophys. Res.*, *86*, 10,1049–10,067, doi:10.1029/JA086iA12p10049.
- Sonnerup, B. U. Ö., E. J. Smith, B. T. Tsurutani, and J. H. Wolfe (1981b), Structure of Jupiter's magnetopause: Pioneer 10 and 11 observations, *J. Geophys. Res.*, *86*, 3321–3334, doi:10.1029/JA086iA05p03321.
- Spreiter, J. R., A. L. Summers, and A. Y. Alksne (1966), Hydromagnetic flow around the magnetosphere, *Planet. Space Sci.*, *14*, 223–253, doi:10.1016/0032-0633(66)90124-3.

- Suess, S. T. and Goldstein, B. E. (1979) Compression of the Hermean magnetosphere by the solar wind, *J. Geophys. Res.*, *84*, 3306.
- Sundberg, T., S. A. Boardsen, J. A. Slavin, L. G. Blomberg, and H. Korth (2010), The Kelvin-Helmholtz instability at Mercury: An assessment, *Planet. Space Sci.*, *58*, 1434–1441, doi:10.1016/j.pss.2010.06.008.
- Sundberg, T., S. A. Boardsen, J. A. Slavin, B. J. Anderson, H. Korth, T. H. Zurbuchen, J. M. Raines, and S. C. Solomon (2012a), MESSENGER orbital observations of large-amplitude Kelvin-Helmholtz waves at Mercury's magnetopause, *J. Geophys. Res.*, *117*, A04216, doi:10.1029/2011JA017268.
- Sundberg, T., J. A. Slavin, S. A. Boardsen, B. J. Anderson, H. Korth, G. C. Ho, D. Schriver, V. M. Uritsky, T. H. Zurbuchen, J. M. Raines, D. N. Baker, S. M. Krimigis, R. L. McNutt Jr., and S. C. Solomon (2012b), MESSENGER observations of dipolarization events in Mercury's magnetotail, *J. Geophys. Res.*, *117*, doi:10.1029/2012JA017756.
- Swisdak, M., B. N. Rogers, J. F. Drake, and M. A. Shay (2003), Diamagnetic suppression of component magnetic reconnection at the magnetopause, *J. Geophys. Res.*, *108*(A5), 1218, doi:10.1029/2002JA009726.
- Swisdak, M., M. Opher, J. F. Drake, and F. A. Bibi (2010), The vector direction of the interstellar magnetic field outside the heliosphere, *Astrophys. J.*, *710*, 1769–1775, doi:10.1088/0004-637X/710/2/1769.
- Tanskanen, E., J. A. Slavin, D. H. Fairfield, D. G. Sibeck, J. Gjerloev, T. Mukai, A. Ieda, T. Nagai (2005), Response of the magnetotail to prolonged southward Bz intervals: Loading, unloading, and continuous dissipation, *J. Geophys. Res.*, *110*, A03216, doi:10.1029/2004JA010561.
- Tanskanen, E. I. (2009), A comprehensive high-throughput analysis of substorms observed by IMAGE magnetometer network: Years 1993–2003 examined, *J. Geophys. Res.*, *114*, A05204, doi:10.1029/2008JA013682.
- Toth, G., and D. Odstril (1996), Comparison of some flux corrected transport and total variation diminishing numerical schemes for hydrodynamic and magnetohydrodynamic problems, *J. Comp. Phys.* *128*, 1, 82-100.
- Trattner, K. J., S. A. Fuselier, and S. M. Petrinec (2004), Location of the reconnection line for northward interplanetary magnetic field, *J. Geophys. Res.*, *109*(A3), L03108, doi:10.1029/2003JA009975.
- Trattner, K. J., J. S. Mulcock, S. M. Petrinec, and S. A. Fuselier (2007), Location of the reconnection line at the magnetopause during southward IMF conditions, *Geophys. Res. Lett.*, *34*, L03108, doi:10.1029/1006GL028397.

- Trávníček, P. M., D. Schriver, P. Hellinger, D. Herčík, B. J. Anderson, M. Sarantos, and J. A. Slavin (2010), Mercury's magnetosphere–solar wind interaction for northward and southward interplanetary magnetic field: Hybrid simulations, *Icarus*, 209, 11–22, doi:10.1016/j.icarus.2010.01.008.
- Trenchi, L., M. F. Marcucci, G. Pallochia, G. Consolini, M. B. Bavassano Cattaneo, A. M. Di Lellis, H. Rème, L. Kistler, C. M. Carr, and J. B. Cao (2008), Occurrence of reconnection jets at the dayside magnetopause: Double star observations, *J. Geophys. Res.*, 113, A07S10, doi:10.1029/2007JA012774.
- Vaivads, A., Y. Khotyaintsev, M. André, A. Retinò, S. C. Buchert, B. N. Rogers, P. Décreau, G. Paschmann, and T. D. Phan (2004), Structure of the magnetic reconnection diffusion region from four-spacecraft observations. *Phys. Rev. Lett.*, 93, doi:10.1103/PhysRevLett.93.105001.
- Vervack, R.J., et al. (2010). Mercury's Complex Exosphere: Results from MESSENGER's Third Flyby, *Science*, 329, 672-675. DOI: <http://dx.doi.org/10.1126/science.1188572>.
- Vogt, M. F., C. M. Jackman, J. A. Slavin, E. J. Bunce, S. W. H. Cowley, M. G. Kivelson, and K. K. Khurana (2014), Structure and statistical properties of plasmoids in Jupiter's magnetotail, *J. Geophys. Res. Space Physics*, 119, 821–843, doi:10.1002/2013JA019393.
- Wang, Y. L., et al. (2005), Initial results of high-latitude magnetopause and low-latitude flank flux transfer events from 3 years of Cluster observations, *J. Geophys. Res.*, 110, A11221, doi:10.1029/2005JA011150.
- Weider, S. Z., and L. R. Nittler (2013), The surface composition of Mercury as seen from MESSENGER, *Elements*, 9, 2, 90–91.
- Went, D. R., M. G. Kivelson, N. Achilleos, C. S. Arridge, and M. K. Dougherty (2011), Outer magnetopause structure: Jupiter and Saturn compared, *J. Geophys. Res.*, 116, A04224, doi:10.1029/2010JA016045.
- Whang, Y. C. (1977), Magnetospheric magnetic field of Mercury, *J. Geophys. Res.*, 82, 7, 1024–1030.
- Willis, D. M. (1975), The microstructure of the magnetopause, *Geophys. J. Roy. Astron. Soc.*, 41, 355–389.
- Winslow, R. M., C. L. Johnson, B. J. Anderson, H. Korth, J. A. Slavin, M. E. Purucker, and S. C. Solomon (2012), Observations of Mercury's northern cusp with MESSENGER's magnetometer, *Geophys. Res. Lett.*, 39, L08112, doi:10.1029/2012GL051472.

- Winslow, R. M., B. J. Anderson, C. L. Johnson, J. A. Slavin, H. Korth, M. E. Purucker, D. N. Baker, S. C. Solomon (2013), Mercury's magnetopause and bow shock from MESSENGER Magnetometer observations, *J. Geophys. Res.*, *118*, 2213–2227, doi:10.1002/jgra.50237.
- Wurz, P., J. A. Whitby, U. Rohner, J. A. Martín-Fernández, H. Lammer, C. Kolb (2010), Self-consistent modelling of Mercury's exosphere by sputtering, micro-meteorite impact and photon-stimulated desorption. *Planet. Space Sci.* *58*, 1599-1616. doi:http://dx.doi.org/10.1016/j.pss.2010.08.003.
- Xie, H., L. Ofman, and G. Lawrence (2004), Cone model for halo CMEs: Application to space weather forecasting, *J. Geophys. Res.*, *109*, A03109, doi:10.1029/2003JA010226.
- Yamada, M., R. Kulsrud, and H. Ji (2010), Magnetic reconnection, *Rev. Mod. Phys.*, *82*, 603–664, doi:10.1103/RevModPhys.82.603.
- Yamada, M., Y. Ono, A. Hayakawa, M. Katsurai, and F. Perkins (1990), Magnetic reconnection of plasma toroids with coelicity and counterhelicity, *Phys. Rev. Lett.*, *65*, 721.
- Yamada, M., H. Ji, S. Hsu, T. Carter, R. Kulsrud, N. Bretz, F. Jobes, Y. Ono, and F. Perkins (1997), Study of driven magnetic reconnection in a laboratory plasma, *Phys. Plasmas*, *4*, 1936, doi:10.1063/1.872336.
- Yamada, M., H. Ji, S. Hsu, T. Carter, R. Kulsrud, and F. Trintchouk (2000), Experimental investigation of the neutral sheet profile during magnetic reconnection, *Phys. Plasmas*, *7*, 1781.
- Yamada, M., Y. Ren, H. Ji, J. Breslau, S. Gerhardt, R. Kulsrud, and A. Kuritsyn (2006), Experimental study of two-fluid effects on magnetic reconnection in a laboratory plasma with variable collisionality, *Phys. Plasmas*, *13*, 052119.
- Zhang, H., K. K. Khurana, M. G. Kivelson, V. Angelopoulos, Z. Y. Pu, Q.-G. Zong, J. Liu, and X.-Z. Zhou (2008), Modeling a force-free flux transfer event probed by multiple THEMIS spacecraft, *J. Geophys. Res.*, *113*, A00C05, doi:10.1029/2008JA013451.
- Zhou, X.-W., and C. T. Russell (1997), The location of the high-latitude polar cusp and the shape of the surrounding magnetopause, *J. Geophys. Res.*, *102*, 105–110, doi:10.1029/96JA02702.
- Zhou, X. -W., C. T. Russell, G. Le, S. A. Fuselier, and J. D. Scudder (2000), Solar wind control of the polar cusp at high latitude, *J. Geophys. Res.*, *105*(A21), 245-251, doi:10.1029/1999JA900412.
- Zurbuchen, T. H., G. Gloeckler, J. C. Cain, S. E. Lasley, and W. Shanks (1998), A low-weight plasma instrument to be used in the inner heliosphere, in *Conference on*

- Missions to the Sun II*, edited by C. M. Korendyke, Proceedings of the Society of Photo-Optical Instrumentation Engineers, vol. 3442, pp. 217–224.
- Zurbuchen, T. H., J. M. Raines, G. Gloeckler, S. M. Krimigis, J. A. Slavin, P. L. Koehn, R. M. Killen, A. L. Sprague, R. L. McNutt Jr., and S. C. Solomon (2008), MESSENGER observations of the composition of Mercury's ionized exosphere and plasma environment, *Science*, *321*, 90–92, doi:10.1126/science.1159314.
- Zurbuchen, T. H., J. M. Raines, J. A. Slavin, D. J. Gershman, J. A. Gilbert, G. Gloeckler, B. J. Anderson, D. N. Baker, H. Korth, S. M. Krimigis, M. Sarantos, D. Schriver, R. L. McNutt Jr., and S. C. Solomon (2011), MESSENGER observations of the spatial distribution of planetary ions near Mercury, *Science*, *333*, 1862–1865, doi:10.1126/science.1211302.
- Zwan, B. J., and R. A. Wolf (1976), Depletion of the solar wind plasma near a planetary boundary, *J. Geophys. Res.*, *81*, 1636–1648, doi:10.1029/JA081i010p01636.